

Copyright
by
Menzer Pehlivan
2013

**The Dissertation Committee for Menzer Pehlivan Certifies that this is the approved
version of the following dissertation:**

**Incorporating Site Response Analysis and Associated
Uncertainties into the Seismic Hazard Assessment of
Nuclear Facilities**

Committee:

Ellen M. Rathje, Supervisor

Robert B. Gilbert, Co-Supervisor

Kenneth H. Stokoe II

Lance Manuel

Brady R. Cox

**Incorporating Site Response Analysis and Associated
Uncertainties into the Seismic Hazard Assessment of
Nuclear Facilities**

by

Menzer Pehlivan, B.S.; M.S.

Dissertation

Presented to the Faculty of the Graduate School of

The University of Texas at Austin

in Partial Fulfillment

of the Requirements

for the Degree of

Doctor of Philosophy

The University of Texas at Austin

May 2013

To My Lovely Mother and Grandfather...

Acknowledgements

I would like to express my sincerest gratitude to my supervisor, Ellen M. Rathje, for believing in me. Her support, encouragement, understanding, mentorship, and guidance brought me to where I am today. She has been a wonderful role model and I am very grateful for all the opportunities she has provided me over past four years.

I would like to thank my co-supervisor, Robert B. Gilbert, for all of his valuable contributions, but more than that, I would like to thank him for his endless support. I consider myself very lucky to have had the opportunity to work with him as he is both a wonderful engineer and mentor.

I would like to acknowledge my dissertation committee Kenneth H. Stokoe II, Chadi El Mohtar, Brady Cox, and Lance Manuel for their valuable feedback on this study and reviewing my dissertation. It was a real pleasure to have the good fortune to know and learn from Dr. Stokoe. His knowledge and personality have definitely helped shape the person that I am today. I would also like to give my special thanks to Dr. Manuel for the guidance and the support he has given me over past four years.

Financial support for this research study was provided by the Nuclear Regulatory Commission under grant NRC-04-09-134. This support is gratefully acknowledged

The geotechnical engineering group at UT became a second family to me. I took many wonderful classes that taught me to think critically and inspired me to do and

explore more. I have had chance to make valuable friendships with people who will become the distinguished professionals of the future.

I would like to thank all of my friends, who have worked on a project, struggled through a homework assignment, discussed a topic, shared an opinion, or who have just shared a drink with me. All of you have made my time at UT exceptional. However there are some who have shared all my journey and who have made major impact in my past 4 years; Dr. Rachelle Howell, soon to be Drs. Onur Kacar, Yiorgos Zalachoris, and Oscar Suncar. My time at UT would not have been the same without you. I am so grateful to know each and every one of you. Yiorgos, thank you for picking me up from the airport on August 15, 2009 and for being there for me ever since. Onur, thank you for being this amazing and supportive friend, it has been a comfort to me to know that you are there. Oscar, thank you for all the dances, shows, concerts, trips, adventures, and good memories that definitely made my last 4 year less ordinary. Rachelle, thank you for reminding me to breathe when I would forget to do so, and for being my superman.

When I look back to last four years of my life in Austin, I can confidently say that I had the time of my life. Words and pages are not enough to thank each wonderful person whose path has crossed mine and who has taught me a something new and special. Thanks to all of you; I can now dance salsa, merengue, and bachata, and I can somehow speak Spanish. Thank you Vasilis Samaras for insisting that I go to that Tango class with you, which became a passion of mine and has given me the chance to meet the many wonderful people who did not hesitate to share my sleepless nights while I was writing my dissertation.

Last, but never the least, I would like to give my deepest appreciation and biggest gratitude to my wonderful mom, Ulku Pehlivan, my exceptional grandfather, Osman Gelisen, and my national champion little brother, Tanzer Pehlivan. Thank you for loving me so much, trusting me unconditionally, and always believing in me even during the times when I doubted myself. Mom and grandfa, there are no expressions that can describe my love and my gratitude to you. I am who I am thanks to you and I owe all my success and recognition to you two. I love you with all my heart.

MENZER PEHLIVAN

Incorporating Site Response Analysis and Associated Uncertainties into the Seismic Hazard Assessment of Nuclear Facilities

Menzer Pehlivan, Ph.D.

The University of Texas at Austin, 2013

Supervisor: Ellen M. Rathje

Co-Supervisor: Robert B. Gilbert

Abstract: The development of a site-specific seismic hazard curve for a soil site requires the incorporation of site effects into the hazard calculation through the use of a site-specific amplification function. This study investigates the effect on the resulting soil hazard curves of different approaches to compute the site-specific amplification functions. Amplification functions and their associated standard deviations can be obtained using one-dimensional (1D) or two-dimensional (2D) equivalent linear site response analyses. For 1D analysis, site response analysis can be performed using either time series (TS) or random vibration theory (RVT) approaches. This study compares the amplification function predictions of these two approaches on a shallow and a deep site at four selected periods. The influence of spatial variability introduced through randomization of site shear wave velocity (V_S) on predicted amplification function and soil hazard curves is also investigated. Site amplification predictions of TS and RVT

approaches are generally similar except for the RVT analysis near the site period, which predicts higher amplification compare to TS. Shear wave velocity profile randomization does not significantly change the predicted amplification functions, except for the periods near the site period. At these periods, V_S randomization reduces the amplification function predicted by RVT making it more similar to the TS analysis prediction. The surface hazard at a site is dependent on the median amplification factor and its associated standard deviation.

Spatial variability and uncertainties in soil properties across a site are often taken into account by modeling multiple 1D profiles in 1D site response analyses. However, this approach assumes that analyzing multiple 1D profiles captures accurately the effects of the true multi-dimensional spatial variability of the soil properties. This study investigates the results of two-dimensional (2D) site response analyses that incorporate spatial variability in the V_S profile through Monte Carlo simulation. Two-dimensional site response analyses are performed for 2D random fields generated with various statistical parameters (i.e. vertical and horizontal correlation distances) to investigate the effect of different levels of spatial variability on surface response across a region of interest (ROI). Two-dimensional site response analyses are performed for a shallow site. Results indicate that horizontal correlation distance has more influence on the analyses results than the vertical correlation distance. As the horizontal correlation distance increases, the median surface response spectrum across the ROI decreases. This reduction in median surface response is more pronounced around the site period. The influence of the vertical correlation distance is more pronounced when the horizontal correlation

distance is large. As the vertical correlation distance increases, the median surface response spectrum across the ROI increases, which is more pronounced around the period of the motion. The predictions of 1D and 2D site response analyses modeling the V_S variability are compared. 1D analyses are performed on separately generated 1D V_S profiles (infinite horizontal correlation) and on the V_S profiles across the ROI of each 2D V_S field realization generated for 2D analysis (finite horizontal correlation). The results indicate that both sets of 1D analyses predict lower median response than 2D analyses. The 1D analyses with finite horizontal correlation display comparable levels of variability in the site response, however 1D analyses with infinite horizontal correlation display higher variability.

Table of Contents

List of Tables	xv
List of Figures	xvii
1 INTRODUCTION	1
1.1 Research Motivation	1
1.2 Objectives and Methodology	2
1.3 Scope of the Dissertation	5
2 PROBABILISTIC SEISMIC HAZARD ANALYSIS AND SITE RESPONSE ANALYSIS	7
2.1 Introduction	7
2.2 Probabilistic Seismic Hazard Analysis (PSHA)	9
2.3 An Overview of Available Site Response Analysis Methods	13
2.4 An Overview of Available Approaches for Integrating PSHA and Site Response	20
2.5 Results from Previous Studies	25
2.6 Summary	33
3 DESCRIPTION OF STUDY SITE AND INPUT PARAMETERS	35
3.1 Introduction	35
3.2 Description of Study Sites	36
3.2.1 Shallow Site: Sylmar County Hospital Site	36
3.2.2 Deep Site: Calvert Cliffs Site	39

3.3	Rock Motion Characterization.....	43
3.4	Summary	55
4	DEVELOPMENT OF SOIL HAZARD CURVES: SHALLOW SOIL SITE	56
4.1	Introduction.....	56
4.2	Amplification Relationships for Known Shear Wave Velocity Profile.....	58
	4.2.1 Results from Time Series Analysis.....	58
	4.2.2 Results from RVT Analysis.....	63
4.3	Amplification Relationships for Varied Shear Wave Velocity Profiles	72
	4.3.1 Results from Time Series Analyses	73
	4.3.2 Results from RVT Analyses	80
4.4	Comparison of Amplification Relationships	93
4.5	Soil Hazard Curves	104
4.6	Summary	114
5	DEVELOPMENT OF SOIL HAZARD CURVES: DEEP SOIL SITE.....	115
5.1	Introduction.....	115
5.2	Amplification Relationships for Known Shear Wave Velocity Profile.....	116
	5.2.1 Results from Time Series Analyses	116
	5.2.2 Results from RVT Analysis.....	120
5.3	Amplification Relationships for Varied Shear Wave Velocity Profiles	124
	5.3.1 Results from Time Series Analyses	125
	5.3.2 Results from RVT Analysis.....	128
5.4	Comparison of Amplification Relationships	132
5.5	Soil Hazard Curves	136
5.6	Summary	142

6	TWO-DIMENSIONAL VELOCITY FIELDS	143
6.1	Introduction.....	143
6.2	Baseline Soil Properties	144
6.3	Generation of 2D Shear Wave Velocity Fields.....	146
6.4	Characteristics of Two-Dimensional Shear Wave Velocity Fields	150
	6.4.1 Variability within a Single 2D Velocity Field Realization.....	150
	6.4.2 Variability across Multiple 2D Velocity Field Realizations.....	162
6.5	SUMMARY.....	169
7	SITE AMPLIFICATION PREDICTIONS FOR TWO-DIMENSIONAL VELOCITY FIELDS.....	170
7.1	Introduction.....	170
7.2	Two-Dimensional Site Response Analysis	171
7.3	Influence of Horizontal Correlation on Two-Dimensional Site Response .	178
7.4	Influence of Vertical Correlation on Two-Dimensional Site Response	187
7.5	Influence of Input Motion Characteristics on Two-Dimensional Site Response	202
7.6	SUMMARY.....	213
8	COMPARISON OF ONE- AND TWO-DIMENSIONAL SITE RESPONSE ANALYSES WITH VARIABLE VELOCITY FIELDS.....	215
8.1	Introduction.....	215
8.2	One-Dimensional Analysis with Infinite Horizontal Correlation	217
8.3	One-Dimensional Analysis with Finite Horizontal Correlation	235
8.4	Summary	241

9	SUMMARY, CONCLUSIONS, AND RECOMMENDATIONS FOR FUTURE WORK	242
9.1	Summary	242
9.2	Conclusions.....	245
9.3	Recommendations for Future Work.....	249
	References.....	251
	Vita	254

List of Tables

Table 3.1 Shallow site (i.e. SCH site) profile with corresponding shear-wave velocity, V_S	37
Table 3.2 Deep site (i.e. CC site) profile with corresponding shear-wave velocity, V_S	41
Table 3.3 Controlling earthquakes obtained from deaggregation of selected probability of exceedance levels.....	52
Table 4.1 Regression coefficients and associated $\sigma_{\ln AF}$ for AF relationships developed for TS analysis.....	63
Table 4.2 Regression coefficients and associated $\sigma_{\ln AF}$ for AF relationships developed for RVT analysis.....	67
Table 4.3 Regression coefficients and associated $\sigma_{\ln AF}$ for AF relationships developed for RVT-CE analysis data	71
Table 4.4 Regression coefficients and associated $\sigma_{\ln AF}$ for AF relationships developed for TS analysis with $\sigma_{\ln V_S} = 0.1$	79
Table 4.5 Regression coefficients and associated $\sigma_{\ln AF}$ for AF relationships developed for TS analysis with $\sigma_{\ln V_S} = 0.2$	79
Table 4.6 Regression coefficients and associated $\sigma_{\ln AF}$ for AF relationships developed for TS analysis with $\sigma_{\ln V_S} = 0.3$	80
Table 4.7 Regression coefficients and associated $\sigma_{\ln AF}$ for AF relationships developed for RVT analysis with $\sigma_{\ln V_S} = 0.2$	84
Table 4.8 Regression coefficients and associated $\sigma_{\ln AF}$ of AF relationships developed for RVT-CE analysis with $\sigma_{\ln V_S} = 0.1$	90

Table 4.9 Regression coefficients and associated $\sigma_{\ln AF}$ of AF relationships developed for RVT-CE analysis with $\sigma_{\ln V_s} = 0.2$	91
Table 4.10 Regression coefficients and associated $\sigma_{\ln AF}$ of AF relationships developed for RVT-CE analysis with $\sigma_{\ln V_s} = 0.3$	92
Table 4.11 Comparison of $\sigma_{\ln AF}$ for different AF relationships.....	101
Table 4.12 Variable $\sigma_{\ln AF}$ with Sa_{ROCK} for AF relationships developed for TS and RVT analyses	102
Table 5.1 Higher order polynomial constants and associated $\sigma_{\ln AF}$ of AF function developed for TS analysis data	120
Table 5.2 Higher order polynomial constants and associated $\sigma_{\ln AF}$ of AF function developed for RVT analysis data.....	124
Table 5.3 Higher order polynomial constants and associated $\sigma_{\ln AF}$ of AF function developed for TS ($\sigma_{\ln V_s} = 0.2$) analysis data	128
Table 5.4 Higher order polynomial constants and associated $\sigma_{\ln AF}$ of AF function developed for RVT ($\sigma_{\ln V_s}=0.2$) analysis data.....	132
Table 5.5 Comparison of $\sigma_{\ln AF}$ of AF relationships developed for different analysis methods	135
Table 5.6 Variation of $\sigma_{\ln AF}$ with Sa_{ROCK} for AF relationships derived for different analysis methods	136

List of Figures

Figure 2.1 (a)Soil hazard curves and (b) uniform hazard spectrum.....	12
Figure 2.2 Refraction process that produces nearly vertical wave propagation near the ground surface (Kramer, 1996).....	14
Figure 2.3 Hysteresis loop of a typical soil under symmetric cyclic loading	16
Figure 2.4 Nonlinear modulus reduction and damping curves	16
Figure 2.5 Comparison of the standard deviation of $\ln AF(f)$ predicted by different combinations of five intensity parameters. (Bazzurro and Cornell, 2004a)	27
Figure 2.6 Regression analyses performed for sand site of $AF(f)$ on $Sa_{ROCK}(f)$ at (a) 1.0 Hz and (b) 100 Hz.....	28
Figure 2.7 Regression analyses on a sand site of $AF(f)$ on $Sa_{ROCK}(f)$ at (a) 1.0 Hz and (b) 100 Hz	29
Figure 2.8 Comparison of UHS of hypothetical site predicted by NRC Approach 1 (i.e., hybrid method) and convolution method for (a) 50%, (b)10%, (c)5%, and (d) 2% probability of exceedance (PE) in 50 years,. (Bazurro and Cornell, 2004)	32
Figure 3.1 Shallow site (i.e. SCH site) shear-wave velocity profile	37
Figure 3.2 (a)Nonlinear modulus reduction and (b)damping curves for SCH site.....	38
Figure 3.3 Shear-wave velocity profile of the deep site (i.e. CC site).....	40
Figure 3.4 Nonlinear modulus reduction and damping curves for CC site.....	42
Figure 3.5 Rock hazards curves for PGA and selected periods.	44
Figure 3.6 Uniform hazard curves for 2% and 10% probability of exceedance levels.	44

Figure 3.7 Magnitude-distance distribution of selected input motions for TS site response analyses	46
Figure 3.8 Input response spectra for TS site response analyses	47
Figure 3.9 Input response spectra for RVT analysis	48
Figure 3.10 Deaggregation results for 2% probability of exceedance in 50 years at 1 Hz, 2 Hz, 5 Hz and 10 Hz	51
Figure 3.11 Input response spectra for RVT analysis selected through deaggregation of site hazard	54
Figure 4.1 AF vs. T from TS analysis of SCH site.....	60
Figure 4.2 AF vs. S_{aROCK} data from TS analysis together with derived AF relationships for different periods (a) PGA, (b) 0.2 s, (c) 0.4 s, and (d) 1.0 s	62
Figure 4.3 AF vs. T from RVT analysis with 146 motions for the SCH site	65
Figure 4.4 AF vs. S_{aROCK} data from RVT analysis together with derived AF relationships for different periods (a) PGA, (b) 0.2 s, (c) 0.4 s, and (d) 1.0 s	66
Figure 4.5 AF vs. T from RVT-CE analysis	69
Figure 4.6 AF vs. S_{aROCK} data from RVT-CE analysis together with derived AF relationships for different periods (a) PGA, (b) 0.2 s, (c) 0.4 s, and (d) 1.0 s	70
Figure 4.7 20 V_S profiles generated for TS analysis together with the median V_S profile and baseline V_S profile for the SCH site with (a) $\sigma_{\ln V_S} = 0.1$, (b) $\sigma_{\ln V_S} = 0.2$, and (c) $\sigma_{\ln V_S} = 0.3$	74

Figure 4.8 AF vs. S_{aROCK} data from TS ($\sigma_{lnV_s} = 0.1$), together with derived AF relationships for different periods (a) PGA, (b) 0.2 s, (c) 0.4 s, and (d) 1.0 s.....	76
Figure 4.9 AF vs. S_{aROCK} data from TS ($\sigma_{lnV_s} = 0.2$), together with derived AF relationships for different periods (a) PGA, (b) 0.2 s, (c) 0.4 s, and (d) 1.0 s.....	77
Figure 4.10 AF vs. S_{aROCK} data from TS ($\sigma_{lnV_s} = 0.3$), together with derived AF relationships for different periods (a) PGA, (b) 0.2 s, (c) 0.4 s, and (d) 1.0 s.....	78
Figure 4.11 Twenty V_s profiles generated for RVT analysis with $\sigma_{lnV_s}=0.2$ together with the median and baseline V_s profile for SCH site.....	82
Figure 4.12 AF vs. S_{aROCK} data from RVT analysis with $\sigma_{lnV_s}=0.2$, together with derived AF relationships for different periods (a) PGA, (b) 0.2 s, (c) 0.4 s and (d) 1.0 s.....	83
Figure 4.13 20 V_s profiles generated for RVT-CE analysis together with the median V_s profile and baseline V_s profile for SCH site with (a) $\sigma_{lnV_s} = 0.1$, (b) $\sigma_{lnV_s} = 0.2$, and (c) $\sigma_{lnV_s} = 0.3$	86
Figure 4.14 AF vs. S_{aROCK} data from RVT-CE analyses with $\sigma_{lnV_s} = 0.1$, together with derived AF relationships for different periods (a) PGA, (b) 0.2 s, (c) 0.4 s and (d) 1.0 s.....	87
Figure 4.15 AF vs. S_{aROCK} data from RVT-CE analysis with $\sigma_{lnV_s}=0.2$, together with derived AF relationships for different periods (a) PGA, (b) 0.2 s, (c) 0.4 s and (d) 1.0 s.....	88

Figure 4.16 AF vs. Sa_{ROCK} data from RVT-CE analysis with $\sigma_{lnV_s}=0.3$, together with derived AF relationships for different periods (a) PGA, (b) 0.2 s, (c) 0.4 s and (d) 1.0 s.....	89
Figure 4.17 Comparison of AF functions of TS and TS analysis performed with σ_{lnV_s} of 0.1, 0.2, and 0.3, respectively at different periods (a) PGA, (b) 0.2 s, (c) 0.4 s, and (d) 1.0 s.....	94
Figure 4.18 Comparison of AF functions of RVT-CE and RVT-CE analysis performed with σ_{lnV_s} of 0.1, 0.2, and 0.3, respectively at different periods (a) PGA, (b) 0.2 s, (c) 0.4 s, and (d) 1.0 s.....	95
Figure 4.19 Comparison of AF relationships from RVT and RVT-CE analyses performed with and without varied V_s profiles ($\sigma_{lnV_s} = 0.2$) at different periods (a) PGA, (b) 0.2 s, (c) 0.4 s, and (d) 1.0 s.....	97
Figure 4.20 Comparison of AF functions predictions of TS and RVT-CE analyses performed with and without spatially varied V_s profiles ($\sigma_{lnV_s} = 0.2$) at different periods (a) PGA, (b) 0.2 s, (c) 0.4 s, and (d) 1.0 s.....	99
Figure 4.21 Variable and constant σ_{lnAF} with Sa_{ROCK} for AF relationships developed for TS and RVT-CE analyses.....	103
Figure 4.22 Comparison of site-specific soil hazard predictions of TS analysis performed with σ_{lnV_s} of 0.0, 0.1, 0.2, and 0.3, respectively at different periods (a) PGA, (b) 0.2 s, (c) 0.4 s, and (d) 1.0 s.....	105
Figure 4.23 Comparison of site-specific soil hazard predictions of RVT-CE and RVT analyses performed with σ_{lnV_s} of 0.0 and 0.2 at (a) PGA, (b) 0.2 s, (c) 0.4 s, and (d) 1.0 s.....	107

Figure 4.24 Comparison of site-specific soil hazard predictions of RVT-CE and RVT analysis performed for $\sigma_{lnVs} = 0.0$ and $\sigma_{lnVs} = 0.2$ at periods (a) PGA, (b) 0.2 s, (c) 0.4 s, and (d) 1.0 s	109
Figure 4.25 Comparison of site-specific soil hazard predictions of TS and RVT-CE analysis performed for $\sigma_{lnVs} = 0.0$ and $\sigma_{lnVs} = 0.2$ at periods (a) PGA, (b) 0.2 s, (c) 0.4 s, and (d) 1.0 s	110
Figure 4.26 Comparison of site-specific soil hazard predictions of TS and RVT analysis performed for $\sigma_{lnVs} = 0.0$ and $\sigma_{lnVs} = 0.2$ using variable σ_{lnAF} (a) PGA, (b) 0.2 s, (c) 0.4 s, and (d) 1.0 s	111
Figure 4.27 Comparison of site-specific soil hazard predictions of TS and RVT-CE analysis performed for σ_{lnVs} of 0.0 and 0.2 with constant and variable (V.S) σ_{lnAF} for (a) PGA, (b) 0.2 s, (c) 0.4 s, and (d) 1.0 s	113
Figure 5.1 AF vs. T from TS analysis for CC site.....	117
Figure 5.2 AF vs. S_{aROCK} data from TS analysis on CC site together with derived AF relationships for different periods (a) PGA, (b) 0.4 s, and (d) 1.6 s	119
Figure 5.3 AF vs. T from RVT analysis for CC site	121
Figure 5.4 AF vs. S_{aROCK} data from RVT analysis on CC site together with derived AF relationships for different periods (a) PGA, (b) 0.4 s and (d) 1.6 s	123
Figure 5.5 Twenty V_S profiles generated for TS ($\sigma_{lnVs} = 0.20$) analysis together with the median and baseline V_S profile for CC site	126
Figure 5.6 AF vs. S_{aROCK} data from TS ($\sigma_{lnVs} = 0.2$) analysis performed on V_S generated for CC site, together with derived AF relationships for different periods (a) PGA, (b) 0.4 s and (d) 1.6 s	127
Figure 5.7 Twenty V_S profiles generated for RVT ($\sigma_{lnVs} = 0.20$) analysis together with the median and baseline V_S profile for CC site	129

Figure 5.8 AF vs. Sa_{ROCK} data from RVT ($\sigma_{lnVs}=0.2$) analysis performed on V_S generated for CC site, together with derived AF relationships for different periods (a) PGA, (b) 0.4 s and (d) 1.6 s	131
Figure 5.9 Comparison of AF functions predictions of TS and RVT analyses performed with $\sigma_{lnVs} = 0.0$ and $\sigma_{lnVs} = 0.2$ at different periods (a) PGA, (b) 0.4 s, and (d) 1.6 s	134
Figure 5.10 Comparison of site-specific soil hazard predictions of TS and RVT analyses performed with $\sigma_{lnVs} = 0.0$ and $\sigma_{lnVs} = 0.2$ for CC site at periods (a) PGA, (b) 0.4 s, and (d) 1.6 s	139
Figure 5.11 Comparison of site-specific soil hazard predictions of TS and RVT analysis performed for $\sigma_{lnVs} = 0.0$ and $\sigma_{lnVs} = 0.2$ using variable σ_{lnAF} for CC site at periods (a) PGA, (b) 0.4 s, and (c) 1.6 s	140
Figure 5.12 Comparison of site-specific soil hazard predictions of TS and RVT-CE analysis performed for σ_{lnVs} of 0.0 and 0.2 with constant and variable σ_{lnAF} for CC site at periods (a) PGA, (b) 0.4 s, and (c) 1.6 s	141
Figure 6.1 Baseline shear-wave velocity profile.....	145
Figure 6.2 2D finite element mesh used for 2D site response analyses (all dimensions are in m). Region of interest (ROI) is shown in red.....	146
Figure 6.3 Variation of correlation coefficient with the relative distance between two locations for different correlation distances.....	148
Figure 6.4 Two dimensional representation of baseline V_S profile.	151
Figure 6.5 Single 2D V_S field realization generated with $\theta_z = 80$ m and θ_x of: (a) 0 m, (b) 100 m, and (c) 600 m	153
Figure 6.6 Single 2D V_S field realization generated with $\theta_x = 600$ m and θ_z of: (a) 0 m, (b) 80 m and (c) 600 m	154

Figure 6.7 Single 2D V_S field realization generated for end-member correlation distances: (a) $\theta_x = 0$ m & $\theta_z = 0$ m, (b) $\theta_x = 0$ m & $\theta_z = 600$ m, (c) $\theta_x = 600$ m & $\theta_z = 0$ m, and (d) $\theta_x = 600$ m & $\theta_z = 600$ m.....	155
Figure 6.8 V_S profiles across the ROI for a single 2D random field realization generated with $\sigma_{\ln V_S}$ of 0.2, θ_z of 80 m, and θ_x of (a) 0 m, (b) 100 m, and (c) 600 m, respectively	157
Figure 6.9 V_S profiles across the ROI for a single 2D random field realization generated with $\sigma_{\ln V_S}$ of 0.2, θ_x of 600 m, and θ_z of (a) 0 m, (b) 80 m, and (c) 600 m, respectively	158
Figure 6.10 V_S profiles across the ROI a single 2D random field realization generated with $\sigma_{\ln V_S}$ of 0.2 and end-member correlation distances.....	160
Figure 6.11 V_S profiles across the ROI for a single 2D random field realization generated with θ_x of 100 m, θ_z of 80 m, and $\sigma_{\ln V_S}$ of (a) 0.1, (b) 0.2, and (c) 0.3, respectively.....	161
Figure 6.12 Colormap plots of the generated 20 velocity fields with $\theta_x = 100$ m, $\theta_z = 80$ m	163
Figure 6.13 Median V_S profiles across the ROI of 20 2D V_S field realizations generated with $\sigma_{\ln V_S}$ of 0.2, θ_z of 80 m, and θ_x of (a) 0 m, (b) 100 m, and (c) 600 m, respectively	165
Figure 6.14 Median V_S profiles across the ROI of 20 2D V_S field realizations generated with $\sigma_{\ln V_S}$ of 0.2, θ_x of 600 m, and θ_z of (a) 0 m, (b) 80 m, and (c) 600 m, respectively	166
Figure 6.15 Median V_S profiles across the ROI of 20 2D random field realization generated with $\sigma_{\ln V_S}$ of 0.2 and boundary value correlation distances	167

Figure 6.16 Median V_S profiles across the ROI of 20 2D random field realization generated with θ_x of 100 m, θ_z of 80 m, and $\sigma_{\ln V_S}$ of (a) 0.1, (b) 0.2, and (c) 0.3, respectively	168
Figure 7.1 Effect of boundary location on (a) surface spectral acceleration, (b) standard deviation of surface acceleration across ROI	173
Figure 7.2 Five selected input ground motion for 2D analysis (a) magnitude-distance distribution, (b) magnitude-PGA distribution, and (c) input response spectra.	175
Figure 7.3 Baseline response spectra of five selected input ground motions (a) surface response spectra, (b) amplification factor.	176
Figure 7.4 Points of comparison: (a) ROI, (b) surface response spectra across ROI for a single V_S realization, and (c) Average response spectra across 20 V_S realizations	177
Figure 7.5 Median(Sa) _{ROI} obtained of twenty 2D analyses performed on the 2D velocity fields generated with $\sigma_{\ln V_S}$ of 0.2, θ_z of 80 m, and θ_x of (a) 0 m, (b) 100 m, and (c) 600 m.	180
Figure 7.6 $\sigma(\ln(Sa)_{ROI})$ for twenty 2D analyses performed on 2D velocity fields generated with $\sigma_{\ln V_S}$ of 0.2, θ_z of 80 m, and θ_x of (a) 0 m, (b) 100 m, and (c) 600 m	181
Figure 7.7 V_S profiles across the ROI for a single 2D random field realization generated with $\sigma_{\ln V_S}$ of 0.2, θ_z of 80 m, and θ_x of (a) 0 m, (b) 100 m, and (c) 600 m, respectively	182
Figure 7.8 Influence of horizontal correlation distances on (a) Average(Median(Sa) _{ROI}), (b) Average(Median(AF) _{ROI}), and (c) $\sigma(\ln(\text{Median}(Sa)_{ROI}))$	184

Figure 7.9 Influence of horizontal correlation distance on (a) Average(Max(Sa) _{ROI}), (b) Average(Max(AF) _{ROI}), and (c) $\sigma(\ln(\text{Max}(\text{Sa})_{\text{ROI}}))$	186
Figure 7.10 Median(Sa) _{ROI} obtained through 2D site response analyses of 20 of the 2D velocity fields generated with $\sigma_{\ln V_s}$ of 0.2, θ_x of 600 m, and θ_z of (a) 0 m, (b) 80 m, and (c) 600 m.....	188
Figure 7.11 $\sigma(\ln(\text{Sa})_{\text{ROI}})$ obtained through 2D site response analyses of twenty 2D velocity fields generated with $\sigma_{\ln V_s}$ of 0.2, θ_x of 600 m, and θ_z of (a) 0 m, (b) 80 m, and (c) 600 m.	189
Figure 7.12 Surface response spectra and shear wave velocity profiles across ROI for a 2D velocity field realization with large $\sigma(\ln(\text{Sa})_{\text{ROI}})$	191
Figure 7.13 Influence of θ_z on 2D site response analysis with large θ_x (a) Average(Median(Sa) _{ROI}), (b) Average(Median(AF) _{ROI}), and (c) $\sigma(\ln(\text{Median}(\text{Sa})_{\text{ROI}}))$	192
Figure 7.14 Median V_s profiles across the ROI of 20 2D V_s field realizations generated with $\sigma_{\ln V_s}$ of 0.2, θ_x of 600 m, and θ_z of (a) 0 m, (b) 80 m, and (c) 600 m, respectively	193
Figure 7.15 2D site response analysis results for 2D V_s field generated with θ_x of 0 m and θ_z of 0 m, 80 m, and 600 m (a) Average(Median(Sa) _{ROI}), (b) Average(Median(AF) _{ROI}), and (c) $\sigma(\ln(\text{Median}(\text{Sa})_{\text{ROI}}))$	195
Figure 7.16 Median(Sa) _{ROI} spectra of 2D analysis performed on velocity fields generated for θ_x of 0 m and θ_z of: (a) 0 m. (b) 80 m, and (c) 600 m.	196
Figure 7.17 2D site response analysis results of 2D velocity fields generated with end-member correlation distances (a) Average(Median(Sa) _{ROI}), (b) Average(Median(AF) _{ROI}), and (c) $\sigma(\ln(\text{Median}(\text{Sa})_{\text{ROI}}))$	198

Figure 7.18 2D site response analysis results of 2D V_S field generated with θ_x of 100 m and θ_z of 0 m and 80 m (a) Average(Median(S_a) _{ROI}), (b) Average(Median(A_F) _{ROI}), and (c) $\sigma(\ln(\text{Median}(S_a)_{ROI}))$	200
Figure 7.19 2D site response analysis results of 2D velocity fields generated with θ_x of 600 m and θ_z of 0 m, 80 m, and 600 m (a) Average(Max(S_a) _{ROI}), (b) Average(Max(A_F) _{ROI}), and (c) $\sigma(\ln(\text{Max}(S_a)_{ROI}))$	201
Figure 7.20 Influence of θ_x on the Average(Median(S_a) _{ROI}) of five input motions	203
Figure 7.21 Influence of θ_x on the Average(Median(A_F) _{ROI}) of five input motions	204
Figure 7.22 Influence of θ_x on the $\sigma(\ln(\text{Median}(A_F)_{ROI}))$ of five input motions	206
Figure 7.23 Influence of θ_z on the Average(Median(S_a) _{ROI}) of five input motions	207
Figure 7.24 Influence of θ_z on the Average(Median(A_F) _{ROI}) of five input motions	208
Figure 7.25 Influence of θ_z on the $\sigma(\ln(\text{Median}(A_F)_{ROI}))$ of five input motions.	209
Figure 7.26 2D site response analysis results for 2D V_S field generated with σ_{InV_S} of 0.2, θ_x of 100 m and θ_z of 80 m using five selected input motions	211
Figure 7.27 Comparison of (a) Average(Median(Peak Strain)) and (b) $\sigma(\text{Median(Peak Strain)})$ over twenty realizations for each input motion.....	212
Figure 8.1 Correlation coefficients corresponding to the vertical correlation distances used to generate 2D velocity field.	219
Figure 8.2 Shear wave velocity profiles in a generated set of 20 realizations for 1D analysis with ρ of: (a) 0.0, (b) 0.8 and (c) 1.0.....	221
Figure 8.3 Median Shear wave velocity profiles from the 50 sets of 20 realizations generated for 1D analysis with ρ of: (a) 0.0, (b) 0.8 and (c) 1.0.....	222
Figure 8.4 Median 1D responses from twenty shear wave velocity realizations generated with different ρ	223

Figure 8.5 $\sigma_{\ln AF}$ from 1D analysis of twenty shear wave velocity realizations generated with different ρ	225
Figure 8.6 Comparison of the transfer functions of 20 velocity realizations generated with $\rho = 0.0$ and $\rho = 1.0$	226
Figure 8.7 Standard deviation and COV of median AF and $\sigma_{\ln AF}$ predictions of 1D analyses across 50 sets of 20 realizations	228
Figure 8.8 Comparison of 2D and 1D analysis results for different ρ	231
Figure 8.9 Median AF and $\sigma_{\ln AF}$ for five input motions for 1D analyses of velocity profiles generated with $\rho = 0.8$ and 1D deterministic analyses with no velocity variability.	233
Figure 8.10 Comparison of AF predictions of 1D and 2D analysis results; reflecting both variability in shear wave velocity and the input motion.	235
Figure 8.11 One-dimensional velocity profiles with finite horizontal correlation obtained from 2D velocity field realization	237
Figure 8.12 Comparison of 1D and 2D site response analyses performed on twenty velocity fields generated with horizontal correlation distance of 100 m	239
Figure 8.13 Comparison of results of 2D and 1D analysis performed on velocity fields with finite and infinite horizontal correlation distances.....	240

1

INTRODUCTION

1.1 Research Motivation

Site-specific soil conditions play an important role in determining the site-specific ground motion levels to be used in the seismic design of nuclear facilities. Several approaches are available in the literature to develop a hazard-consistent, site-specific acceleration response spectrum for design, and these approaches require a suite of seismic site response analyses to define the site amplification for the site-specific soil properties at the site. Among these approaches, the convolution approach (Bazzurro and Cornell, 2004) can be used to predict fully probabilistic seismic hazard curves for the soil conditions at a site. The convolution approach simply convolves the rock hazard curve with a model for site amplification to generate a hazard curve at the surface of the site. The model for site amplification predicts the median site amplification and its variability (i.e., standard deviation) as a

function of the intensity of shaking, and this model can be derived from site response analyses.

While the basic convolution approach has been outlined in Bazzurro and Cornell (2004), the practical implementation of the approach requires investigation and some underlying assumptions require evaluation. The important issues that require investigation relate to the different types of site response analysis available (i.e., time series, random vibration theory), the influence of parametric uncertainty on these different types of analysis, and the influence of one-dimensional vs. two-dimensional variability on the site amplification model. These issues need to be investigated such that recommended approaches can be developed to guide the implementation of the convolution approach in engineering practice for nuclear facilities.

1.2 Objectives and Methodology

There are three main objectives to this research. These objectives and the proposed methodology used to achieve these objectives are outlined below.

Comparison of site amplification models obtained through different methods of analysis and their effect on the predicted hazard curves.

One-dimensional (1D) site response analysis is the most common approach used to assess the effect of soil conditions on ground shaking. Traditional equivalent linear analysis using time domain input motions or random vibration theory (RVT) can be used to compute site amplification due to 1D shear wave propagation. An important difference between time series and RVT site response analysis is that RVT analysis does not incorporate motion-to-motion variability, and thus the variability in the amplification factors derived by time series and RVT analyses are very different. Additionally, previous research has shown that RVT site response analysis generates systematically different responses than time series analyses at some periods. A comparison of the site amplification models developed from these two different methods of analysis and their effect on the predicted soil hazard curves is investigated in this research.

Evaluation of the effect of introducing parametric uncertainty in the soil properties required for the site response analyses on the amplification models and associated soil hazard curves.

The Monte Carlo simulation technique is used to incorporate the effects of parametric uncertainty on the site response results. This parametric uncertainty represents the aleatory variability in the properties across the footprint of a site,

as well as some epistemic uncertainty in the measured baseline velocity profile. Therefore, Monte Carlo simulation enables quantification of variability in the amplification function due to shear wave velocity variability and uncertainty. Monte Carlo simulations are performed for time series and RVT site response analyses and the results are used to generate models of site amplification. The influence of the Monte Carlo simulations on the resulting soil hazard curves is investigated.

Evaluation of the effectiveness of analyzing multiple one-dimensional soil properties to capture the effect of two-dimensional spatial variability in soil properties

The use of Monte Carlo simulations to incorporate parametric variability within one-dimensional (1D) site response analyses implicitly assumes that multiple 1D profiles accurately models the influence of lateral variability of soil properties across the footprint of a site. However, it is not clear whether multiple 1D profiles provide ground motions that are representative of a laterally variable two-dimensional (2D) site. For this purpose 2D shear wave velocity fields are generated using Monte Carlo simulation and these velocity fields are used in 2D site response analysis. The results from 2D site response analyses with variable shear wave velocity fields are compared with results from 1D analyses with variable shear wave velocity profiles.

1.3 Scope of the Dissertation

This dissertation presents the findings of the research study. The results obtained for the research are discussed in detail in the following chapters.

Chapter 1 provides a general motivation and overview of the scope of this research. It summarizes the content and the objectives of the research.

Chapter 2 introduces the general concepts of the research such as probabilistic seismic hazard analysis and site response analysis. Moreover it provides a literature review regarding the available methods for predicting the site-specific hazard curves and discusses the limitations of the current methods of practice.

Chapter 3 presents a description of the study sites that are used for the site response analyses, together with the site-specific rock hazard curves. This chapter also discusses the input ground motions used in the different methods of site response analysis (i.e., time series and RVT).

Chapter 4 discusses the results of the site response analyses performed on a shallow soil site using time series and RVT approaches. The amplification functions obtained through these different methods of analysis are introduced and the effect of parametric variability on the amplification models is observed. The generated amplification models are convolved with the rock hazard curves to calculate site-specific soil hazard curves. Chapter 5 performs similar analyses for a deep soil site.

Chapter 6 describes the statistical generation of 2D shear wave velocity fields and discusses the influence of the different statistical parameters used in the Monte Carlo simulation on the generated velocity fields.

Chapter 7 presents the results of 2D site response analysis performed on the 2D velocity fields generated in Chapter 6. The effects of the different statistical parameters used to generate 2D velocity fields (i.e., vertical and horizontal correlation distances) on the computed response are observed.

Chapter 8 compares the 2D Monte Carlo simulation results in Chapter 7 with the Monte Carlo simulation results from 1D analysis.

Chapter 9 summarizes the overall objectives of this research study and presents the major conclusions of the current study. This chapter concludes with suggestions for further research studies.

PROBABILISTIC SEISMIC HAZARD ANALYSIS AND SITE RESPONSE ANALYSIS

2.1 Introduction

Excessive damage during previous earthquakes has pointed out the importance of the earthquake-resistant design of structures and facilities. Earthquake-resistant design aims to ensure that a structure or facility under consideration can withstand a certain level of shaking without excessive damage. The level of shaking for design is defined by the design ground motion. Prediction of the design ground motion requires decisions based on uncertain and insufficient information, such as: the location, time and size of future earthquakes, and the expected ground motion levels given a specific earthquake. Seismic hazard analysis provides quantitative estimates of design earthquake shaking at a site. Seismic

hazard analysis can be performed either deterministically, by considering a specific earthquake scenario event (i.e., magnitude and distance), or probabilistically, by considering all possible earthquake scenarios and ground motion levels along with their associated probability of occurrence.

Probabilistic seismic hazard analysis, PSHA, provides earthquake-induced shaking levels at a particular site as a function of the annual probability of exceedance. PSHA typically provides the earthquake shaking levels for rock conditions. However, difficulties arise when incorporating the effects of the local soil conditions in the PSHA-derived ground shaking levels because the uncertainties in the ground response must be incorporated. The fact that most structures and facilities are founded on soil rather than rock suggests the need for PSHA hazard curves that are site-specific and soil-specific. These soil-specific hazard curves can be generated through the integration of PSHA and site response analyses.

The soil hazard at the surface of a specific site can be estimated through a number of different approaches. The U.S Nuclear Regulatory Commission (2001) describes four different approaches to produce site-specific design motions for a soil site. The major differences in the suggested approaches are related to how the uncertainty in the ground response is incorporated through site response analysis.

This chapter presents background information on PSHA and the available site response analysis methods, followed by a description of the procedures for

integrating PSHA and site response analyses. This chapter also reviews the results from the previous research on this topic.

2.2 Probabilistic Seismic Hazard Analysis (PSHA)

PSHA provides a method for the consideration of uncertainties in the magnitude, location and the recurrence rate of earthquakes, together with the uncertainty in the prediction of ground motions as a function of magnitude, M , and distance, R . Therefore, PSHA offers a complete estimate of the seismic hazard by considering all possible earthquake scenarios rather than identifying only one scenario event, as is done in the deterministic approach. (Kramer 2006)

PSHA utilizes the theorem of total probability to compute the probability of exceedance of a particular value, y , of a ground motion parameter, Y , given the occurrence of an earthquake on a fault (EQ).

$$P[Y > y|EQ] = P[Y > y|X] P[X] = \int P[Y > y|X] f_x(X) dx \quad (2.1)$$

where X represents the random variables that influence Y . These variables include magnitude (M), distance (R), along with others, and $f_x(X)$ represents the probability density function of these variables. M and R are usually assumed to be statistically independent. Thus the probability of exceedance can be written as:

$$P[Y > y|EQ] = \int \int P[Y > y|m, r] f_M(m) f_R(r) dm dr \quad (2.2)$$

$P[Y > y|m, r]$ is obtained through a ground motion prediction relationship and $f_M(m)$ and $f_R(r)$ are the probability density functions for M and R , respectively. $f_M(m)$ is obtained from the magnitude recurrence relationships for the fault, and $f_R(r)$ is evaluated from the relative location of the site and the earthquakes on the fault. Incorporating the annual rate of earthquakes on the fault (v), also known as the activity rate, an annual rate of exceedance (λ_y) of the ground motion level, y , can then be computed as:

$$\lambda_y = v \int \int P[Y > y|m, r] f_M(m) f_R(r) dm dr \quad (2.3)$$

If the particular site is located in a region with N potential earthquake sources each with its own activity rate, v_i , the total annual rate of exceedance rate for the site can be estimated by:

$$\lambda_y = \sum_{i=1}^N v_i \int \int P[Y > y|m, r] f_{M_i}(m) f_{R_i}(r) dm dr \quad (2.4)$$

The evaluation of the integrals of each component is typically calculated through numerical integration in which small magnitude and distance bins are defined. Then the integral becomes a sum and represented by:

$$\lambda_y = \sum_{i=1}^N v_i \sum_{j=1}^{N_M} \sum_{k=1}^{N_R} v_i P[Y > y|m_j, r_k] P[M = m_{j,i}] P[R = r_{k,i}] \quad (2.5)$$

where N_M and N_R represent the number of magnitude and distance bins, respectively. The results of the PSHA are typically presented through seismic hazard curves, each of which plot λ_y vs. y for a different response spectral period. A uniform hazard spectrum can be defined from the hazard curves by identifying ground motion levels with the same annual rate of exceedance (also called a hazard level) for each period.

Figure 2.1a presents hazard curves calculated for four different spectral periods for a hypothetical site. Note that the intensity of shaking increases as the annual rate of exceedance (i.e., hazard level) decreases. A uniform hazard spectrum can be obtained from the hazard curves by identifying spectral accelerations with the same hazard level at each period (Figure 2.1a) and plotting these values of S_a vs. their associated periods (Figure 2.1b). Typically, the hazard curves are derived for rock conditions, and therefore the procedure outlined above does not account for the effects of the soil response.

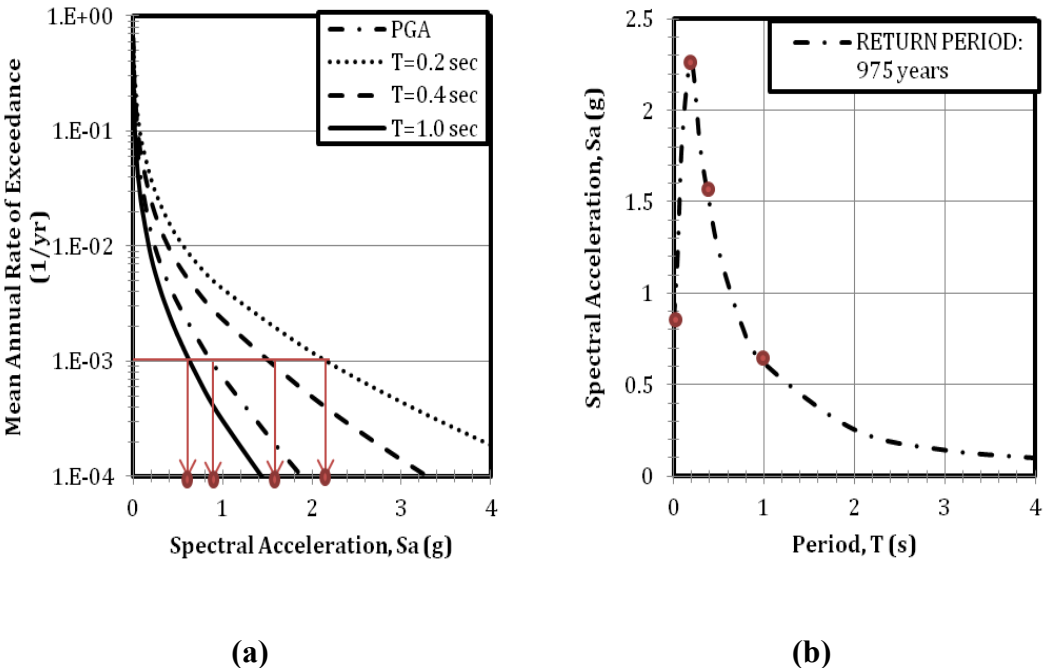


Figure 2.1 (a) Soil hazard curves and (b) uniform hazard spectrum

2.3 An Overview of Available Site Response Analysis Methods

The dynamic response of the soil layers plays an important role in determining the characteristics of earthquake shaking at the ground surface. Therefore, prediction of the site response is an important problem in geotechnical earthquake engineering. Typically, the expected level of ground shaking at a site is predicted using empirical ground motion prediction equations (GMPEs). These GMPEs predict response spectral values as a function of M, R, and a range of additional parameters. These empirical relationships are used in PSHA for the prediction of the rock ground motions at a specific site. The remaining issue is to evaluate the response of the overlying soil deposit due to this bedrock motion. The most commonly used approaches to evaluate the response of soil deposits are one-dimensional and two-dimensional dynamic response analyses. These approaches that are used in this study are described below.

Body waves travel from the earthquake fault rupture to the surface of the earth. These waves are reflected and refracted as they propagate through different geologic materials within the earth. The direction of wave propagation is initially inclined, but becomes more vertical as the propagating waves approach the near surface where the geologic materials have relatively smaller wave propagation

velocities (Figure 2.2). By the time the waves reach to the surface, they are almost vertical. One-dimensional (1D) analyses generally are based on the assumption that the response of the soil in the near surface is mainly caused by vertically propagating horizontal shear waves travelling from the underlying bedrock through the horizontal boundaries of the surficial soil layers. This type of analysis requires that the shear wave velocity profile (V_S vs. depth) of the site be specified. 1D site response can be calculated through several different approaches that differ predominantly in how the stress-strain properties of the soil are modeled (linear-elastic, equivalent-linear, or nonlinear).

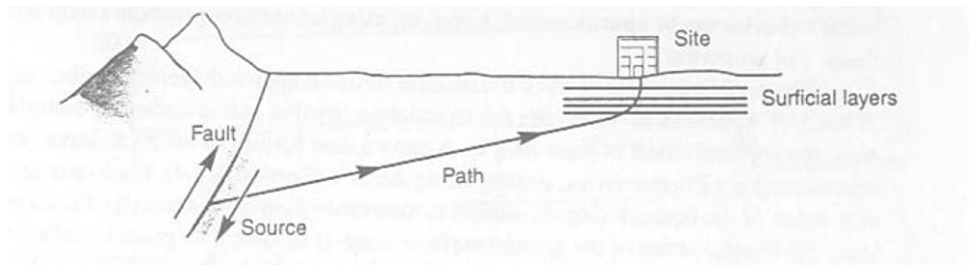


Figure 2.2 Refraction process that produces nearly vertical wave propagation near the ground surface (Kramer, 1996)

Soil exhibits nonlinear soil behavior in which the stiffness decreases with increasing strain. The nonlinear dynamic response of soil to a symmetric cycle of

loading can be represented by a hysteresis loop as shown in Figure 2.3 (Kramer, 2006). The hysteresis loop can be defined either by the loop itself or through equivalent-linear properties, which describe the general characteristics of the loop. The equivalent-linear properties are: (a) the secant shear modulus, G , of the loop (Figure 2.3) and (b) the equivalent viscous damping ratio, D , which is the viscous damping ratio that produces energy loss in a single cycle that is equivalent to the hysteresis loop. These equivalent-linear soil properties are shear strain dependent and can be modeled through shear modulus reduction and damping ratio curves (Figure 2.4). These curves are often called nonlinear property curves.

Nonlinear site response analysis defines the nonlinear soil response directly through the hysteresis loop, while equivalent-linear analysis uses the nonlinear property curves. Equivalent-linear analysis actually performs linear elastic wave propagation, but uses shear modulus and damping ratio values for each soil layer that are modified to account for soil nonlinearity. The nonlinear property curves are used to select the soil properties (G and D) that are consistent with the shear strain level induced in the soil during earthquake shaking. Since the computed strain-level is dependent on the properties used in analysis, an iterative procedure is required to identify the appropriate properties in equivalent-linear analysis. Additionally, the dynamic response of a layered soil system is commonly computed in the frequency domain using frequency domain transfer functions (Schnabel et al. 1972).

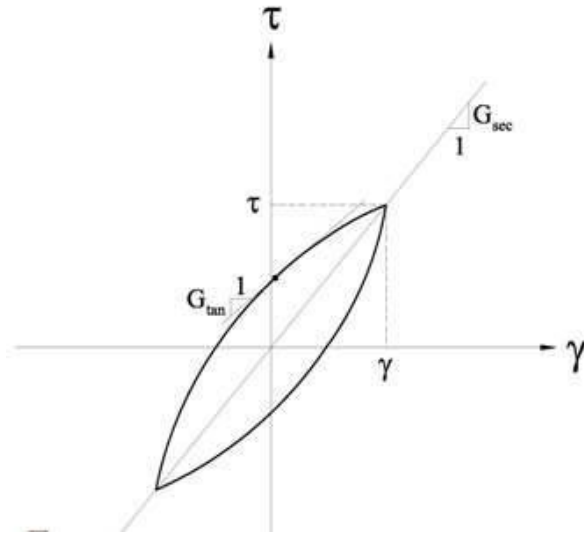


Figure 2.3 Hysteresis loop of a typical soil under symmetric cyclic loading

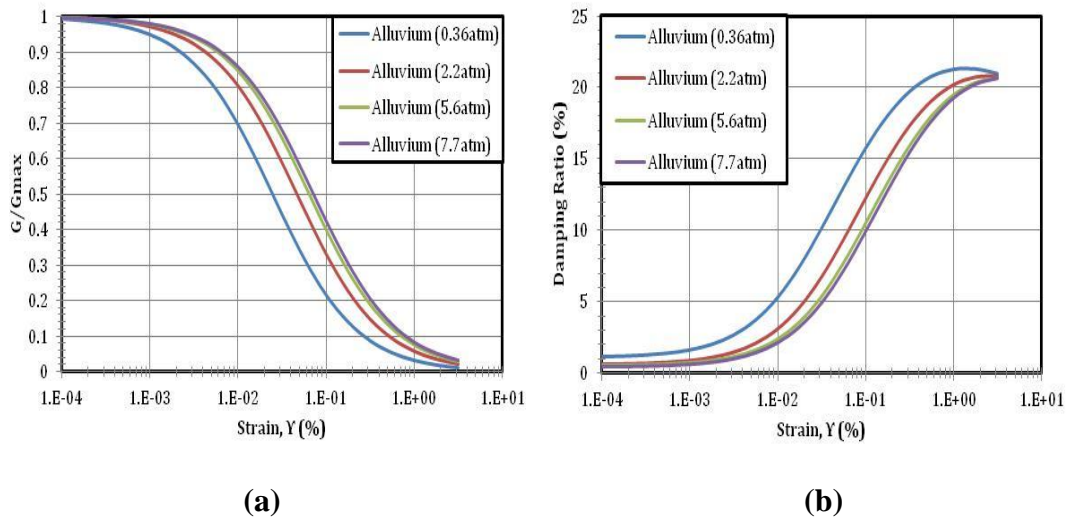


Figure 2.4 Nonlinear modulus reduction and damping curves

In traditional equivalent-linear analysis, a bedrock acceleration-time series is provided as an input motion. This approach requires that the input earthquake motion be transformed into the frequency domain using the Fast Fourier Transform (FFT) such that the transfer functions for the site can be applied. The resulting Fourier Spectrum at the surface is then converted back to the time domain using the inverse FFT. Computer programs such as SHAKE (Schnabel et al., 1972) and Strata (Kottke and Rathje, 2010) are available to perform 1D site response analyses of layered media. The input acceleration-time histories for site response analysis are commonly obtained from available strong ground motion databases and are actual recordings on rock sites. Typically, a suite of motions (5 to 7 motions) is used as input to incorporate motion-to-motion variability.

Random vibration theory (RVT), as applied to seismological simulations (e.g., Hanks and McGuire 1981) and then to site response analysis (e.g., Schneider et al. 1991, Rathje and Ozbey 2006), uses a Fourier amplitude spectrum (without the associated phase angles) to describe ground shaking at a site. Extreme value statistics (e.g., Cartwright and Longuet-Higgins 1956, Boore 2003) are used to relate the Fourier amplitude spectrum (FAS) to peak time domain parameters, such as peak ground acceleration and spectral acceleration. For RVT site response analysis, the FAS of the input motion can be specified directly from seismological theory or it can be derived from an acceleration response spectrum using inverse RVT. The same frequency domain transfer functions used in traditional equivalent-linear analysis are

used in RVT analysis to propagate the input FAS to the ground surface. Extreme value statistics are used to convert the surface FAS into a surface response spectrum. RVT enables prediction of stable estimates of the surface response spectrum without the need to prescribe a suite of input rock motions in the time domain. RVT site response predictions are comparable to the median response spectrum obtained through site response analysis performed using a suite of input rock motion. Therefore, RVT analysis does not reflect motion-to-motion variability, which exists in results from time series analyses.

One-dimensional analysis of ground response is useful for level surfaces with layered material properties that extend infinitely in the horizontal direction. In reality, a site may not be level, its layers may not be horizontal, and the soil properties may vary in the horizontal direction. In these cases the two-dimensional (2D) or even three-dimensional (3D) dynamic response can be important. Most commonly, dynamic finite element analyses are used to solve 2D and 3D dynamic response problems. For 2D analysis, which will be used in this study, the finite element method divides a 2D region into discrete elements (i.e., finite element mesh) with the element corners defined by nodal points. The dynamic equations of equilibrium are solved at the nodes to compute the nodal accelerations, velocities, and displacements.

Similar to 1D analysis, the stress-strain response of the soil in a finite element analysis can be modeled as either equivalent-linear or nonlinear. When modeling the soil as equivalent-linear, the dynamic equations of equilibrium can be solved using frequency domain or time domain methods. The 2D frequency domain methods are similar to those for 1D analysis, in which the input motion is converted to frequency domain using the FFT, transfer functions are used to compute the response at different locations, and the Fourier Spectrum at each node is converted to the time domain using the inverse FFT. The 2D time domain methods solve the dynamic equations of equilibrium at each time step using a time-stepping method (Kramer, 1996). Damping is modeled by Rayleigh damping, which relates the damping matrix to the mass and stiffness matrices. One consequence of Rayleigh damping is that the damping becomes frequency dependent. Frequency domain methods have frequency-independent damping. As a result, higher frequencies may be over-damped when using the time domain methods, unless the Rayleigh damping is applied judiciously (Hudson et al., 1994).

2.4 An Overview of Available Approaches for Integrating PSHA and Site Response

The site-specific uniform hazard spectrum for the design of a structure or a facility should represent the hazard level required for design for the specific soil conditions at the site. In PSHA, the effects of the soil response and its uncertainty on the site-specific seismic hazard are often given less attention than this critical aspect deserves. The traditional approach is to specify a uniform hazard spectrum for rock conditions, use this spectrum to select input motions for site response analysis, and propagate these motions to the surface to develop the soil surface motion. A suite of input motions may be used to incorporate motion-to-motion variability and a few different velocity profiles may be used to consider the uncertainty in the site characteristics, but the approach is decoupled from the full PSHA. Therefore, the hazard level corresponding to the resulting soil motion is unknown.

The U.S. Nuclear Regulatory Commission provides regulatory guidance for developing hazard-consistent ground motions for soil sites (US-NUREG/CR-6728 and US-NUREG/CR-6769). These guides present four approaches for developing site-specific ground motion response spectra. These approaches vary in complexity from simple deterministic amplification of the probabilistically derived rock

response spectrum to rigorous treatment of soil amplification within the PSHA. The four approaches are described briefly below.

Approach 1 is essentially the traditional approach discussed above, in which the input motions for the site response analysis are defined based on the uniform hazard spectra (UHS) predicted by PSHA for rock conditions. However, while one earthquake magnitude may dominate the high-frequency segment of the UHS, another may dominate the low-frequency segment. Consequently, a single motion fitting the entire UHS is unlikely and typically results in excessive nonlinearity in the soil column. Therefore, the surface-ground motion levels predicted by Approach 1 are generally unconservative, inconsistent across frequency, and have unknown hazard level (US-NUREG/CR-6769). Approach 1 is not recommended.

Approach 2 intends to account for one of the shortcomings of Approach 1 by accounting for the fact that different earthquake scenarios dominate different frequencies. This approach uses different input motion spectra for the high-frequency (HF) and low-frequency (LF) segments of the input response spectrum, each anchored to the UHS in their frequency range. Two variants of Approach 2 are described, one of which considers a single magnitude for each spectrum (Approach 2A) and the other considers multiple magnitudes for each spectrum (Approach 2B).

Approach 2A defines the HF and LF input response spectra by considering the controlling earthquake scenarios (i.e., magnitude and distance based on the hazard deaggregation) at 10 Hz for the HF spectrum and 1 Hz for the LF spectrum.

Each controlling earthquake scenario is used to define a response spectrum and then the spectrum is scaled to the rock UHS at the corresponding frequency (i.e., 10 Hz or 1Hz). These two spectra are used to select input motions for site response analysis and to develop frequency-dependent amplification factors. The mean amplification factors for each input motion are applied to the rock UHS and the soil UHS is defined by enveloping the computed soil motions. Approach 2B identifies mean, high, and low percentile magnitudes from the deaggregation at 10 Hz and 1 Hz, and uses each of these scenarios to develop input spectra for each frequency (i.e., three input spectra for each frequency). Again, motions are fit to each input spectrum and propagated through the soil column. The amplification factors for each spectrum are weighted, based on the weights derived from deaggregation, to obtain the mean amplification factors. The mean amplification factors for the HF and LF spectra are applied in the same way as Approach 2A. While Approach 2 addresses the issues related to excessive nonlinearity from Approach 1, it still does not provide surface ground motions with known hazard levels.

Approach 3 involves the convolution of the entire rock hazard curve at a given frequency with the probability distribution of the soil amplification to generate the hazard curve on soil (Bazzurro and Cornell, 2004). The annual probability of exceedence of a soil motion (Sa_{SOIL}) can be derived from the rock hazard curve using:

$$P[Sa_{SOIL} > z] = \int_{Sa_{ROCK}} \int_m \int_r P[Sa_{SOIL} > z | m, r, Sa_{ROCK}] \cdot f(m, r | Sa_{ROCK}) \cdot f(Sa_{ROCK}) \cdot dr \cdot dm \cdot dSa_{ROCK} \quad (2.6)$$

where Sa_{ROCK} is the spectral acceleration on rock, $f(Sa_{ROCK})$ is the probability density function for Sa_{ROCK} and can be derived from the rock hazard curve, and $f(m, r | Sa_{ROCK})$ is the magnitude and distance deaggregation for each value of Sa_{ROCK} . Equation 2.6 can be written in terms of an amplification factor (AF , where $AF = Sa_{SOIL}/Sa_{ROCK}$), resulting in:

$$P[Sa_{SOIL} > z] = \int_{Sa_{ROCK}} \int_m \int_r P \left[AF > \frac{z}{Sa_{ROCK}} | m, r, Sa_{ROCK} \right] \cdot f(m, r | Sa_{ROCK}) \cdot f(Sa_{ROCK}) \cdot dr \cdot dm \cdot dSa_{ROCK} \quad (2.7)$$

Equation 2.7 is equivalent to Equation 2.6, except that Equation 2.7 defines the probability of exceedance for the soil motion for a given (m, r, Sa_{ROCK}) in terms of amplification factor. This expression can be written in discrete form as:

$$P[Sa_{SOIL} > z] = \sum_{Sa_{ROCK_i}} \sum_{m_j} \sum_{r_k} P \left[AF > \frac{z}{Sa_{ROCK}} | m_j, r_k, Sa_{ROCK_i} \right] \quad (2.8)$$

$$\cdot P[m_j, r_k | Sa_{ROCK_i}] \cdot P[Sa_{ROCK_i}]$$

In Equation 2.8, $P[m_j, r_k | Sa_{ROCK_i}]$ represents the probability of occurrence of different m and r combinations given the rock acceleration level Sa_{ROCK_i} . $P[Sa_{ROCK_i}]$ represents the annual probability of occurrence of the rock acceleration level Sa_{ROCK_i} . Both of these terms can be derived from the rock hazard information: $P[m_j, r_k | Sa_{ROCK_i}]$ is the disaggregation information and $P[Sa_{ROCK_i}]$ is computed from the rock hazard curve. The term $P \left[AF > \frac{z}{Sa_{ROCK}} | m_j, r_k, Sa_{ROCK_i} \right]$ in Equation 2.8 is derived from a predictive model for AF that is conditioned on m , r , and Sa_{ROCK} . The AF model predicts both the median and the standard deviation of AF and can be developed from a suite of site response analysis. This framework enables calculations of the soil hazard curve to be performed separately from the calculations of the rock hazard information.

Approach 4 is the most rigorous way to compute a hazard curve for a soil site. It involves the direct integration of the magnitude and distance distributions with a ground motion prediction equation developed specifically for the site. This ground motion prediction equation is developed by performing statistical regression on computed surface motions from a large number of site response analyses for a

large range of input motions. Thus, Approach 4 calculates the hazard at a soil site using the standard PSHA equation:

$$P[Sa_{SOIL} > z] = \int \int P[Sa_{SOIL} > z|m, r] f_{m,r}(m, r) dm dr \quad (2.9)$$

where, z is soil amplitude, m is magnitude, r is distance, and $P[Sa_{SOIL} > z|m, r]$ is computed for the site-specific ground motion prediction equation. However, Approach 4 is not easy to implement because the site-specific ground motion prediction equation is difficult to develop.

2.5 Results from Previous Studies

Bazzurro and Cornell (2004a, b) presented a convolution approach that is similar to Approach 3 from the NRC. Bazzurro and Cornell (2004a) investigated the dependence of amplification factors at different frequencies, $AF(f)$, on five different event/ground motion parameters (i.e., magnitude, M , and source-to-site distance, R ,

peak ground acceleration, PGA, spectral acceleration, $Sa_{ROCK}(f)$, and spectral acceleration at the initial site frequency, $Sa_{ROCK}(f_{sc})$, while Bazzurro and Cornell (2004b) used the preferred AF model from Bazzurro and Cornell (2004a) to develop soil hazard curves using the convolution approach.

In Bazzurro and Cornell (2004a) amplification factors were computed for a sand site and a clay site using nonlinear site response analysis and 78 rock motions. The computed values of AF were used in a multiple regression analyses of $AF(f)$ to statistically investigate the relationship between AF and the event and ground motion parameters. The analysis showed that $AF(f)$ diminishes in amplitude with increasing input intensity. Moreover, a systematic shift of the first resonant peak toward longer periods with increasing intensity is noted. These trends are expected for nonlinear soil behavior.

Combinations of the five different event/ground motion parameters were investigated to predict $AF(f)$. The different predictive models were compared in terms of the standard deviation of the natural log of AF ($\sigma_{\ln AF}$) and the coefficient of multiple determination (R^2). Figure 2.5 shows $\sigma_{\ln AF}$ obtained at different frequencies for different predictive models for the sand site. This figure shows that at most frequencies the predictive model that includes $Sa_{ROCK}(f)$ and a second order polynomial (black squares) has the smallest $\sigma_{\ln AF}$. Introducing other parameters only reduces $\sigma_{\ln AF}$ at very low frequencies. As a result, Bazzurro and Cornell (2004a)

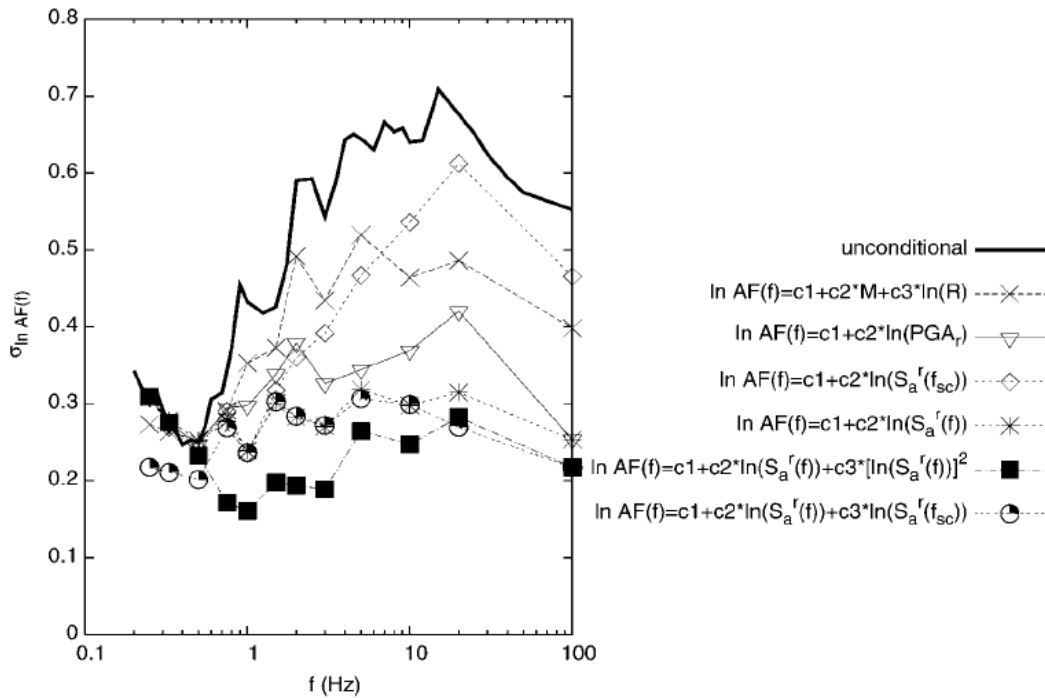


Figure 2.5 Comparison of the standard deviation of $\ln AF(f)$ predicted by different combinations of five intensity parameters. (Bazzurro and Cornell, 2004a)

concluded that that $AF(f)$ can be predicted accurately with the knowledge of $Sa_{ROCK}(f)$ alone. Figure 2.6 shows the second order polynomial $\ln(AF) - \ln(Sa_{ROCK})$ models for the sand site along with the $AF(f)$ data at 1 Hz and 100 Hz. These fitted models once more indicate the accuracy of using $Sa_{ROCK}(f)$ to estimate $AF(f)$.

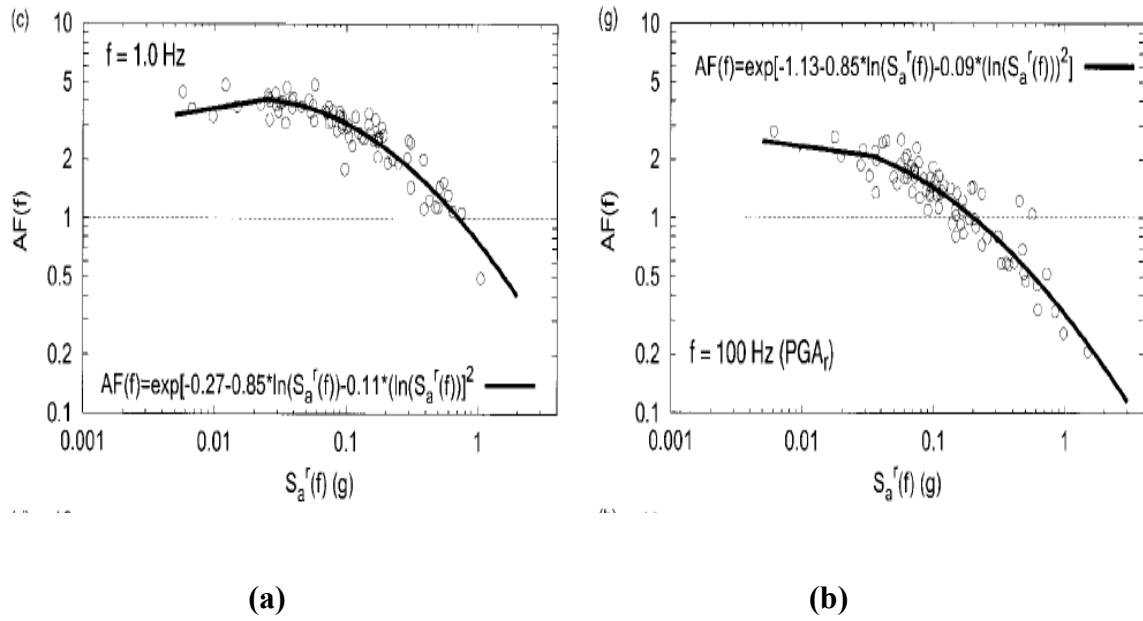


Figure 2.6 Regression analyses performed for sand site of $AF(f)$ on $Sa_{ROCK}(f)$ at (a) 1.0 Hz and (b) 100 Hz

The Bazzurro and Cornell (2004a) study also investigated the effect of statistically varied soil properties on the predicted amplification function (Figure 2.7). These analyses used Monte Carlo simulations to model the variable properties and they found that the extra variability introduced by the soil property variability

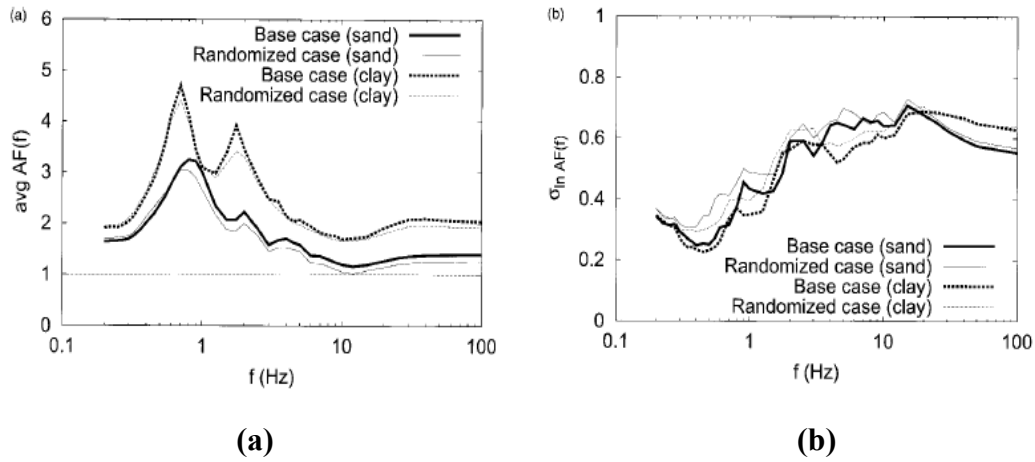


Figure 2.7 Regression analyses on a sand site of $AF(f)$ on $Sa_{ROCK}(f)$ at (a) 1.0 Hz and (b) 100 Hz

did not have major influence on the average amplification factors across all motions. A slight shift in the predicted $AF(f)$ is observed at the resonant frequencies in the varied (i.e., randomized case), which results in a smoother average $AF(f)$ due to the variation between weak and strong profiles generated in the Monte Carlo simulations (Figure 2.7a). Accordingly, the authors concluded that the variability in $AF(f)$ due to uncertainty in soil properties does not affect the amplification models derived from previous multiple-regression analyses. Introducing uncertainty in the soil properties increases the standard deviation by 10% to 15%, especially at low frequencies (Figure 2.7b).

The companion study (Bazzurro and Cornell 2004b) integrated the developed AF predictive models into a PSHA to obtain soil-specific hazard estimates for a given site. Based on the results from Bazzurro and Cornell (2004a), the surface hazard curves are computed assuming that $AF(f)$ is dependent on $Sa_{ROCK}(f)$. As a result equation (2.8) simplifies to:

$$\begin{aligned}
 P[Sa_{SOIL}(f) \geq z] & \qquad \qquad \qquad (2.10) \\
 & = \sum_{Sa_{ROCK_i}} P \left[AF(f) \geq \frac{z}{Sa_{ROCK}} \middle| Sa_{ROCK_i} \right] P[Sa_{ROCK_i}]
 \end{aligned}$$

where $P[Sa_{ROCK_i}]$ is the annual probability of occurrence for $Sa_{ROCK}(f)$ equal to Sa_{ROCK_i} . This probability is obtained by differentiating a previously defined rock hazard curve. $P \left[AF(f) \geq \frac{z}{Sa_{ROCK}} \middle| Sa_{ROCK_i} \right]$ can be computed by assuming $AF(f)$ is lognormally distributed and is a function of Sa_{ROCK_i} .

$$P \left[AF(f) \geq \frac{z}{x} \middle| x \right] = \hat{\Phi} \left(\frac{\ln \left[\frac{z}{x} \right] - \mu_{\ln AF|x}}{\sigma_{\ln AF|x}} \right) \qquad (2.11)$$

where $\mu_{\ln AF|X}$ is the mean value of $\ln[AF(f)]$ given $Sa_{ROCK}(f) = x$, $\sigma_{\ln AF|X}$ is the standard deviation of $\ln[AF(f)]$ given $Sa_{ROCK}(f) = x$, and $\hat{\Phi}(\cdot)$ is the standard Gaussian complementary cumulative distribution function. Parameters $\mu_{\ln AF|X}$ and $\sigma_{\ln AF|X}$ are obtained from the developed $AF(f)$ relationship and are a function of bedrock amplitude, x .

Bazzurro and Cornell (2004b) provide a comparison of the UHS predicted by the convolution approach and the deterministic amplification of the rock UHS (i.e., NRC Approach 1). Figure 2.8 compares the resulting surface spectra for a sand site and a clay site for four different hazard levels (i.e., annual probabilities of exceedance of 50%, 10%, 5% and 2% in 50 years). Note that Approach 1 is labeled as the hybrid method in Figure 2.8. NRC Approach 1 generally underestimates the ground motion as compared with the convolution approach; and the underestimation is larger at smaller hazard levels. Moreover, the degree of underestimation varies across period, with the underestimation being most significant at higher frequencies.

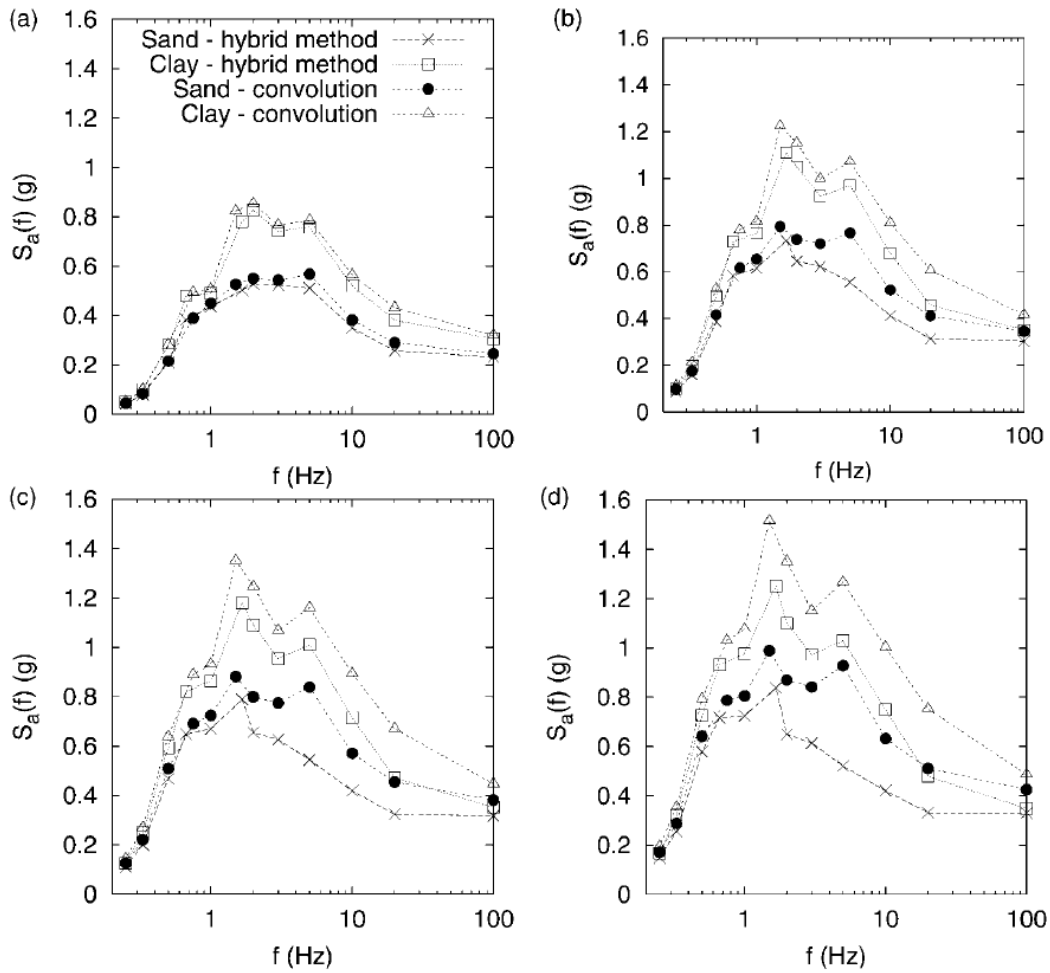


Figure 2.8 Comparison of UHS of hypothetical site predicted by NRC Approach 1 (i.e., hybrid method) and convolution method for (a) 50%, (b) 10%, (c) 5%, and (d) 2% probability of exceedance (PE) in 50 years, (Bazurro and Cornell, 2004)

2.6 Summary

This chapter presented an overview of probabilistic seismic hazard analysis (PSHA) and the available methods of site response analysis. PSHA intends to predict the site-specific hazard by considering all possible earthquake scenarios and associated uncertainties of each variable within that scenario event through a probabilistic framework. The nonlinear nature of the soil response makes it difficult to integrate the uncertainties associated with the soil response into the PSHA to predict soil hazard levels. Therefore, site response analyses are performed outside of the PSHA to predict an amplification model with quantified uncertainties of soil properties.

There are several different approaches available in practice for the prediction of the site-specific soil hazard, most of which are summarized in US-NUREG 6728 and US-NUREG 6769. Among these approaches, the convolution approach (Bazzurro and Cornell 2004b), also known as NRC Approach 3, provides an accurate estimate of the hazard level at the surface since it involves convolution of rock hazard with the probability distribution of soil amplification to generate the hazard curve on soil.

Bazzurro and Cornell (2004) showed that the amplification function for a site is mostly dependent on rock spectral acceleration. Definition of amplification as a

function of rock spectral acceleration for a given oscillator frequency facilitates the incorporation of the site amplification and its uncertainty into PSHA, resulting in a fully-probabilistic prediction of hazard levels at the soil surface.

3

DESCRIPTION OF STUDY SITE AND INPUT PARAMETERS

3.1 Introduction

Estimation of ground motion hazard at a specific site requires analyses be performed for a realistic site profile. The site response analyses performed throughout this work will be based on two actual sites: a 100-m deep alluvium site in California and very deep site in Maryland. To evaluate site-specific soil hazard curves, these sites will be placed at a specific location in California with an associated rock hazard curve.

This chapter provides detailed information on the characteristics of the two soil sites (i.e., shallow and deep) including the shear-wave velocity profiles and the modulus reduction and damping curves. The rock hazard curves for the selected location are described, and the input rock motions to be used in subsequent time series and RVT site response analyses are presented.

3.2 Description of Study Sites

3.2.1 SHALLOW SITE: SYLMAR COUNTY HOSPITAL SITE

The Sylmar County Hospital (SCH) site is located in the San Fernando Valley of Southern California. The shear wave velocity (V_S) profile is shown in Figure 3.1. The site has about 90 m of alluvium above bedrock, with V_S ranging from about 250 m/s at the surface and increasing to above 700 m/s at 60 m (Gibbs et al. 1999). The nonlinear modulus reduction and damping curves are assigned for the four main velocity layers based on the empirical model of Darendeli (2001). The mean confining pressure (σ'_m), overconsolidation ratio (OCR), and plasticity index (PI) used to generate these curves are listed in Table 3.1. The number of cycles and excitation frequency are assumed to be 10 and 1 Hz, respectively, for the Darendeli (2001) model. Figure 3.2 shows the nonlinear modulus reduction and damping curves used in the site response analyses for the shallow site. Damping of the half-space below the site was assumed to be 1 %. The small strain natural period of the site is about 0.8 s based on the quarter-wavelength method.

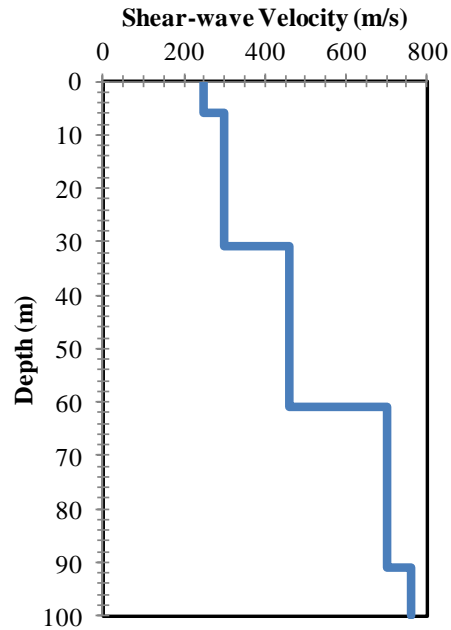
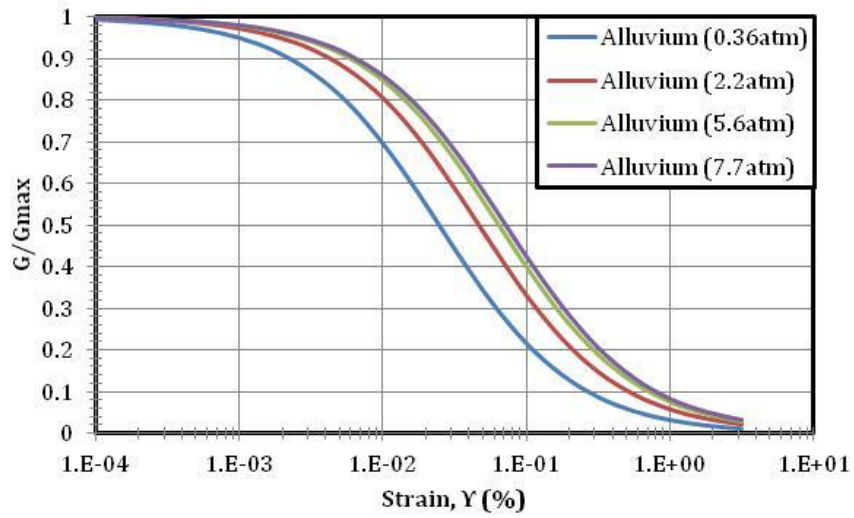


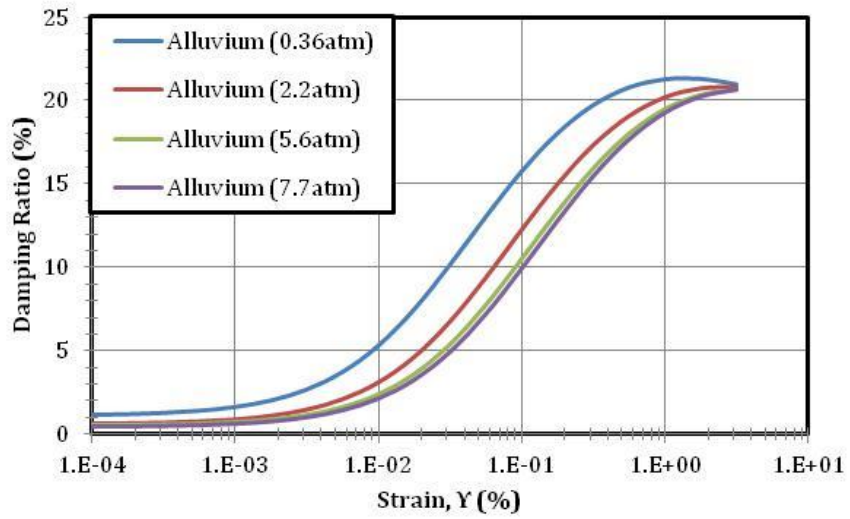
Figure 3.1 Shallow site (i.e. SCH site) shear-wave velocity profile

Table 3.1 Shallow site (i.e. SCH site) profile with corresponding shear-wave velocity, V_s

<i>Material</i>	<i>Unit Weight (kN/m³)</i>	<i>σ'_m (atm)</i>	<i>PI</i>	<i>OCR</i>
<i>Alluvium (0.36atm)</i>	18	0.36	0	1
<i>Alluvium (2.2 atm)</i>	18	2.2	0	1
<i>Alluvium (5.6 atm)</i>	19	5.6	0	1
<i>Alluvium (7.7 atm)</i>	22	7.7	0	1



(a)



(b)

Figure 3.2 (a)Nonlinear modulus reduction and (b)damping curves for SCH site

3.2.2 DEEP SITE: CALVERT CLIFFS SITE

The Calvert Cliffs (CC) site is located on the Chesapeake Bay of Maryland. The shear wave velocity (V_S) profile for the site, as reported by UniStar Nuclear Services (2007), is shown in Figure 3.3. The site has about 750 m of sand and clay/silt layers alternating until bedrock with V_S ranging from about 250 m/s at the surface and increasing to above 600 m/s around 100 m. The V_S increases moderately from 600 m/s to 850 m/s over depths of 100 m to 750 m before reaching hard rock ($V_S = 2,800$ m/s). The nonlinear modulus reduction and damping curves are assigned to the soil layers based on the empirical model of Darendeli (2001). The mean confining pressure (σ'_m), overconsolidation ratio (OCR), and plasticity index (PI) used to generate these curves are obtained from the report of Unistar Nuclear Services (2007) and listed in Table 3.2. The number of cycles and excitation frequency are assumed to be 10 and 1 Hz, respectively, for the Darendeli (2001) model. Figure 3.4 shows the nonlinear modulus reduction and damping curves used in the site response analyses for the deep site. Damping of the half-space was assumed to be 1 %. The natural frequency of the site is about 0.21 Hz based on the quarter-wavelength method.

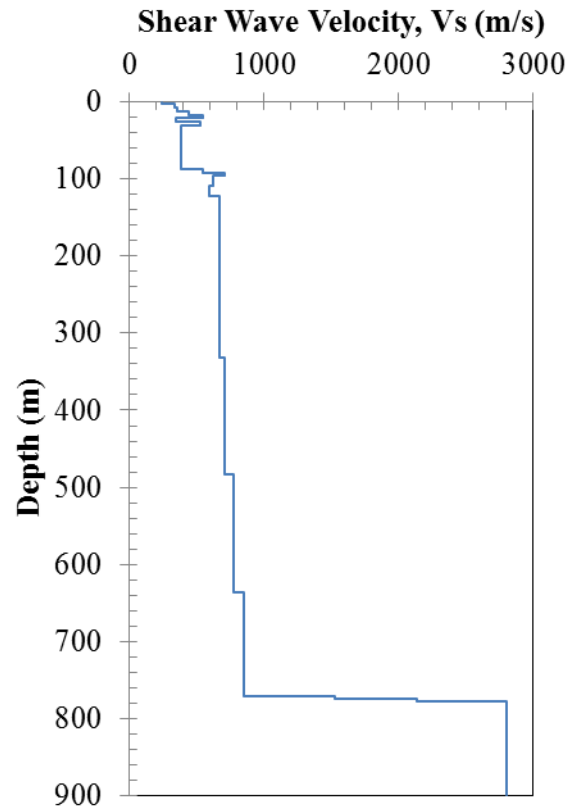
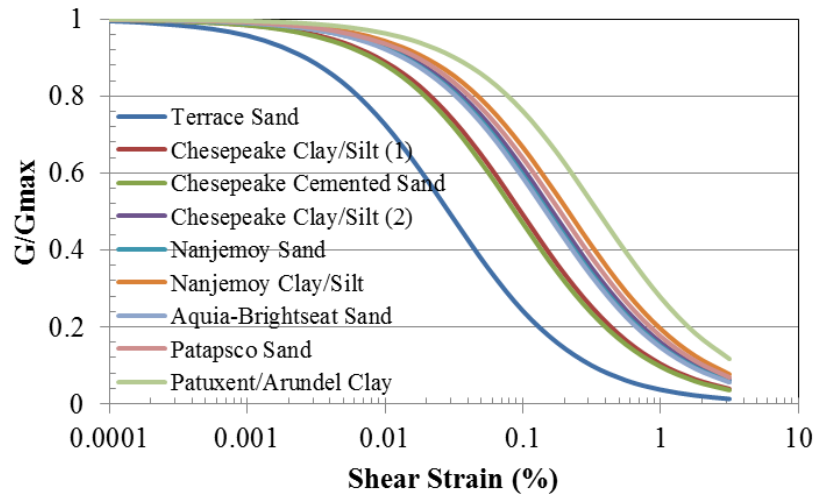


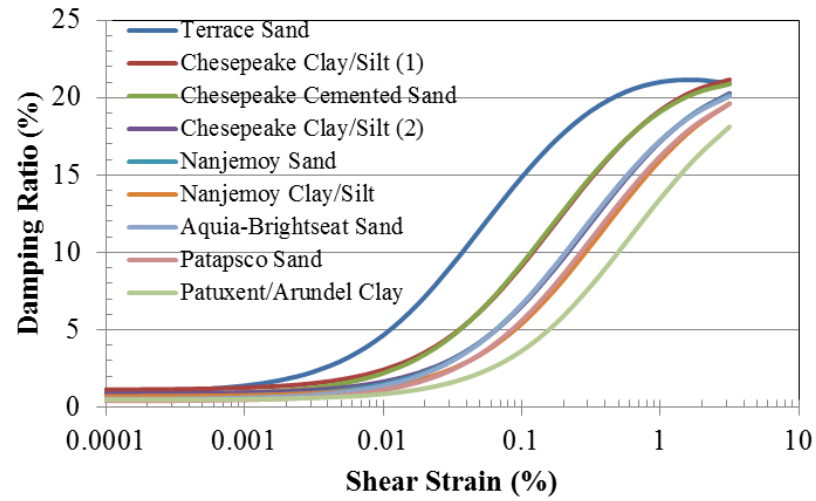
Figure 3.3 Shear-wave velocity profile of the deep site (i.e. CC site)

Table 3.2 Deep site (i.e. CC site) profile with corresponding shear-wave velocity, V_s

Depth (m)	Thickness (m)	Soil Type	V_s (m/s)	σ'_m (atm)	Unit Weight, γ (kN/m ³)	OCR	PI
0	2.4	Terrace Sand	241	0.57	18.85	4	0
2.4	5.2	Terrace Sand	335	0.57	18.85	4	0
7.6	4.6	Chesapeake Clay/Silt (1)	355	1.22	18.07	4	35
12.2	4.6	Chesapeake Cemented Sand	442	2.51	18.85	3	20
16.8	4.5	Chesapeake Cemented Sand	549	2.51	18.85	3	20
21.3	4.6	Chesapeake Cemented Sand	344	2.51	18.85	3	20
25.9	4.6	Chesapeake Cemented Sand	530	2.51	18.85	3	20
30.5	10.7	Chesapeake Clay/Silt (2)	381	4.25	17.28	3	45
41.1	45.7	Chesapeake Clay/Silt (2)	381	4.25	17.28	3	45
86.9	6.1	Nanjemoy Sand	546	6.9	18.85	3	30
93	3	Nanjemoy Sand	710	6.9	18.85	3	30
96	12.2	Nanjemoy Sand	619	6.9	18.85	3	30
108	13.7	Nanjemoy Sand	588	6.9	18.85	3	30
122	30.5	Nanjemoy Clay/Silt	671	8.94	17.28	3	45
152	39.9	Aquia-Brightseat Sand	671	11.1	20.42	3	20
192	139	Patapsco Sand	671	25.6	20.42	2	20
331	152	Patapsco Sand	710	25.6	20.42	2	20
483	44.5	Patapsco Sand	777	25.6	20.42	2	20
528	108	Patuxent/Arundel Clay	777	39.4	19.64	2	50
636	136	Patuxent/Arundel Clay	853	39.4	19.64	2	50
772	3	Weathered Granite	1524	-	22	-	-
775	3	Weathered Granite	2134	-	22	-	-
778		Bedrock	2804	-	25.13	-	-



(a)



(b)

Figure 3.4 Nonlinear modulus reduction and damping curves for CC site

3.3 Rock Motion Characterization

The ground motion hazard used in subsequent analyses for the SCH and CC sites is from the Sylmar County Hospital site location (34.327N, 118.444W) in Southern California. The ground motion hazard curves are computed using the NSHMP Hazard Curve Application (Petersen et al., 2008) of the U.S. Geological Survey (USGS) for NEHRP B/C site class conditions ($V_{S,30} = 760$ m/s). The hazard curves for peak ground acceleration (PGA) and spectral accelerations (Sa) at $T = 0.2$ s, 0.4 s, 1.0 s, and 1.6 s are shown in Figure 3.5. At a hazard level of 0.002 1/yr. (i.e., 10% of probability of exceedance in 50 years), the design bedrock accelerations are 0.59 g, 1.46 g, 1.04 g, 0.43 g, and 0.28 g for PGA and for Sa at $T = 0.2$ s, 0.4 s, 1.0 s, and 1.6 s, respectively. At a hazard level of 0.0004 1/yr. (i.e., 2% of probability of exceedance in 50 years), the design bedrock accelerations are 1.14 g, 2.91 g, 2.08 g, 0.87 g, and 0.55 g for PGA and Sa at $T = 0.2$ s, 0.4 s, 1.0 s, and 1.6 s, respectively. Figure 3.6 illustrates uniform hazard curves for 2 % and 10 % probability of exceedance in 50 years for SCH site.

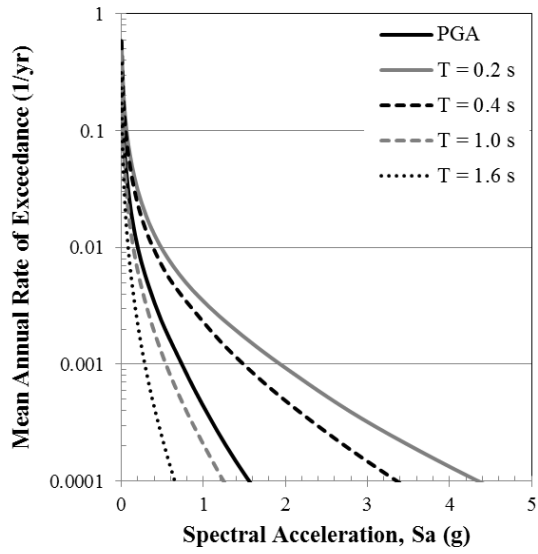


Figure 3.5 Rock hazards curves for PGA and selected periods.

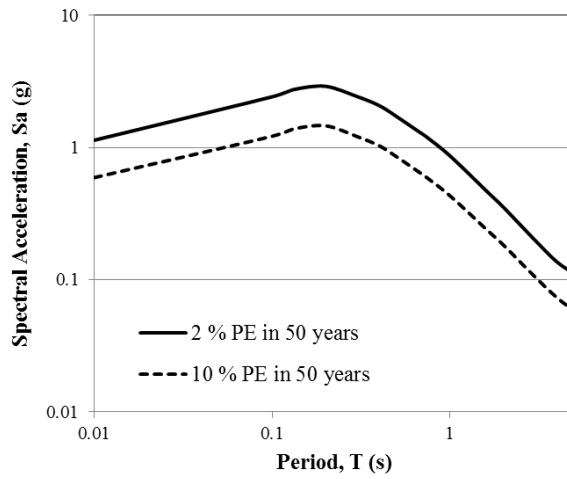


Figure 3.6 Uniform hazard curves for 2% and 10% probability of exceedance levels.

The goal of the site response analyses when incorporated in the convolution approach (Chapter 2.5) is to generate site amplification factors for a large range of input intensities. These amplification factors are used to develop amplification factor relationships that predict amplification as a function of input intensity. Thus, input motions over a large range of input intensities are required for the site response analyses.

For the time series (TS) site response analyses performed in this research, input motions are selected from the NGA strong motion database (peer.berkeley.edu/nga). Input motions are selected from sites with an average shear wave velocity in the top 30 m ($V_{s,30}$) greater than 600 m/s. Although this $V_{s,30}$ is smaller than the value typically representing rock ($V_{s,30} \geq 760$ m/s), a smaller $V_{s,30}$ was required in order to identify a significant number of potential input motions. Using this criterion, 130 recorded ground motions are identified and selected for use in the TS analyses. These motions come from earthquakes with magnitudes ranging from 6.1 to 7.9 and they were recorded at distances ranging from 1.5 km to 90 km. Figure 3.7 presents the distribution of the selected input motions in terms of earthquake magnitude and distance. This figure shows that the selected input motions cover a wide range of magnitudes and distances. Even though the distances are mainly concentrated at distances greater than 20 km, there are several motions that were recorded at distances less than 10 km. The input response spectra of the selected motions for site response analysis are shown in Figure 3.8. The PGA of the

input motions range from about 0.005 g to 1.0 g, representing a wide range of bedrock input intensities. The input motions are not scaled from their recorded intensities.

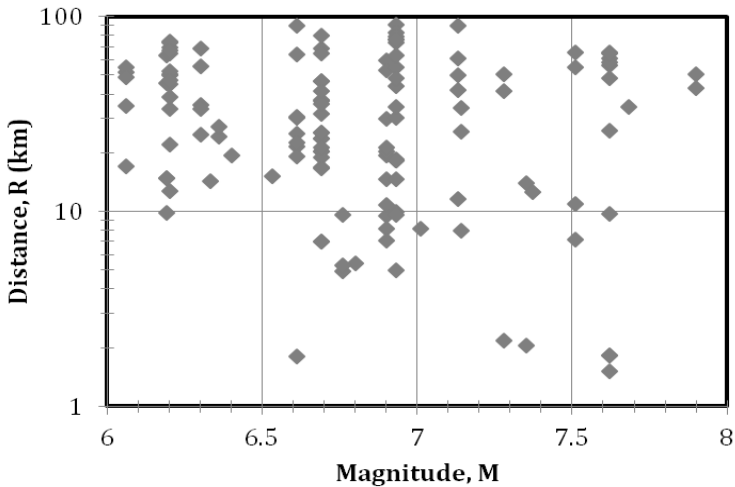


Figure 3.7 Magnitude-distance distribution of selected input motions for TS site response analyses.

For the RVT analyses, input motions are specified based on an acceleration response spectrum and duration. Input response spectra are generated using the Abrahamson and Silva (2008) ground motion prediction equation for $V_{S,30} = 760$ m/s and scenario earthquakes with magnitudes ranging from 5.0 to 8.0 and distances

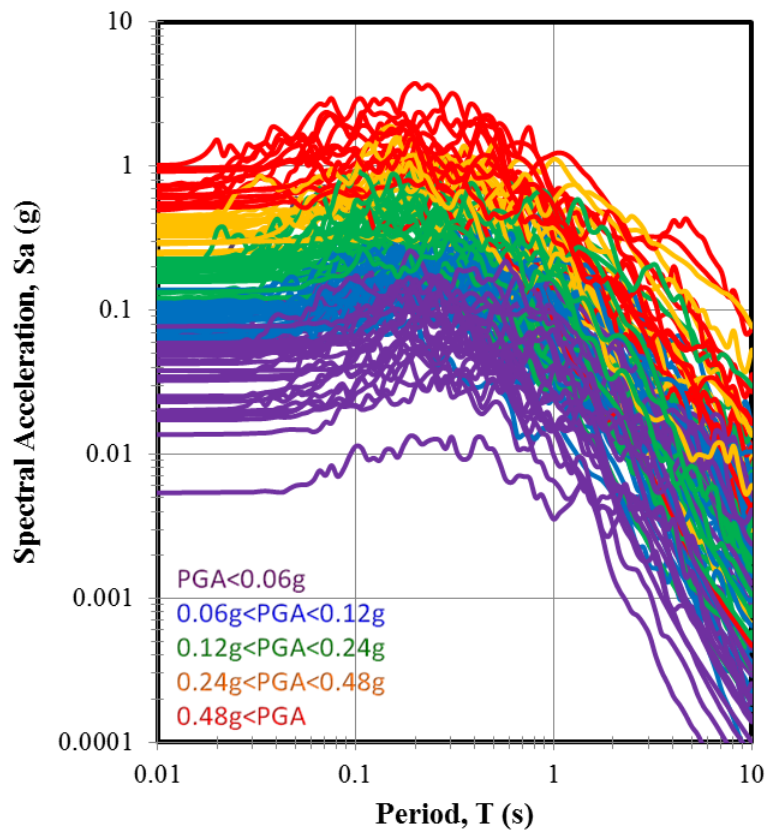


Figure 3.8 Input response spectra for TS site response analyses

ranging from 0 to 100 km. Under these conditions the maximum input PGA is only 0.53 g, and therefore median plus two standard deviation motions were considered for some magnitude/distance combinations in an effort to increase the range of input PGA. A total of 146 input response spectra are used in the RVT analyses, and the corresponding response spectra are shown in Figure 3.9. The range of PGA values

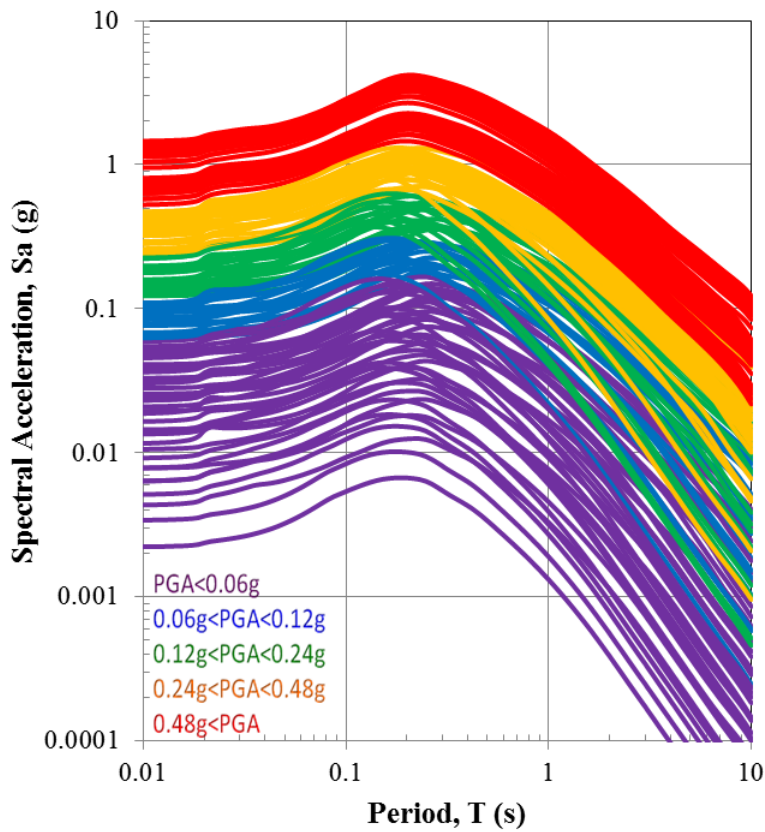


Figure 3.9 Input response spectra for RVT analysis

for the RVT input motions is 0.002 g to 0.8 g. The associated durations for these motions are specified based on the significant duration D_{5-95} (i.e., the time between 5 % and 95 % of the Arias Intensity of the acceleration-time history). D_{5-95} for each scenario is estimated using the empirical relationship of Abrahamson and Silva (1996).

An important advantage of RVT site response analysis is that fewer analyses need to be performed than when performing TS analysis. Fewer analyses are required because the stochastic process incorporated in RVT predicts the average response of the site in one analysis, while TS analyses requires a suite of 7-10 motions to generate the average response. The RVT input motions shown in Figure 3.9 represent the same range of input intensities at the TS input motions in Figure 3.8, but fewer RVT input motions could potentially provide the required amplification. Therefore, a second set of 19 RVT motions are generated based on the information from the rock hazard curves.

The generation of the 19 RVT motions is guided by NUREG 1.208, which uses the deaggregation of the mean hazard curves at low and high frequencies to estimate the controlling earthquakes to be used in site response analyses. Accordingly, the deaggregation of the mean hazard curves at various probabilities of exceedance (i.e. 1 %, 2 %, 5 %, 10 %, 20 % and 50 % probabilities of exceedance in 50 years and 50 % probability of exceedance in 21 years) are obtained using the 2008 NSHMP PSHA Interactive Deaggregation Tool (Peterson et al., 2008) provided by USGS. The hazard levels are used based on their availability in the USGS Deaggregation Tool. Deaggregation of the mean hazard curves are obtained at spectral frequencies of 1 Hz, 2 Hz, 5 Hz, and 10 Hz. Figure 3.10 shows the deaggregation results for 2 % probability of exceedance in 50 years at these four frequencies. This figure shows that for this hazard level the highest contribution to

the hazard comes from similar magnitude-distance combinations for low and high frequencies (i.e., magnitudes between 6.5 and 7.5; distances between 0 and 10 km). The mean magnitudes are very similar across the frequencies, ranging from 6.7 to 6.8, and all of the distances are about 4 km.

The deaggregation results for 1 and 2 Hz are averaged to develop the controlling low frequency earthquake scenario and the deaggregation results for 5 and 10 Hz are used averaged to develop the controlling low frequency earthquake scenario. Table 3.3 lists the low and high frequency controlling earthquakes obtained for the selected probabilities of exceedance. This table shows that there are not significant differences between the controlling earthquakes estimated at low and high frequencies for this site location. For low frequencies, the controlling earthquake magnitude ranges between 6.78 and 6.85 and the associated distance ranges between 3.86 km and 36.72 km; whereas for high frequencies the controlling earthquake magnitude ranges between 6.66 and 6.72 and the associated distance ranges between 3.66 km and 29.10 km. In general, as the probability of exceedance increases, the distance for the controlling earthquake increases.

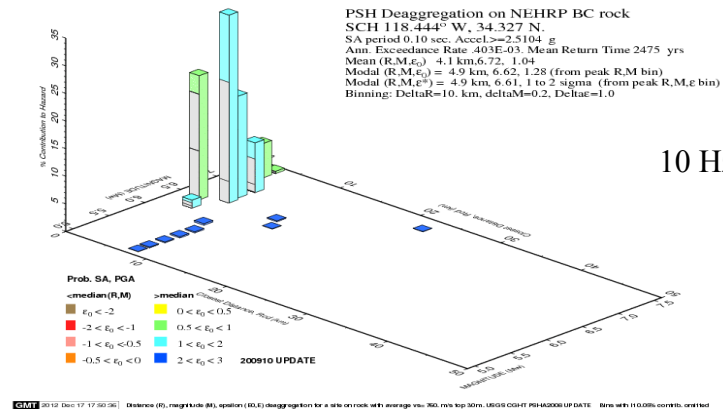
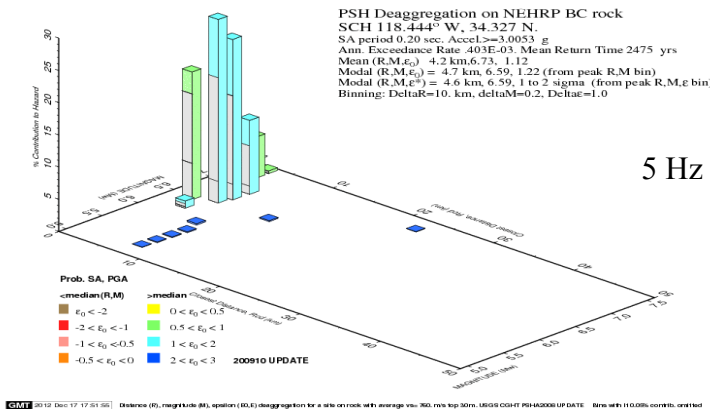
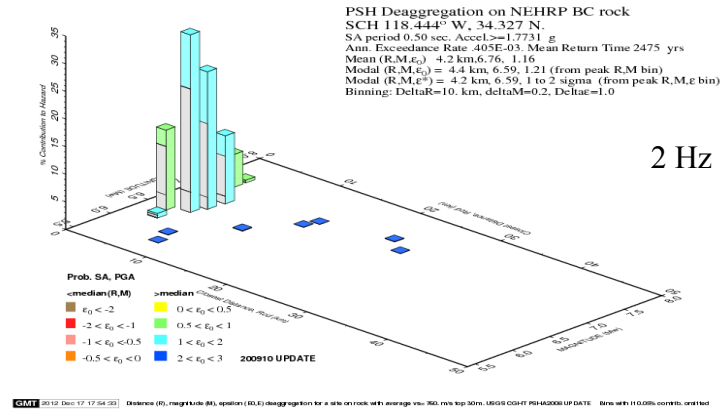
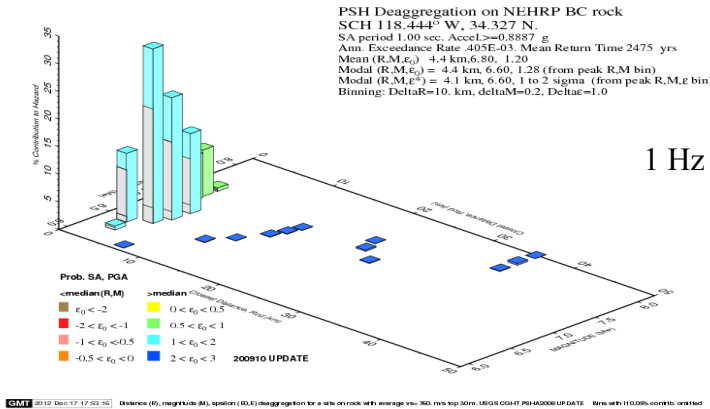


Figure 3.10 Deaggregation results for 2% probability of exceedance in 50 years at 1 Hz, 2 Hz, 5 Hz and 10 Hz

Table 3.3 Controlling earthquakes obtained from deaggregation of selected probability of exceedance levels.

Probability of Exceedance	Low Frequency (1.5 Hz)		High Frequency (7.5 Hz)	
	M	R (km)	M	R (km)
1 % in 50 years	6.78	3.86	6.72	3.66
2 % in 50 years	6.77	4.29	6.71	4.10
5 % in 50 years	6.77	5.30	6.70	4.82
10 % in 50 years	6.78	7.00	6.70	5.96
20 % in 50 years	6.81	10.62	6.71	8.75
50 % in 50 years	6.88	22.09	6.72	18.17
50 % in 21 years	6.85	36.72	6.66	29.10

The response spectra for the specified controlling earthquakes are estimated by averaging the ground motion predictions from four of the Next Generation Attenuation relations (NGA) for rock conditions ($V_{s,30} = 760$ m/s). The NGA relationships used are Abrahamson and Silva (2008), Boore and Atkinson (2008), Campbell and Bozorgnia (2008), and Chiou and Youngs (2008). Equal weight of 0.25 is assigned to each NGA model to obtain the resulting response spectra. The computed response spectra obtained for low and high frequency motions for each probability of exceedance level are then scaled to match the uniform hazard spectrum (UHS) corresponding to the same probability of exceedance level. The response spectrum from the low frequency controlling earthquake is scaled to the UHS at 1.5 Hz (i.e., the average of 1 and 2 Hz) and the response spectrum from the high frequency controlling earthquake is scaled to the UHS at 7.5 Hz (i.e., the

average of 5 and 10 Hz). The smallest PGA for the resulting response spectra is only about 0.1 g. To ensure accurate amplification factors are obtained for low levels of shaking, additional low intensity motions are obtained by scaling the response spectra obtained for 50 % of probability of exceedance in 21 years to PGA levels of 0.01 g and 0.03 g. Additionally, to generate a motion with a large S_a at a period of 1.6 s, a motion is added by scaling the response spectrum for 1% probability of exceedance in 50 years motion to 1.0 g at $T = 1.6$ s. Figure 3.11 plots the final set of 19 input motions for RVT analyses, obtained through the deaggregation analyses. The range of PGA values for this set of RVT input motions is 0.01 g to 2.4 g.

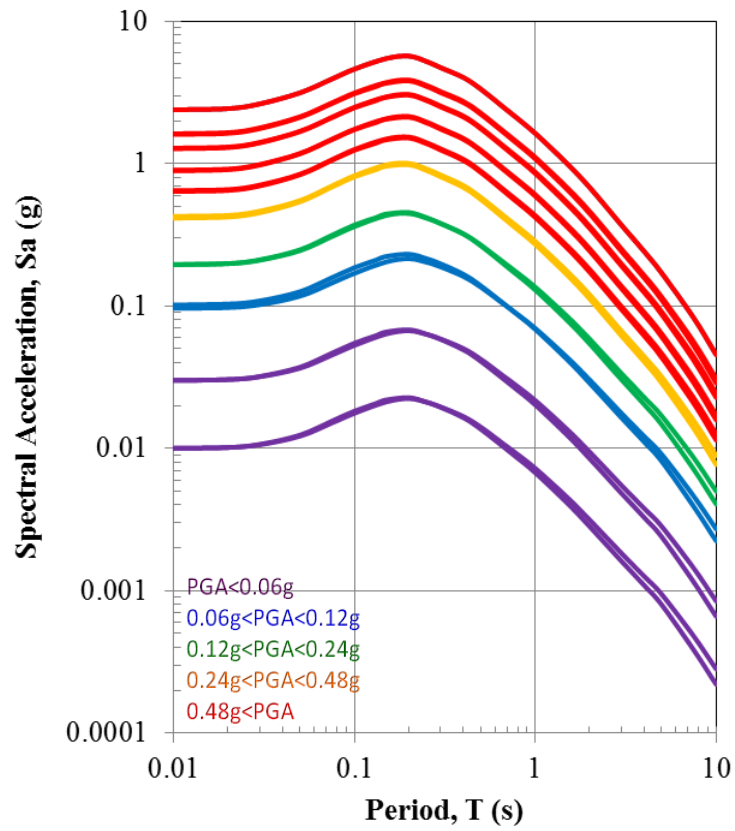


Figure 3.11 Input response spectra for RVT analysis selected through deaggregation of site hazard

3.4 Summary

A shallow (Sylmar County Hospital) site profile and a deep (Calvert Cliffs) site profile will be used in subsequent site response analyses. The shallow site has about 90 m alluvium above the bedrock and the shear wave velocity profile ranges from 250 m/s to 700 m/s in the top 60 m of depth. The deep site has 750 m of sand and clay/silt layers alternating above the bedrock with a shear wave velocity profile ranging from 240 m/s at the surface to about 800 m/s above the bedrock. Rock hazard curves associated with the Sylmar County Hospital site, located in Southern California, are developed and used to select appropriate input motions for site response analysis. 130 input motions are selected from the NGA strong motion database for use in time series site response analyses. Two sets of RVT input motions are developed. The first set includes 146 input response spectra developed from ground motion prediction equations for a large range of magnitudes and distances. The second set of RVT input motions is composed of 19 input response spectra developed based on the controlling earthquakes obtained through deaggregation of the rock hazard curves at various probabilities of exceedance for representative low and high frequencies.

4

DEVELOPMENT OF SOIL HAZARD CURVES: SHALLOW SOIL SITE

4.1 Introduction

The convolution approach requires a site-specific amplification function that predicts site amplification at different frequencies as a function of the input Sa_{ROCK} . These amplification functions are later convolved with rock hazard curves to predict soil hazard curves. Site response analyses are used to compute site amplification factors (AF) that are the basis of the developed amplification functions. One-dimensional TS and RVT equivalent linear site response analyses can be performed to compute the surface acceleration response spectrum and associated AF at each frequency. At a given frequency, computed AF values and input Sa_{ROCK} values from each input motion are used to develop the amplification function as a function of Sa_{ROCK} at that frequency. The convolution method then integrates this amplification

function together with the hazard curve for the given frequency to estimate the soil hazard curve at that frequency.

This chapter describes the development of amplification relationships for the shallow soil located at Sylmar County Hospital (SCH). The amplification relationships are developed using two different site response approaches: time series (TS) and random vibration theory (RVT). The TS and RVT equivalent-linear site response analyses are performed using the software program Strata (Kottke and Rathje, 2008). For each input motion, the surface response spectra and the associated AF values at each period are computed. The computed AF for both the TS and RVT analyses are presented and used to develop amplification functions. The effect of parametric variability in the shear wave velocity profile on the computed amplification functions is investigated. For this purpose, 20 realizations of the shear wave velocity profile are generated through Monte Carlo simulations. The convolution approach is then used to develop soil hazard curves for the Sylmar County Hospital site using the different derived amplification relationships.

4.2 Amplification Relationships for Known Shear Wave Velocity Profile

Equivalent linear site response analyses are performed for the SCH site with the site response program Strata (Kottke and Rathje, 2008) using the selected input motions presented in Chapter 3 for time series (TS) and random vibration theory (RVT) analysis. The response spectra at the surface and the associated AF values are computed for each input motion and the site response analysis results are analyzed in terms of AF . The ultimate goal of the site response analyses is to represent AF as a function of Sa_{ROCK} so that site amplification can be implemented into the hazard calculations to predict the hazard at the soil surface.

4.2.1 RESULTS FROM TIME SERIES ANALYSIS

Equivalent linear time series analyses are performed for the SCH site with the site response program Strata (Kottke and Rathje, 2008) using the 130 selected input ground motion time series presented in Chapter 3. Figure 4.1 presents the AF results for each input motion as a function of period, with the results separated based on the input PGA. Careful observation of AF results indicates the effect of soil nonlinearity

through the observed reduction in short period amplification and the elongation of the site period with increasing input intensity.

The ultimate goal of the site response analyses is to represent AF as a function of Sa_{ROCK} at a given period so that site amplification can be implemented into the hazard calculations to predict the hazard at the soil surface. Thus, the AF values from Figure 4.1 are plotted versus Sa_{ROCK} in Figure 4.2 for various periods: PGA and periods of 0.2 s, 0.4 s and 1.0 s. At short periods ($T \leq 0.4$ s), a reduction is observed in AF at large intensities (i.e., large Sa_{ROCK}) due to soil nonlinearity (i.e., increased soil damping). The rate of reduction is more pronounced at shorter periods. However, at a period of 1.0 s, which is close to site period, there is first an initial increase in AF with increasing intensity (up to an Sa_{ROCK} of about 0.4 g) which is followed by a decrease in AF . The increase in AF at moderate intensities is also caused by soil nonlinearity, specifically period elongation associated with a reduction in stiffness. The small-strain site period for the SCH site is about 0.8 s, such that as the site period elongates at moderate input intensities the AF at $T = 1.0$ s increases. However, at larger input intensities the period continues to elongate past $T = 1.0$ s and, consequently, the AF at $T = 1.0$ s decreases.

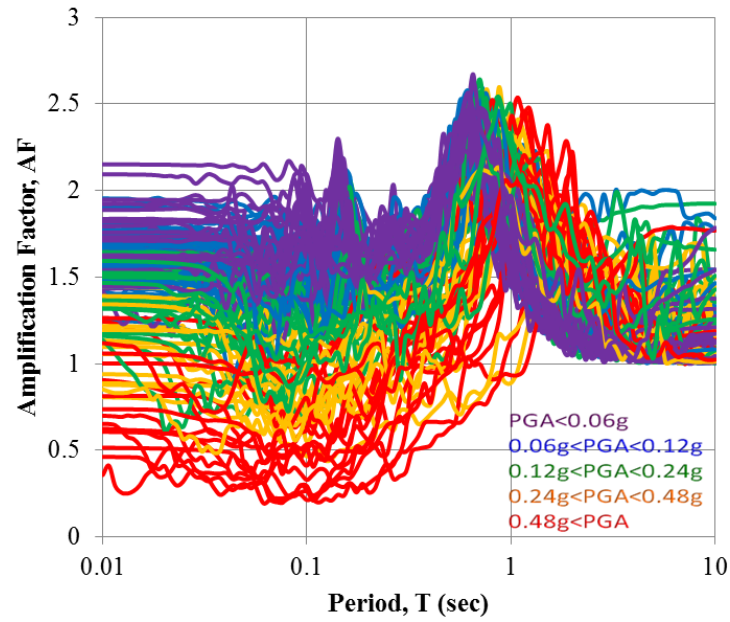


Figure 4.1 AF vs. T from TS analysis of SCH site

AF relationships are developed for the data in Figure 4.2 by fitting a higher order polynomial to $\ln(AF)$ and $\ln(Sa_{ROCK})$:

$$\ln (AF) = a_0 + \sum_{k=1}^n a_k \cdot [\ln(Sa_{ROCK})]^k \quad (4.1)$$

When fitting equation (4.1) to the data, the order of the polynomial (i.e., n) is selected to smoothly fit the available data. Residuals are used to compute the standard deviation of $\ln(AF)$, $\sigma_{\ln AF}$. It is important to note that the developed relationships are valid only for the range of Sa_{ROCK} that is represented by the available data (in this case, up to about 2.0 g, 4.0 g, 3.0 g, and 1.0 g for PGA, and $T = 0.2$ s, 0.4 s, and 1.0 s, respectively). The derived AF relationships are shown in Figure 4.2 together with the data points. Table 4.1 presents the regression coefficients for the fitted polynomials, together with the associated $\sigma_{\ln AF}$. The $\sigma_{\ln AF}$ is highest for $T = 0.2$ s due to the variability observed around 1.0 g (Figure 4.2b). The $\sigma_{\ln AF}$ is similar for PGA and $T = 0.4$ s and slightly higher for $T = 1.0$ s. The standard deviations given in Table 4.1 represent only the motion-to-motion variability and do not include variability due to variations in site properties.

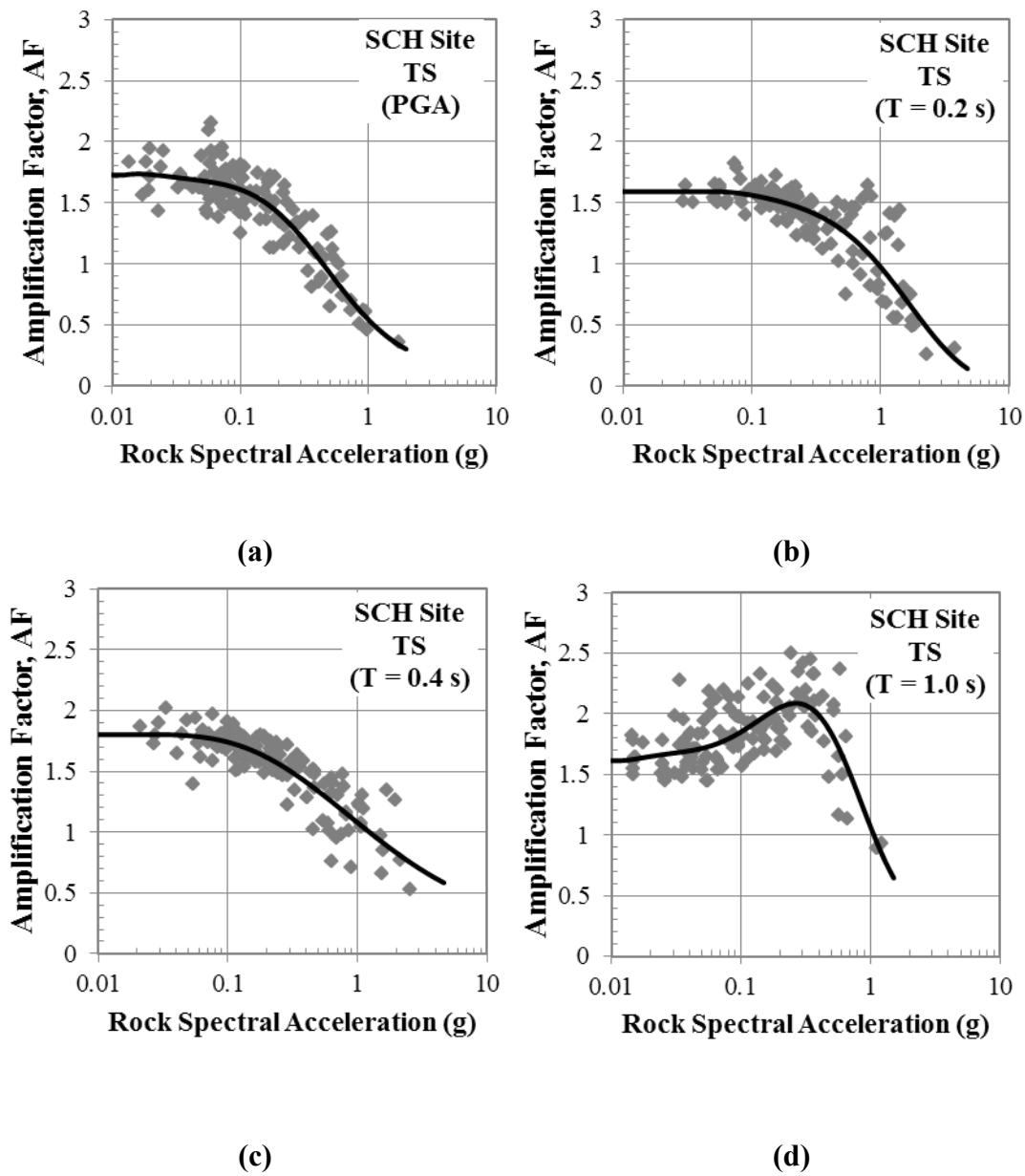


Figure 4.2 AF vs. Sa_{ROCK} data from TS analysis together with derived AF relationships for different periods (a) PGA, (b) 0.2 s, (c) 0.4 s, and (d) 1.0 s

Table 4.1 Regression coefficients and associated $\sigma_{\ln AF}$ for AF relationships developed for TS analysis

	PGA	T = 0.2 s	T = 0.4 s	T = 1.0 s
a₀	-0.6066	-0.0259	0.0764	0.0684
a₁	-0.8566	-0.5571	-0.3473	-1.0962
a₂	-0.0825	-0.2883	-0.0516	-0.3928
a₃	0.0933	-0.0799	0.0085	0.1729
a₄	0.0309	-0.0092	0.0020	0.1340
a₅	0.0028	-	-	0.0288
a₆	-	-	-	0.0021
$\sigma_{\ln AF}$	0.12	0.18	0.13	0.12

4.2.2 RESULTS FROM RVT ANALYSIS

Equivalent-linear site response analyses are also performed for the SCH site using the RVT approach, as implemented in the program Strata (Kottke and Rathje, 2008). The 146 rock response spectra presented in Chapter 3 are used as input motions, along with a ground motion duration corresponding to each scenario earthquake event defined as the significant duration D_{5-95} (i.e., the time between 5 % and 95 % of the Arias Intensity of the acceleration-time history). D_{5-95} for each scenario is estimated using the empirical relationship of Abrahamson and Silva (1996) and range from 2.5 s to 46.4 s.

The response spectra at the surface and the associated AF values are computed through site response analyses for each input motion. Figure 4.3 presents the AF values obtained for each input rock motion, with the results color-coded based on the input PGA. Unlike the AF values obtained through TS analyses, the AF values from RVT analysis vary smoothly with period due to the input motions varying smoothly with period. As a result, the RVT results more clearly indicate the effect of soil nonlinearity through the observed reduction in short period amplification and the elongation of the site period with increasing input intensity.

The AF values from Figure 4.3 are plotted versus Sa_{ROCK} in Figure 4.4 for PGA and three other spectral periods: 0.2 s, 0.4 s and 1.0 s. Similar to Figure 4.2, Figure 4.4 shows that at shorter periods there is a reduction in AF at large intensities due to soil nonlinearity and the rate of reduction is more pronounced at shorter periods. At a period of 1.0 s, an increase in AF with increasing input intensity (up to a Sa_{ROCK} of about 0.4 g) is followed by a decrease in AF with further increases in input intensity. The increase in AF followed by a decrease at larger intensities is again associated with period elongation and increased material damping associated with soil nonlinearity as previously discussed. The smooth AF curves from the RVT analysis (Figure 4.3) more clearly show the relationship between period elongation and amplification at $T = 1.0$ s. For $PGA < 0.24$ g, the AF values at 1.0 s are between about 1.6 and 1.8, and the peaks

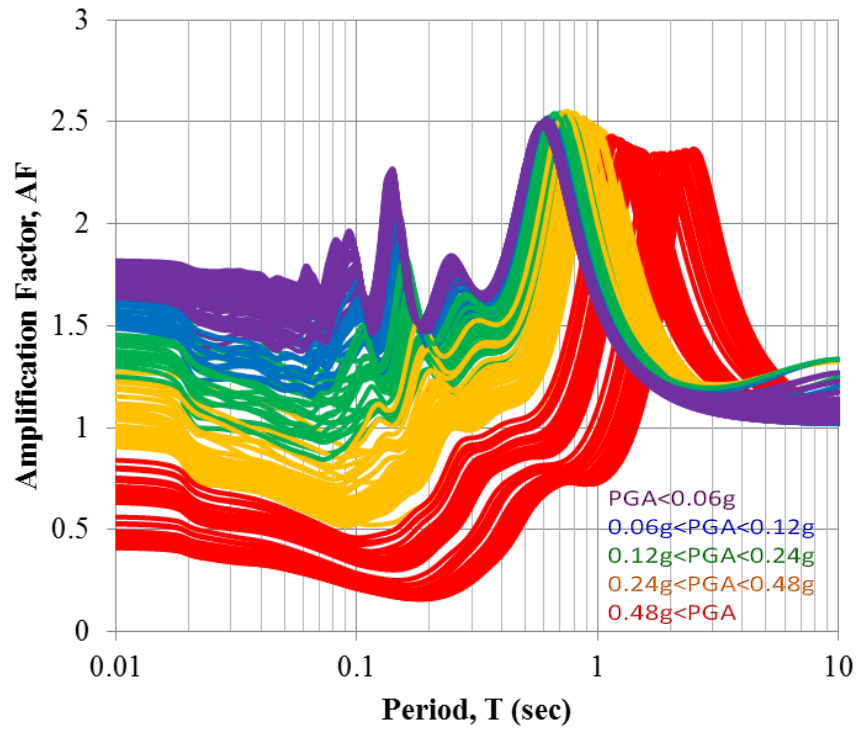
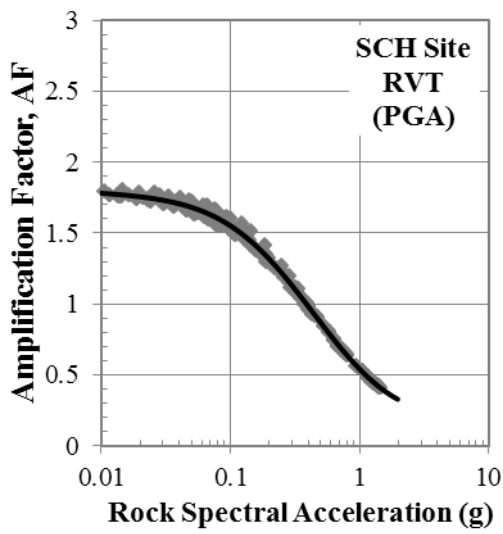
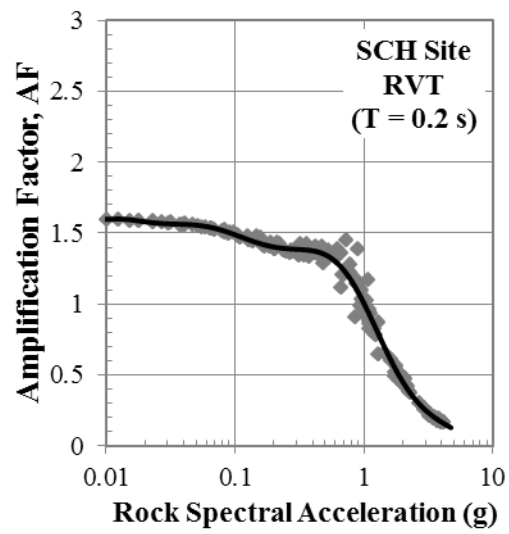


Figure 4.3 AF vs. T from RVT analysis with 146 motions for the SCH site

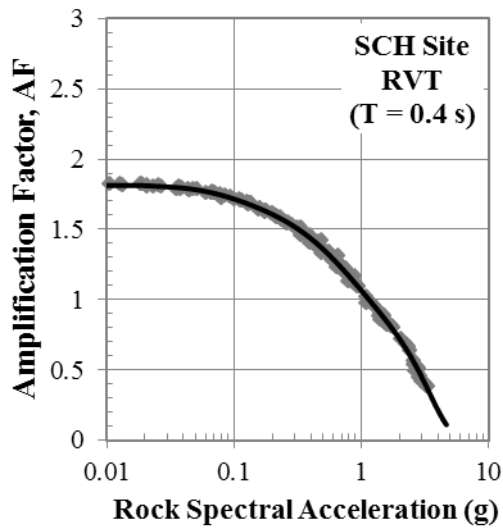
observed in the AF curves are located at periods less than 1.0 s. For $PGA = 0.24$ to 0.48 g, the AF values at 1.0 s are close to 2.4, and the peaks in the AF functions are located at periods close to 1.0 s. Finally, for larger input intensities the AF at 1.0 s is reduced to between 1.5 and 1.8, and the peaks in the AF curves are located at periods greater than 1.0 s.



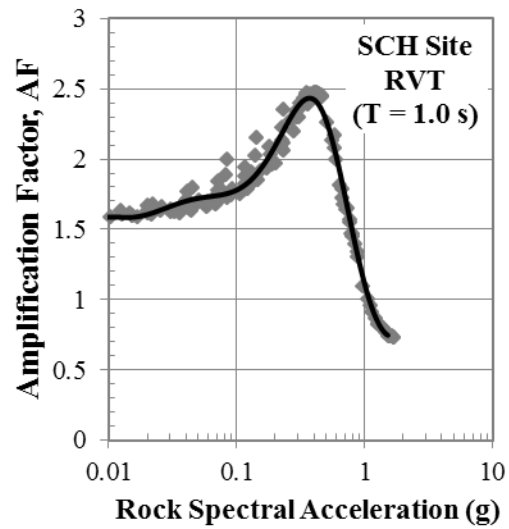
(a)



(b)



(c)



(d)

Figure 4.4 AF vs. Sa_{ROCK} data from RVT analysis together with derived AF relationships for different periods (a) PGA, (b) 0.2 s, (c) 0.4 s, and (d) 1.0 s

AF relationships are developed for the data in Figure 4.4 by fitting a higher order polynomial to $\ln(AF)$ and $\ln(Sa_{ROCK})$ using the functional form given in equation 4.1. The derived AF relationships are shown in Figure 4.4. Table 4.2 presents the regression coefficients for the polynomials fit to the RVT data, together with the associated $\sigma_{\ln AF}$. The variability in AF for the RVT analyses is very small ($\sigma_{\ln AF} \sim 0.02$ to 0.05) because RVT analysis does not include the effects of motion-to-motion variability.

Table 4.2 Regression coefficients and associated $\sigma_{\ln AF}$ for AF relationships developed for RVT analysis

	PGA	T = 0.2 s	T = 0.4 s	T = 1.0 s
a₀	-0.6142	0.0050	0.0630	0.1026
a₁	-0.7497	-0.7872	-0.4358	-1.3211
a₂	-0.0532	-0.5951	-0.1232	0.2547
a₃	0.0827	-0.0180	-0.0217	1.3728
a₄	0.0319	0.1521	-0.0527	0.5301
a₅	0.0051	0.0345	-0.0545	-0.2139
a₆	0.0004	-0.0185	-0.0246	-0.2214
a₇	1.06E-05	-0.0097	-0.0057	-0.0724
a₈	-	-0.0016	-0.0007	-0.0119
a₉	-	-9.50E-05	-3.07E-05	-0.0010
a₁₀	-	-	-	-3.42E-05
$\sigma_{\ln AF}$	0.017	0.055	0.020	0.031

One of the main advantages of RVT analysis is that the stochastic process incorporated in the approach generates in one analysis the same response generated by TS analysis using a suite of input motions. As a result, fewer RVT analyses are required than TS analyses to develop an AF relationship over a wide range of input intensities. However, the RVT analyses shown in Figures 4.3 and 4.4 use a similar number of input motions as the TS analyses. To investigate the ability of RVT analysis to develop AF relationships using fewer input motions, a smaller set of RVT input motions are developed using 19 scenario input response spectra generated based on the controlling earthquakes defined from the mean rock hazard curves at different hazard levels, as presented in Chapter 3. These response spectra from the controlling earthquakes are used as input into RVT equivalent-linear site response analyses. The results are called RVT-CE for RVT- Controlling Earthquakes. Figure 4.5 presents the AF curves obtained for each input rock motion, with the results color-coded based on the input PGA. The same general trends from the previous RVT analyses are observed (i.e. site period elongation and reduction in amplification at low periods with increasing input intensity) although significantly fewer motions are used.

The AF values from Figure 4.5 are plotted versus Sa_{ROCK} in Figure 4.6 for PGA and three other spectral periods: 0.2 s, 0.4 s and 1.0 s. Even though the RVT-CE analyses are performed with significantly fewer input response spectra compared to the full RVT analysis (19 vs. 146 input motions), Figure 4.6 shows

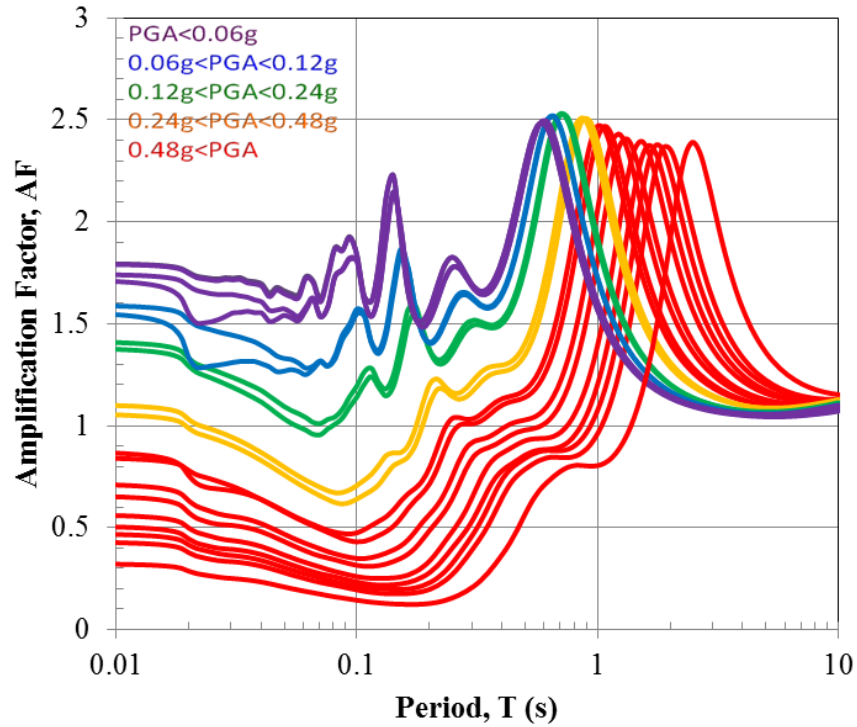


Figure 4.5 AF vs. T from RVT-CE analysis

that data points are distributed wide enough to capture the nonlinear behavior observed in the previous RVT analyses with 146 input motions. Specifically, the RVT-CE data show the reduction in AF at large intensities, as well as the increase in AF with increasing intensity at a period of 1.0 s, followed by a decrease in AF with further increases in intensity. Figure 4.6 also presents the AF relationships developed by fitting a higher order polynomial to $\ln(AF)$ and $\ln(Sa_{ROCK})$ using the functional form given in equation 4.1. Table 4.3 presents

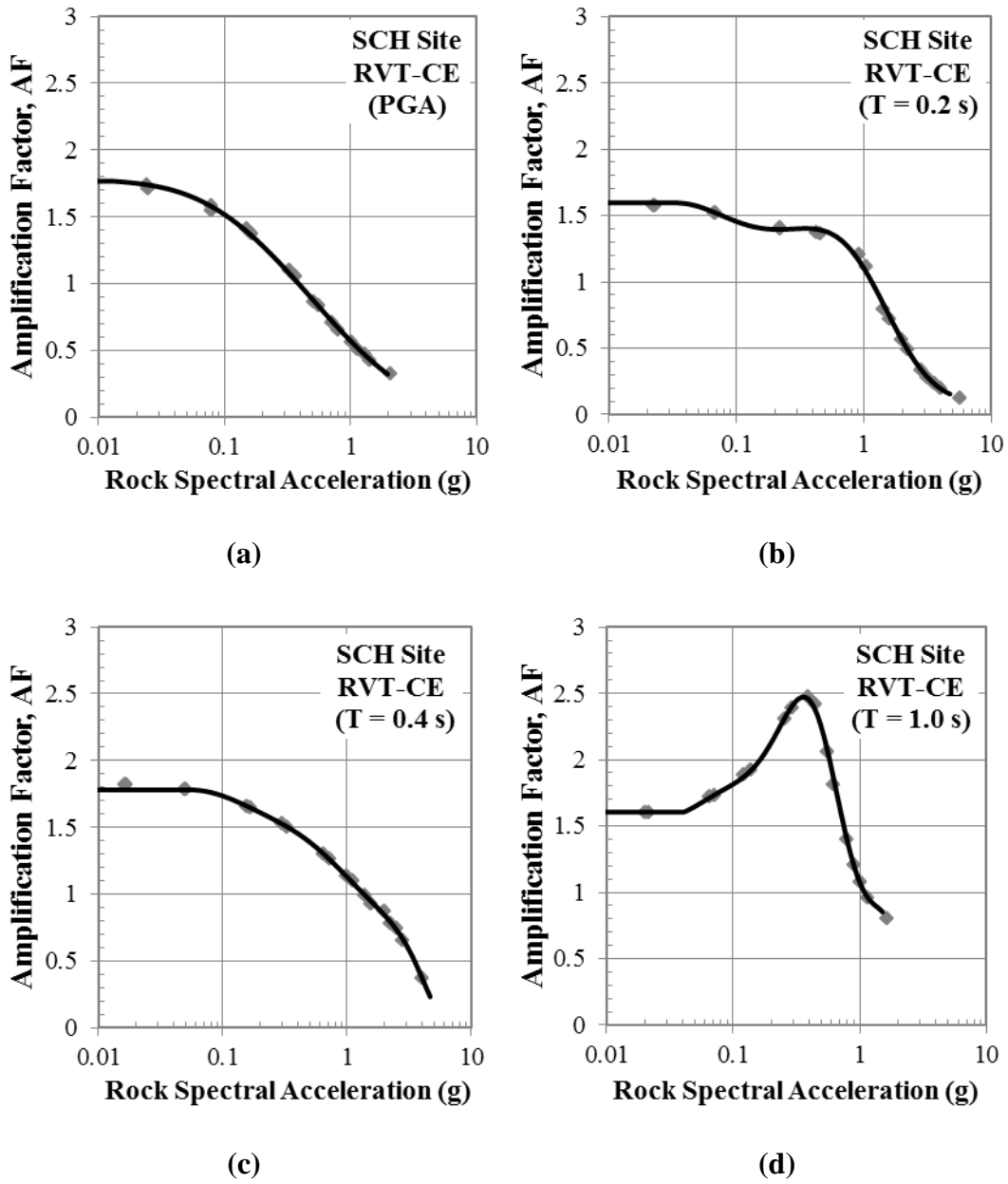


Figure 4.6 AF vs. Sa_{ROCK} data from RVT-CE analysis together with derived AF relationships for different periods (a) PGA, (b) 0.2 s, (c) 0.4 s, and (d) 1.0 s

the regression coefficients for the polynomials fit to the RVT-CE data, together with the associated $\sigma_{\ln AF}$.

Table 4.3 Regression coefficients and associated $\sigma_{\ln AF}$ for AF relationships developed for RVT-CE analysis data

	PGA	T = 0.2 s	T = 0.4 s	T = 1.0 s
a₀	-0.5611	0.0965	0.1197	0.0735
a₁	-0.7311	-0.6151	-0.3668	-0.9452
a₂	-0.1610	-0.4999	-0.0732	1.0533
a₃	-0.0121	-0.0935	0.0357	0.9550
a₄		0.0535	-0.0165	-1.7015
a₅		0.0230	-0.0490	-2.6006
a₆		0.0024	-0.0257	-1.5017
a₇			-0.0054	-0.4645
a₈			-0.0004	-0.0813
a₉				-0.0076
a₁₀				-0.0003
$\sigma_{\ln AF}$	0.017	0.020	0.011	0.008

4.3 Amplification Relationships for Varied Shear Wave Velocity Profiles

In nature soil properties vary laterally across a site. The shear wave velocity profiles measured across a site quantify the shear wave velocity variability across the site. The effects of this spatial variability, as well as the uncertainty in the shear wave velocity distribution that exists across the site, commonly is taken into account by performing 1D analyses for multiple realizations of 1D shear wave velocity profiles. Multiple 1D profile realizations are generated by randomizing the site shear-wave velocity profiles using Monte Carlo simulation. In this study, multiple 1D realizations are generated through the randomization tool implemented in the program Strata (Kottke and Rathje, 2008).

This study uses the random field models of Toro (1995) to generate a shear wave velocity profile. These models assume that the shear-wave velocity is log-normally distributed at any given depth and correlated between adjacent layers. The statistical parameters required for generation of the velocity profiles are the standard deviation of the natural logarithm of the shear wave velocity ($\sigma_{\ln V_s}$) and the interlayer correlation (ρ_{IL}). For this study, ρ_{IL} is specified as 0.8 and the effect of different levels of variability is explored by taking $\sigma_{\ln V_s}$ as 0.1, 0.2, and 0.3 (representing coefficients of variation of about 10%, 20%, and 30%, respectively).

Minimum and maximum limits of the shear wave velocity assigned to any layer are specified at $\pm 2\sigma_{lnV_s}$. Both TS and RVT site response analyses are performed with varied shear wave velocity profiles to develop site amplification functions that include the effects of site variability.

4.3.1 RESULTS FROM TIME SERIES ANALYSES

Time series analyses are performed for a suite of varied shear-wave velocity profiles generated through Monte Carlo simulation with different levels of variability. The V_s profile realizations generated for the TS analyses with three different σ_{lnV_s} levels are shown in Figure 4.7, together with the baseline V_s profile and the corresponding median V_s profile from the generated twenty realizations. Figure 4.7 shows the increasing variability in the generated profiles with increasing σ_{lnV_s} , the effect being more significant for profiles generated with $\sigma_{lnV_s} = 0.3$. The median V_s profiles of the varied profiles agree well with the specified baseline V_s profile.

All the input motions selected for TS analyses are propagated through the twenty generated V_s profiles for each σ_{lnV_s} and the surface response spectra and associated AF are computed. The AF values are plotted versus Sa_{ROCK} for the four periods under consideration in Figures 4.8, 4.9 and 4.10 for analyses

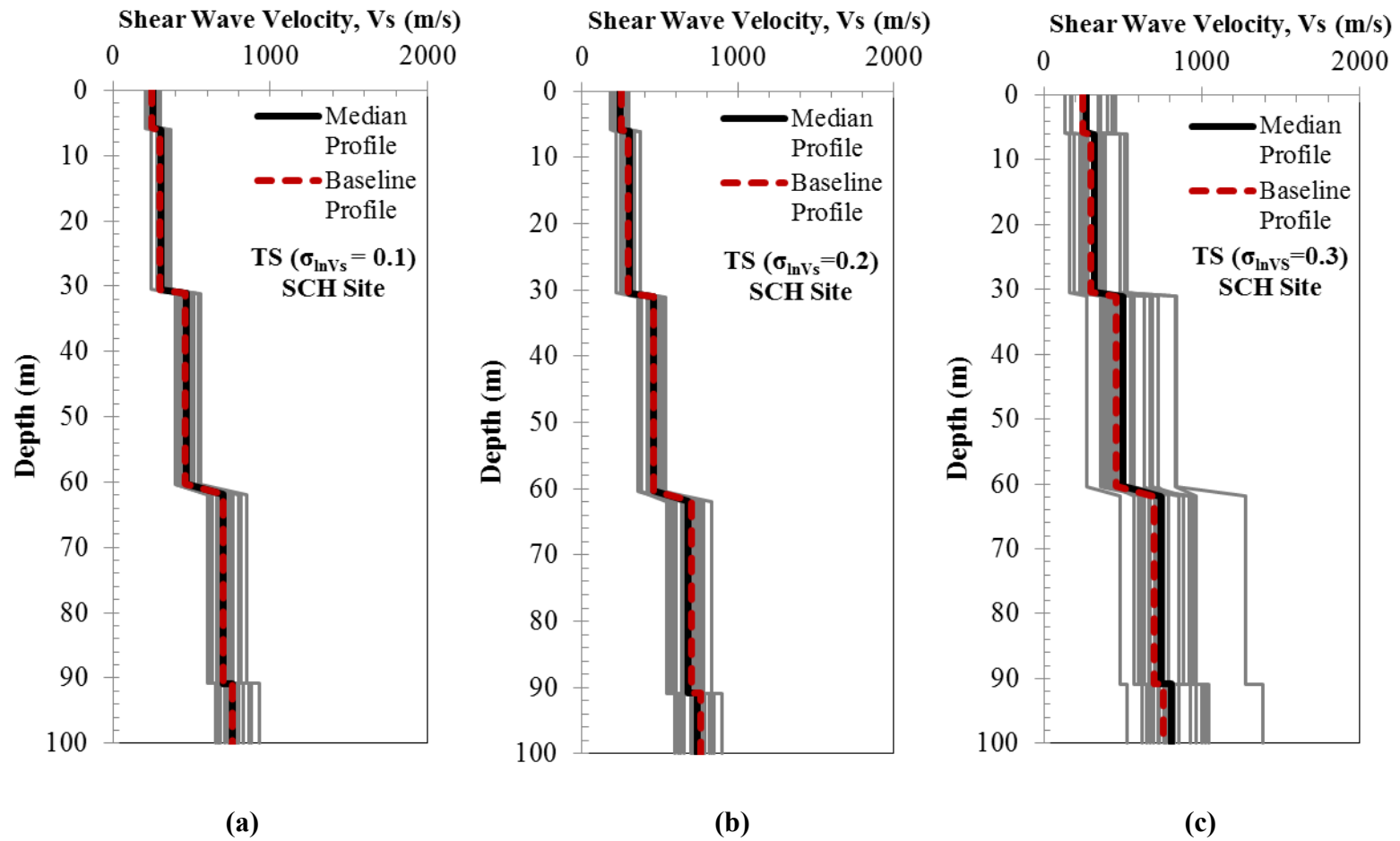
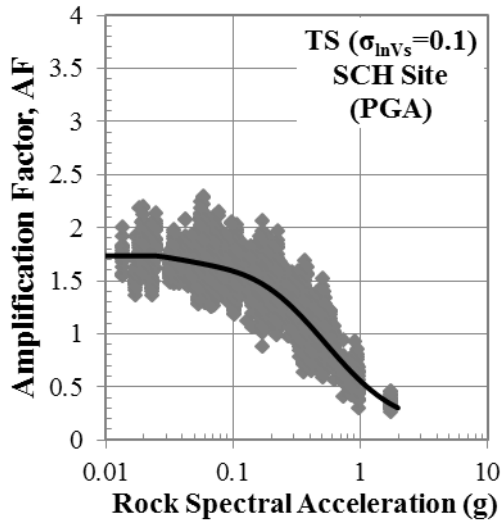


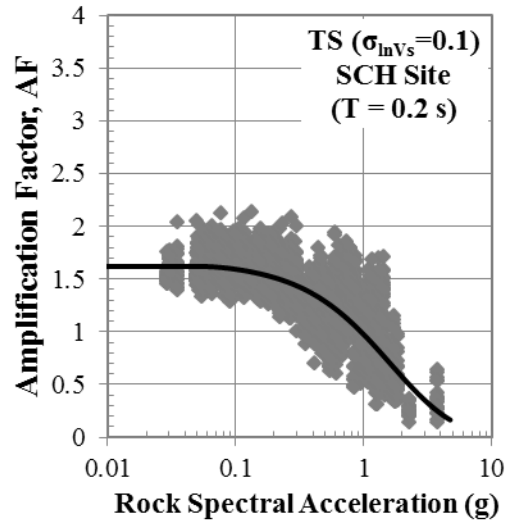
Figure 4.7 20 V_s profiles generated for TS analysis together with the median V_s profile and baseline V_s profile for the SCH site with (a) $\sigma_{\ln V_s} = 0.1$, (b) $\sigma_{\ln V_s} = 0.2$, and (c) $\sigma_{\ln V_s} = 0.3$

performed for $\sigma_{\ln V_S}$ of 0.1, 0.2, and 0.3, respectively. The data presented in Figures 4.8, 4.9, and 4.10 look generally similar to those in Figure 4.2 for non-varied V_S , but the data in Figures 4.8, 4.9, and 4.10 exhibit more scatter than the data in Figure 4.2, indicating that the variability in AF is influenced by the variability in the V_S profiles. The scatter in the AF data increases with increasing $\sigma_{\ln V_S}$, with the largest variability observed for $\sigma_{\ln V_S} = 0.3$.

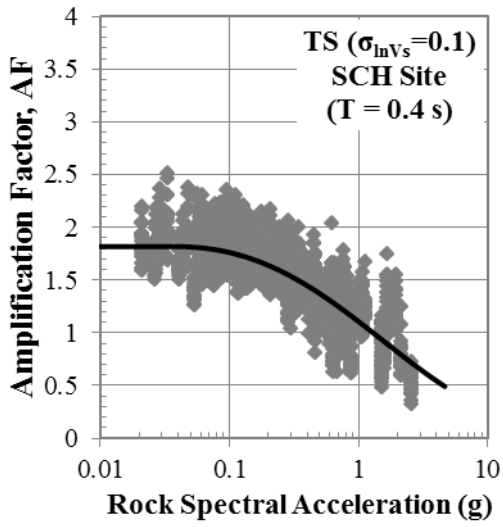
AF relationships are developed for the data in Figures 4.8, 4.9, and 4.10 by fitting a higher order polynomial to $\ln(AF)$ and $\ln(Sa_{ROCK})$. The derived AF relationships are shown with the data in these figures. Tables 4.4, 4.5, and 4.6 present the regression coefficients for the fitted polynomials for the TS data together with the associated $\sigma_{\ln AF}$ for $\sigma_{\ln V_S}$ of 0.1, 0.2, and 0.3, respectively. The $\sigma_{\ln AF}$ values range from 0.14 to 0.21, 0.22 to 0.30, and 0.24 to 0.33 for TS analyses performed for $\sigma_{\ln V_S}$ of 0.1, 0.2, and 0.3, respectively. The $\sigma_{\ln AF}$ values increase by 17%, 67%, and 83% with increasing $\sigma_{\ln V_S}$ compared to the values obtained for $\sigma_{\ln V_S} = 0.0$ (i.e. non-varied, Table 4.1). These standard deviations include both motion-to-motion and site-to-site variability, and thus one would expect an increase in standard deviation as compared with the non-varied ($\sigma_{\ln V_S} = 0.0$) case.



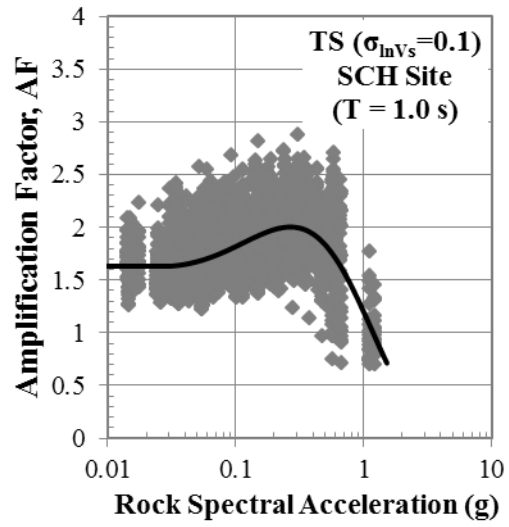
(a)



(b)

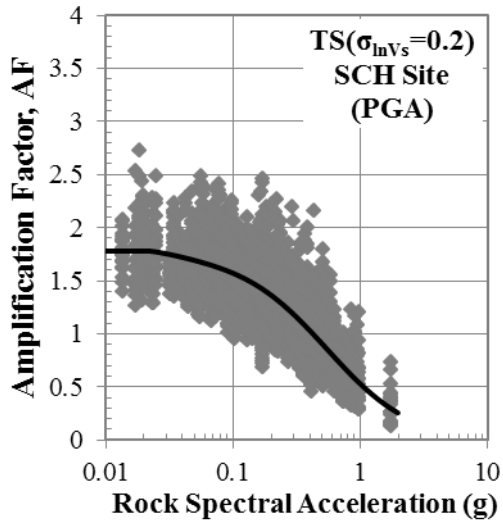


(c)

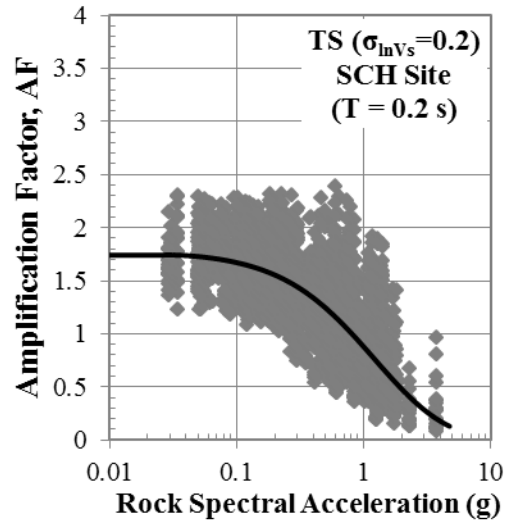


(d)

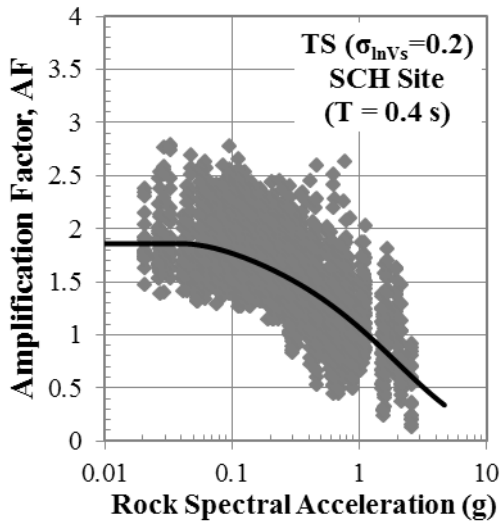
Figure 4.8 AF vs. Sa_{ROCK} data from TS ($\sigma_{\ln V_s} = 0.1$), together with derived AF relationships for different periods (a) PGA, (b) 0.2 s, (c) 0.4 s, and (d) 1.0 s



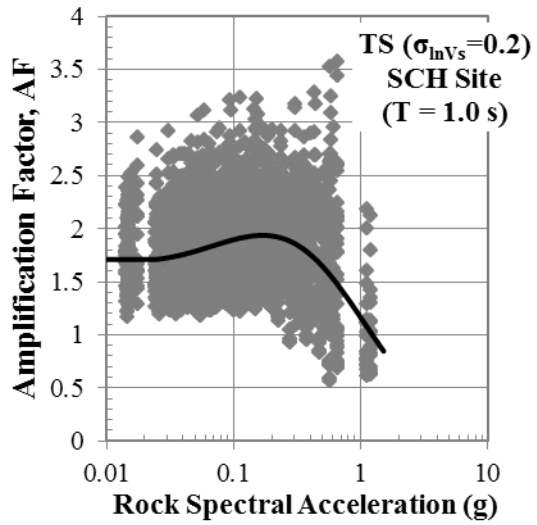
(a)



(b)



(c)



(d)

Figure 4.9 AF vs. Sa_{ROCK} data from TS ($\sigma_{\ln V_s} = 0.2$), together with derived AF relationships for different periods (a) PGA, (b) 0.2 s, (c) 0.4 s, and (d) 1.0 s

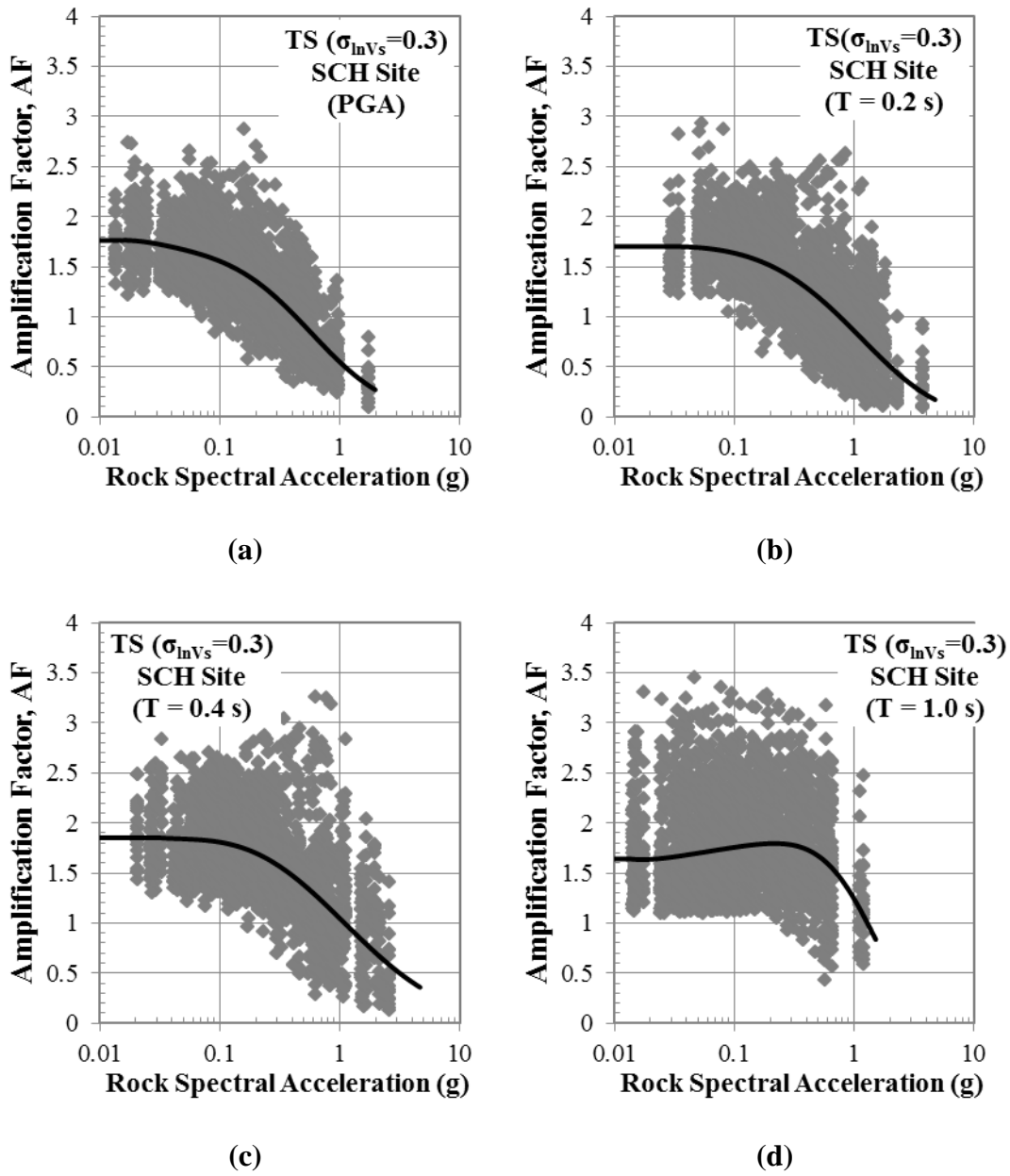


Figure 4.10 AF vs. Sa_{ROCK} data from TS ($\sigma_{\ln V_s} = 0.3$), together with derived AF relationships for different periods (a) PGA, (b) 0.2 s, (c) 0.4 s, and (d) 1.0 s

Table 4.4 Regression coefficients and associated $\sigma_{\ln AF}$ for AF relationships developed for TS analysis with $\sigma_{\ln V_s} = 0.1$

	PGA	T = 0.2 s	T = 0.4 s	T = 1.0 s
a₀	-0.5846	-0.0269	0.1015	0.1788
a₁	-0.8790	-0.5549	-0.3684	-0.9709
a₂	-0.1123	-0.2607	-0.0898	-0.6009
a₃	0.0948	-0.0648	-0.0085	-0.1362
a₄	0.0361	-0.0069	-0.0004	-0.0104
a₅	0.0037	-	-	-
$\sigma_{\ln AF}$	0.14	0.21	0.15	0.15

Table 4.5 Regression coefficients and associated $\sigma_{\ln AF}$ for AF relationships developed for TS analysis with $\sigma_{\ln V_s} = 0.2$

	PGA	T = 0.2 s	T = 0.4 s	T = 1.0 s
a₀	-0.6385	-0.1301	0.0648	0.1509
a₁	-0.9349	-0.6652	-0.4232	-0.6662
a₂	-0.2168	-0.2683	-0.1466	-0.2438
a₃	0.0194	-0.0543	-0.0349	0.0008
a₄	0.0156	-0.0045	-0.0042	0.0139
a₅	0.0018	-	-	0.0023
a₆	-	-	-	0.0001
$\sigma_{\ln AF}$	0.22	0.30	0.23	0.23

Table 4.6 Regression coefficients and associated $\sigma_{\ln AF}$ for AF relationships developed for TS analysis with $\sigma_{\ln V_S} = 0.3$

	PGA	T = 0.2 s	T = 0.4 s	T = 10 s
a₀	-0.6032	-0.1522	0.0454	0.2165
a₁	-0.8993	-0.6103	-0.4890	-0.7090
a₂	-0.2180	-0.2117	-0.1294	-0.5114
a₃	0.0107	-0.0354	-0.0057	-0.1771
a₄	0.0126	-0.0025	0.0013	-0.0315
a₅	0.0015	-	-	-0.0023
$\sigma_{\ln AF}$	0.24	0.33	0.28	0.26

4.3.2 RESULTS FROM RVT ANALYSES

RVT analyses are performed for a separate set of twenty varied shear wave velocity profiles, generated through Monte Carlo simulations for $\sigma_{\ln V_S} = 0.2$. The twenty V_S profile realizations generated for the RVT analyses are shown in Figure 4.11, together with the baseline and the median V_S profile of the twenty realizations. Again, the median V_S profile from the Monte Carlo simulations agrees well with the baseline V_S profile. All 146 input motions developed for RVT analysis are propagated through the generated V_S profiles, and the response spectra at the surface and the associated AF values are computed. The AF values are plotted versus Sa_{ROCK} in Figure 4.12 for the four spectral periods under consideration. The data presented

in Figure 4.12 look similar to the RVT data presented in Figure 4.4, except for $T = 1.0$ s. At this period a large peak was observed in the RVT data with no V_S variability (Figure 4.4d) but this peak is less pronounced in the RVT data with $\sigma_{\ln V_S} = 0.2$.

AF relationships are developed for the data in Figure 4.12 by fitting a higher order polynomial to $\ln(AF)$ vs. $\ln(Sa_{ROCK})$. The derived AF relationships are shown in Figure 4.12. Table 4.7 presents the regression coefficients for the fitted polynomials for the RVT data with $\sigma_{\ln V_S} = 0.2$, together with the associated $\sigma_{\ln AF}$. The $\sigma_{\ln AF}$ values range from 0.17 to 0.24 and these values are about 5 to 10 times larger than the values obtained when the V_S profile was not varied (Table 4.2). This increase in $\sigma_{\ln AF}$ is significantly larger than what was observed when shear wave velocity variation was added to the TS analyses. However, the RVT analysis with $\sigma_{\ln V_S} = 0.0$ does not include any motion-to-motion variability and thus there is almost no variability in the computed AF relationships. Thus, a significant increase in standard deviation occurs when shear wave velocity variability is included in the RVT analysis.

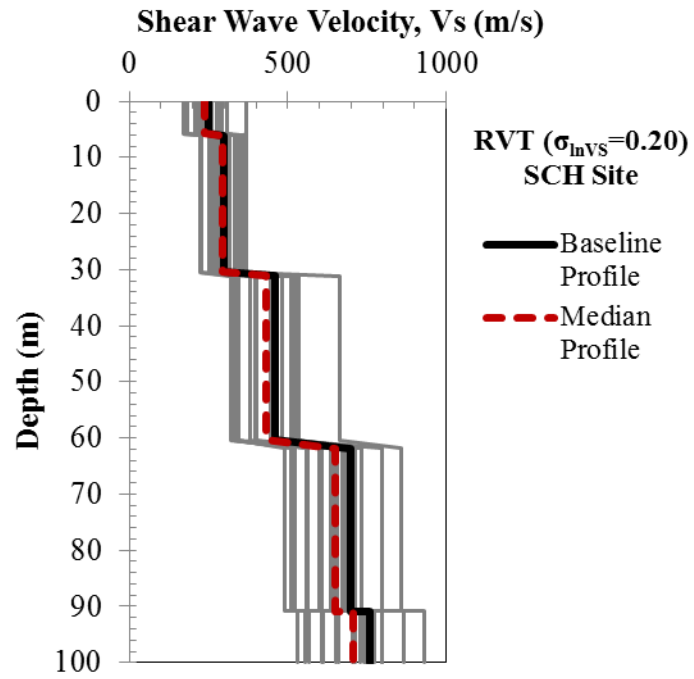
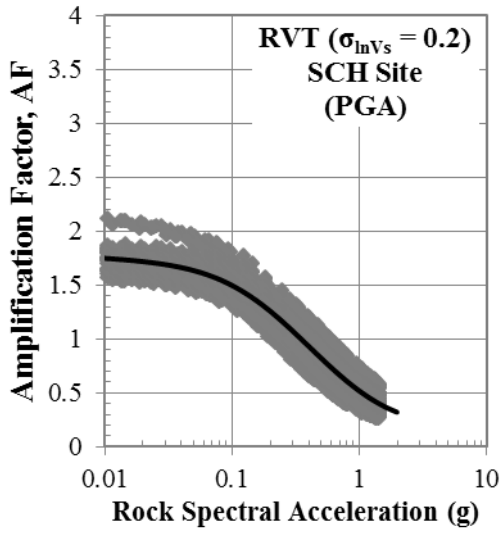
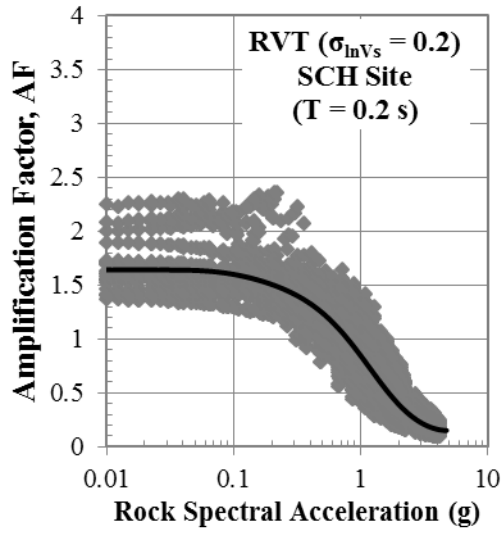


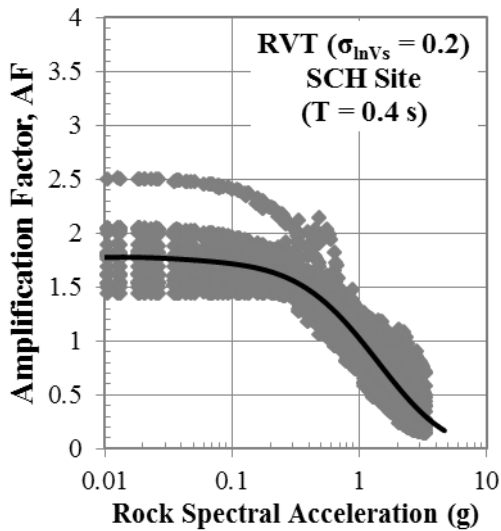
Figure 4.11 Twenty V_s profiles generated for RVT analysis with $\sigma_{\ln V_s}=0.2$ together with the median and baseline V_s profile for SCH site



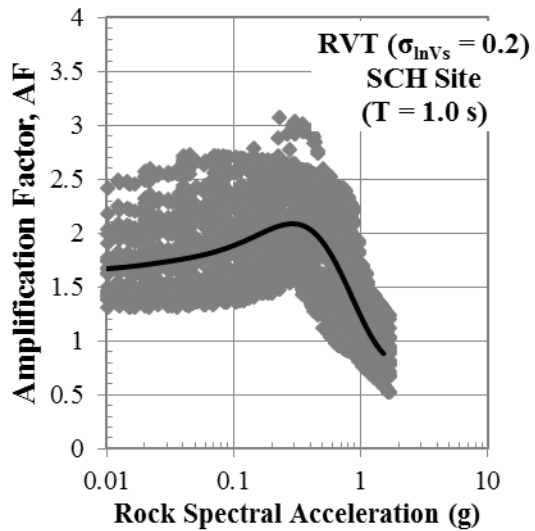
(a)



(b)



(c)



(d)

Figure 4.12 AF vs. Sa_{ROCK} data from RVT analysis with $\sigma_{lnVs}=0.2$, together with derived AF relationships for different periods (a) PGA, (b) 0.2 s, (c) 0.4 s and (d) 1.0 s

Table 4.7 Regression coefficients and associated $\sigma_{\ln AF}$ for AF relationships developed for RVT analysis with $\sigma_{\ln V_S} = 0.2$

	PGA	T = 0.2 s	T = 0.4 s	T = 1.0 s
a₀	-0.6576	-0.1684	0.0228	0.2084
a₁	-0.7221	-0.8107	-0.6085	-0.8743
a₂	-0.0371	-0.4311	-0.2773	-0.1264
a₃	0.0761	-0.0663	-0.0566	0.5335
a₄	0.0254	0.0566	-0.0023	0.4252
a₅	0.0033	0.0372	8.23E-04	0.1515
a₆	1.56E-04	0.0095	8.65E-05	0.0298
a₇		0.0011		0.0033
a₈		5.28E-05		0.0002
a₉				4.32E-06
a₁₀				
$\sigma_{\ln AF}$	0.148	0.266	0.233	0.208

Similar to the RVT analyses with $\sigma_{\ln V_S} = 0.2$, RVT-CE analyses are performed for varied shear wave velocities. The RVT-CE analyses are performed on separate sets of twenty varied shear wave velocity profiles, generated through Monte Carlo simulations with $\sigma_{\ln V_S} = 0.1, 0.2, \text{ and } 0.3$ to explore the effect of different levels of variability on the RVT-CE results.. The twenty V_S profile realizations generated with the different levels of $\sigma_{\ln V_S}$ for the RVT-CE analyses are shown in Figure 4.13, together with the baseline V_S profile and their associated median V_S profile of the twenty realizations. Again, the median V_S profiles from the Monte

Carlo simulations agree well with the baseline V_S profile. Similar to Figure 4.7, Figure 4.13 clearly shows increasing variability in the generated V_S profiles around the baseline V_S profile with increasing level of $\sigma_{\ln V_S}$.

All 19 input motions developed for RVT-CE analysis are propagated through the generated V_S profiles, and the response spectra at the surface and the associated AF values are computed. The AF values are plotted versus Sa_{ROCK} in Figures 4.14, 4.15, and 4.16 for analyses with $\sigma_{\ln V_S}$ of 0.1, 0.2, and 0.3, respectively. The data presented in these figures look similar to the RVT data presented in Figure 4.12 for $\sigma_{\ln V_S} = 0.2$.

AF relationships are developed for the data in Figure 4.14, 4.15, and 4.16 by fitting a higher order polynomial to $\ln(AF)$ vs. $\ln(Sa_{ROCK})$. The derived AF relationships are shown in these figures. Tables 4.8, 4.9 and 4.10 present the regression coefficients for the fitted polynomials for the data obtained from RVT-CE with varied V_S velocities, together with the associated $\sigma_{\ln AF}$. The $\sigma_{\ln AF}$ values range from 0.10 to 0.16, 0.22 to 0.33, and 0.30 to 0.53 for analyses performed with $\sigma_{\ln V_S}$ of 0.1, 0.2, and 0.3, respectively. The $\sigma_{\ln AF}$ values generally increase by more than a factor of 10 as compared to the values obtained when the V_S profile was not varied (Table 4.3).

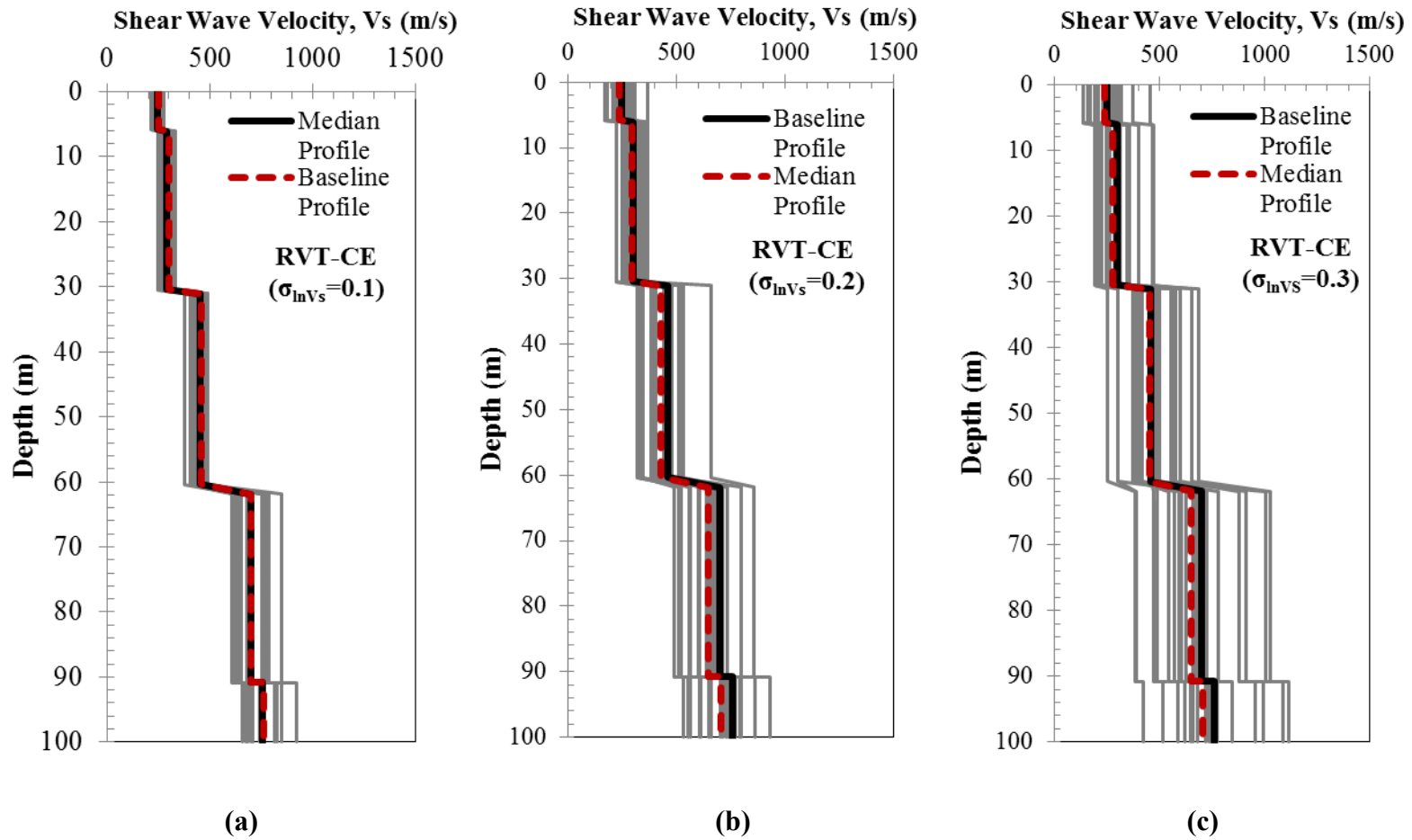


Figure 4.13 20 V_s profiles generated for RVT-CE analysis together with the median V_s profile and baseline V_s profile for SCH site with (a) $\sigma_{\ln V_s} = 0.1$, (b) $\sigma_{\ln V_s} = 0.2$, and (c) $\sigma_{\ln V_s} = 0.3$

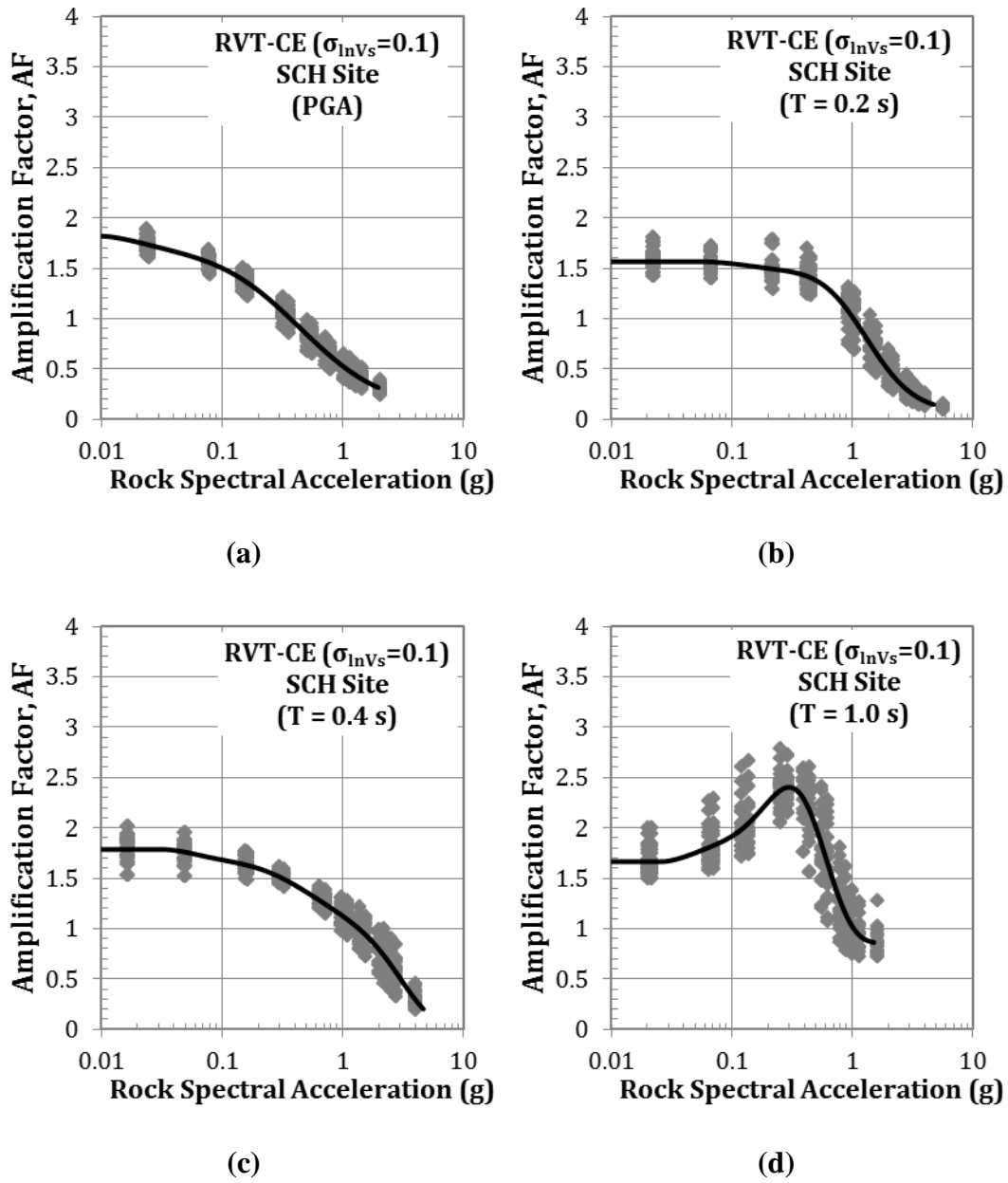
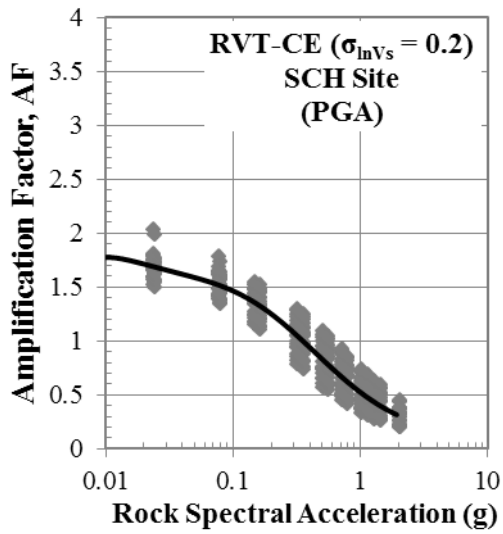
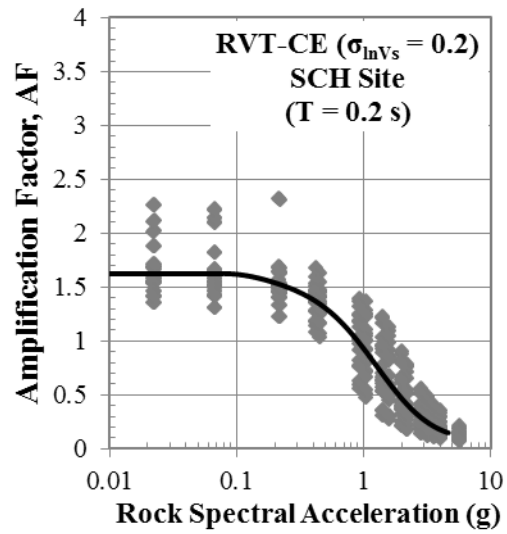


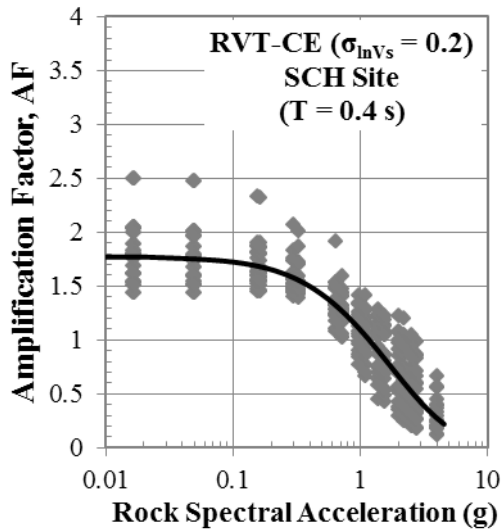
Figure 4.14 AF vs. Sa_{ROCK} data from RVT-CE analyses with $\sigma_{\ln V_s} = 0.1$, together with derived AF relationships for different periods (a) PGA, (b) 0.2 s, (c) 0.4 s and (d) 1.0 s



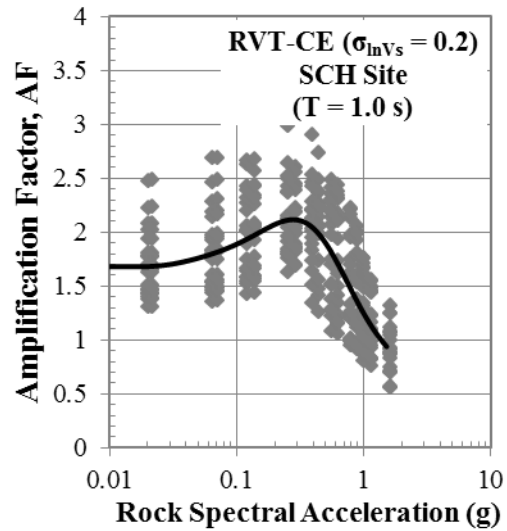
(a)



(b)



(c)



(d)

Figure 4.15 AF vs. Sa_{ROCK} data from RVT-CE analysis with $\sigma_{lnVs}=0.2$, together with derived AF relationships for different periods (a) PGA, (b) 0.2 s, (c) 0.4 s and (d) 1.0 s

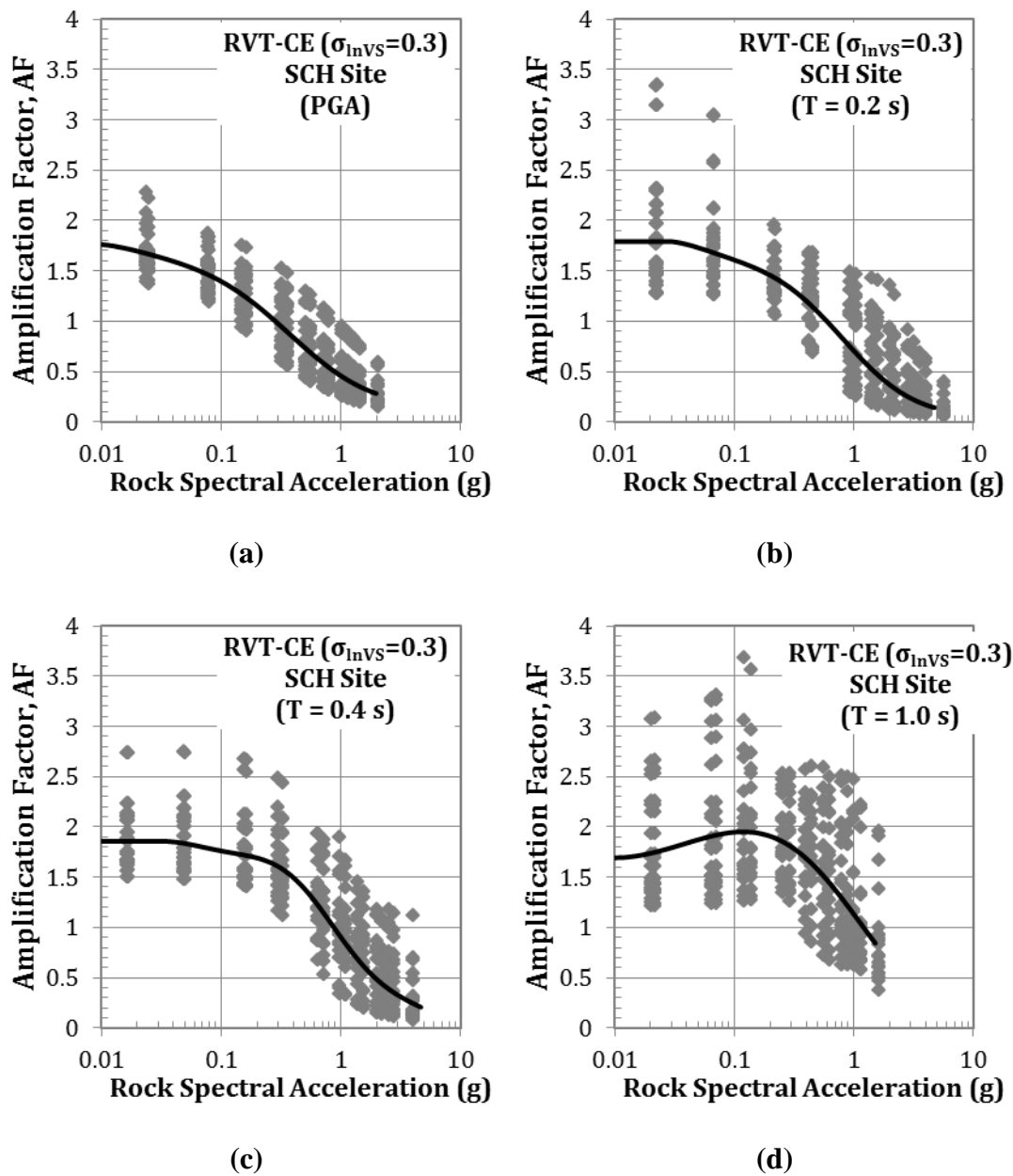


Figure 4.16 AF vs. Sa_{ROCK} data from RVT-CE analysis with $\sigma_{lnVS}=0.3$, together with derived AF relationships for different periods (a) PGA, (b) 0.2 s, (c) 0.4 s and (d) 1.0 s

Table 4.8 Regression coefficients and associated $\sigma_{\ln AF}$ of AF relationships developed for RVT-CE analysis with $\sigma_{\ln V_s} = 0.1$

	PGA	T = 0.2 s	T = 0.4 s	T = 1.0 s
a₀	-0.6362	0.0187	0.1176	0.0223
a₁	-0.7516	-0.7285	-0.3324	-0.8040
a₂	-0.0714	-0.4866	-0.1253	0.8869
a₃	0.0615	-0.0576	-0.1144	0.7501
a₄	0.0197	0.0762	-0.0817	-0.8479
a₅	0.0017	0.0260	-0.0173	-1.1971
a₆	-	-0.0027	0.0043	-0.5952
a₇	-	-0.0022	0.0022	-0.1538
a₈	-	-0.0002	0.0002	-0.0216
a₉	-	-	-	-0.0015
a₁₀	-	-	-	-3.94E-05
$\sigma_{\ln AF}$	0.10	0.16	0.13	0.13

Table 4.9 Regression coefficients and associated $\sigma_{\ln AF}$ of AF relationships developed for RVT-CE analysis with $\sigma_{\ln V_s} = 0.2$

	PGA	T = 0.2 s	T = 0.4 s	T = 1.0 s
a₀	-0.6459	-0.0739	0.0893	0.2207
a₁	-0.7419	-0.7209	-0.5215	-0.7208
a₂	-0.0803	-0.3874	-0.2429	0.0197
a₃	0.0462	-0.0619	-0.0608	0.2653
a₄	0.0115	0.0380	-0.0082	-0.1059
a₅	-1.37E-04	0.0189	-4.91E-04	-0.2282
a₆	-1.49E-04	0.0024		-0.1135
a₇				-0.0270
a₈				-0.0032
a₉				-1.52E-04
a₁₀				
$\sigma_{\ln AF}$	0.175	0.310	0.275	0.214

Table 4.10 Regression coefficients and associated $\sigma_{\ln AF}$ of AF relationships developed for RVT-CE analysis with $\sigma_{\ln V_s} = 0.3$

	PGA	T = 0.2 s	T = 0.4 s	T = 1.0 s
a₀	-0.7819	-0.3472	-0.1025	0.1243
a₁	-0.7372	-0.7908	-0.7967	-0.6167
a₂	-0.0265	-0.2352	-0.2267	-0.2212
a₃	0.0786	0.0108	0.0814	-0.0253
a₄	0.0238	0.0203	0.0368	-0.0005
a₅	0.0025	0.0029	-0.0114	-
a₆	0.0001	-	-0.0072	-
a₇	-	-	-0.0011	-
a₈	-	-	0.0000	-
a₉	-	-	-	-
a₁₀	-	-	-	-
$\sigma_{\ln AF}$	0.30	0.53	0.45	0.33

4.4 Comparison of Amplification Relationships

The results from each different type of site response analysis are compared at the four selected periods through the developed AF relationships and their standard deviations. Figure 4.17 presents the median AF relationships developed using TS analysis with different levels of σ_{lnV_S} between 0.0 (i.e. no variation) and 0.3. For PGA, the relationships derived from all analyses are very similar. At $T = 0.2$ s there are slight differences between the relationships, with larger σ_{lnV_S} predicting slightly larger AF at low intensities ($Sa_{ROCK} < 0.1$ g). At $T = 0.4$ s, most of the relationships are similar; however at high intensities ($Sa_{ROCK} > 1$ g) larger values of σ_{lnV_S} result in smaller AF . The most significant effect is seen at $T = 1.0$ s, where introducing V_S variability into the TS analysis reduces the observed peak at $Sa_{ROCK} \sim 0.3$ g. As the V_S variability increases, the peak diminishes further. The TS analysis with $\sigma_{lnV_S} = 0.3$ predicts AF values at $Sa_{ROCK} \sim 0.3$ g about 15% smaller compared to $\sigma_{lnV_S} = 0.0$ (i.e. non-varied).

The effect of V_S variability on the median AF relationships developed from RVT analysis is presented in Figure 4.18 using the RVT-CE input motions. For RVT analysis the effect of introducing V_S variability is more significant at all periods compared to TS analysis. This result is most noticeable for $T = 0.2$ s and 1.0 s. For $T = 0.2$ s, there is a 12% increase in AF at smaller input intensities and

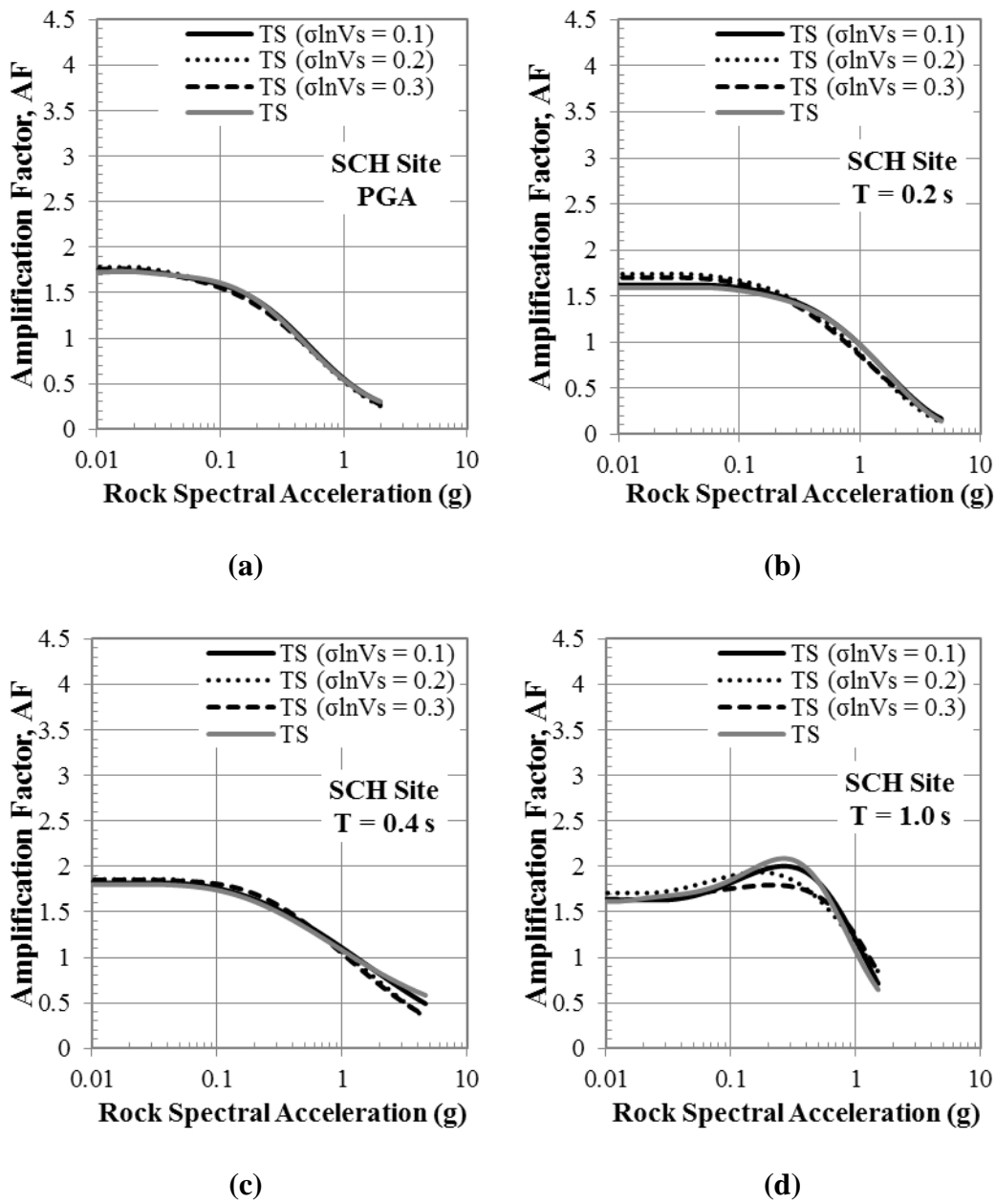
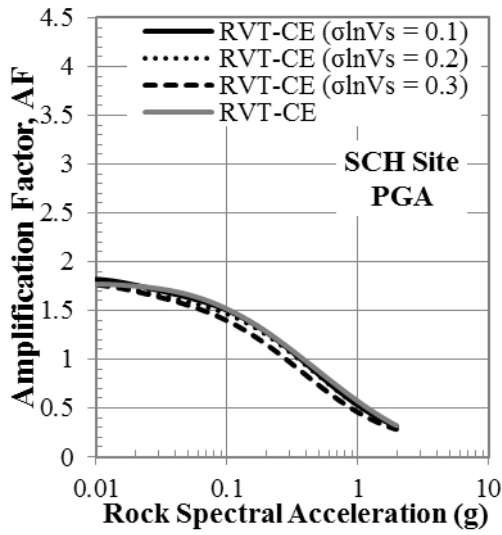
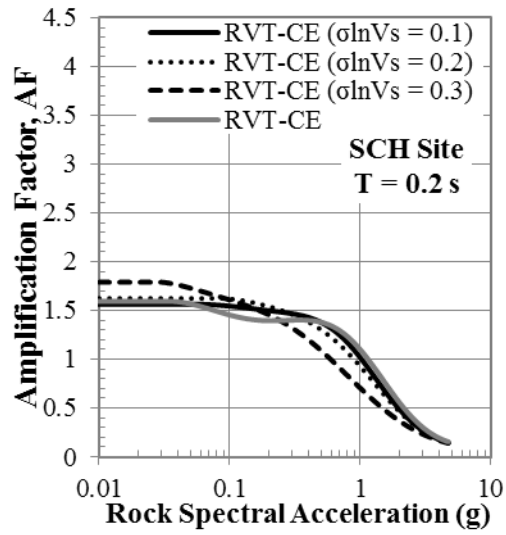


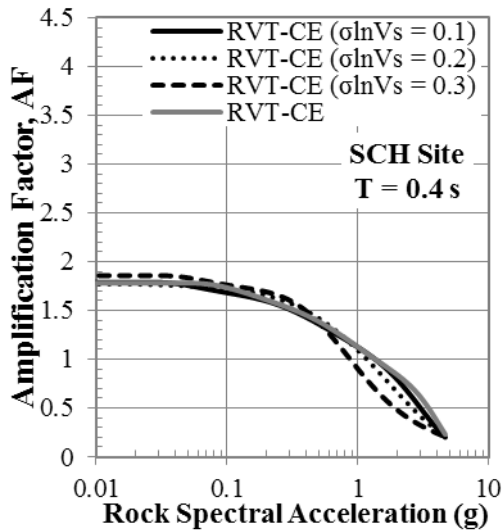
Figure 4.17 Comparison of *AF* functions of TS and TS analysis performed with σ_{lnVs} of 0.1, 0.2, and 0.3, respectively at different periods (a) PGA, (b) 0.2 s, (c) 0.4 s, and (d) 1.0 s



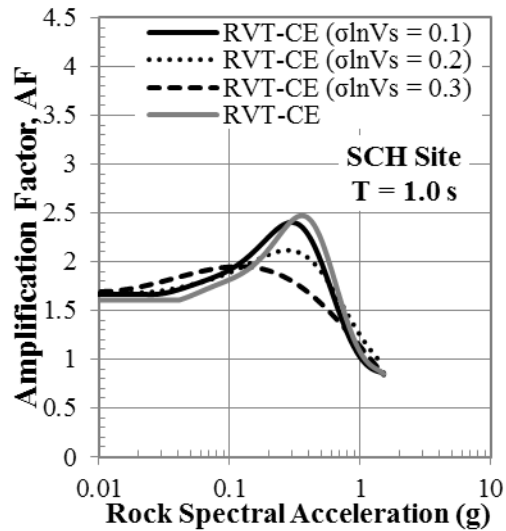
(a)



(b)



(c)



(d)

Figure 4.18 Comparison of AF functions of RVT-CE and RVT-CE analysis performed with σ_{lnVs} of 0.1, 0.2, and 0.3, respectively at different periods (a) PGA, (b) 0.2 s, (c) 0.4 s, and (d) 1.0 s

a reduction in AF at moderate intensities for $\sigma_{lnV_S} = 0.3$. For $T = 1.0$ s, σ_{lnV_S} greater than 0.1 results in a large reduction in the AF peak around $Sa_{ROCK} \sim 0.3$ g. This reduction is as large as 30%. The increased sensitivity to variations in V_S for RVT analysis is caused by the fact that motion-to-motion variability is not incorporated in RVT and thus changes in V_S more strongly affect the computed AF .

The AF relationships developed using the 146 RVT input motions (RVT) and 19 RVT controlling earthquake input motions (RVT-CE) are compared in Figure 4.19 for $\sigma_{lnV_S} = 0.0$ and $\sigma_{lnV_S} = 0.20$. For all four periods, the median AF relationships for RVT and RVT-CE are similar for the cases with and without variation in V_S . Figure 4.19 shows that RVT-CE analysis with fewer input motions predicts AF relationships that are very similar to those from RVT analysis with 146 input motions. Therefore, the results of RVT-CE analysis are used for the rest of this study.

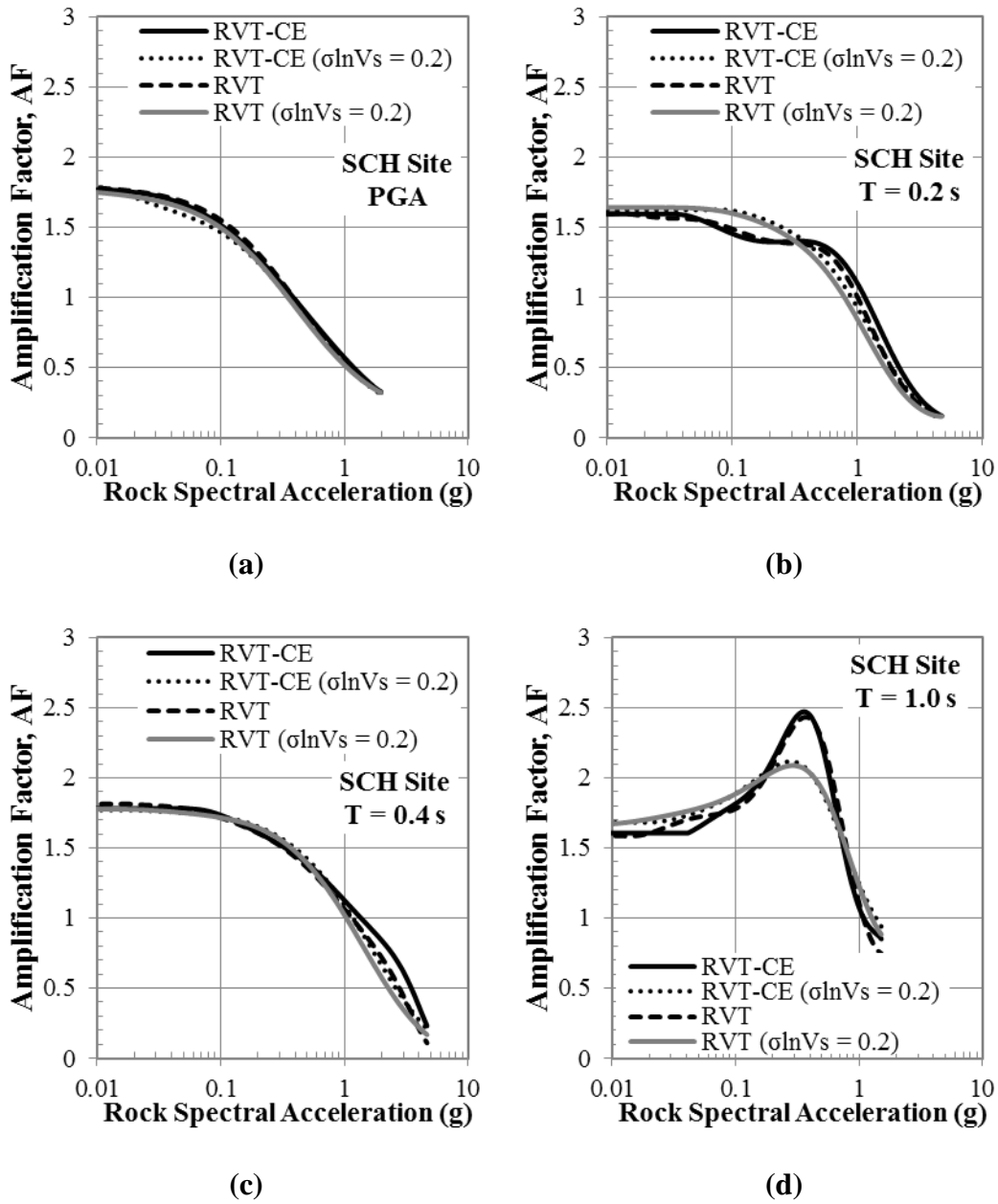


Figure 4.19 Comparison of AF relationships from RVT and RVT-CE analyses performed with and without varied V_s profiles ($\sigma_{\ln V_s} = 0.2$) at different periods (a) PGA, (b) 0.2 s, (c) 0.4 s, and (d) 1.0 s

The median AF relationships from TS and RVT-CE analyses with $\sigma_{\ln V_S} = 0.0$ and $\sigma_{\ln V_S} = 0.2$ are compared in Figure 4.20. Similar to the previous comparisons, the different analyses provide generally similar results for PGA and $T = 0.4$ s. The TS results are slightly larger than the others at large intensities for $T = 0.4$ s, but this appears to be influenced by just a few motions at high intensity. The difference in the AF relationships due to V_S variation is more pronounced at 0.2 s and 1.0 s. At $T = 0.2$ s, TS with $\sigma_{\ln V_S} = 0.2$ predicts slightly larger AF at smaller input intensities than the other analyses. At $T = 1.0$ s, both TS with $\sigma_{\ln V_S} = 0.20$ and RVT-CE with $\sigma_{\ln V_S} = 0.2$ predict smaller peaks than their non-varied counterparts (i.e., $\sigma_{\ln V_S} = 0.0$). However, the TS with $\sigma_{\ln V_S} = 0.2$ results remain below those from RVT-CE with $\sigma_{\ln V_S} = 0.2$. The reduction in the AF peak at $T = 1.0$ s for RVT-CE with $\sigma_{\ln V_S} = 0.2$ is about 15% relative to RVT-CE with $\sigma_{\ln V_S} = 0.0$, while the reduction is about 10% for TS with $\sigma_{\ln V_S} = 0.2$ relative to TS with $\sigma_{\ln V_S} = 0.0$. The peak shifts to smaller intensities when V_S is varied, but the shift is larger for the TS analyses than for the RVT-CE analyses.

Both the median amplification relationship and its standard deviation influence the computed surface hazard curve. Two different descriptions of the standard deviation of the natural logarithm of AF are examined in this study. Initially a single value of $\sigma_{\ln AF}$ is defined across all values of Sa_{ROCK} . These values were previously presented, and Table 4.11 summarizes the values of $\sigma_{\ln AF}$

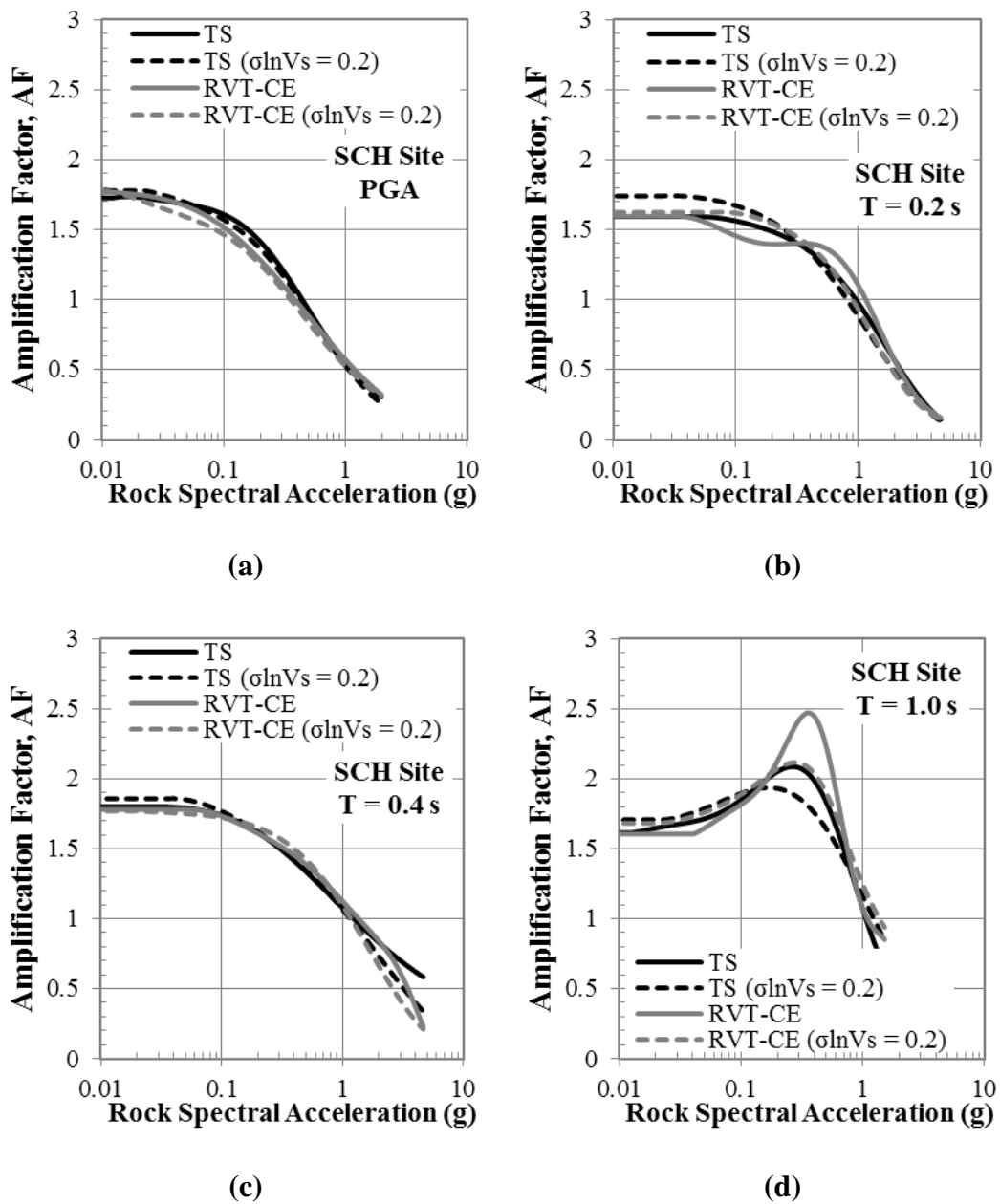


Figure 4.20 Comparison of *AF* functions predictions of TS and RVT-CE analyses performed with and without spatially varied V_s profiles ($\sigma_{lnV_s} = 0.2$) at different periods (a) PGA, (b) 0.2 s, (c) 0.4 s, and (d) 1.0 s

associated with the different AF relationships. As discussed in the previous section, introducing shear wave velocity variability increases the $\sigma_{\ln AF}$ associated with the amplification relationships developed from both TS and RVT analyses. The $\sigma_{\ln AF}$ for RVT analyses without V_S variability (i.e., $\sigma_{\ln V_S} = 0$) does not include V_S or motion-to-motion variability, and therefore the $\sigma_{\ln AF}$ values for RVT and RVT-CE are very close to zero. These small values of $\sigma_{\ln AF}$ associated with RVT and RVT-CE analysis without V_S variability makes these amplification relationships inappropriate for the convolution method because they essentially represent deterministic conditions. When V_S variability is included in the RVT and RVT-CE analyses, the resulting $\sigma_{\ln AF}$ are comparable with those obtained from TS analysis with variability even though RVT analyses only includes the effects of V_S variability (no motion-to-motion variability).

The $\sigma_{\ln AF}$ associated with RVT and RVT-CE analyses (i.e., analyses performed with a large and small set of RVT input motions) are somewhat different from each other. For $\sigma_{\ln V_S} = 0.0$, the RVT amplification relationships have a larger $\sigma_{\ln AF}$ than the RVT-CE relationships because the large suite of RVT input motions generates some variation in the computed AF values. For $\sigma_{\ln V_S} = 0.2$, $\sigma_{\ln AF}$ is generally larger for RVT-CE analysis because the fewer input motions coupled with a large variability in AF results in a larger standard deviation as compared with the large number of input motions associated with RVT.

Table 4.11 Comparison of $\sigma_{\ln AF}$ for different AF relationships

$\sigma_{\ln V_s}$	$\sigma_{\ln AF}$			
	0.0	0.1	0.2	0.3
TS				
PGA	0.12	0.14	0.22	0.24
0.2 s	0.18	0.21	0.30	0.33
0.4 s	0.13	0.15	0.23	0.28
1.0 s	0.12	0.15	0.23	0.26
RVT-CE				
PGA	0.02	0.10	0.17	0.30
0.2 s	0.02	0.16	0.31	0.53
0.4 s	0.01	0.13	0.28	0.45
1.0 s	0.01	0.13	0.21	0.33
RVT				
PGA	0.02	--	0.15	--
0.2 s	0.06	--	0.27	--
0.4 s	0.02	--	0.23	--
1.0 s	0.03	--	0.21	--

The AF data presented previously indicate that the variability in the amplification factors varies with Sa_{ROCK} . Generally, the scatter increases with increasing Sa_{ROCK} because the different motions and different velocity profiles induce different levels of nonlinearity and these differences influence the computed AF . To investigate the relationship between $\sigma_{\ln AF}$ and Sa_{ROCK} the AF data obtained from TS and RVT-CE analyses for $\sigma_{\ln V_s} = 0.0$ and $\sigma_{\ln V_s} = 0.2$ are divided into bins of Sa_{ROCK} and the $\sigma_{\ln AF}$ is calculated within each bin (Table 4.12). Table 4.12

clearly shows that the variability in the AF data is significantly larger at large input intensities for all periods. Figure 4.21 plots σ_{lnAF} versus Sa_{ROCK} together with the constant σ_{lnAF} values for the four selected periods. At large levels of Sa_{ROCK} , the variability in AF is generally larger than the values represented by a constant σ_{lnAF} . The only exception is RVT analysis, which does not display a significant level of variability at any Sa_{ROCK} . TS analysis with $\sigma_{lnVs} = 0.2$ generally has the largest σ_{lnAF} , followed by RVT analysis with $\sigma_{lnVs} = 0.2$ analysis. The value of the σ_{lnAF} increases up to 4 times with increasing input intensity.

Table 4.12 Variable σ_{lnAF} with Sa_{ROCK} for AF relationships developed for TS and RVT analyses

	PGA		T = 0.2 s		T = 0.4 s		T = 1.0 s	
	Sa_{ROCK}	σ_{lnAF}	Sa_{ROCK}	σ_{lnAF}	Sa_{ROCK}	σ_{lnAF}	Sa_{ROCK}	σ_{lnAF}
TS	<0.1	0.094	<0.1	0.066	<0.1	0.069	<0.1	0.106
	0.1-0.3	0.114	0.1-1.0	0.133	0.1-1.0	0.122	0.1-0.3	0.100
	>0.3	0.186	>1.0	0.376	>1.0	0.232	>0.3	0.162
TS ($\sigma_{lnVs} = 0.2$)	<0.1	0.147	<0.1	0.141	<0.1	0.154	<0.1	0.193
	0.1-0.3	0.207	0.1-1.0	0.247	0.1-1.0	0.222	0.1-0.3	0.208
	>0.3	0.333	>1.0	0.540	>1.0	0.413	>0.3	0.334
RVT	<0.1	0.012	<0.1	0.001	<0.1	0.000	<0.1	0.004
	0.1-0.3	0.003	0.1-1.0	0.026	0.1-1.0	0.003	0.1-0.3	0.006
	>0.3	0.020	>1.0	0.025	>1.0	0.018	>0.3	0.010
RVT ($\sigma_{lnVs} = 0.2$)	<0.1	0.067	<0.1	0.135	<0.1	0.128	<0.1	0.175
	0.1-0.3	0.097	0.1-1.0	0.161	0.1-1.0	0.119	0.1-0.3	0.174
	>0.3	0.221	>1.0	0.403	>1.0	0.400	>0.3	0.253

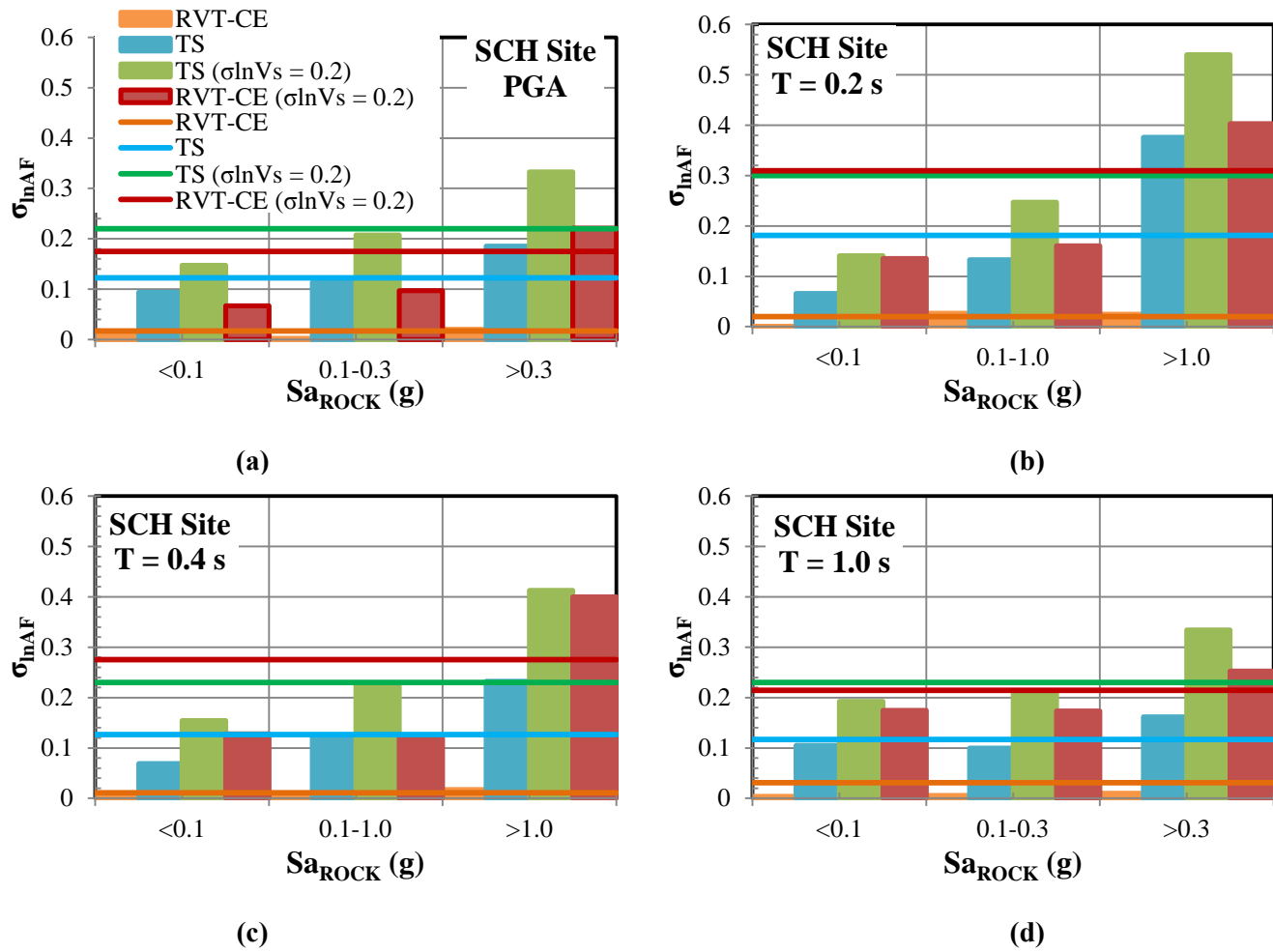


Figure 4.21 Variable and constant σ_{InAF} with Sa_{ROCK} for AF relationships developed for TS and RVT-CE analyses

4.5 Soil Hazard Curves

Soil hazard curves for the SCH site are computed using the convolution approach (e.g., Bazzurro and Cornell 2004) and the amplification function relationships developed presented previously. The convolution approach requires the site-specific rock hazard curve as well as the amplification relationship and its variability, as described in Chapter 2.5.

Figure 4.22 presents the site-specific soil hazard curves obtained using the AF relationships derived from the TS analyses performed with $\sigma_{\ln V_S}$ between 0.0 and 0.3. The computed surface hazard curves show that larger values of V_S variability are associated with larger ground motions, predominantly at smaller hazard levels (i.e. less than about 0.001 1/yr). The similarity at larger hazard levels is driven by the AF functions being very similar (Figures 4.17), while the differences at smaller hazard levels are driven by differences in $\sigma_{\ln AF}$. Larger values of $\sigma_{\ln AF}$ would causes differences to initiate at larger hazard levels. The effect of $\sigma_{\ln V_S}$ is small for PGA and $T = 0.4$ s, but more significant for $T = 0.2$ s and 1.0 s.

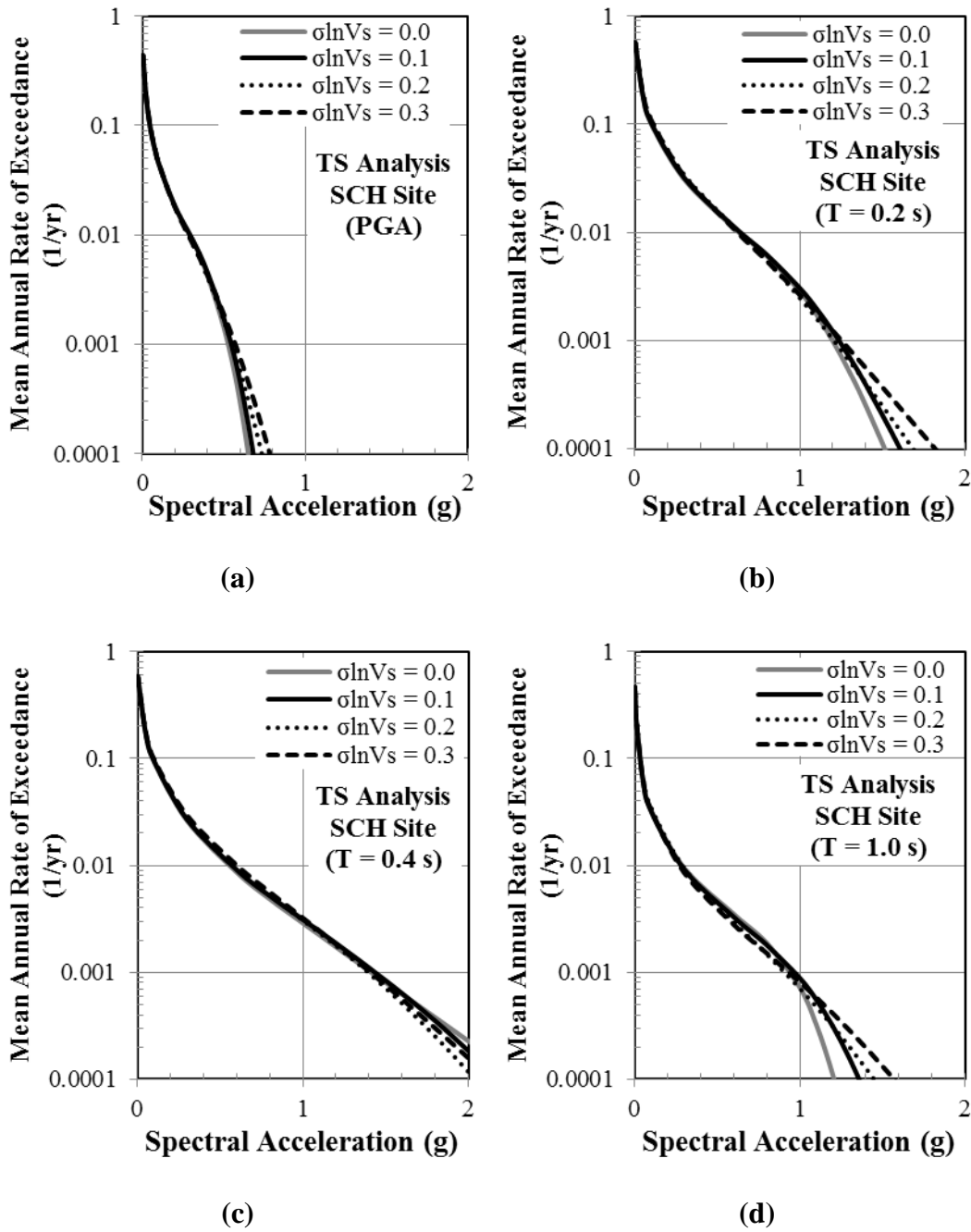


Figure 4.22 Comparison of site-specific soil hazard predictions of TS analysis performed with $\sigma_{\ln V_s}$ of 0.0, 0.1, 0.2, and 0.3, respectively at different periods (a) PGA, (b) 0.2 s, (c) 0.4 s, and (d) 1.0 s

Figure 4.23 presents the site-specific soil hazard curves are obtained using the AF relationships derived from the RVT-CE analyses performed with σ_{lnV_S} between 0.0 and 0.3. Similar to the results for TS analysis in Figure 4.22, Figure 4.23 shows that increasing the V_S variability increases the ground motions at smaller hazard levels. However, the effect of increasing V_S variability is more significant for RVT-CE analysis as compared to the effect for TS analysis. The RVT-CE ground motion hazard curves vary more significantly with σ_{lnV_S} because the σ_{lnAF} associated with the AF relationships developed from RVT-CE analyses vary more significantly with σ_{lnV_S} due to the absence of motion-to-motion variability in the AF data.

It is important to note also the combined effect of the median amplification function and σ_{lnAF} on the results in Figure 4.23. This effect is most noticeable for the $T = 1.0$ s. The differences in the ground motion levels observed at intermediate hazard levels (i.e., between 0.01 1/yr. and 0.002 1/yr.) are influenced most by the median AF function, where the $\sigma_{lnV_S} = 0.0$ AF function (Figure 4.18d) has a larger peak. This peak diminishes with increasing V_S variability, thus the predicted ground motions at these intermediate hazard levels decrease with increasing σ_{lnV_S} . However, at smaller hazard levels (less than 0.001 1/yr.), the predicted ground motions generally increase with increasing σ_{lnV_S} because at these hazard levels the motions are influenced more by σ_{lnAF} . It is interesting that the hazard curves for $\sigma_{lnV_S} = 0.2$ and $\sigma_{lnV_S} = 0.3$ are very

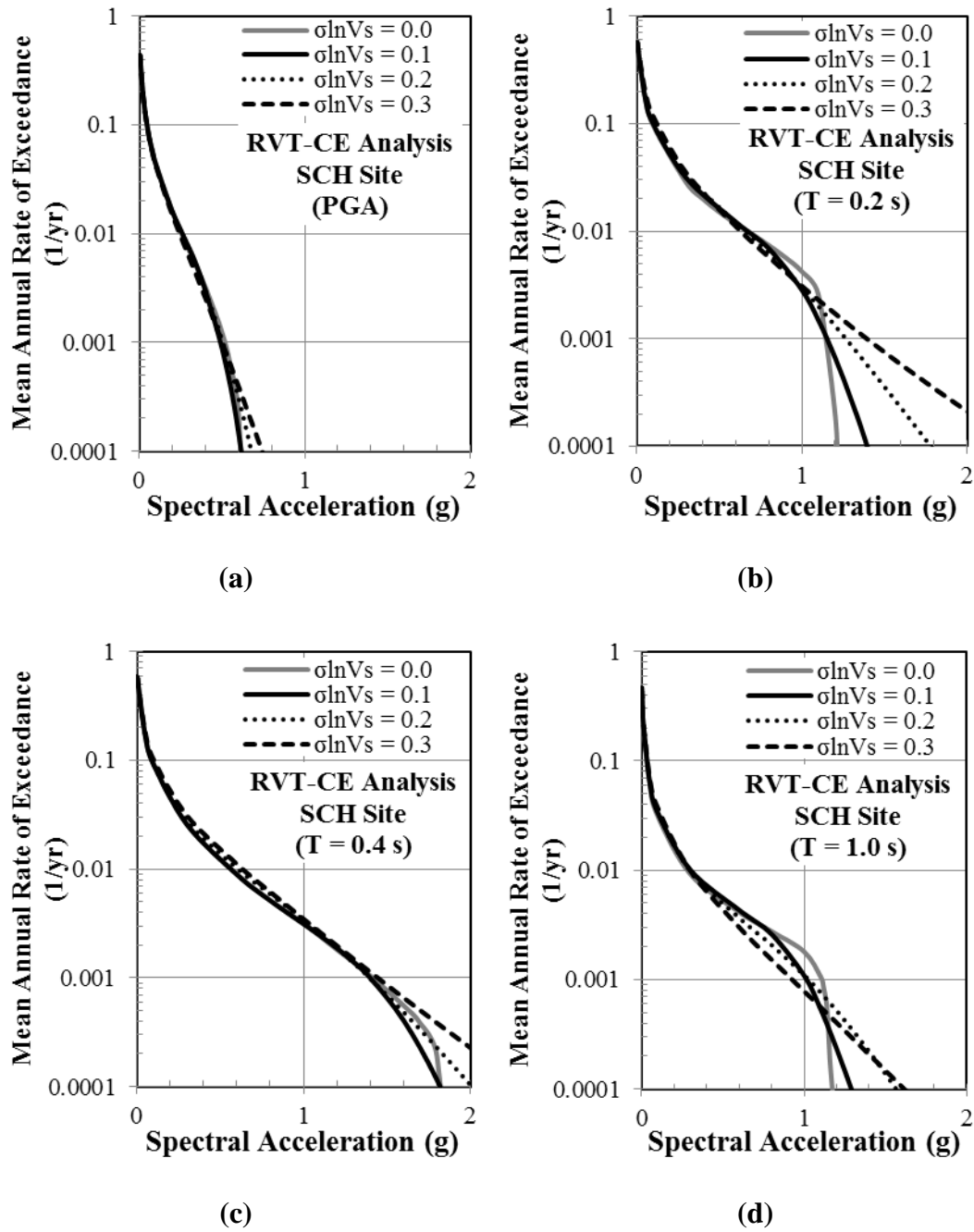


Figure 4.23 Comparison of site-specific soil hazard predictions of RVT-CE and RVT analyses performed with $\sigma_{\ln V_s}$ of 0.0 and 0.2 at (a) PGA, (b) 0.2 s, (c) 0.4 s, and (d) 1.0 s

similar. This result occurs because the reduction in the AF relationship associated with the larger σ_{lnV_s} is counterbalanced by the larger σ_{lnAF} .

Figure 4.24 presents a comparison of site-specific soil hazard curves that are obtained using the AF relationships derived from the RVT analysis performed with small and large sets of input motions (i.e., RVT-CE and RVT) for σ_{lnV_s} of 0.0 and 0.2. In general the hazard curves from RVT and RVT-CE are very similar due to the similarities in the developed AF relationships (Figure 4.19). However, in some cases the hazard from RVT-CE is larger because of the larger σ_{lnAF} associated with the AF relationship due to the fewer input motions.

The site-specific soil hazard curves computed using the AF relationships from TS and RVT-CE analyses are compared in Figure 4.25 for $\sigma_{lnV_s} = 0.0$ and $\sigma_{lnV_s} = 0.2$. For $\sigma_{lnV_s} = 0.0$, the hazard curves for TS consistently are larger than those for RVT-CE because σ_{lnAF} is essentially zero for the RVT analyses. For $\sigma_{lnV_s} = 0.2$, the hazard curves for RVT often are larger.

Figure 4.26 compares the site-specific soil hazard curves computed using the AF relationships from TS and RVT-CE analyses and including the variation of σ_{lnAF} with Sa_{ROCK} (Figure 4.21). Similar to previous analyses, the predicted ground motion level at low hazard levels is controlled by the level of σ_{lnAF} at corresponding input intensities. At all periods the largest ground motion is predicted by TS analysis with $\sigma_{lnV_s} = 0.2$, because this analysis has the highest σ_{lnAF} at larger intensities (Figure 4.21).

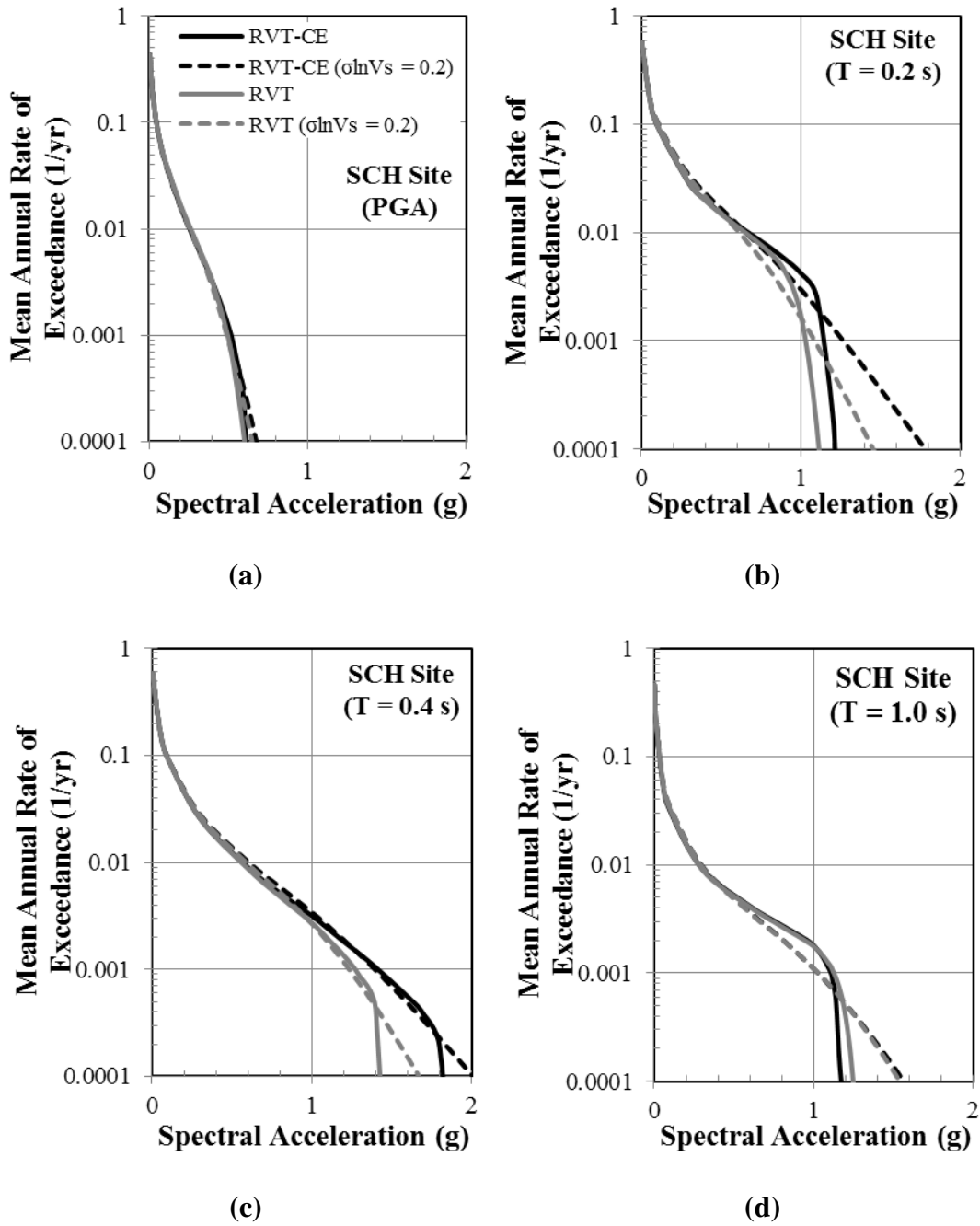


Figure 4.24 Comparison of site-specific soil hazard predictions of RVT-CE and RVT analysis performed for $\sigma_{lnVs} = 0.0$ and $\sigma_{lnVs} = 0.2$ at periods (a) PGA, (b) 0.2 s, (c) 0.4 s, and (d) 1.0 s

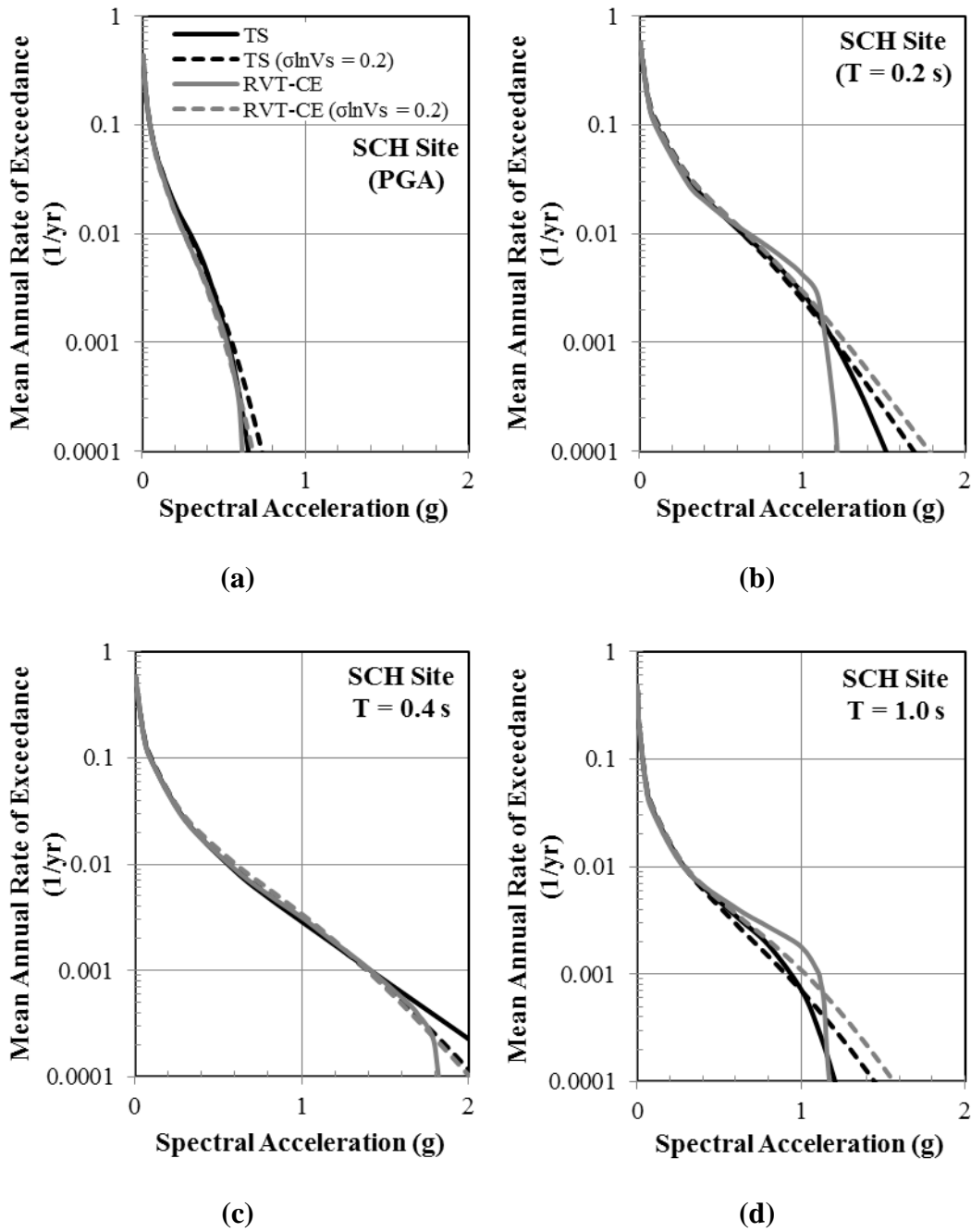


Figure 4.25 Comparison of site-specific soil hazard predictions of TS and RVT-CE analysis performed for $\sigma_{lnVs} = 0.0$ and $\sigma_{lnVs} = 0.2$ at periods (a) PGA, (b) 0.2 s, (c) 0.4 s, and (d) 1.0 s

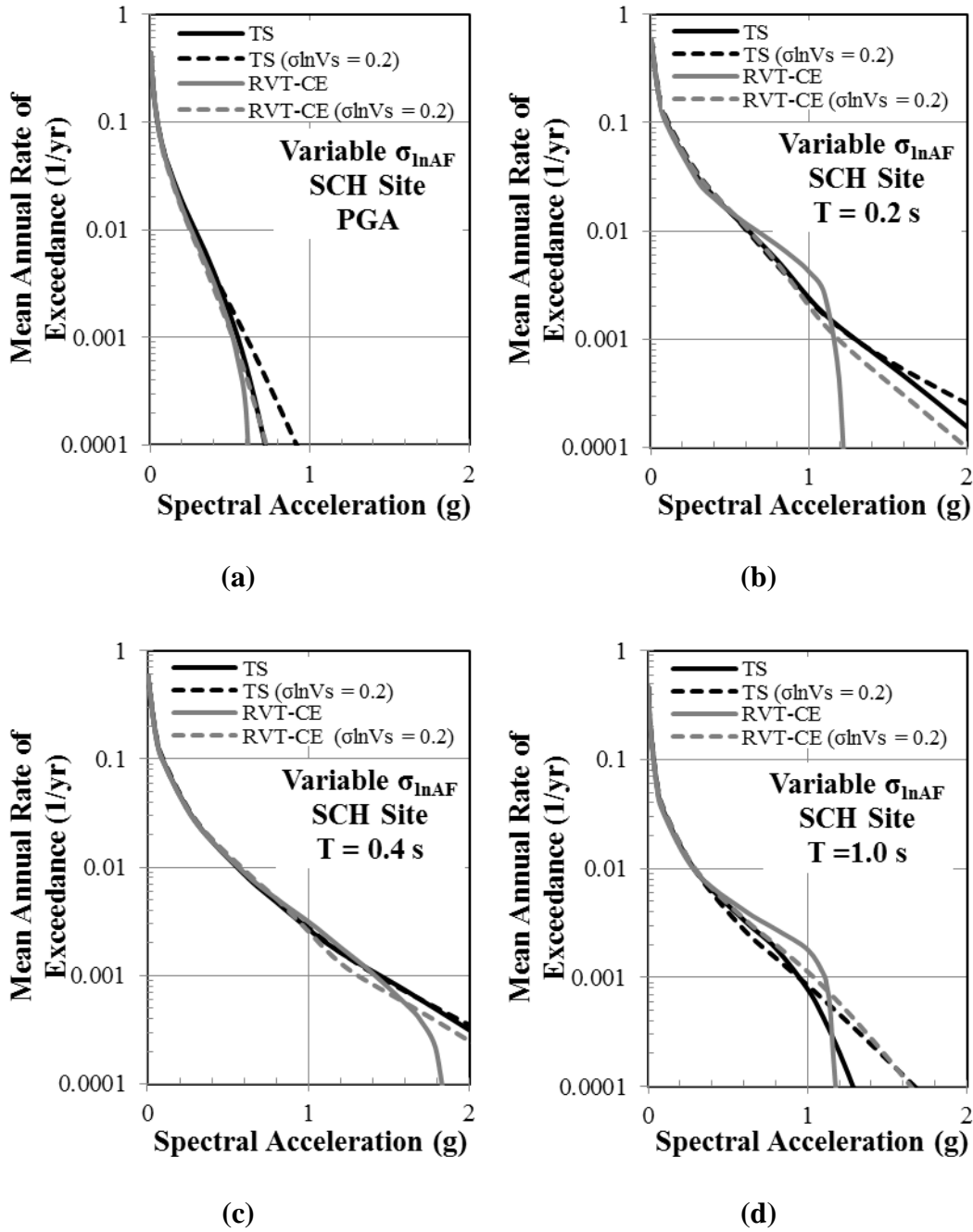


Figure 4.26 Comparison of site-specific soil hazard predictions of TS and RVT analysis performed for $\sigma_{lnVs} = 0.0$ and $\sigma_{lnVs} = 0.2$ using variable σ_{lnAF} (a) PGA, (b) 0.2 s, (c) 0.4 s, and (d) 1.0 s

Figure 4.27 compares the site-specific soil hazard curves for constant and variable σ_{lnAF} . The soil hazard curves computed with variable σ_{lnAF} generally predict larger ground motions for all methods of analysis at all four selected periods (i.e., PGA, 0.2 s, 0.4 s, and 1.0 s). The soil hazard curves predicted for TS analysis with $\sigma_{lnVs} = 0.2$ with variable σ_{lnAF} predicts the largest ground motion at low hazard levels for all periods because it has the highest σ_{lnAF} at high intensities corresponding to these low hazard levels (Figure 4.21).

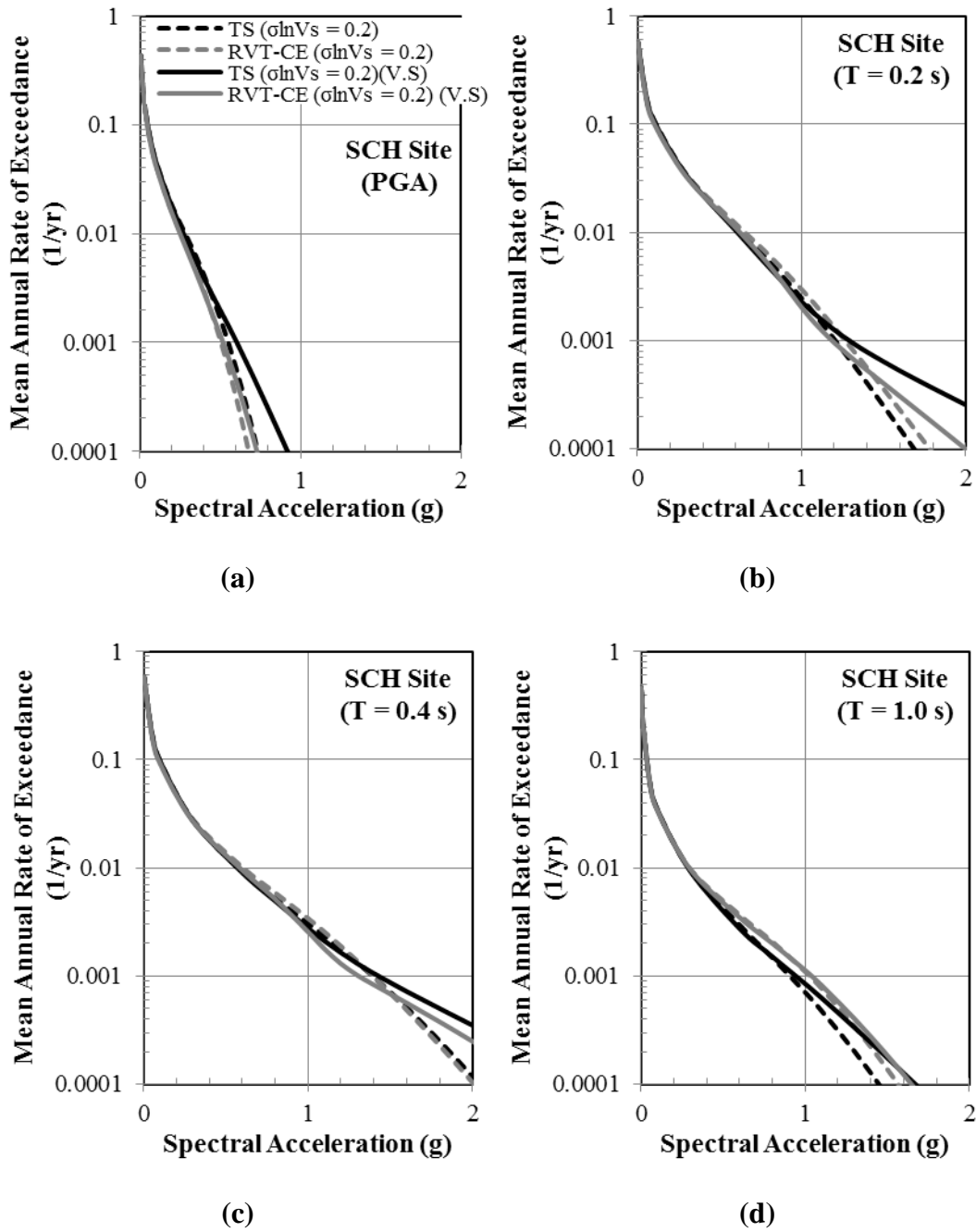


Figure 4.27 Comparison of site-specific soil hazard predictions of TS and RVT-CE analysis performed for σ_{lnVs} of 0.0 and 0.2 with constant and variable (V.S) σ_{lnAF} for (a) PGA, (b) 0.2 s, (c) 0.4 s, and (d) 1.0 s

4.6 Summary

This chapter used time series and RVT site response analyses to develop AF relationships and soil hazard curves for the shallow soil site at Sylmar County Hospital. The AF relationships and soil hazard curves for the different approaches to site response analysis were compared. The influence of shear wave velocity variability on the predicted AF relationship and soil hazard curves was investigated. Additionally, the effect of different levels of V_S variability on the predicted AF relationships and hazard curves was observed for the SCH site. RVT site response analyses were performed using both a large and small set of input motions. The small set of input motions was selected based on controlling earthquake scenarios. The effect of the number of input motions used in RVT analysis on the predicted AF relationships and soil hazard curves was examined.

5

DEVELOPMENT OF SOIL HAZARD CURVES: DEEP SOIL SITE

5.1 Introduction

Site-specific amplification functions and associated soil hazard curves are developed for the deep soil site at Calvert Cliffs (CC). Analyses are performed for this deeper site because previous research has shown that RVT significantly over-predicts the response at the CC site as compared to TS analysis due to its short natural frequency and stiff rock half-space (Kottke 2010, Kottke and Rathje 2013). The effect of varying the shear wave velocity is investigated and the effect on the computed surface hazard curves is presented.

5.2 Amplification Relationships for Known Shear Wave Velocity Profile

Equivalent linear time series analyses are performed for the CC site with the site response program Strata (Kottke and Rathje, 2008) using the time series and RVT input motions presented in Chapter 3.

5.2.1 RESULTS FROM TIME SERIES ANALYSES

Figure 5.1 presents the AF results for each input motion as a function of period, with the results separated based on the input PGA. This deep site has an initial site period of about 4.0 s and second and third modes around periods of 1.4 s and 0.9 s, respectively. These periods show amplification between 4 and 5. Careful observation of AF results indicates the effect of soil nonlinearity through the observed reduction in short period amplification and a slight elongation of the site period with increasing input intensity.

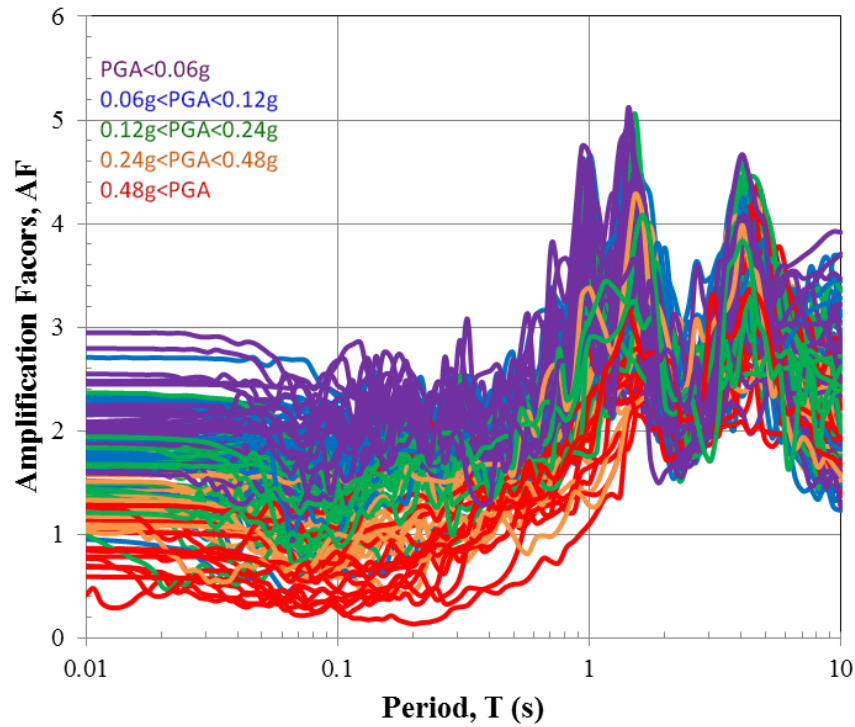
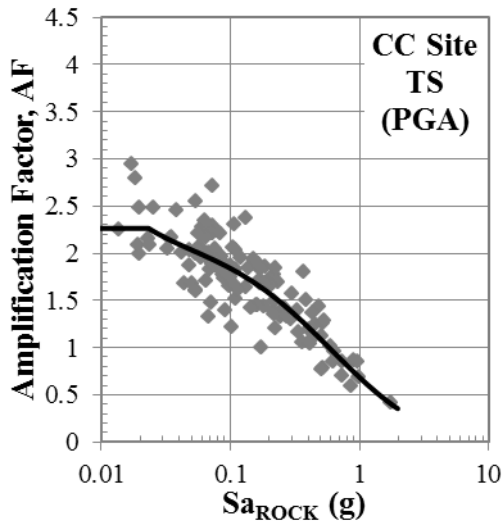


Figure 5.1 AF vs. T from TS analysis for CC site

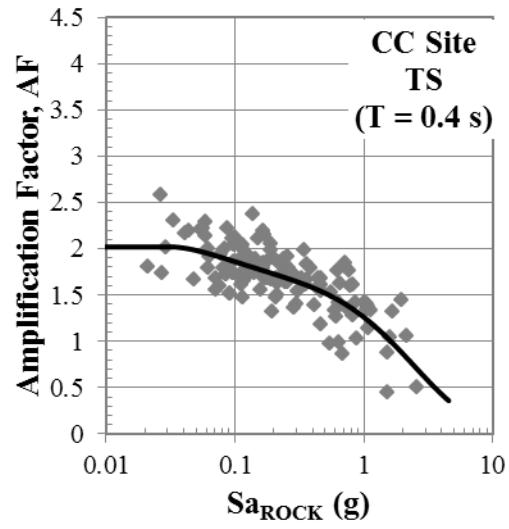
AF values from Figure 5.1 are plotted versus Sa_{ROCK} in Figure 5.2 for PGA and periods of 0.4 s and 1.6 s. At PGA and $T = 0.4$ s, a reduction is observed in AF at large intensities (i.e., large Sa_{ROCK}) due to soil nonlinearity. The rate of reduction is more pronounced for PGA. At a period of 1.6 s, which is slightly larger than the second mode period of the site, a slight initial increase in AF with increasing intensity (up to an Sa_{ROCK} of about 0.1 g) is followed by a subsequent decrease in AF . The change in AF with input intensity is again associated with soil nonlinearity.

The initial increase in AF at $T = 1.6$ s is caused by the elongation of the second mode (~ 1.4 s at small strains) towards 1.6 s, and thus the AF at $T = 1.6$ s increases. At larger input intensities the period continues to elongate past $T = 1.6$ s and, consequently, the AF at $T = 1.6$ s decreases.

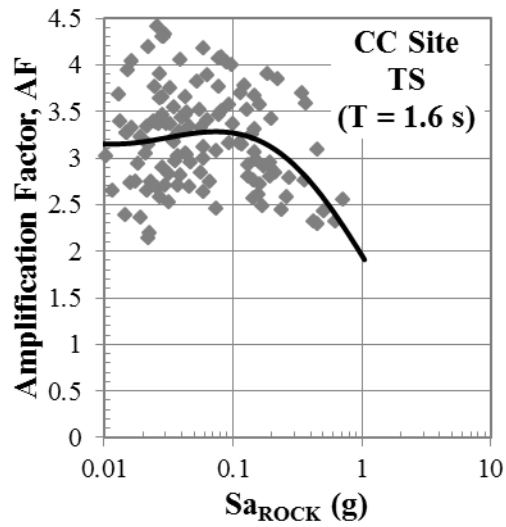
Amplification relationships are developed for the data in Figure 5.2 by fitting a higher order polynomial to $\ln(AF)$ and $\ln(Sa_{ROCK})$. It is important to note that the developed relationships are valid only for the range of Sa_{ROCK} that is represented by the available data (in this case, up to about 2.0 g, 3.0 g, and 0.80 g for PGA, and $T = 0.4$ s, and 1.6 s, respectively). The derived AF relationships are shown in Figure 5.2 together with data points. Table 5.1 presents the regression coefficients for the fitted polynomials for the TS data, together with the associated $\sigma_{\ln AF}$. The $\sigma_{\ln AF}$ values are very similar for each period. The $\sigma_{\ln AF}$ given in Table 5.1 represent only the motion-to-motion variability and do not include variability due to the variability in shear wave velocity.



(a)



(b)



(c)

Figure 5.2 AF vs. Sa_{ROCK} data from TS analysis on CC site together with derived AF relationships for different periods (a) PGA, (b) 0.4 s, and (d) 1.6 s

Table 5.1 Higher order polynomial constants and associated $\sigma_{\ln AF}$ of AF function developed for TS analysis data

	PGA	T = 0.4 s	T = 1.6 s
a₀	-0.380	0.232	0.671
a₁	-0.812	-0.375	-0.496
a₂	-0.221	-0.190	-0.151
a₃	-0.024	-0.061	-0.014
a₄	-	-0.008	-
$\sigma_{\ln AF}$	0.15	0.17	0.16

5.2.2 RESULTS FROM RVT ANALYSIS

Equivalent-linear site response analyses are also performed for the CC site using the RVT approach, as implemented in the program Strata (Kottke and Rathje, 2008). The smaller set of input motions obtained based on control earthquakes with 19 rock response spectra presented in Chapter 3 are used as input motions.

Figure 5.3 presents the AF values obtained for each input rock motion, with the results color-coded based on the input PGA. Unlike the AF values obtained through TS analyses, the AF values from RVT analysis vary smoothly with period due to the input motions varying smoothly with period. As a result, the RVT results more clearly indicate the effect of soil nonlinearity through the

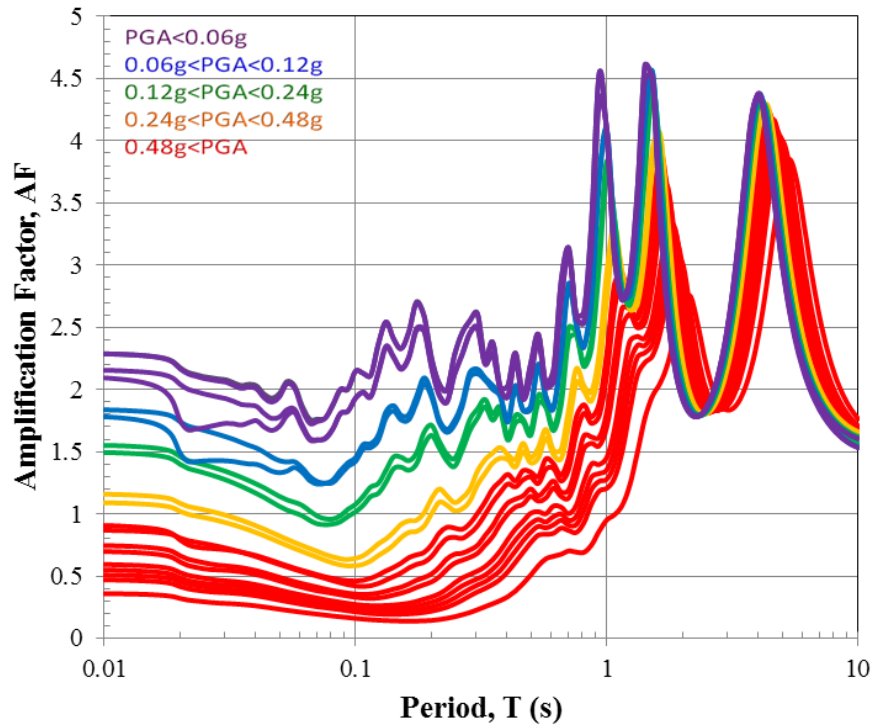


Figure 5.3 AF vs. T from RVT analysis for CC site

observed reduction in short period amplification and the elongation of the site period with increasing input intensity.

The AF values from Figure 5.3 are plotted versus Sa_{ROCK} in Figure 5.4 for PGA and periods of 0.4 s and 1.6 s. Similar to the results for TS analysis (Figure 5.2), the RVT results show that at short periods there is a reduction in AF at large intensities due to soil nonlinearity and the rate of reduction is more pronounced for PGA than 0.4 s. At a period of 1.6 s, an increase in AF with increasing intensity (up

to an Sa_{ROCK} of about 0.1 g) is followed by a decrease in AF with further increases in intensity. The reduction seen in AF at large intensities is again associated with soil nonlinearity and period elongation, as previously discussed for the TS results. The smooth AF data from the RVT analysis in Figures 5.3 and 5.4 more clearly show the relationship between period elongation and amplification at $T = 1.6$ s as compared to the TS results.

AF relationships are developed for the data in Figure 5.4 by fitting a higher order polynomial to $\ln(AF)$ and $\ln(Sa_{ROCK})$. The derived AF relationships are shown in Figure 5.4. Table 5.2 presents the regression coefficients for fitted polynomials for the RVT data, together with the associated $\sigma_{\ln AF}$. The variability in AF for the RVT analyses is very small ($\sigma_{\ln AF} \sim 0.02$ to 0.05) because RVT analysis does not include the effects of motion-to-motion variability.

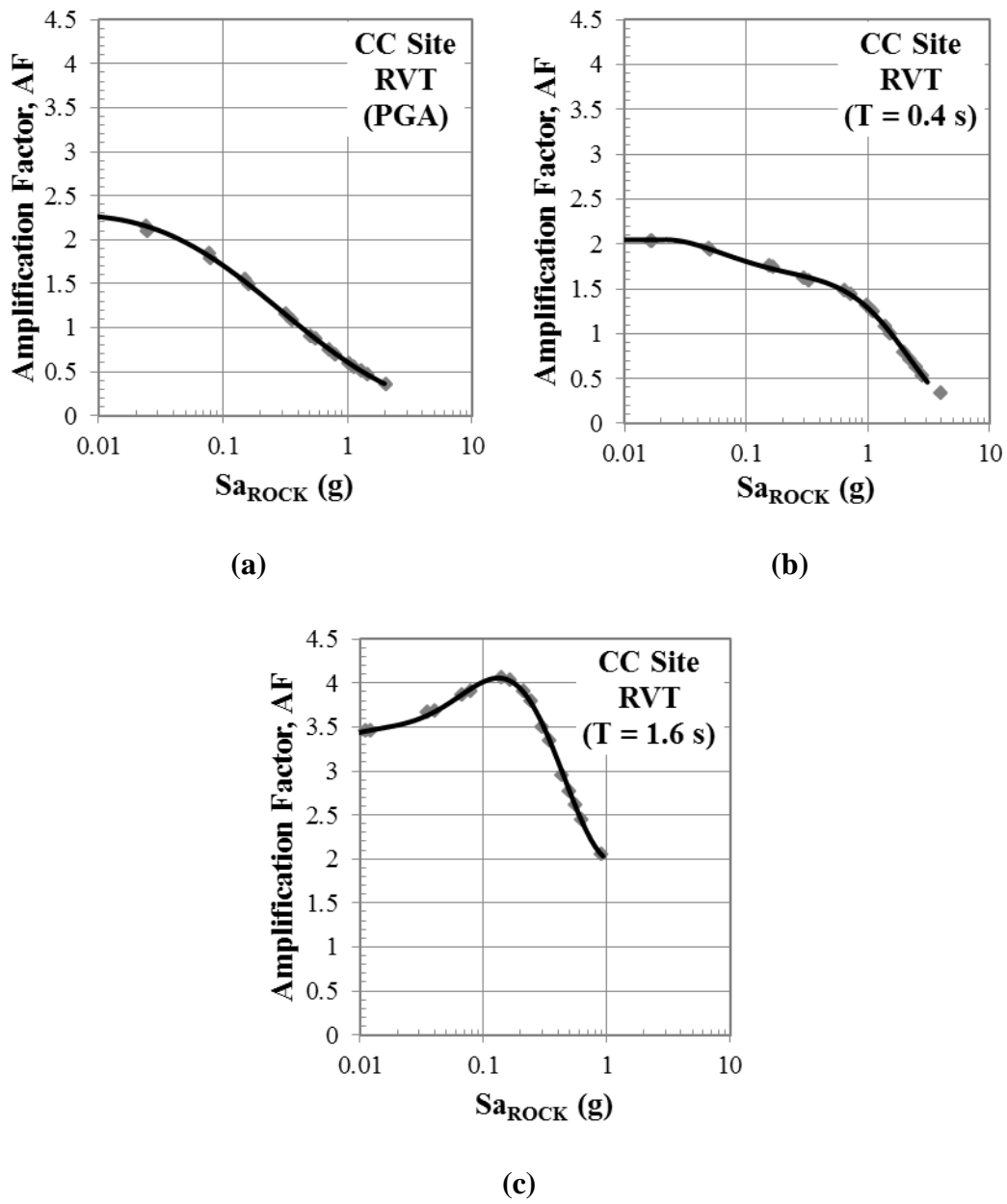


Figure 5.4 AF vs. Sa_{ROCK} data from RVT analysis on CC site together with derived AF relationships for different periods (a) PGA, (b) 0.4 s and (d) 1.6 s

Table 5.2 Higher order polynomial constants and associated $\sigma_{\ln AF}$ of AF function developed for RVT analysis data

	PGA	T = 0.4 s	T = 1.6 s
a₀	-0.4969	0.2470	0.6952
a₁	-0.6778	-0.4568	-0.1489
a₂	-0.1143	-0.2879	0.8576
a₃	-0.0063	-0.0701	0.7355
a₄		0.0020	0.2484
a₅		0.0017	0.0406
a₆			0.0031
a₇			7.96E-05
a₈			
a₉			
a₁₀			
$\sigma_{\ln AF}$	0.013	0.016	0.005

5.3 Amplification Relationships for Varied Shear Wave Velocity Profiles

The effect of soil property variability on the developed amplification relationships is investigated through Monte Carlo simulations in which multiple site realizations are generated by statistically generating site shear-wave velocity profiles. Similar to the SCH site, the varied V_s profiles for the CC site are generated

using ρ_{IL} equal to 0.8 and $\sigma_{\ln V_S}$ equal to 0.2 (representing a coefficient of variation of about 20%). Minimum and maximum limits on the V_S in the generated soil profiles are specified as $\pm 2\sigma_{\ln V_S}$

5.3.1 RESULTS FROM TIME SERIES ANALYSES

The V_S profile realizations generated for the TS analyses with $\sigma_{\ln V_S}=0.2$ are shown in Figure 5.5, together with the baseline V_S profile and the median V_S profile of the generated 20 realizations. The median V_S profile of the varied profiles agrees well with the specified baseline V_S .

The computed AF values for the TS analyses with $\sigma_{\ln V_S}=0.2$ are plotted versus Sa_{ROCK} for the three periods under consideration in Figure 5.6. The data presented in Figure 5.6 look similar to those in Figure 5.3 for the non-varied V_S case ($\sigma_{\ln V_S}=0.0$), indicating that the variation in AF with Sa_{ROCK} is not significantly influenced by including variability in the V_S profile. However, the data in Figure 5.6 are more scattered than the data for the $\sigma_{\ln V_S}=0.0$ case (Figure 5.2), showing the influence of the variability in the V_S profiles on the variability in the predicted AF .

AF relationships are developed for the data in Figure 5.6 by fitting a higher order polynomial to $\ln(AF)$ and $\ln(Sa_{ROCK})$. The derived AF functions are shown together with the data points in Figure 5.6. Table 5.3 presents the regression coefficients for the fitted polynomials together with the associated $\sigma_{\ln AF}$. The $\sigma_{\ln AF}$

values range from 0.23 to 0.30. The σ_{lnAF} values increased by 53% to 88% compared to the values obtained when the V_S profile was not varied (Table 5.1).

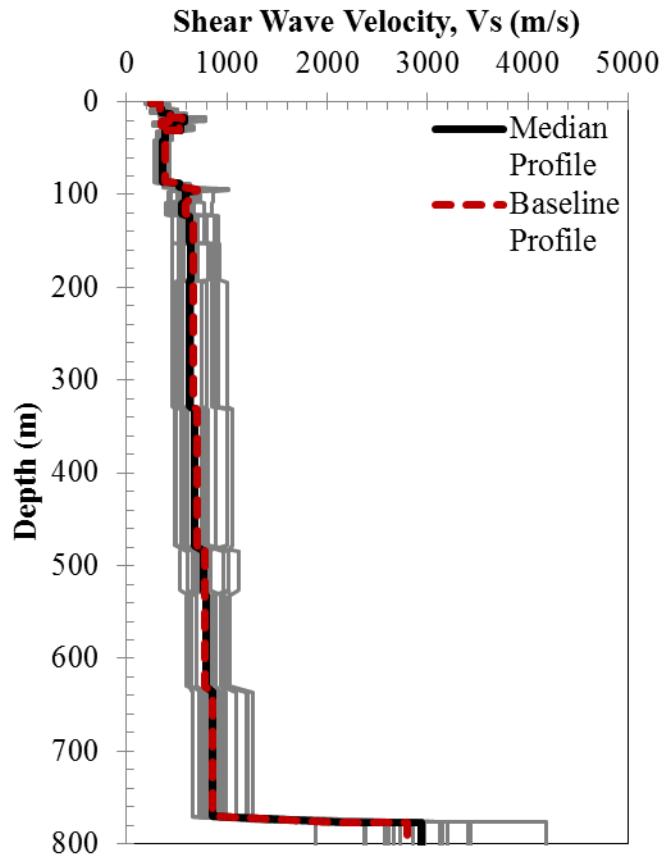


Figure 5.5 Twenty V_S profiles generated for TS ($\sigma_{lnVs} = 0.20$) analysis together with the median and baseline V_S profile for CC site

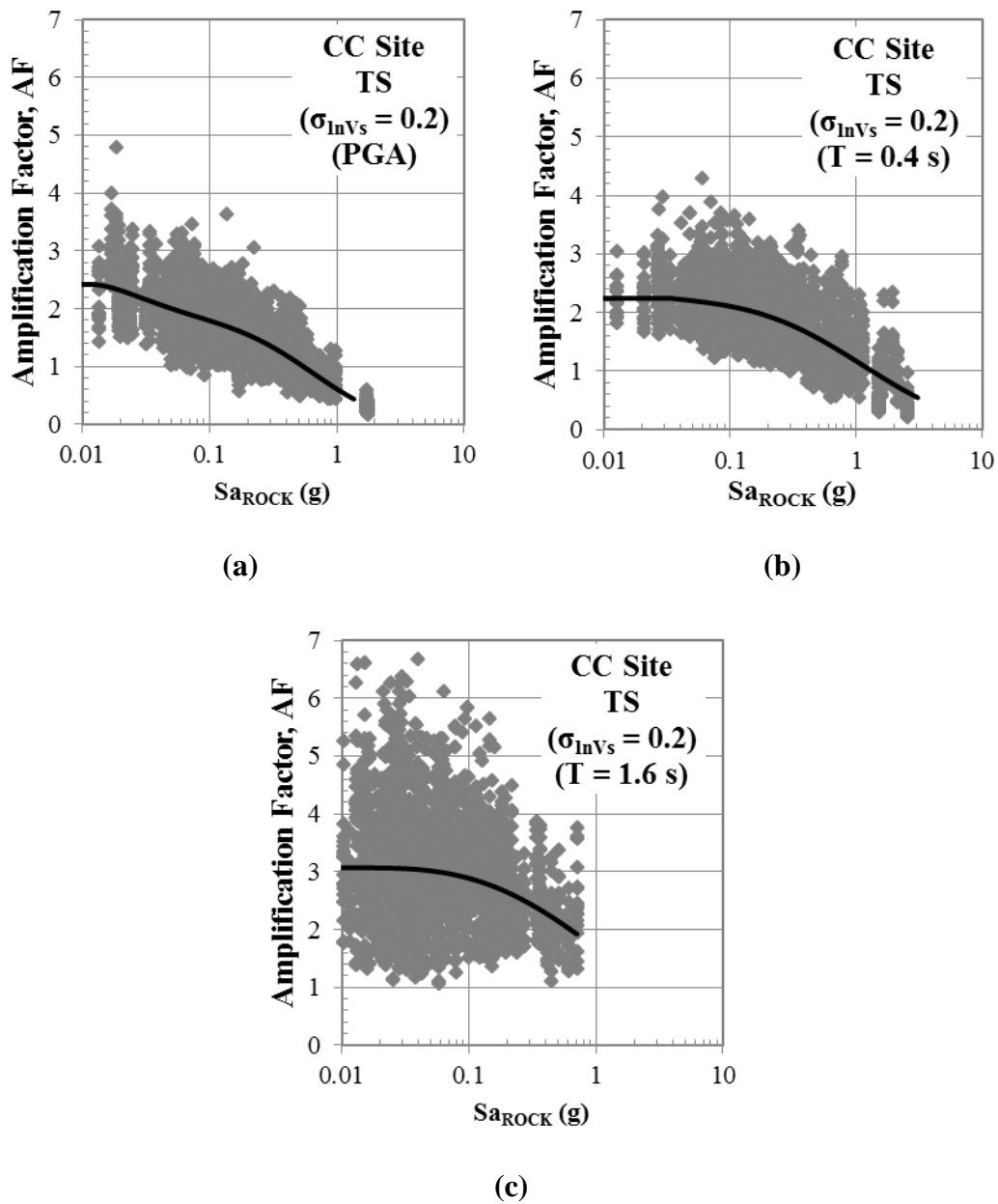


Figure 5.6 AF vs. Sa_{ROCK} data from TS ($\sigma_{\ln V_s} = 0.2$) analysis performed on V_s generated for CC site, together with derived AF relationships for different periods (a) PGA, (b) 0.4 s and (d) 1.6 s

Table 5.3 Higher order polynomial constants and associated $\sigma_{\ln AF}$ of AF function developed for TS ($\sigma_{\ln V_S} = 0.2$) analysis data

	PGA	T = 0.4 s	T = 1.6 s
a_0	-0.4872	0.157	0.5205
a_1	-0.9848	-0.5021	-0.4185
a_2	-0.3041	-0.1406	-0.0971
a_3	-0.0178	-0.0145	-0.0075
a_4	0.0108		
a_5	0.0016		
$\sigma_{\ln AF}$	0.23	0.27	0.30

5.3.2 RESULTS FROM RVT ANALYSIS

RVT analyses are similarly performed for a separate set of 20 varied shear wave velocity profiles generated through Monte Carlo simulations for $\sigma_{\ln V_S}=0.2$. The twenty V_S profile realizations generated for RVT with $\sigma_{\ln V_S}=0.2$ analyses are shown in Figure 5.7, together with the baseline and the median V_S profile of the twenty realizations. Again, the median V_S profile from the Monte Carlo simulations agrees well with the baseline V_S profile.

The AF values from the RVT analyses with $\sigma_{\ln V_S}=0.2$ are plotted versus Sa_{ROCK} in Figure 5.8 for the three spectral periods under consideration. The data presented in Figure 5.8 look similar to the RVT data presented in Figure 5.4, except

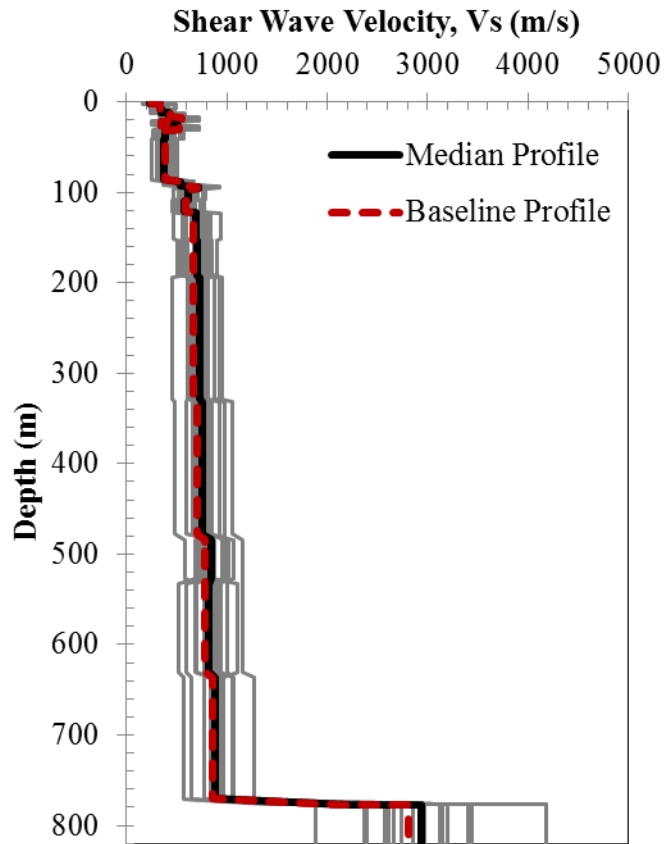


Figure 5.7 Twenty V_S profiles generated for RVT ($\sigma_{lnV_S} = 0.20$) analysis together with the median and baseline V_S profile for CC site

for $T = 1.6$ s. At this period a larger peak is observed in the RVT data when the V_S is not varied ($AF \sim 4$, Figure 5.4), but this peak is less pronounced when $\sigma_{lnV_S}=0.2$ ($AF \sim 3.4$, Figure 5.8).

AF relationships are developed for the data in Figure 5.8 by fitting a higher order polynomial to $\ln(AF)$ and $\ln(Sa_{ROCK})$. The derived AF relationships are shown in Figure 5.8. Table 5.4 presents the regression coefficients of the fitted polynomials for the RVT data with $\sigma_{\ln V_S}=0.2$ together with the associated $\sigma_{\ln AF}$. The $\sigma_{\ln AF}$ values range from 0.22 to 0.45 and these values are about 16 to 50 times larger than the values obtained for RVT analysis when the V_S profile was not varied (i.e., $\sigma_{\ln V_S}=0.0$, Table 5.2). The standard deviations for the RVT analysis with $\sigma_{\ln V_S}=0.2$ include the effect of shear wave velocity variability, while the RVT analysis with $\sigma_{\ln V_S}=0.0$ does not. Thus, one would expect a significantly large increase in standard deviation as compared to the RVT case with $\sigma_{\ln V_S}=0.0$.

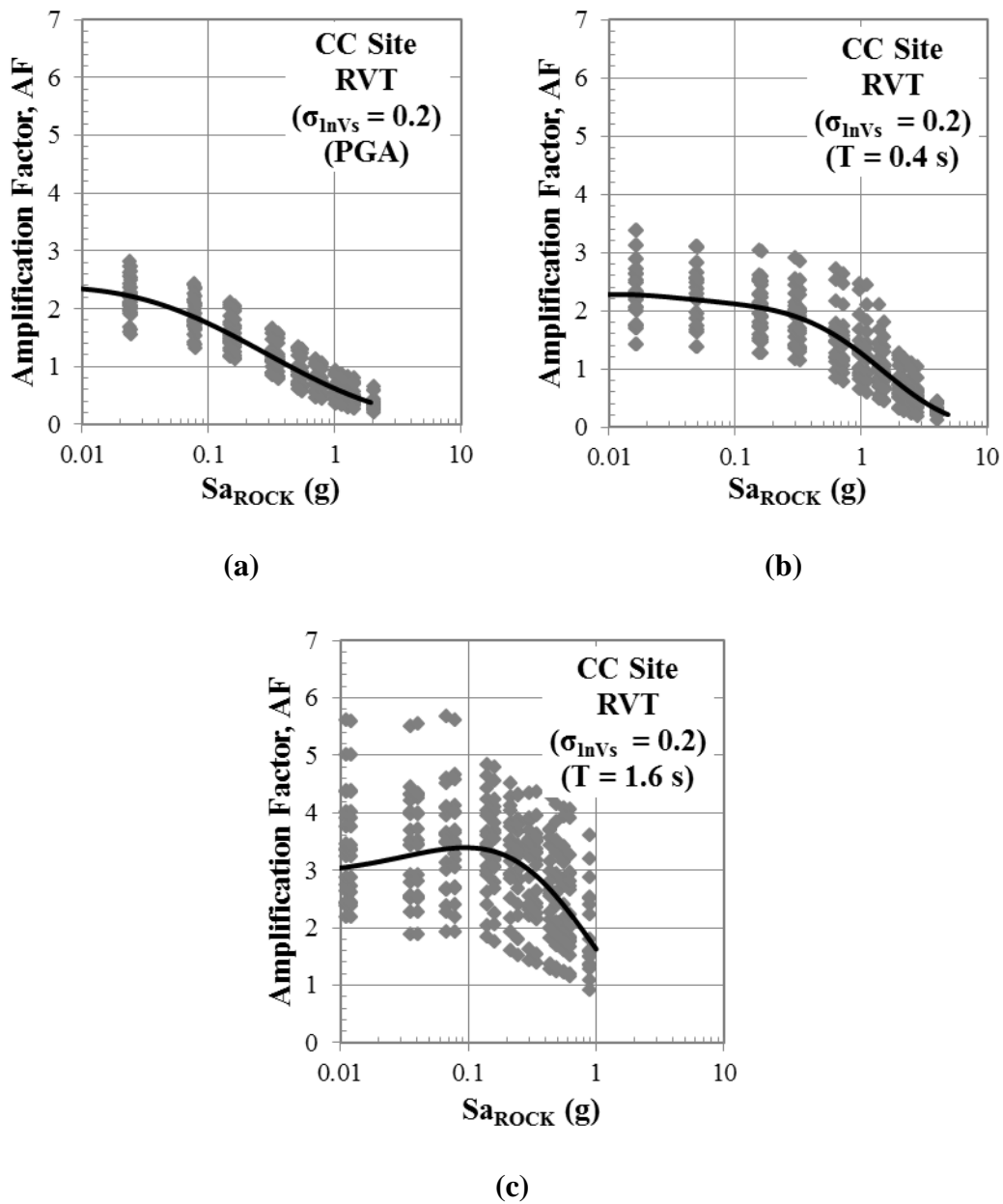


Figure 5.8 AF vs. Sa_{ROCK} data from RVT ($\sigma_{lnVs}=0.2$) analysis performed on V_S generated for CC site, together with derived AF relationships for different periods (a) PGA, (b) 0.4 s and (d) 1.6 s

Table 5.4 Higher order polynomial constants and associated $\sigma_{\ln AF}$ of AF function developed for RVT ($\sigma_{\ln V_S}=0.2$) analysis data

	PGA	T = 0.4 s	T = 1.6 s
a₀	-0.4752	0.2361	0.4819
a₁	-0.6756	-0.5705	-0.7599
a₂	-0.1131	-0.2522	-0.2705
a₃	-0.0063	-0.0541	-0.0387
a₄		-0.0044	-0.0019
$\sigma_{\ln AF}$	0.22	0.31	0.30

5.4 Comparison of Amplification Relationships

The results from TS and RVT analyses are compared at the three selected periods through the developed AF relationships and their standard deviations. Figure 5.9 presents the median AF relationships previously developed using TS and RVT analyses. For PGA (Figure 5.9a), the relationships derived from all methods are very similar, except at very low input intensities (< 0.04 g). At $T = 0.4$ s (Figure 5.9b), again the results are very similar but including V_S variability generates larger AF at input intensities less than about 0.2 g for both RVT and TS analyses.

For $T = 1.6$ s (Figure 5.9c), significant differences are observed in the predicted AF relationships. When V_S variability is not taken into account ($\sigma_{\ln V_S} =$

0.0), the peak in the AF relationship is about 25% larger for RVT as compared to TS. The significantly larger AF from RVT analysis for the CC site at some periods has been reported by Kottke (2010) and Kottke and Rathje (2013), and the difference attributed to changes in ground motion duration not taken into account in RVT site response analysis. The larger amplification from RVT is diminished by introducing some shear wave velocity variability into the site response analyses such that the peak observed in the RVT analysis with $\sigma_{\ln V_S}=0.2$ is comparable with the peak observed in the TS analysis with $\sigma_{\ln V_S}=0.0$. However, the peak in the TS analysis is also reduced when V_S variability is included. Therefore, the peak for RVT analysis with $\sigma_{\ln V_S}=0.2$ at about $Sa_{ROCK} = 0.1$ g is still about 15% larger than for the TS analysis with $\sigma_{\ln V_S}=0.2$. Thus, the peak observed in both TS and RVT analyses is reduced with the introduction of V_S variability but the level of reduction is more significant for RVT analysis.

Table 5.5 summarizes the values of $\sigma_{\ln AF}$ associated with the RVT and TS analyses with $\sigma_{\ln V_S}=0.0$ and $\sigma_{\ln V_S}=0.2$ for the three selected periods. As discussed in the previous section, introducing shear wave velocity variability increases the $\sigma_{\ln AF}$ associated with the amplification relationships. The RVT analyses with $\sigma_{\ln V_S}=0.0$ do not include shear wave velocity or motion-to-motion variability, and therefore the $\sigma_{\ln AF}$ are very small. Because motion-to-motion variability is not included, the small value of $\sigma_{\ln AF}$ is not appropriate for the convolution method. For $\sigma_{\ln V_S}=0.2$, the TS analysis and RVT analysis have similar values of $\sigma_{\ln AF}$, except for $T = 0.4$ s where

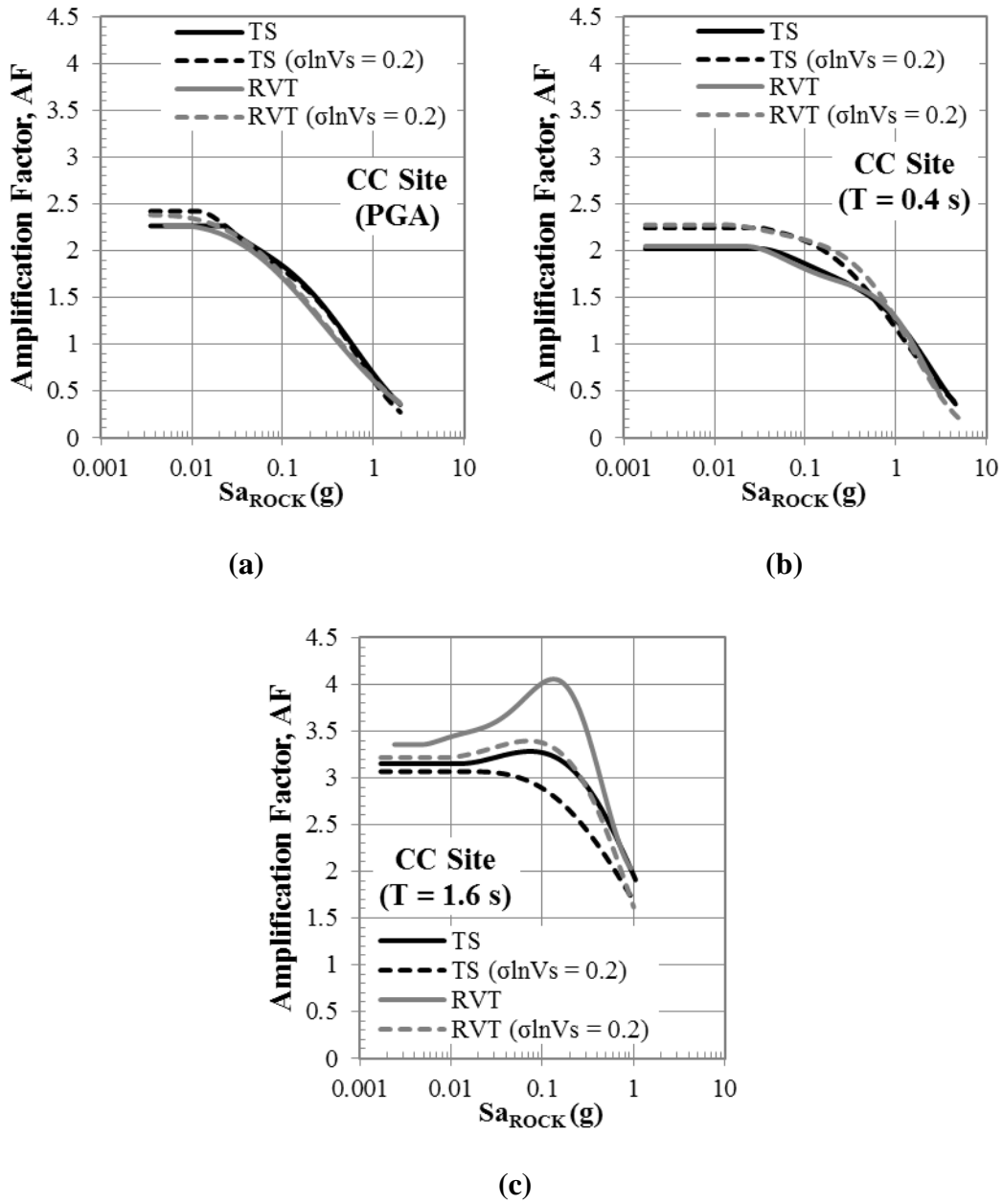


Figure 5.9 Comparison of *AF* functions predictions of TS and RVT analyses performed with $\sigma_{lnVs} = 0.0$ and $\sigma_{lnVs} = 0.2$ at different periods (a) PGA, (b) 0.4 s, and (d) 1.6 s

Table 5.5 Comparison of σ_{lnAF} of AF relationships developed for different analysis methods

σ_{lnVs}	TS	TS	RVT	RVT
	$\sigma_{lnVs}=0.0$	$\sigma_{lnVs}=0.2$	$\sigma_{lnVs}=0.0$	$\sigma_{lnVs}=0.2$
PGA	0.15	0.23	0.013	0.22
0.4 s	0.17	0.27	0.016	0.31
1.6 s	0.16	0.30	0.005	0.30

the σ_{lnAF} for RVT is slightly larger. This result may be caused by the fewer input motions used in the RVT analyses.

To investigate the relationship between σ_{lnAF} and Sa_{ROCK} , the AF data obtained from TS and RVT analyses without variability ($\sigma_{lnVs} = 0.0$) and with variability ($\sigma_{lnVs} = 0.2$) are divided into Sa_{ROCK} bins and the σ_{lnAF} within each bin is calculated (Table 5.6). Table 5.6 shows that the variability in the AF data is generally larger at high input intensities for all analyses. The variability in AF is usually higher than the one represented by a constant σ_{lnAF} (Table 5.6). In most cases, TS with $\sigma_{lnVs} = 0.2$ has the largest variability, followed by RVT with $\sigma_{lnVs} = 0.2$. The variation in the σ_{lnAF} increases up to 4 times with increasing input intensity.

Table 5.6 Variation of $\sigma_{\ln AF}$ with Sa_{ROCK} for AF relationships derived for different analysis methods

	PGA		T = 0.4 s		T = 1.6 s	
	Sa_{ROCK}	$\sigma_{\ln AF}$	Sa_{ROCK}	$\sigma_{\ln AF}$	Sa_{ROCK}	$\sigma_{\ln AF}$
TS $\sigma_{\ln Vs}=0.0$	<0.1	0.138	<0.1	0.124	<0.03	0.183
	0.1-0.3	0.159	0.1-0.3	0.111	0.03-0.1	0.136
	>0.3	0.180	>0.3	0.237	>0.1	0.141
TS $\sigma_{\ln Vs}=0.2$	<0.1	0.210	<0.1	0.205	<0.03	0.319
	0.1-0.3	0.237	0.1-0.3	0.286	0.03-0.1	0.307
	>0.3	0.277	>0.3	0.353	>0.1	0.248
RVT $\sigma_{\ln Vs}=0.0$	<0.3	0.015	<0.3	0.013	<0.1	0.004
	0.3-1.0	0.011	0.3-1.0	0.020	0.1-0.3	0.003
	>1	0.013	>1	0.015	>0.3	0.006
RVT $\sigma_{\ln Vs}=0.2$	<0.3	0.162	<0.3	0.223	<0.1	0.242
	0.3-1.0	0.226	0.3-1.0	0.286	0.1-0.3	0.263
	>1	0.282	>1	0.375	>0.3	0.328

5.5 Soil Hazard Curves

Soil hazard curves for the CC site are computed using the convolution approach (e.g., Bazzurro and Cornell 2004) and the amplification function relationships developed through various methods of analysis. Figure 5.10 shows the site-specific soil hazard curves obtained using the AF relationships derived from TS

and RVT analyses with $\sigma_{lnVs} = 0.0$ and $\sigma_{lnVs} = 0.2$. For these curves, a constant σ_{lnAF} is used across all values of Sa_{ROCK} .

For PGA (Figure 5.10a), the four curves are very similar, except that RVT with $\sigma_{lnVs} = 0.0$ shows smaller hazard levels because of the very small σ_{lnAF} . For $T = 0.4$ s (Figure 5.10b), the predicted hazard curves show more variation. The ground motions for RVT with $\sigma_{lnVs} = 0.2$ are slightly larger than the others, which is mostly due to the larger σ_{lnAF} associated with the amplification relationship. RVT generates the smallest motions because it has almost zero σ_{lnAF} .

For $T = 1.6$ s (Figure 5.10c), the differences in the hazard curves can again be related to the different AF relationships and σ_{lnAF} values. The larger peak observed in the AF function for RVT analysis with $\sigma_{lnVs} = 0.0$ generates larger ground motions at hazard levels larger than 0.0003 1/yr. However, the very small σ_{lnAF} value for RVT analysis with $\sigma_{lnVs} = 0.0$ leads to these analyses generating the smallest ground motions at smaller hazard levels (about 0.0001 1 /yr.). For the other analyses, the predicted ground motions at low hazard levels (less than 0.0002 1/yr) are driven by both median AF and σ_{lnAF} predictions; such that RVT with $\sigma_{lnVs} = 0.2$ generates the largest motions because it has the larger median AF prediction compared to TS with $\sigma_{lnVs} = 0.2$ and the TS and RVT amplification functions have the same σ_{lnAF} .

Figure 5.11 compares the site-specific soil hazard curves computed using the AF relationships from TS and RVT analyses including the variation of σ_{lnAF} with

Sa_{ROCK} (Table 5.6). Similar to previous analyses, the predicted ground motion level at low hazard levels is controlled mainly by the level of σ_{lnAF} at corresponding input intensities. At short periods the predicted ground motion is similar for all analysis except RVT. At $T = 1.6$ s the largest ground motion is predicted by RVT analysis with $\sigma_{lnVs} = 0.2$, because this analysis has the highest σ_{lnAF} at larger intensities (Table 5.6).

Figure 5.12 compares the site-specific soil hazard curves for constant and variable σ_{lnAF} . Soil hazard curves computed with variable σ_{lnAF} for RVT analysis generally predict the same hazard as those with a constant σ_{lnAF} . This result may be caused by the variable σ_{lnAF} not being significantly larger than the constant σ_{lnAF} for RVT analyses. However for TS analysis soil hazard curves computed with variable σ_{lnAF} predicts larger ground motions at selected periods except at $T = 1.6$ s. At PGA, and $T = 0.4$ s variable σ_{lnAF} is higher than constant σ_{lnAF} for TS. The soil hazard curves predicted for TS analysis with $\sigma_{lnVs} = 0.2$ with variable σ_{lnAF} predicts the slightly lower ground motion at low hazard levels at $T = 1.6$ s due lower σ_{lnAF} observed at high input intensities compared to the constant σ_{lnAF} (0.248 vs. 0.3, Table 5.6 and Table 5.5).

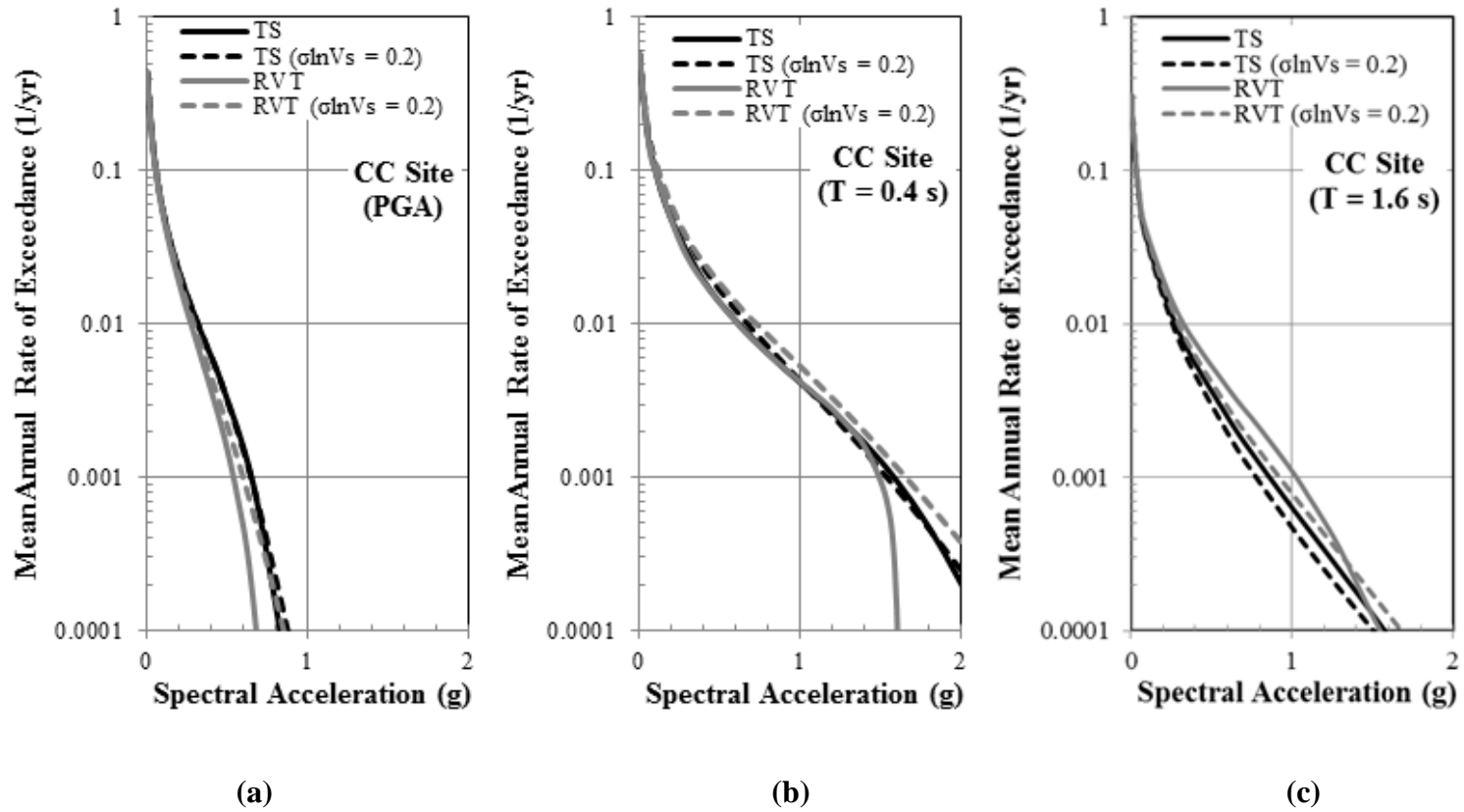


Figure 5.10 Comparison of site-specific soil hazard predictions of TS and RVT analyses performed with $\sigma_{lnVs} = 0.0$ and $\sigma_{lnVs} = 0.2$ for CC site at periods (a) PGA, (b) 0.4 s, and (d) 1.6 s

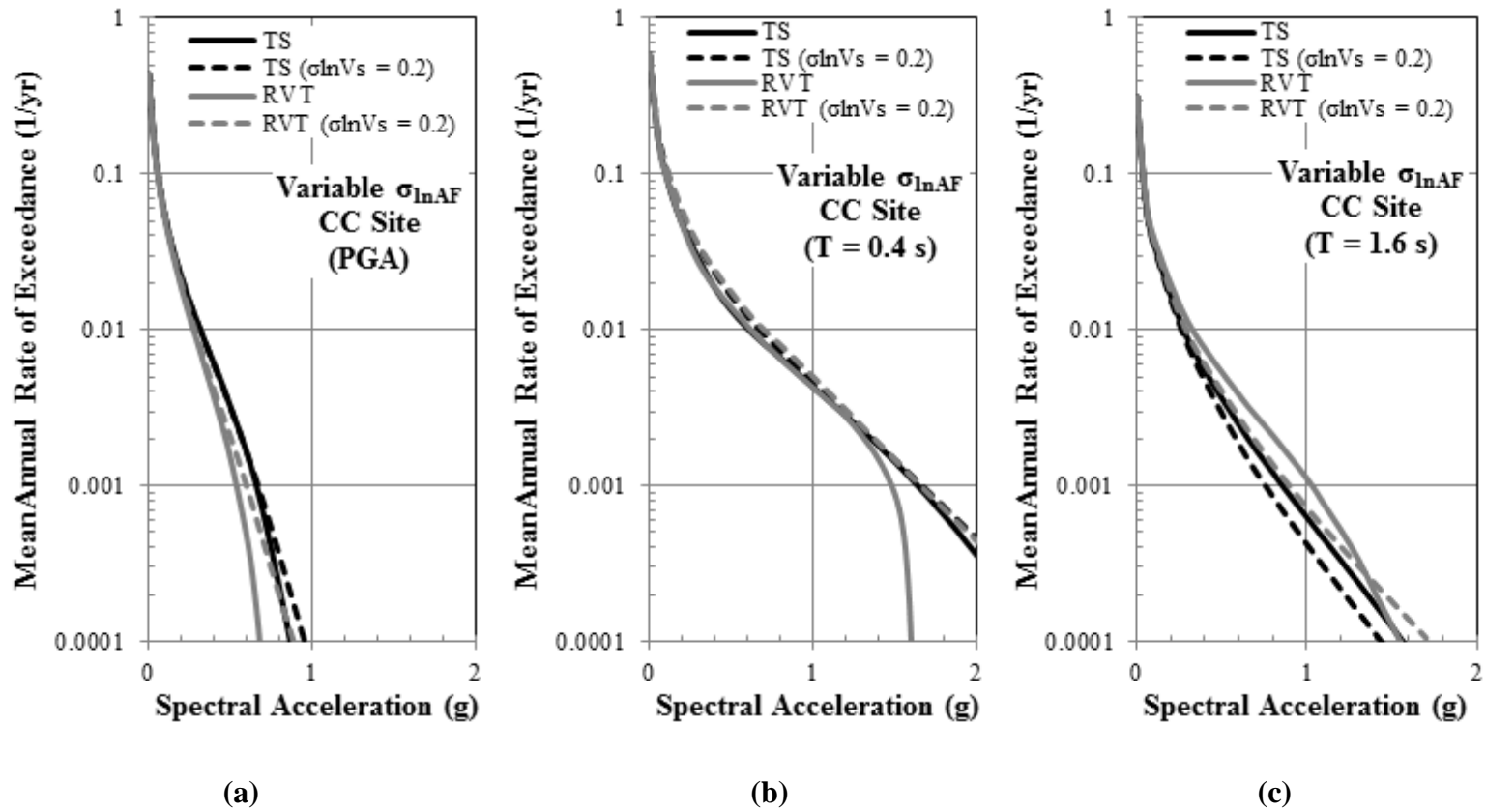


Figure 5.11 Comparison of site-specific soil hazard predictions of TS and RVT analysis performed for $\sigma_{\ln V_s} = 0.0$ and $\sigma_{\ln V_s} = 0.2$ using variable $\sigma_{\ln A_F}$ for CC site at periods (a) PGA, (b) 0.4 s, and (c) 1.6 s

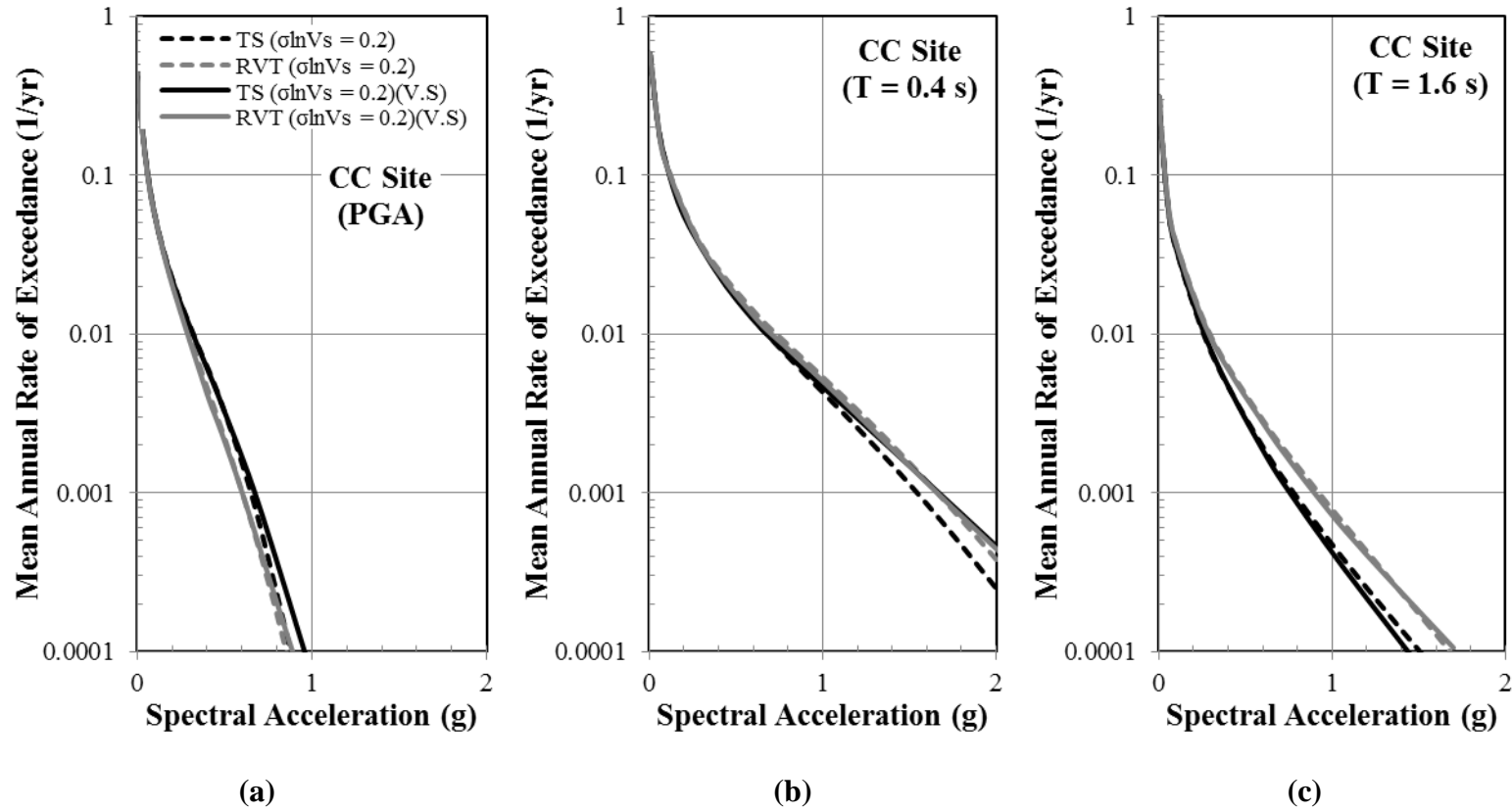


Figure 5.12 Comparison of site-specific soil hazard predictions of TS and RVT-CE analysis performed for σ_{lnVs} of 0.0 and 0.2 with constant and variable σ_{lnAF} for CC site at periods (a) PGA, (b) 0.4 s, and (c) 1.6 s

5.6 Summary

This chapter uses TS and RVT site response analyses to develop AF relationships and soil hazard curves for a deep (i.e., CC) site. The AF relationships and soil hazard curves for the different approaches to site response analysis are compared. The influence of shear wave velocity variability on the predicted AF relationship and soil hazard curves is investigated.

6

TWO-DIMENSIONAL VELOCITY FIELDS

6.1 Introduction

The main soil properties required for site response analysis are the shear-wave velocity (V_s) profile and the nonlinear modulus reduction and damping curves. Spatial variability and uncertainties in these properties across a site are often taken into account by modeling multiple one-dimensional (1D) profiles in 1D site response analyses. This was the approach taken in Chapter 4 and 5 when performing Monte Carlo simulations on the 1D shear wave velocity profiles. However, this approach assumes that analyzing multiple 1D velocity profiles appropriately captures the effects of the true two-dimensional (2D) and three-dimensional (3D) spatial variability of the soil properties. The effect of spatial variability of soil properties can be more realistically accounted for through 2D site response analyses.

Two-dimensional site response analyses require generation of 2D velocity fields. Two dimensional velocity fields are generated for the SCH site through Monte Carlo simulation. This chapter investigates the influence of the statistical parameters, such as the vertical and horizontal correlation distances and variability of shear wave velocity with in the velocity field, used in Monte Carlo simulations to generate the 2D velocity field.

6.2 Baseline Soil Properties

The two dimensional site profiles are generated based on the characterization of the Sylmar County Hospital (SCH) site as introduced in Chapter 3. The shear wave velocity for the 2D analyses is shown in Figure 6.1. The site consists of 100 m of alluvium above bedrock, with the V_s ranging from about 250 m/s at the surface and increasing to above 700 m/s at 60 m (Figure 6.1). The nonlinear modulus reduction and damping curves are assigned to the four main velocity layers based on the empirical model of Darendeli (2001). The velocity of the bedrock is taken as 760 m/s and the damping ratio of the bedrock is assumed to be 1%. The small strain

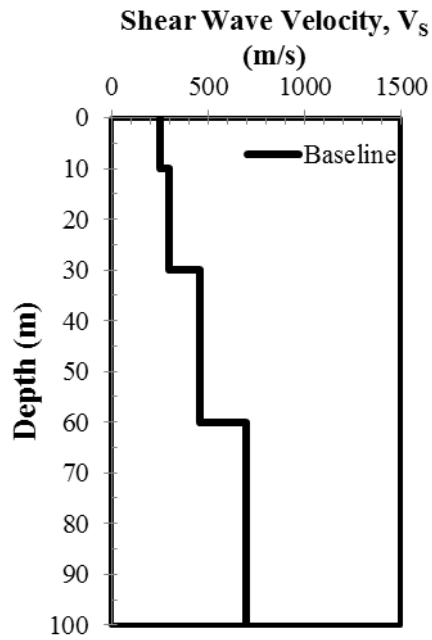


Figure 6.1 Baseline shear-wave velocity profile

natural period of the site is about 0.8 s. The shear wave velocity profile in Figure 6.1 is used as the baseline profile to generate the 2D realizations of the velocity fields.

The region of interest over which the 2D ground surface response is investigated is assumed to be 100 m wide. Therefore, the dynamic response of the region of interest is 100 m x 100 m. The geometry of the 2D finite element mesh is illustrated in Figure 6.2. The area shown by the red square is the 100-m wide region of interest (ROI) and the 2D mesh extends a significant distance outside the ROI to minimize the possible effects of the boundary conditions, as discussed in Chapter 7.

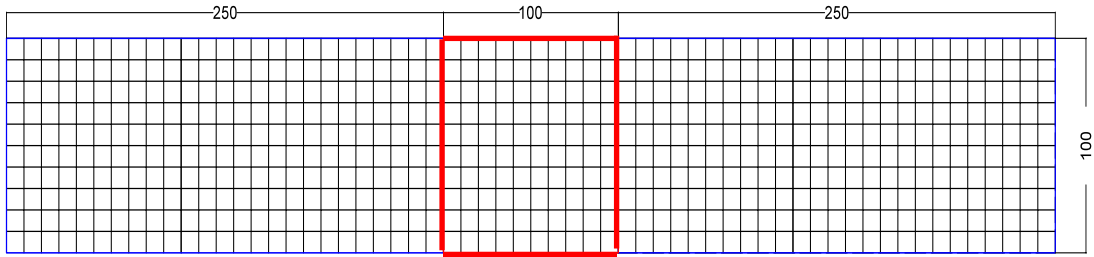


Figure 6.2 2D finite element mesh used for 2D site response analyses (all dimensions are in m). Region of interest (ROI) is shown in red.

The mesh is formed by 10 m by 10 m 4-node elements. Even though the generated mesh is somewhat coarse, the size of the elements is sufficient to capture frequencies up to about 10 Hz for the lowest velocity layers.

6.3 Generation of 2D Shear Wave Velocity Fields

Monte Carlo simulations are used to generate 2D realizations of velocity fields for the 2D site response analyses. The shear wave velocity distribution across the ROI is influenced by the horizontal and vertical correlation distances. A 2D realization of the velocity field is generated by developing a covariance matrix that

represents the strength of correlation between velocities at different locations. This covariance matrix is defined as (Vanmarcke 1983):

$$COV(i,j) = \sigma_{lnV_s}^2 \cdot \left[\exp\left(\frac{-2|x_i - x_j|}{\theta_x}\right) \right] \cdot \left[\exp\left(\frac{-2|z_i - z_j|}{\theta_z}\right) \right] \quad (6.1)$$

in which i and j represent the shear wave velocities in elements i and j , located respectively at locations (x_i, z_i) and (x_j, z_j) . In Equation 6.1, σ_{lnV_s} is the standard deviation of the natural logarithm of V_s , while θ_x and θ_z are the horizontal and vertical correlation distances, respectively. The σ_{lnV_s} is used because shear wave velocities have been shown to be log-normally distributed (Toro 1995). The exponential terms in Equation 6.1 represent the correlation coefficient between shear wave velocities at different locations. The correlation coefficient varies from 1.0 when considering the shear wave velocities of adjacent locations (i.e, $x_i \sim x_j, z_i \sim z_j$) and tends towards zero as the distance between two locations exceed the correlation distances. Figure 6.3 presents the variation of the correlation coefficient with distance for one-dimensional correlation (i.e., one of the exponential terms in Equation 6.1) for different values of θ . The correlation coefficient is equal to 1.0 at short distances and becomes zero as the distance between two locations approaches about twice the correlation distance.

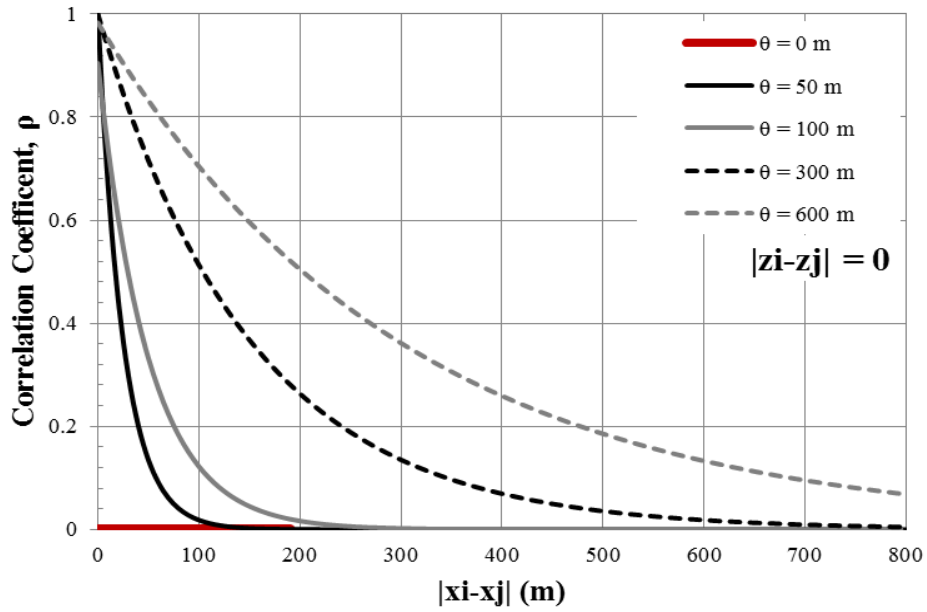


Figure 6.3 Variation of correlation coefficient with the relative distance between two locations for different correlation distances.

The covariance matrix (*COV*) along with a baseline shear wave velocity profile and a vector of independent random variables generated from a standard normal distribution (Vs') are used to generate the 2D velocity field of Vs using the linear transformation (Vanmarcke, 1983).

$$Vs = A \cdot Vs' + M \quad (6.2)$$

Because the shear wave velocity profile is assumed to have a lognormal distribution (Toro, 1995), M is the vector of the natural logarithm of the baseline shear wave velocity profile, so that it can be represented by a normal distribution. Vs' is a matrix of independent variables with zero mean and unit standard deviation. The matrix A transforms the random values in Vs' to have the appropriate standard deviation and covariance, while the vector M scales the values to obtain the appropriate mean. The matrix A is computed from the desired covariance matrix (COV) using:

$$COV = AC_{Vs'}A^T \quad (6.3)$$

where $C_{Vs'}$ is the covariance matrix of Vs' , a vector of random variables with zero mean and unit standard deviation, and thus $C_{Vs'}$ is the identity matrix.

6.4 Characteristics of Two-Dimensional Shear Wave Velocity Fields

The shear wave velocity distribution within the ROI is controlled by the horizontal and vertical correlation distances and the standard deviation of the $\ln V_S$. The influence of each of these statistical parameters on the generated 2D velocity fields is investigated. The influence of these parameters is explored in terms of the V_S variability within a single 2D velocity field realization and across multiple 2D velocity field realizations.

6.4.1 VARIABILITY WITHIN A SINGLE 2D VELOCITY FIELD REALIZATION

The shear wave velocity distribution across the ROI is influenced by the horizontal and vertical correlation distances. As the correlation distance approaches zero the shear wave velocity field becomes more random (i.e., uncorrelated), while larger correlation distances result in more correlated velocities within the ROI. Figure 6.4 shows the 2D velocity field for the baseline profile (i.e., perfect horizontal and vertical correlation) which is equivalent to the model used in 1D site response

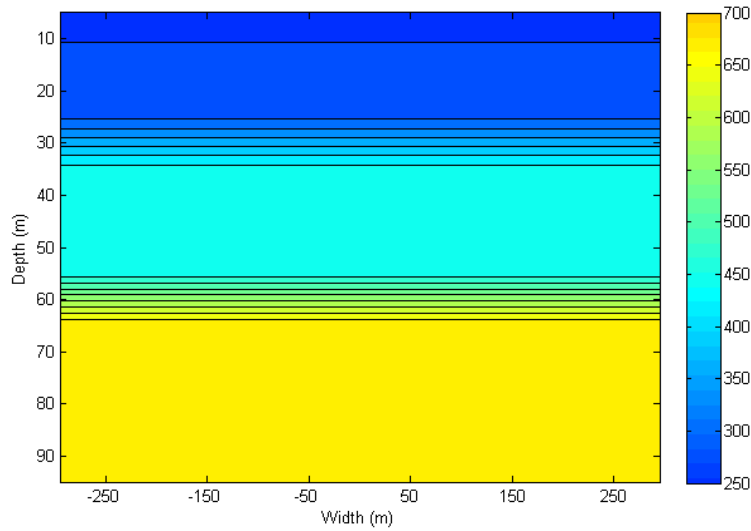


Figure 6.4 Two dimensional representation of baseline V_S profile.

analysis where the given baseline V_S profile extends infinitely in the horizontal direction.

In nature, the shear wave velocity field has spatial variability in both the vertical and horizontal directions. This spatial variability can be modeled through the statistical parameters used in the Monte Carlo simulations of the velocity field. Figure 6.5 shows generated 2D velocity fields for $\sigma_{\ln V_S}$ equal 0.2, a vertical correlation distance (θ_z) of 80 m, and horizontal correlation distances (θ_x) of 0 m, 100 m and 600 m, respectively. The horizontal variability in the velocity fields generated with $\theta_x = 0$ m (Figure 6.5a) is significantly greater than the horizontal

variability in the velocity fields generated with larger horizontal correlation distances of 100 m (Figure 6.5b) and 600 m (Figure 6.6c). As Figure 6.5 illustrates, the generated velocity field has a more uniform horizontal distribution with increasing horizontal correlation distance. Figure 6.6 presents 2D velocity fields for a horizontal correlation distance of 600 m and vertical correlation distances of 0 m, 80 m, and 600 m. The variability observed between the vertical elements of the generated 2D velocity field increases as the vertical correlation distance decreases. The velocity field with horizontal and vertical correlation distances of 600 m (Figure 6.7b) has a most uniform distribution and starts to approach a 1D approximation.

To better illustrate the impact of the horizontal and vertical correlation distances on the generated velocity fields, Figure 6.7 presents 2D velocity fields generated using four “end-member” combinations of horizontal and vertical correlation distances: (a) $\theta_x = 0$ m and $\theta_z = 0$ m, (b) $\theta_x = 0$ m and $\theta_z = 600$ m, (c) $\theta_x = 600$ m and $\theta_z = 0$ m, and (d) $\theta_x = 600$ m and $\theta_z = 600$ m. Comparing Figures 6.7a and 6.7b, the increase in θ_z from 0 m to 600 m when θ_x is equal to 0 m results in more correlation vertically but significant variability is still present horizontally. Comparing Figures 6.7c and 6.7d, the increase in θ_z from 0 m to 600 m has a bigger effect when θ_x is equal to 600 m and results in a significantly more coherent velocity field.

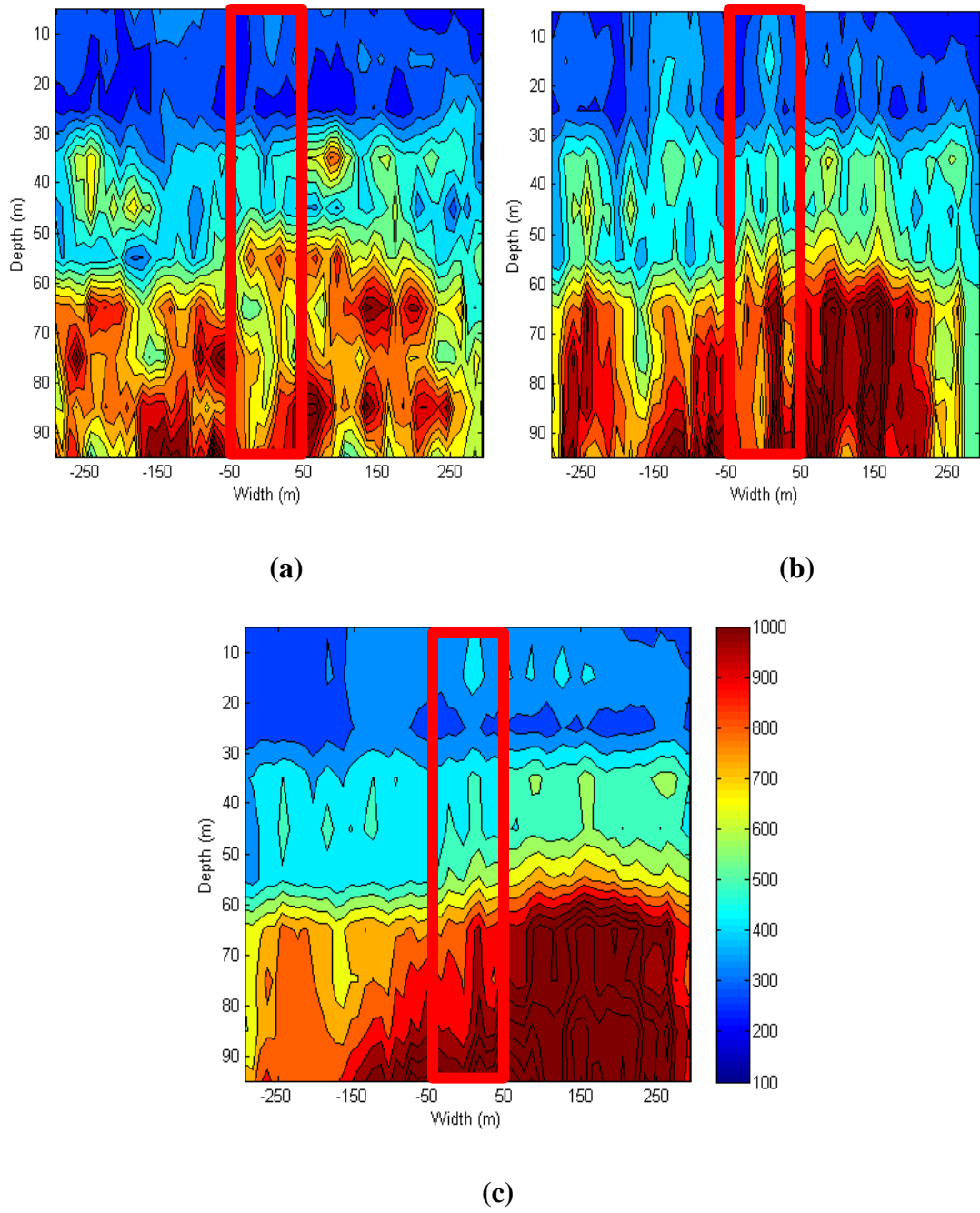


Figure 6.5 Single 2D V_s field realization generated with $\theta_z = 80$ m and θ_x of: (a) 0 m, (b) 100 m, and (c) 600 m

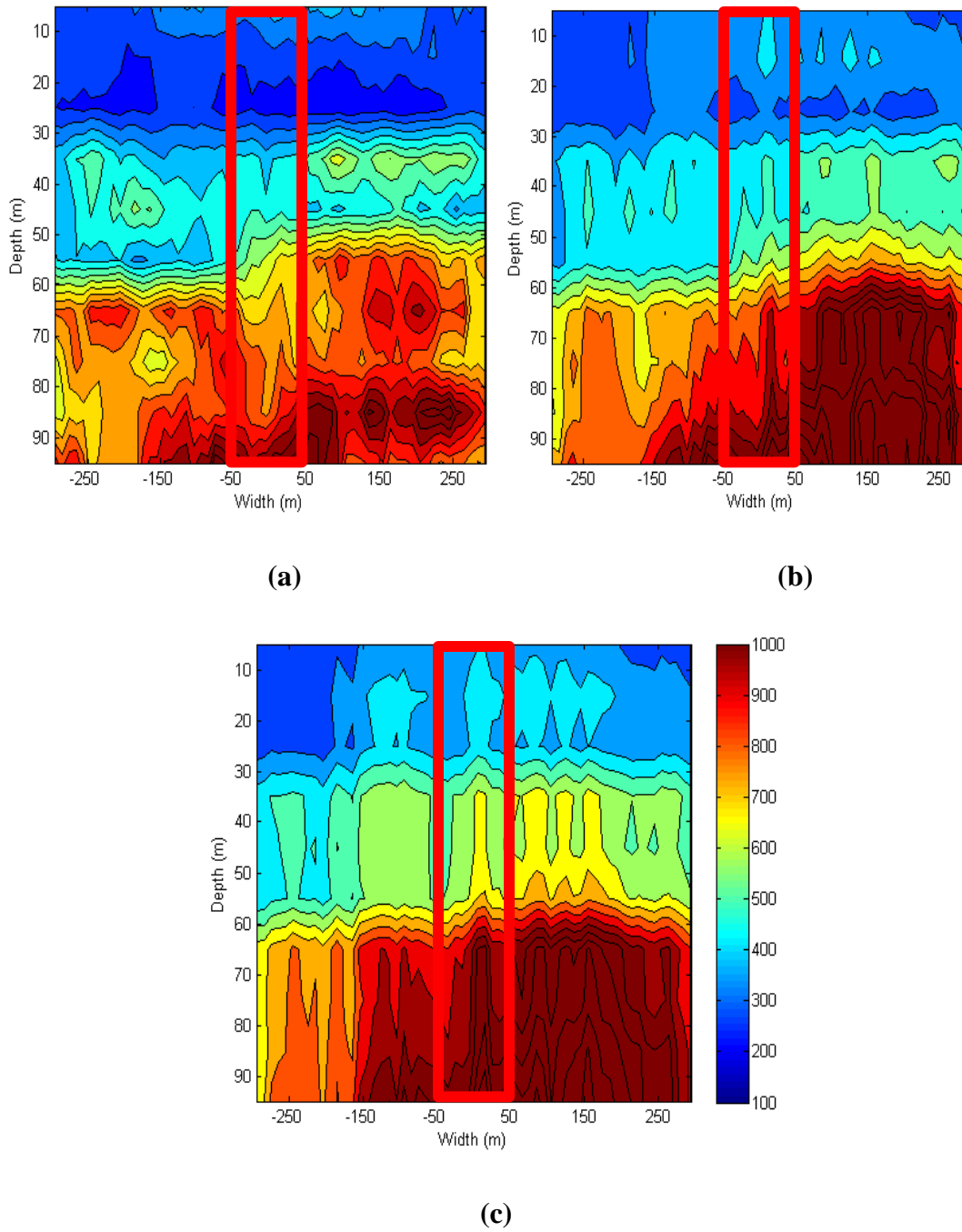
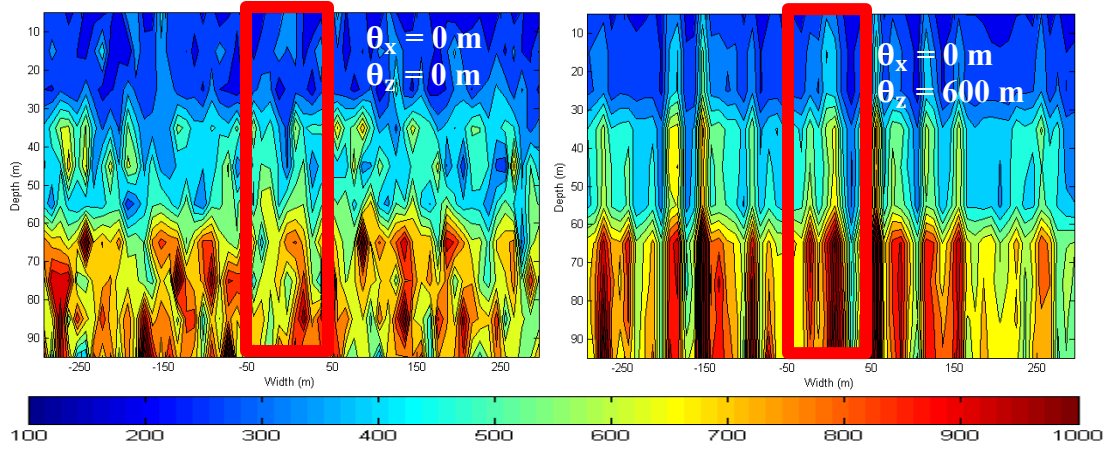
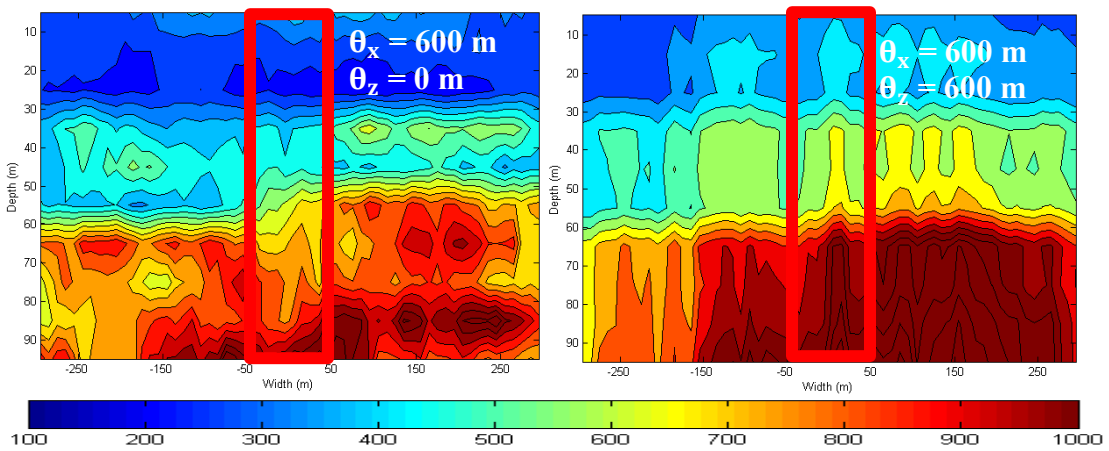


Figure 6.6 Single 2D V_S field realization generated with $\theta_x = 600$ m and θ_z of: (a) 0 m, (b) 80 m and (c) 600 m



(a)

(b)



(c)

(d)

Figure 6.7 Single 2D V_S field realization generated for end-member correlation distances: (a) $\theta_x = 0$ m & $\theta_z = 0$ m, (b) $\theta_x = 0$ m & $\theta_z = 600$ m, (c) $\theta_x = 600$ m & $\theta_z = 0$ m, and (d) $\theta_x = 600$ m & $\theta_z = 600$ m

The effect of correlation distances on the shear wave velocity variability across the ROI can be further illustrated through the individual shear wave velocity profiles across the ROI. Figures 6.8 shows influence of horizontal correlation distance on the V_S profiles of the 10 columns of elements across the ROI for single 2D realizations generated with σ_{lnV_S} of 0.2, θ_z of 80 m, and θ_x of 0 m (Figure 6.8a), 100 m (Figure 6.8b), and 600 m (Figure 6.8c). As θ_x increases, the velocities tend to assemble on one side of the baseline profile and show less variation across the ROI, such that the median velocity profile across the ROI deviates from the baseline profile. Figures 6.9 presents the influence of vertical correlation distance on the V_S profiles of the 10 columns of elements across the ROI for single 2D realizations generated with σ_{lnV_S} of 0.2, θ_x of 600 m, and θ_z of 0 m (Figure 6.9a), 80 m (Figure 6.9b), and 600 m (Figure 6.9c). As θ_z increases, the difference between the velocities of the adjacent vertical elements shows less variation and the median velocity profile across the ROI tends to deviate further from the baseline profile.

Figure 6.10 compares the V_S profiles across the ROI for a single 2D realization generated with σ_{lnV_S} of 0.2 and the “end-member” correlation distances of $\theta_x = 0$ m and $\theta_z = 0$ m (Figure 6.10a), $\theta_x = 0$ m and $\theta_z = 600$ m (Figure 6.10b), $\theta_x = 600$ m and $\theta_z = 0$ m (Figure 6.10c), and $\theta_x = 600$ m and $\theta_z = 600$ m (Figure 6.10d). The V_S profiles obtained with no horizontal correlation (Figures 6.10a and 6.10b), have median V_S profiles across the ROI that are very similar to the baseline profile. When the horizontal correlation distance is increased to 600 m (Figure 6.10c and

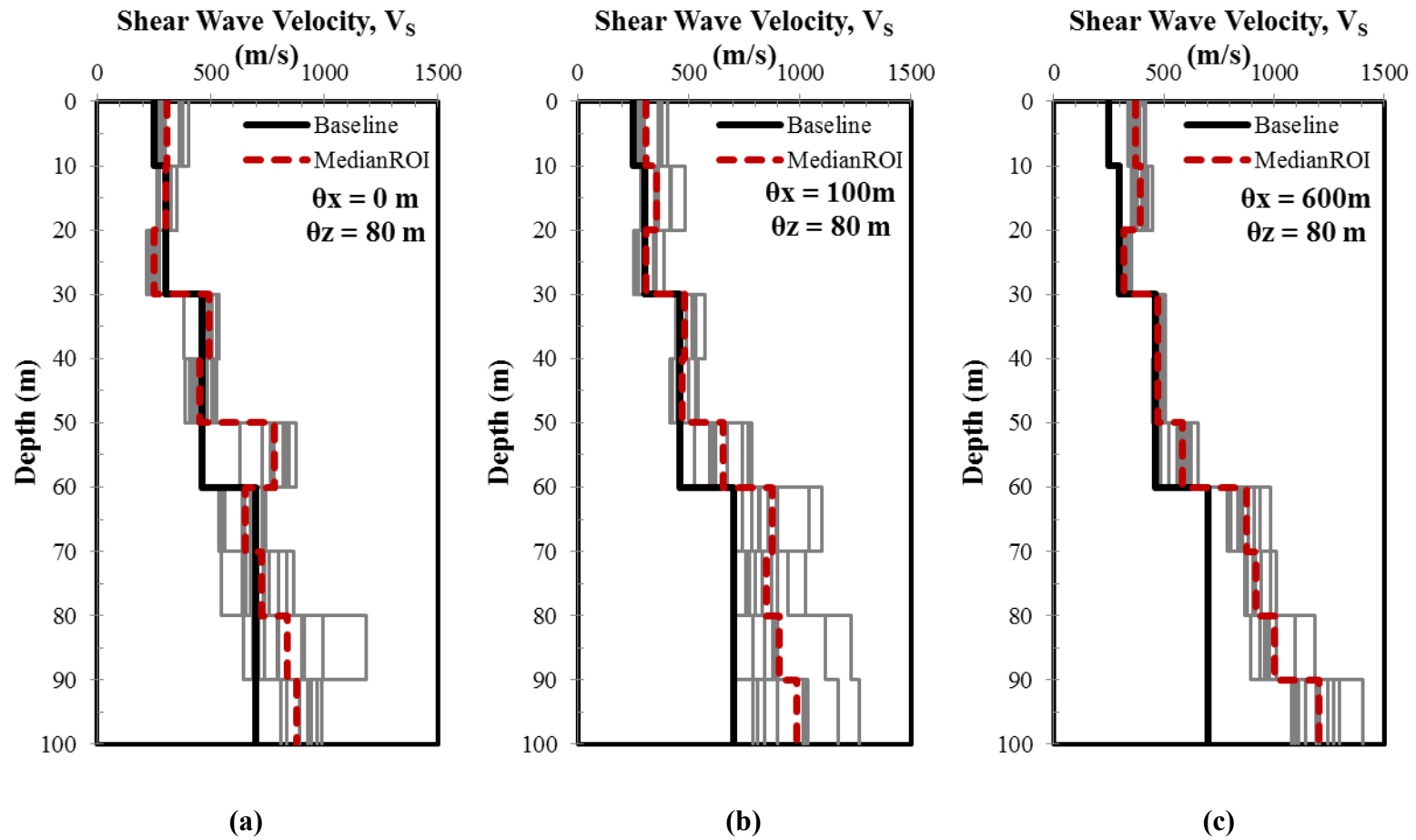


Figure 6.8 V_s profiles across the ROI for a single 2D random field realization generated with σ_{lnV_s} of 0.2, θ_z of 80 m, and θ_x of (a) 0 m, (b) 100 m, and (c) 600 m, respectively

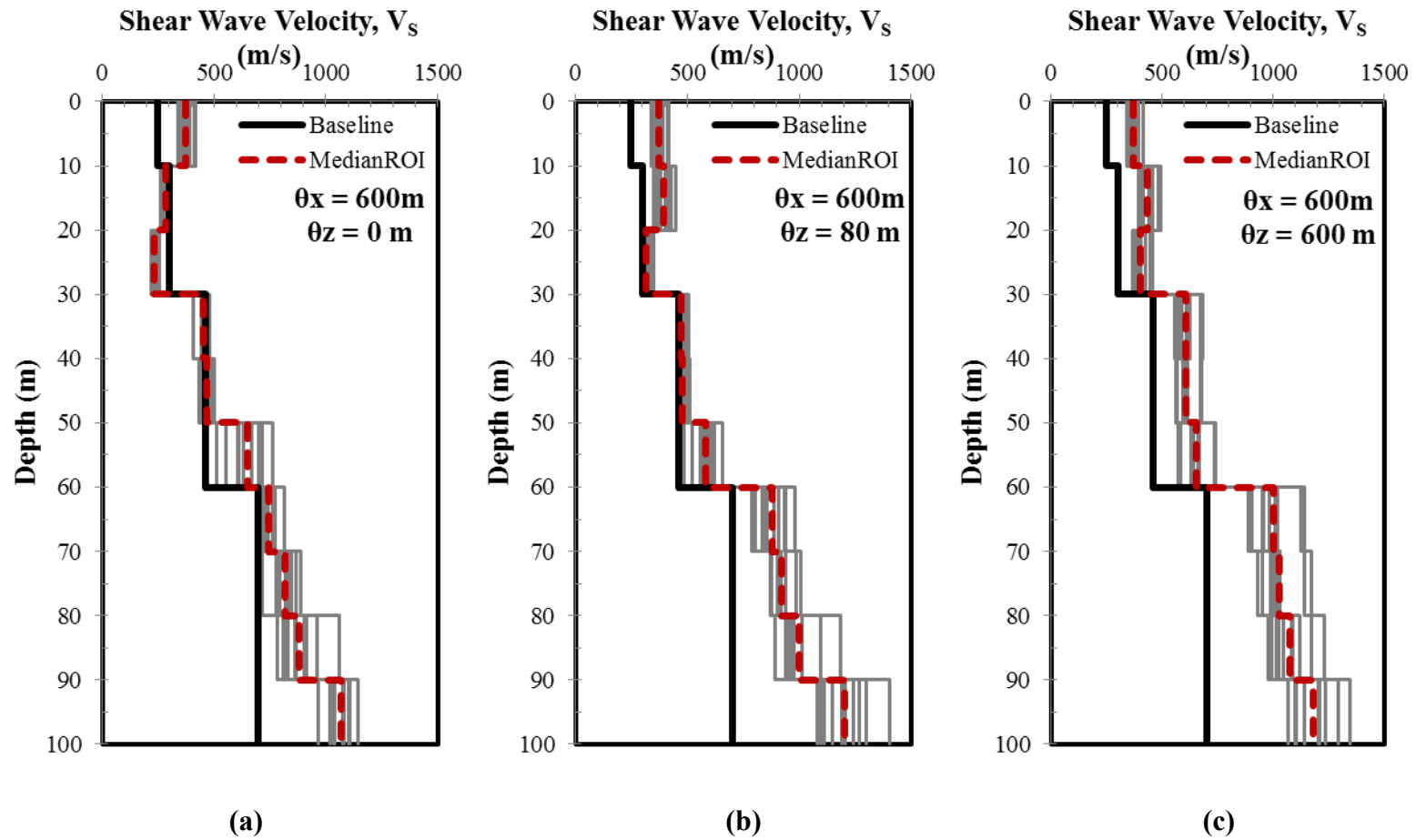


Figure 6.9 V_s profiles across the ROI for a single 2D random field realization generated with σ_{lnV_s} of 0.2, θ_x of 600 m, and θ_z of (a) 0 m, (b) 80 m, and (c) 600 m, respectively

6.10d), the V_S profiles tend to assemble on one side of the baseline profile because horizontally adjacent velocities are more correlated. Therefore, the median V_S profile across the ROI deviates from the baseline V_S profile as horizontal correlation distance increases. The difference between the median and baseline V_S profiles becomes more pronounced as the vertical correlation distance increases due to less variability within each vertical V_S profile. The influence of vertical correlation distance is more significant when the horizontal correlation is large. Accordingly, the largest deviation of the median V_S profile from the baseline V_S profile is obtained for the profiles generated with large vertical and horizontal correlation distances.

The effect of different levels of σ_{lnV_S} is investigated by generating 2D velocity fields with σ_{lnV_S} of 0.1 (Figure 6.11a), 0.2 (Figure 6.11b) and 0.3 (Figure 6.11c) for horizontal and vertical correlation distances of 100 m and 80 m, respectively. The variation in the V_S profiles within the ROI increases significantly with increasing σ_{lnV_S} , with the variation being largest for the analysis with $\sigma_{lnV_S}=0.3$. Accordingly, the median V_S profile deviates more from the baseline V_S profile as σ_{lnV_S} increases.

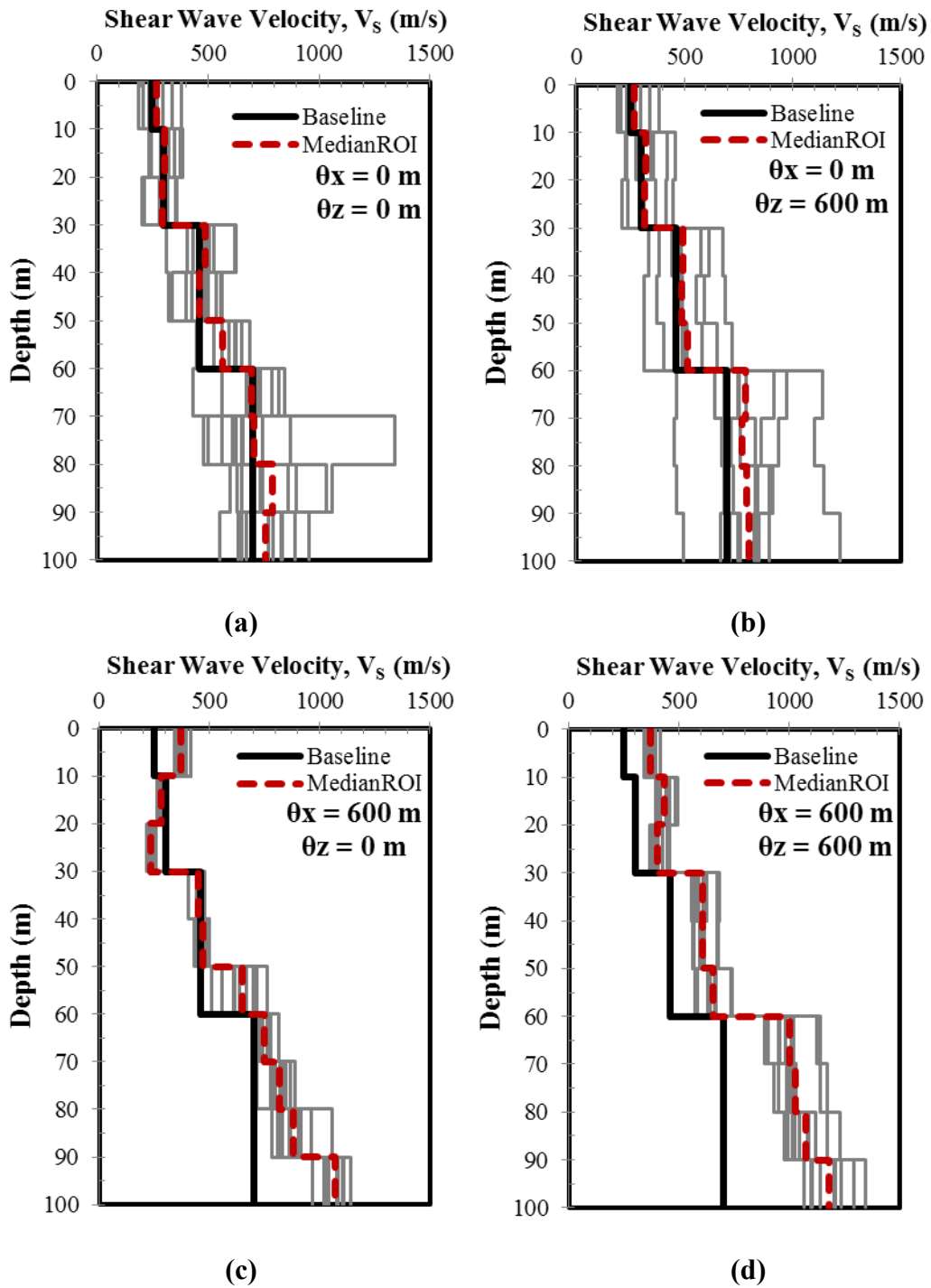


Figure 6.10 V_s profiles across the ROI a single 2D random field realization generated with $\sigma_{\ln V_s}$ of 0.2 and end-member correlation distances

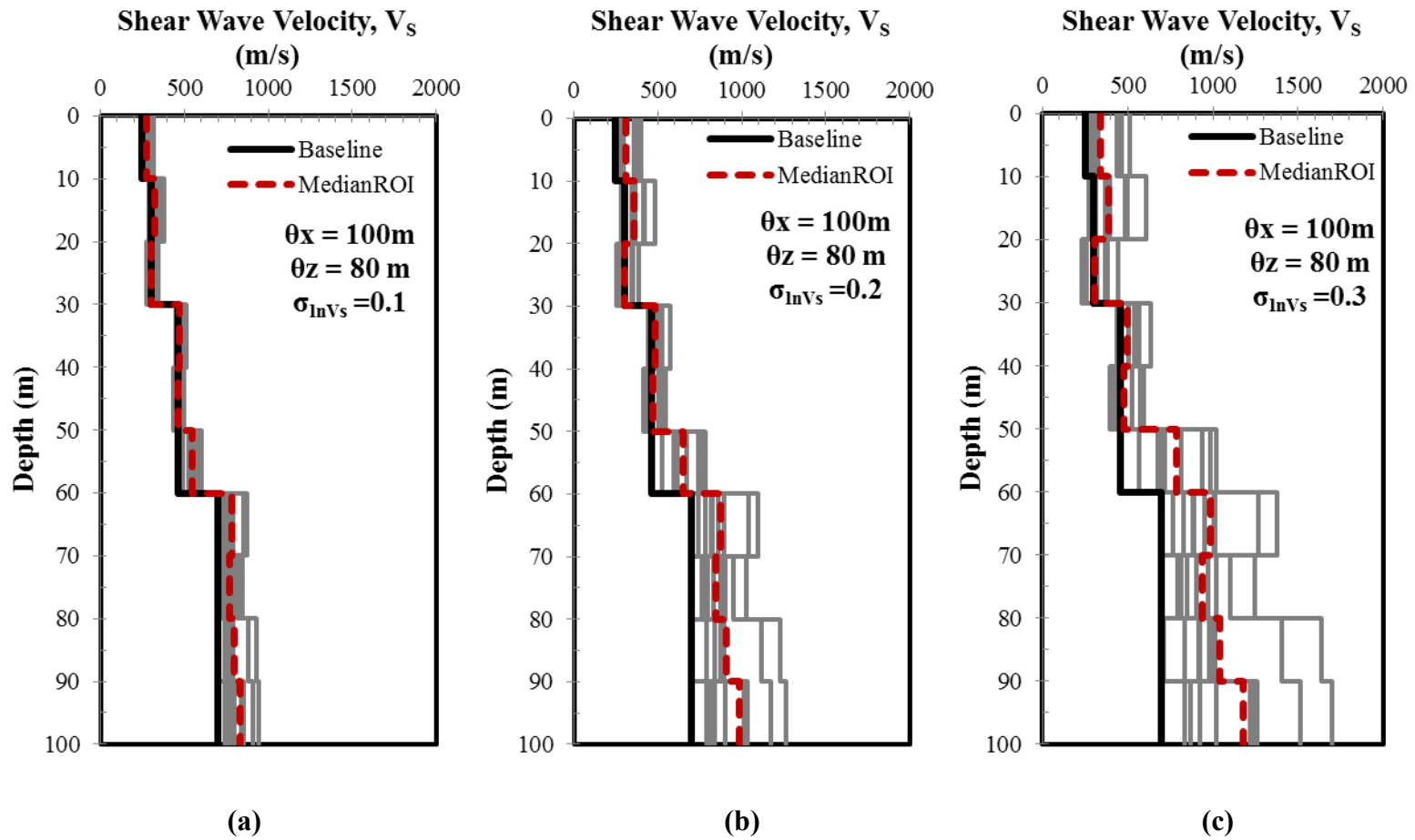


Figure 6.11 V_s profiles across the ROI for a single 2D random field realization generated with θ_x of 100 m, θ_z of 80 m, and $\sigma_{\ln V_s}$ of (a) 0.1, (b) 0.2, and (c) 0.3, respectively

6.4.2 VARIABILITY ACROSS MULTIPLE 2D VELOCITY FIELD REALIZATIONS

The influence of the statistical parameters used in Monte Carlo simulations on the generated velocity field has been investigated within a single realization. For the 2D site response analyses twenty 2D velocity field realizations will be generated in order to get an accurate median estimate of site response across the ROI. Figure 6.12 presents a sample of twenty 2D velocity fields generated using σ_{lnV_S} of 0.2 and horizontal and vertical correlation distances of 100 m and 80 m, respectively. The region of interest (ROI) is illustrated with a red rectangle for each realization. The level of spatial variability introduced into the analysis over twenty velocity field realizations can be further visualized by comparing the median V_S profiles across the ROI for each of the twenty V_S field realizations.

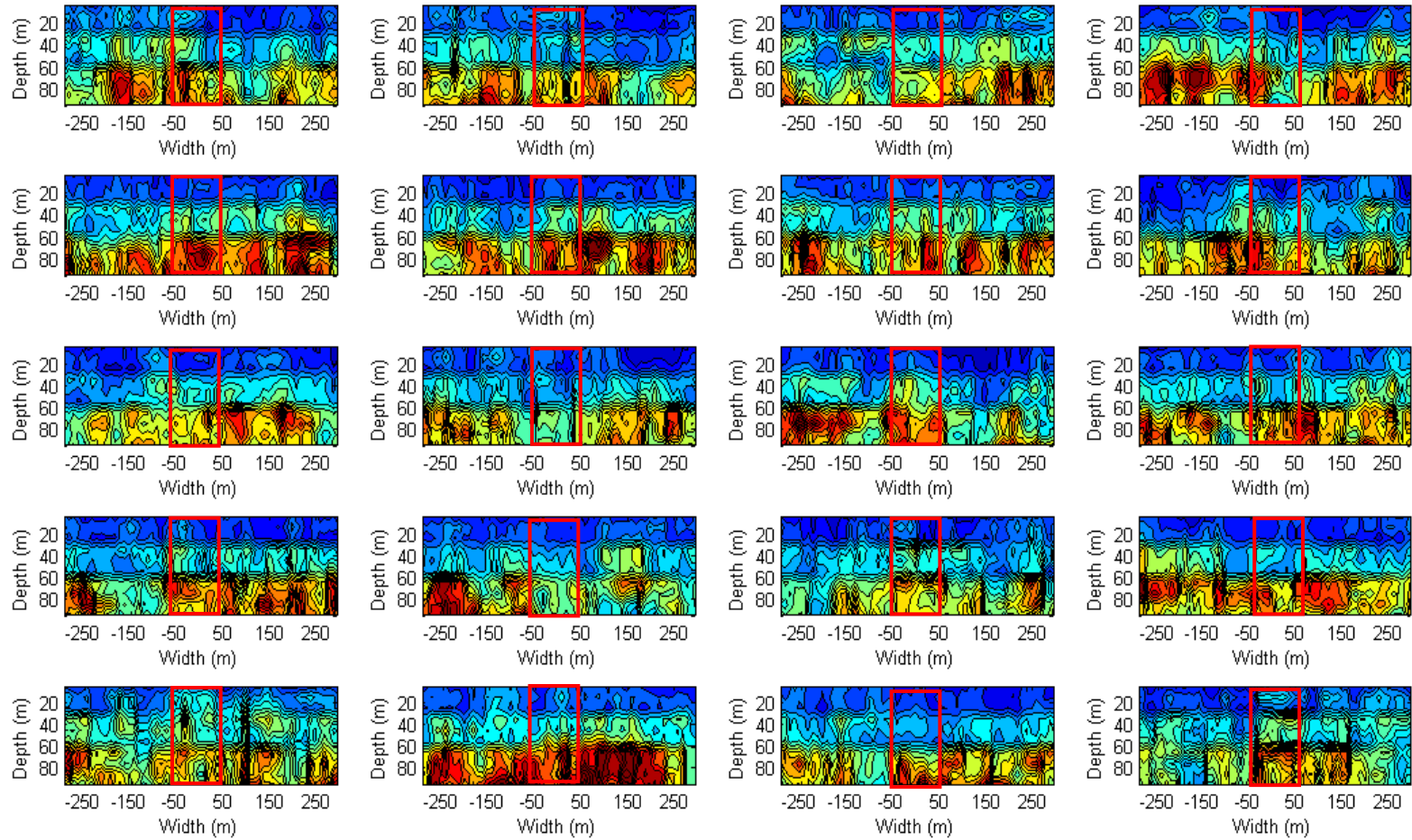


Figure 6.12 Colormap plots of the generated 20 velocity fields with $\theta_x = 100$ m, $\theta_z = 80$ m

Figure 6.13 show the median V_S profile across the ROI for each of the 20 realizations, as well as median V_S profile over all 20 realizations generated, with σ_{lnV_S} of 0.2, θ_z of 80 m, and θ_x of 0 m (Figure 6.13a), 100 m (Figure 6.13b), and 600 m (Figure 6.13c). Over all 20 realizations, the median velocity profile across the ROI is similar to the baseline profile for different θ_x although the variation around the baseline profile increases as θ_x increases. Figure 6.14 presents the median V_S profile across the ROI for each of the 20 realizations, as well as median V_S profile over all 20 realizations, generated with σ_{lnV_S} of 0.2, θ_x of 600 m, and θ_z of 0 m (Figure 6.14a), 80 m (Figure 6.14b), and 600 m (Figure 6.14c). Over all 20 realizations the variation around the baseline profile increases as θ_z increases.

A comparison of median V_S profiles across twenty realizations generated for the “end-member” correlation distances of 0 m and 600 m is shown in Figure 6.15. These profiles show that the median velocity profile across all twenty realizations is again very similar to the baseline profile. However, the median V_S profile for each realization deviates more from the baseline V_S profile as the θ_x increases, and this deviation is slightly more significant when the vertical correlation is small.

Figure 6.16 illustrates the comparison of median V_S profiles across 20 realizations for profiles generated with θ_x of 100 m and θ_z of 80 m and for σ_{lnV_S} of 0.1, 0.2 and 0.3. As σ_{lnV_S} increases the variability across the realizations increases. The median and baseline V_S profiles are similar for all levels of σ_{lnV_S} .

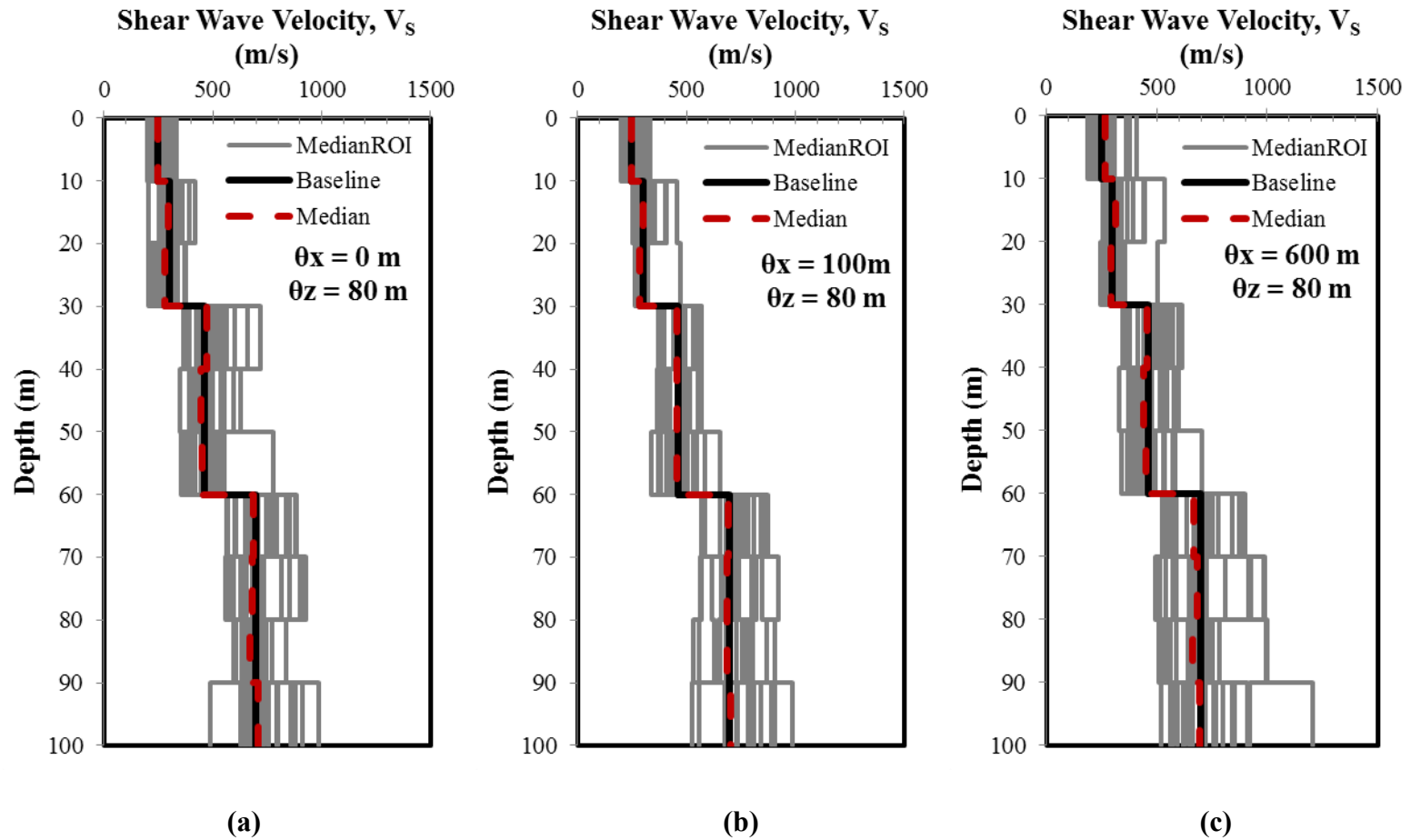


Figure 6.13 Median V_S profiles across the ROI of 20 2D V_S field realizations generated with σ_{lnV_S} of 0.2, θ_z of 80 m, and θ_x of (a) 0 m, (b) 100 m, and (c) 600 m, respectively

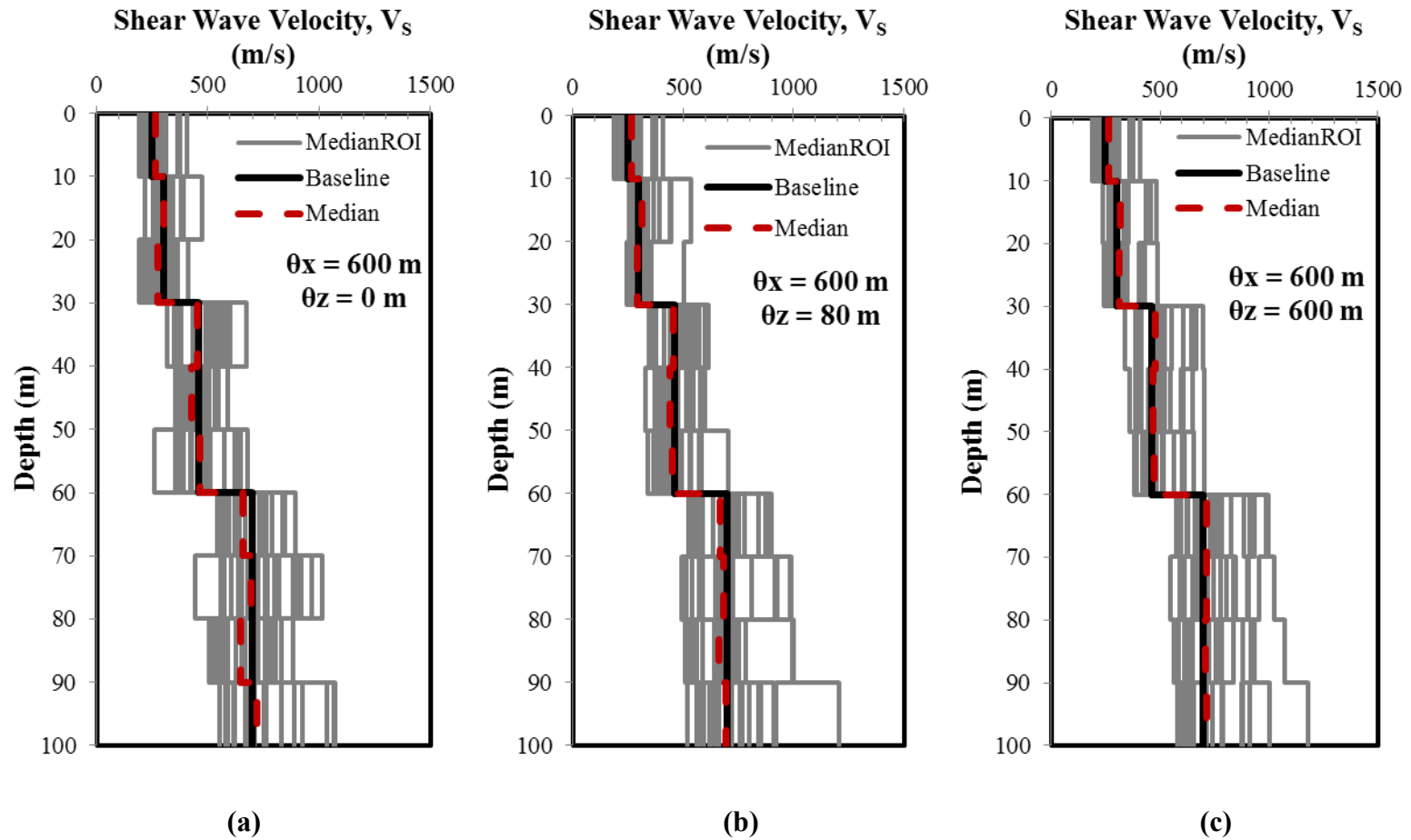


Figure 6.14 Median V_s profiles across the ROI of 20 2D V_s field realizations generated with $\sigma_{\ln V_s}$ of 0.2, θ_x of 600 m, and θ_z of (a) 0 m, (b) 80 m, and (c) 600 m, respectively

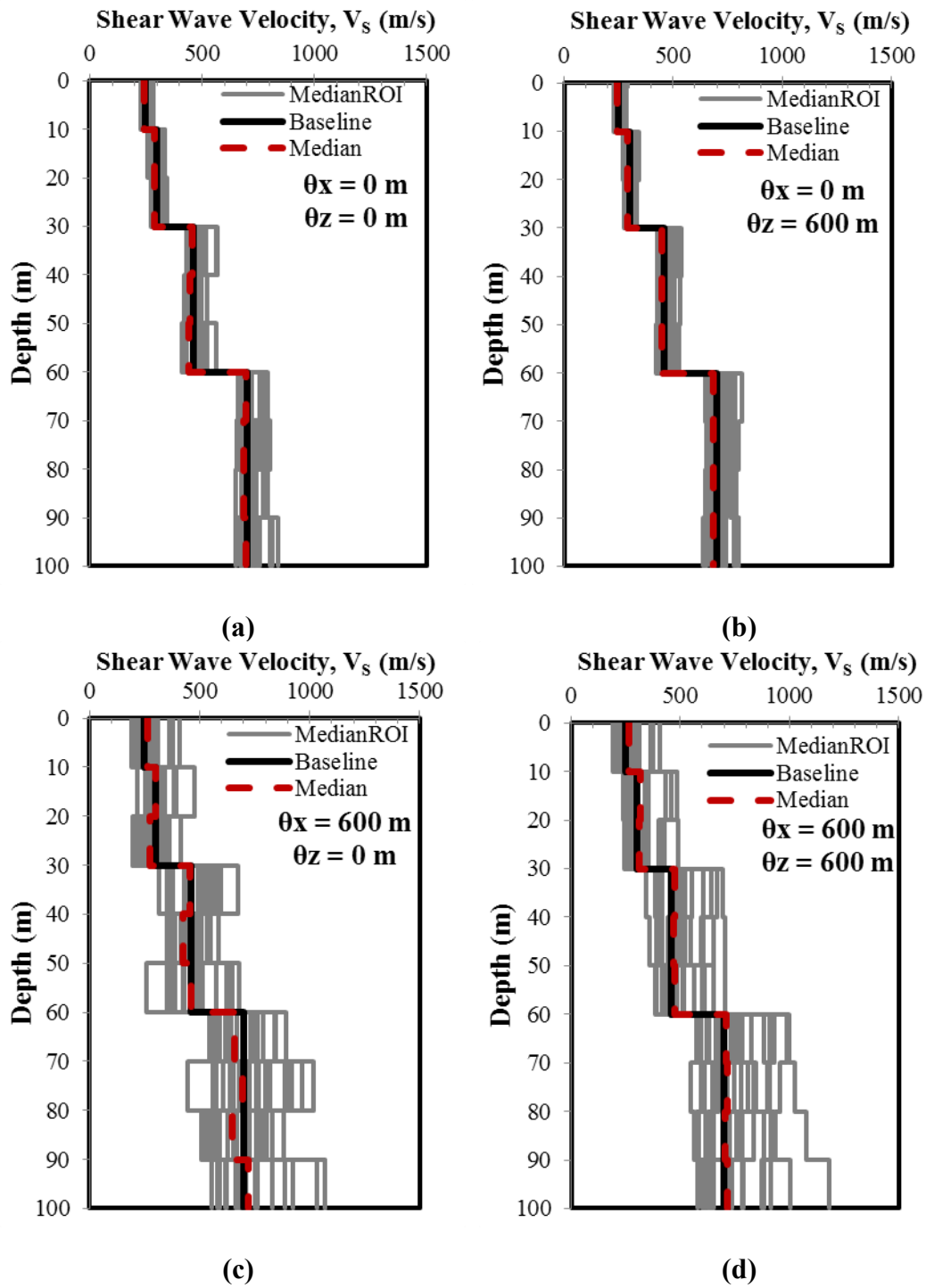


Figure 6.15 Median V_s profiles across the ROI of 20 2D random field realization generated with $\sigma_{\ln V_s}$ of 0.2 and boundary value correlation distances

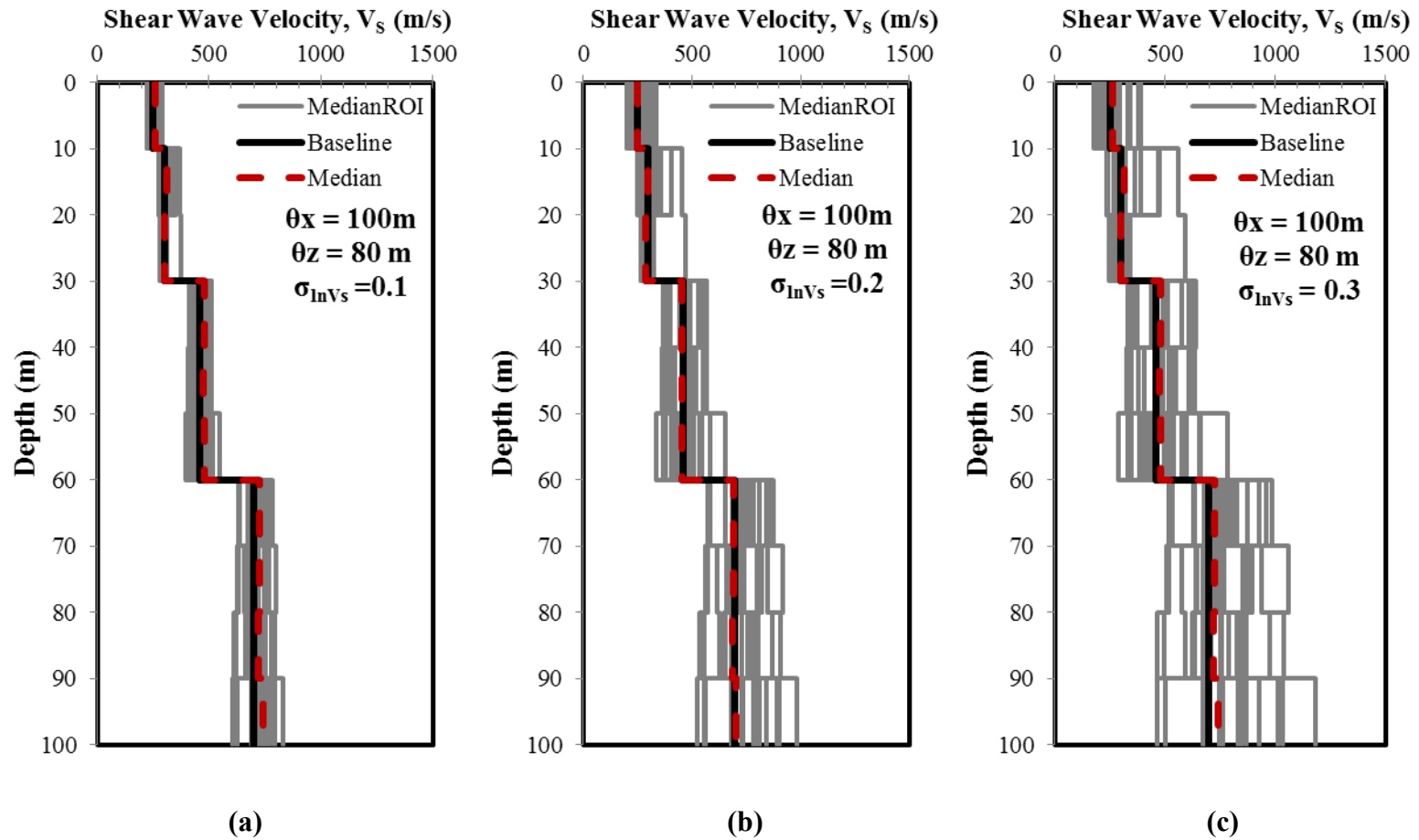


Figure 6.16 Median V_s profiles across the ROI of 20 2D random field realization generated with θ_x of 100 m, θ_z of 80 m, and $\sigma_{\ln V_s}$ of (a) 0.1, (b) 0.2, and (c) 0.3, respectively

6.5 Summary

This chapter describes the generation of 2D shear wave velocity fields for a 100-m deep site within a 100-m wide region of interest using Monte Carlo simulation. The boundaries are placed 250 m away from the 100 m x 100 m ROI to minimize the boundary conditions. The Monte Carlo simulation technique is used to generate a 2D velocity field using horizontal and vertical correlation distances and standard deviation of $\ln V_S$. The influence of different statistical parameters on the generated 2D velocity fields is investigated. For a single realization, increasing the horizontal correlation distance results in less V_S variability across the ROI but also causes the V_S to assemble on one side of the baseline profile. Over 20 realizations, increasing the horizontal correlation results in an increase in the variability of the median V_S . The influence of vertical correlation distance is more significant when the horizontal correlation distance is high, such that increasing vertical correlation distance results in a reduction in the variability in median V_S profiles.

SITE AMPLIFICATION PREDICTIONS FOR TWO-DIMENSIONAL VELOCITY FIELDS

7.1 Introduction

This chapter compares site amplification predictions for the 2D velocity fields presented in Chapter 6. The influence of the statistical parameters used to generate the velocity field, such as the vertical and horizontal correlation distances, is investigated. The surface response spectra and amplification factors computed for a 100-m wide segment of the site are compared. The effect of the characteristics of the input motions is observed by using five different input motions with different spectral shapes that induce different levels of nonlinearity in the 2D site response analysis.

7.2 Two-Dimensional Site Response Analysis

Two-dimensional site response analyses are generally solved by dynamic finite-element analysis in the frequency domain or time domain. The finite element method divides the 2D geometry of a site into discrete quadrilateral elements and dynamic material properties (i.e., shear modulus, damping ratio) are assigned to each of these elements. The input motion is specified at the base nodes of the model and the response at each node is computed by solving the dynamic equations of equilibrium. The 2D equivalent-linear (EQL) approach is similar to the 1D EQL approach such that the shear modulus and damping ratio for each element are iteratively modified until they are compatible with the induced shear strains for that element. When performed in the time domain, 2D EQL analysis incorporates Rayleigh damping to model the material damping. In this study, the computer program QUAD4M (Hudson et al., 1994) is used to perform 2D site response analyses. QUAD4M performs the 2D dynamic finite element analyses in the time domain.

As noted in Chapter 6, region of interest (ROI) is 100-m wide and the 2D mesh extends a significant distance outside the ROI to minimize the possible effects of the boundary conditions. Different realizations of 2D random velocity fields are generated for five different boundary distances to estimate the minimum boundary

distance after which the median response and variability across the ROI is stable. For the analyses, the ROI is assumed to be located in the middle of each random velocity field and analyses are performed with the mesh boundaries extending different distances from the edges of the ROI. The computed response spectra along the surface of the ROI for each analysis are used to calculate the median spectral acceleration (Sa) and the standard deviation of $\ln(Sa)$, $\sigma_{\ln Sa_{SOIL}}$, across the surface of the ROI. The computed median Sa and $\sigma_{\ln Sa_{SOIL}}$ for each of the five 2D velocity field realizations are averaged and shown in Figure 7.1 as a function of the boundary distance. The results are shown for peak ground acceleration (PGA) and spectral acceleration at periods of 0.36 s and 0.66 s. These periods represent locations where peaks are observed in the surface acceleration response spectra. Figure 7.1 shows that the computed response and its variability are stable for boundary distances greater than or equal to 250 m (i.e., 2.5 times the ROI). Therefore, in this study the boundaries are placed 250 m away from the edges of the ROI on both sides, resulting in a 600 m x 100 m 2D mesh for the 2D site response analyses.

The two-dimensional site response analyses are performed using five input bedrock motions selected from the PEER Ground Motion Database (http://peer.berkeley.edu/peer_ground_motion_database). The earthquake magnitude-distance and magnitude-PGA distribution of the five selected motions are shown in Figure 7.2, along with the response spectra for each of the motions. The

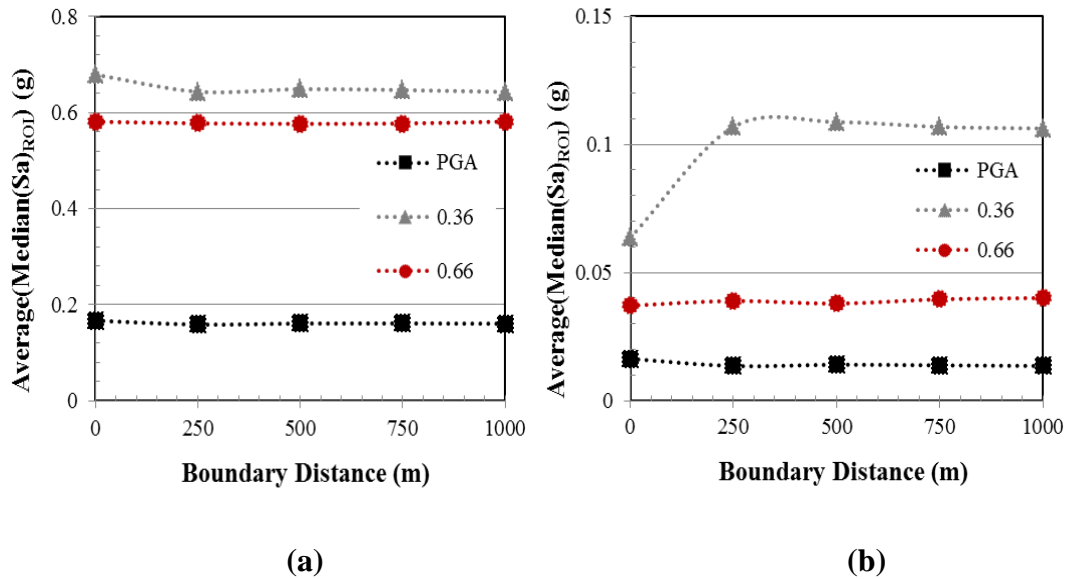


Figure 7.1 Effect of boundary location on (a) surface spectral acceleration, (b) standard deviation of surface acceleration across ROI

earthquake magnitude ranges from 6.7 to 7.5, the distance ranges from 7 km to 38 km, and the recorded peak ground acceleration ranges from 0.14 g to 0.43 g. These motions have different intensities and spectral shapes that will induce different levels of nonlinearity into the 2D site response analysis.

The baseline response obtained for the site subjected to the five motions is plotted in Figure 7.3 in terms of surface response spectra. The surface motions have PGA values ranging between 0.18 g and 0.4 g, spectral peaks occur between 0.2 s and 1.0 s, and the maximum spectral acceleration range from 0.6 to 1.4 g. Figure

7.3b plots the AF obtained for the baseline response, which shows that the peak amplification ranges from 2.1 to 2.5 at periods between 0.6 s and 1.1 s.

The ground surface response varies with location in 2D site response analysis with a variable velocity field. To compare responses between shear wave velocity realizations, motions are calculated along the surface of the ROI at 11 nodes (Figure 7.4a) for each realization and these motions are used to compute various measures of ground shaking and its variability. For each velocity realization, the computed response spectra at the 11 nodes along the surface of the ROI are used to calculate the median spectral acceleration ($\text{Median}(Sa)_{\text{ROI}}$) and the standard deviation of $\ln(Sa)$ across the surface of the ROI ($\sigma(\ln(Sa)_{\text{ROI}})$) at each spectral period (Figure 7.4b).

These parameters measure the average spectral acceleration and the variability in spectral acceleration across the ROI for a single velocity realization. To quantify the average response and variability of the responses across multiple shear wave velocity realizations, the average of the median spectral accelerations across the different realizations ($\text{Average}(\text{Median}(Sa)_{\text{ROI}})$) is computed as well as the standard deviation of the median spectral accelerations in natural log units across the different realizations ($\sigma(\ln(\text{Median}(Sa)_{\text{ROI}}))$) (Figure 7.4c). Finally, structural response can be influenced by the maximum ground motion observed below the structure rather than the average motion. To consider maximum motions, the maximum Sa across the ROI at each period is considered for each velocity realization ($\text{Max}(Sa)_{\text{ROI}}$), Figure

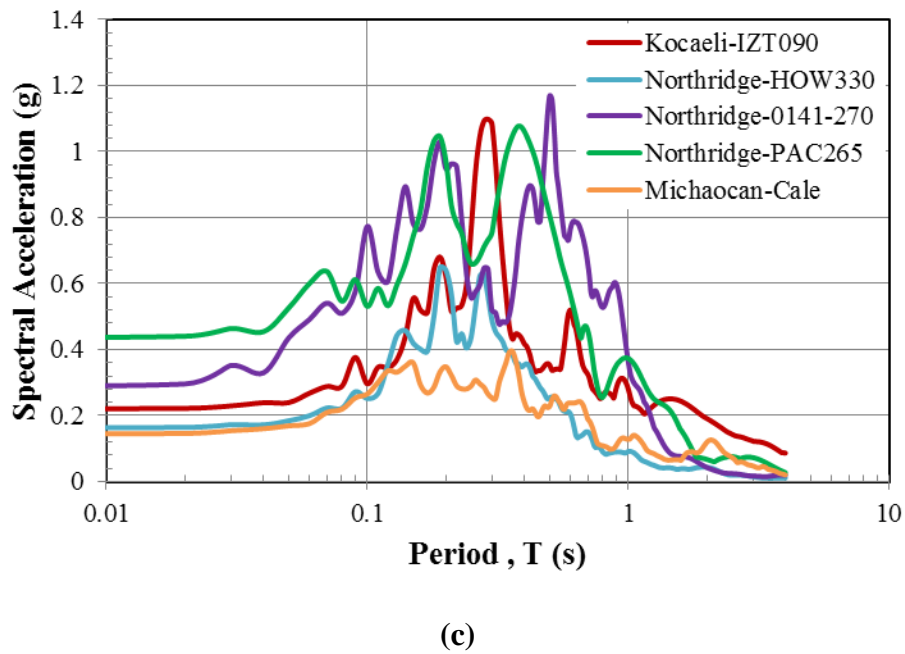
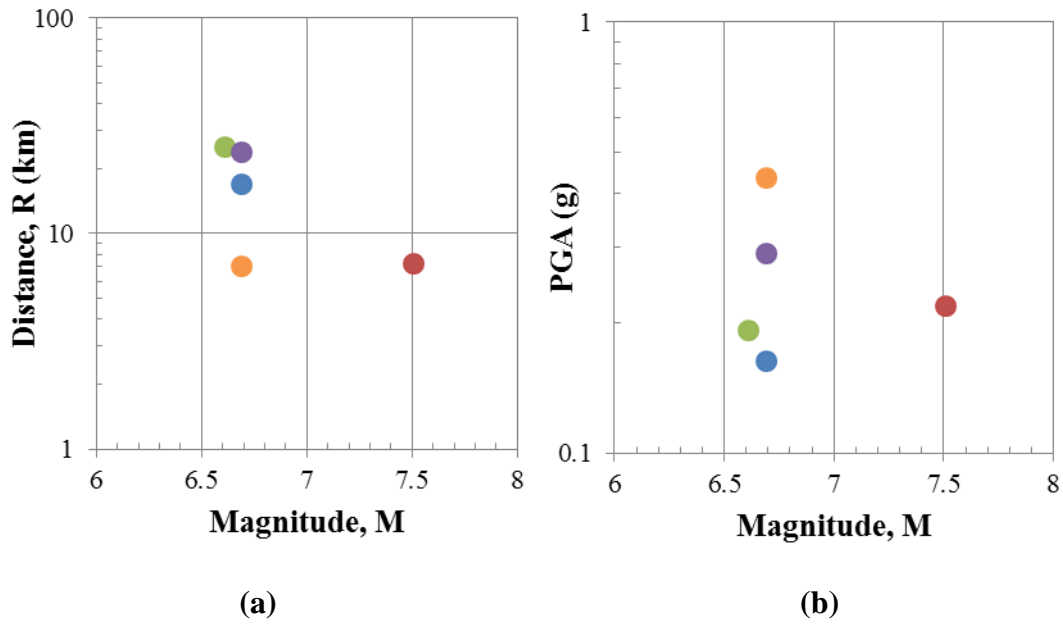
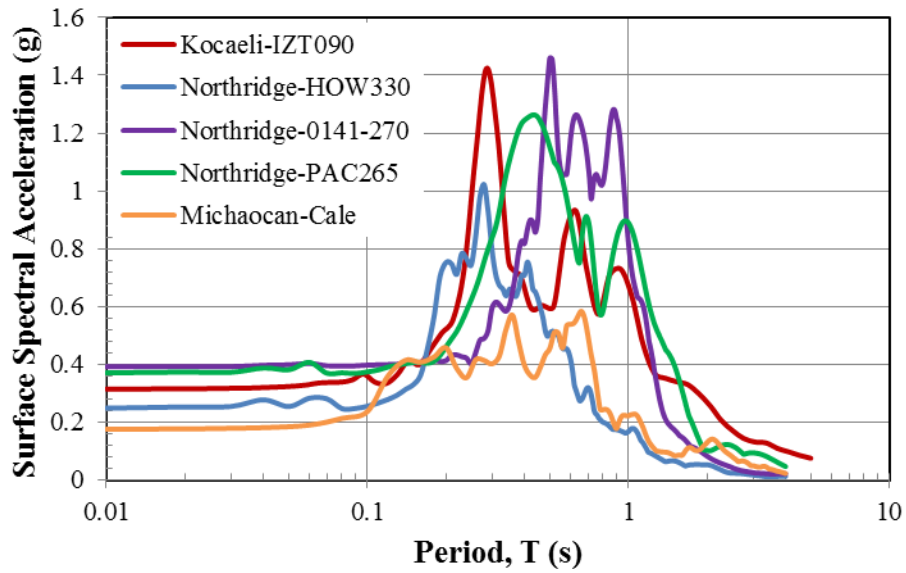
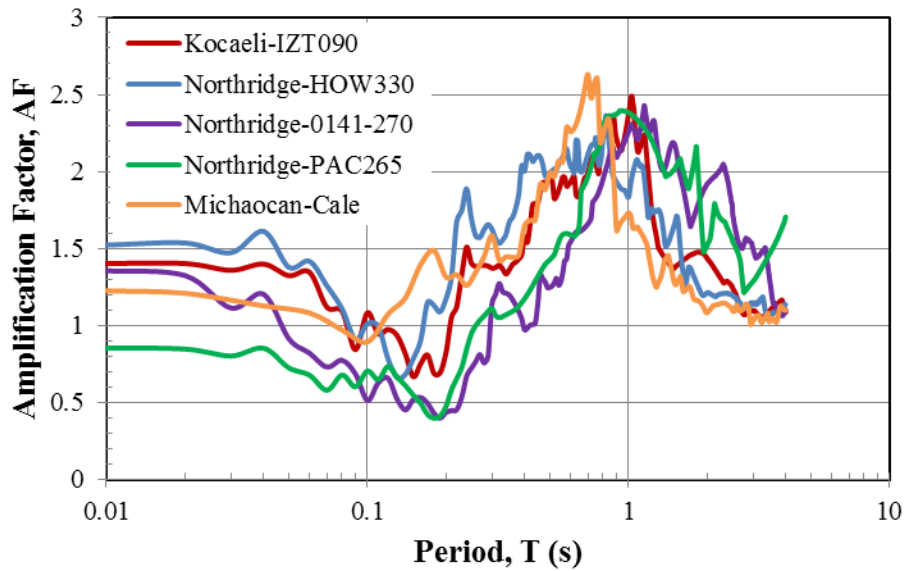


Figure 7.2 Five selected input ground motion for 2D analysis (a) magnitude-distance distribution, (b) magnitude-PGA distribution, and (c) input response spectra.



(a)



(b)

Figure 7.3 Baseline response spectra of five selected input ground motions (a) surface response spectra, (b) amplification factor.

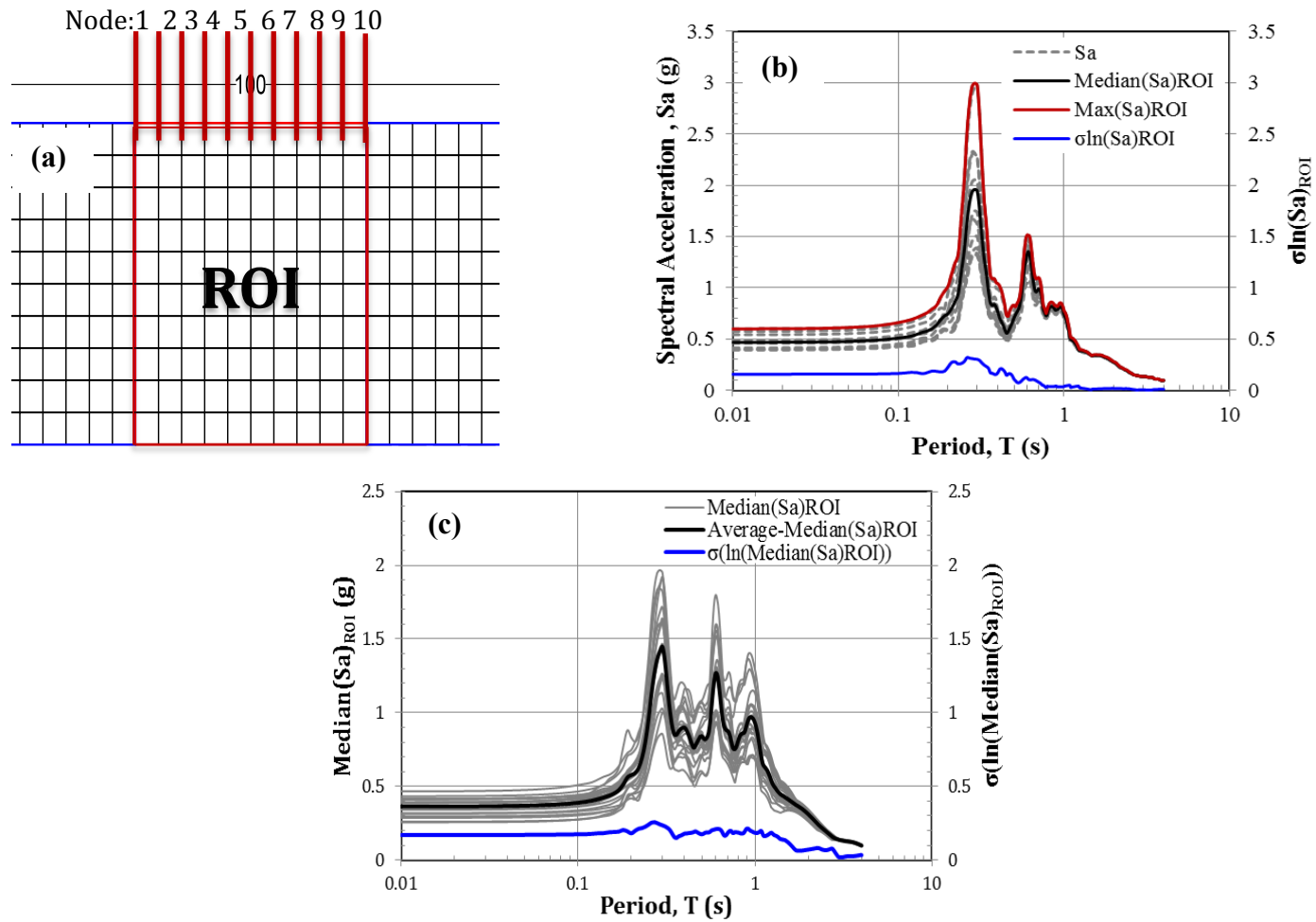


Figure 7.4 Points of comparison: (a) ROI, (b) surface response spectra across ROI for a single V_S realization, and (c) Average response spectra across 20 V_S realizations.

7.4b) and averaged across the different velocity realizations ($Average(\text{Max}(Sa)_{ROI})$). The standard deviation of the ln of the $\text{Max}(Sa)_{ROI}$ ($\sigma(\ln(\text{Max}(Sa)_{ROI}))$) across the different velocity realizations is also computed.

7.3 Influence of Horizontal Correlation on Two-Dimensional Site Response

Site response analyses are performed for 2D velocity fields generated using different horizontal correlation distances. Horizontal correlation distances of 0 m, 100 m and 600 m (i.e., $\theta_x/ROI = 0.0, 1.0, \text{ and } 6.0$) are considered along with a vertical correlation distance of 80 m (i.e., $\theta_z/ROI = 0.8$). The horizontal correlation distances are selected based on the size of ROI, such that the results investigate high correlation and no correlation as well as moderate levels of horizontal correlation.

The influence of the horizontal correlation distance on the site response results is investigated by propagating the Kocaeli motion through twenty 2D velocity fields generated with σ_{lnVs} of 0.2, θ_z of 80 m, and θ_x of 0 m, 100 m, and 600 m. Figure 7.5 illustrates the $\text{Median}(Sa)_{ROI}$ versus period for each 2D velocity field realization, as well as the average response over the twenty realizations, (i.e.,

Average(Median(Sa)_{ROI})). These spectra are plotted separately for the three different horizontal correlation distances. For all the results shown, the Median(Sa)_{ROI} generally show a major peak at a period of around 0.3 s and subsequent peaks are observable around 0.6 s and 0.9 s. The variability in the Median(Sa)_{ROI} between realizations is largest between periods of about 0.2 s and 1.1 s, which correspond to the periods of amplification. The variability between the Median(Sa)_{ROI} across the twenty realizations increases with the increasing horizontal correlation distance. Longer periods are not influenced by variations in shear wave velocity because these periods are much longer than the first mode period of the site.

Figure 7.6 presents the $\sigma(\ln(Sa)$ _{ROI}) versus period for each velocity field realization. $\sigma(\ln(Sa)$ _{ROI}) represents the spatial variability in Sa across the ROI. $\sigma(\ln(Sa)$ _{ROI}) varies significantly from realization to realization as it depends specifically on the values of shear wave velocity within the ROI. On average, $\sigma(\ln(Sa)$ _{ROI}) is between 0.05 and 0.15 at shorter periods and peaks at 0.2 to 0.3 at a period of 0.3 s. The results obtained for different horizontal correlation distances indicate that increasing the horizontal correlation distance to 600 m, which is greater than the width of the ROI, reduces the $\sigma(\ln(Sa)$ _{ROI}) considerably because the shear wave velocities within the ROI are more uniform for this correlation distance. The shear wave velocity profiles across the ROI for velocity realizations generated with different values of horizontal correlation distance are plotted in Figure 7.7 and show

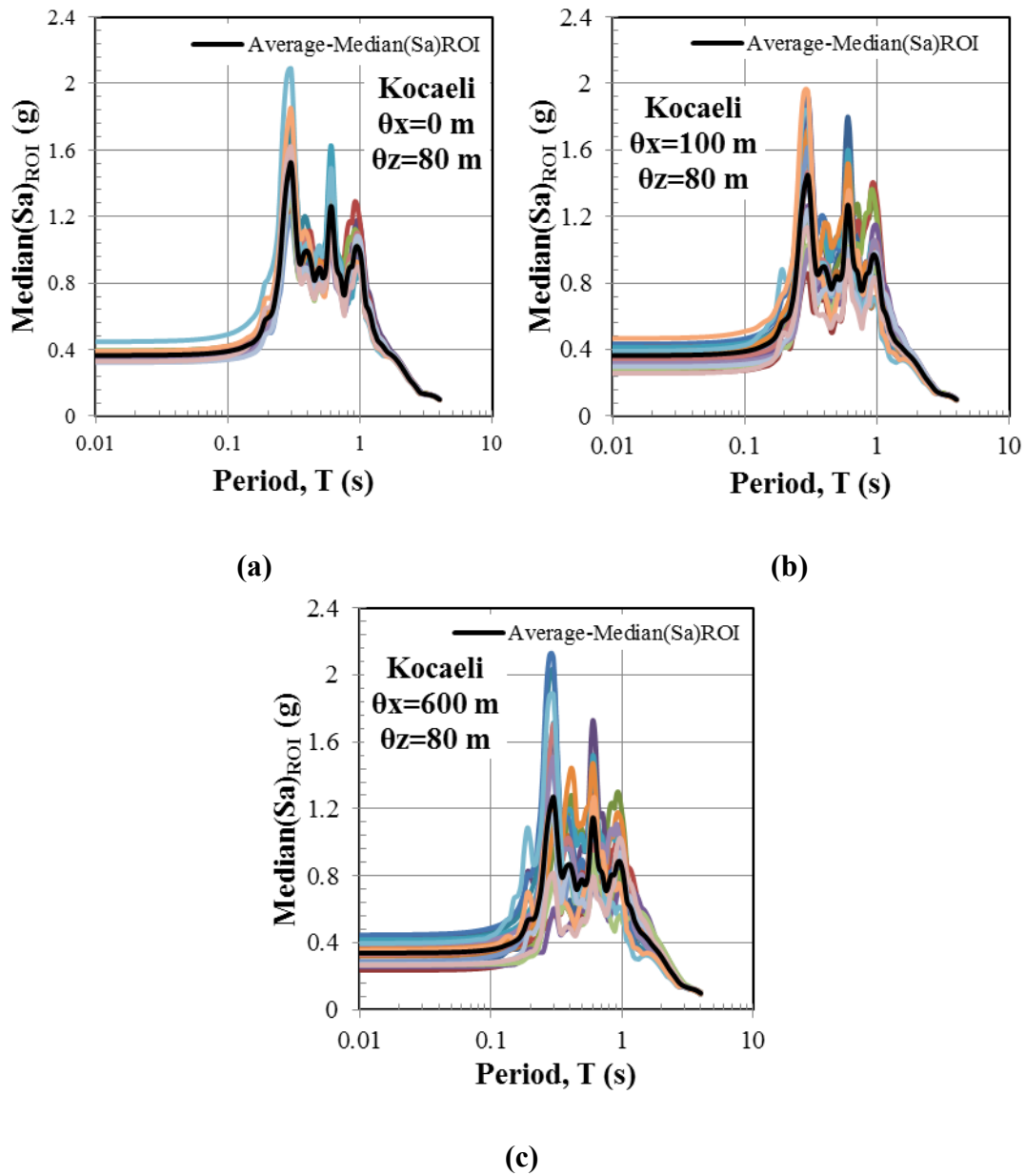


Figure 7.5 Median(Sa)_{ROI} obtained of twenty 2D analyses performed on the 2D velocity fields generated with σ_{lnV_S} of 0.2, θ_z of 80 m, and θ_x of (a) 0 m, (b) 100 m, and (c) 600 m.

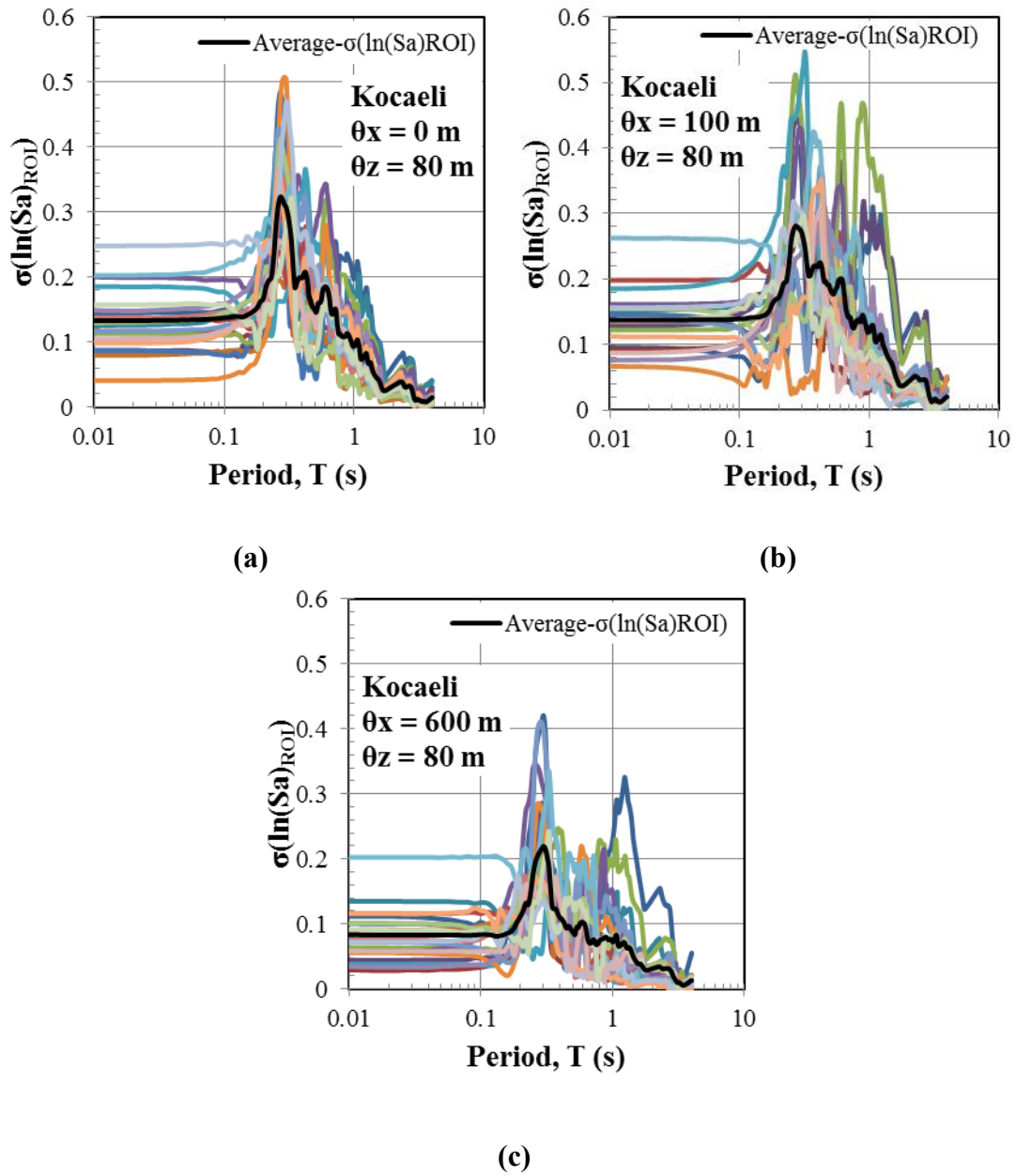


Figure 7.6 $\sigma(\ln(Sa)_{ROI})$ for twenty 2D analyses performed on 2D velocity fields generated with σ_{lnVs} of 0.2, θ_z of 80 m, and θ_x of (a) 0 m, (b) 100 m, and (c) 600 m

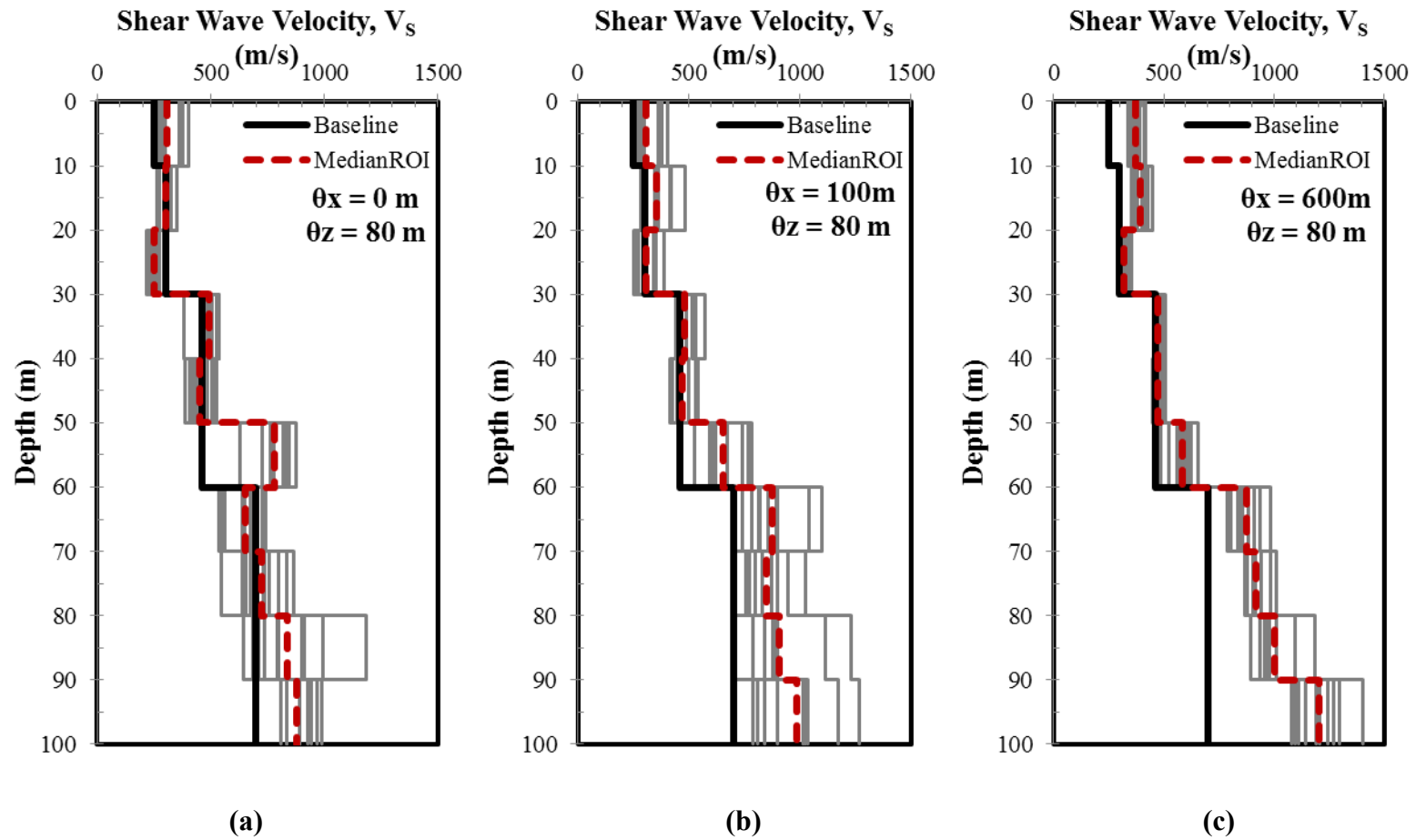


Figure 7.7 V_s profiles across the ROI for a single 2D random field realization generated with $\sigma_{\ln V_s}$ of 0.2, θ_z of 80 m, and θ_x of (a) 0 m, (b) 100 m, and (c) 600 m, respectively

that the uniformity of the velocity profiles across the ROI increases with increasing correlation distance.

Figure 7.8 compares the average response spectra (Average(Median(Sa)ROI)) over the twenty velocity realizations for each set of correlation distances. The Average(Median(Sa)ROI) obtained for different θ_x are similar. Some differences are noticeable around the peaks, where the analysis performed with $\theta_x = 0$ m predicts the largest response and this peak reduces slightly (15 to 20%) as the horizontal correlation distance increases. Figure 7.8b plots the average AF over the twenty velocity realizations (Average(Median(AF)ROI)) for each set of correlation distances. Similar to the Sa data, the Average(Median(AF)ROI) decreases with increasing θ_x . Figure 7.8c compares the standard deviation of the natural logarithm of the median spectral acceleration ($\sigma(\ln(\text{Median}(Sa)\text{ROI}))$) across realizations, which is a measure of the variability in the median response across different velocity realizations. The variability between realizations is largest for the analysis performed with the largest horizontal correlation distance ($\theta_x = 600$ m), the variability decreases as θ_x gets smaller and the generated velocity field becomes more random. The larger variability for more correlated velocity fields (i.e., larger θ_x) may initially appear counter-intuitive. However, the response variability between realizations is influenced by the shear wave velocity variability across the ROI between realizations. The variability in shear wave velocity within a single realization is smaller for larger θ_x , but the

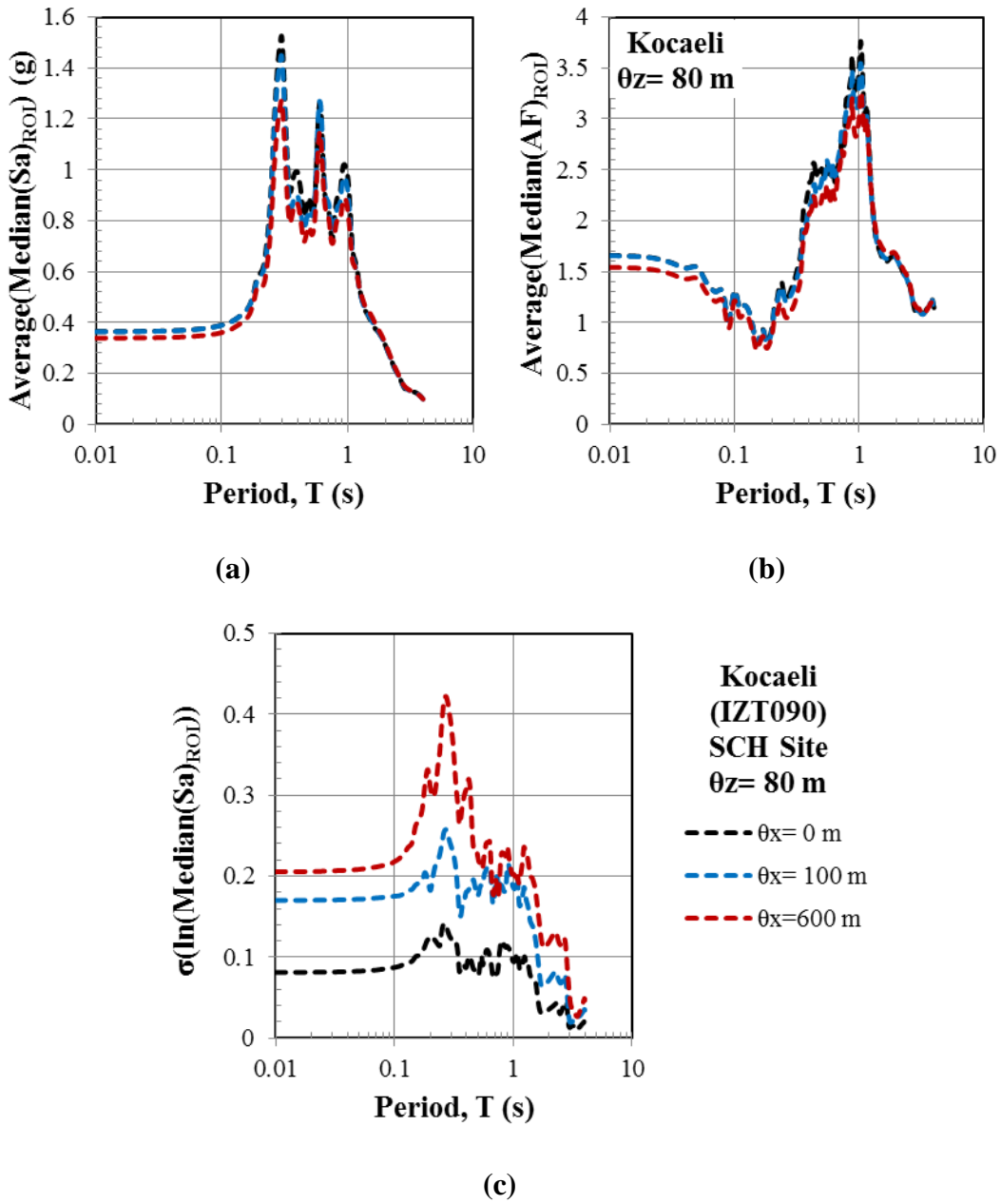


Figure 7.8 Influence of horizontal correlation distances on (a) Average(Median(Sa)_{ROI}), (b) Average(Median(AF)_{ROI}), and (c) $\sigma(\ln(\text{Median}(Sa)_{ROI}))$

variability in shear wave velocity between realizations is larger for larger θ_x . This result is caused because larger θ_x generate similar velocities across the ROI for a single realization (Figure 7.7) and these similar velocities will be larger or smaller than the average velocities. As a result, the response between different velocity realizations is more variable.

The influence of different horizontal correlation distances on the maximum response across the ROI (i.e., $\text{Average}(\text{Max}(Sa)_{\text{ROI}})$, $\text{Average}(\text{Max}(AF)_{\text{ROI}})$ and $\sigma(\ln(\text{Max}(Sa)_{\text{ROI}}))$) are illustrated in Figure 7.9. The results for the maximum responses are similar to those for the median responses (Figure 7.8) in that the average response (both Sa and AF , Figures 7.9a and 7.9b) across realizations is similar for smaller θ_x but decreases for $\theta_x = 600$ m and mostly near the periods of amplification. The decrease for $\theta_x = 600$ m is 20 to 26%, which is larger than it was for the median response (12 to 16%, Figure 7.8). These results show that the maximum Sa is more influenced by shear wave velocity variability. The variability in the $\text{Max}(Sa)_{\text{ROI}}$ between realizations (i.e., $\sigma(\ln(\text{Max}(Sa)_{\text{ROI}}))$) increases with increasing horizontal correlation distance (Figure 7.9c). Again, this result is because there is more variability between velocity realizations for larger horizontal correlation distances (Figure 7.7). The $\sigma(\ln(\text{Max}(Sa)_{\text{ROI}}))$ values in Figure 7.9c take on similar values as $\sigma(\ln(\text{Median}(Sa)_{\text{ROI}}))$ in Figure 7.8c.

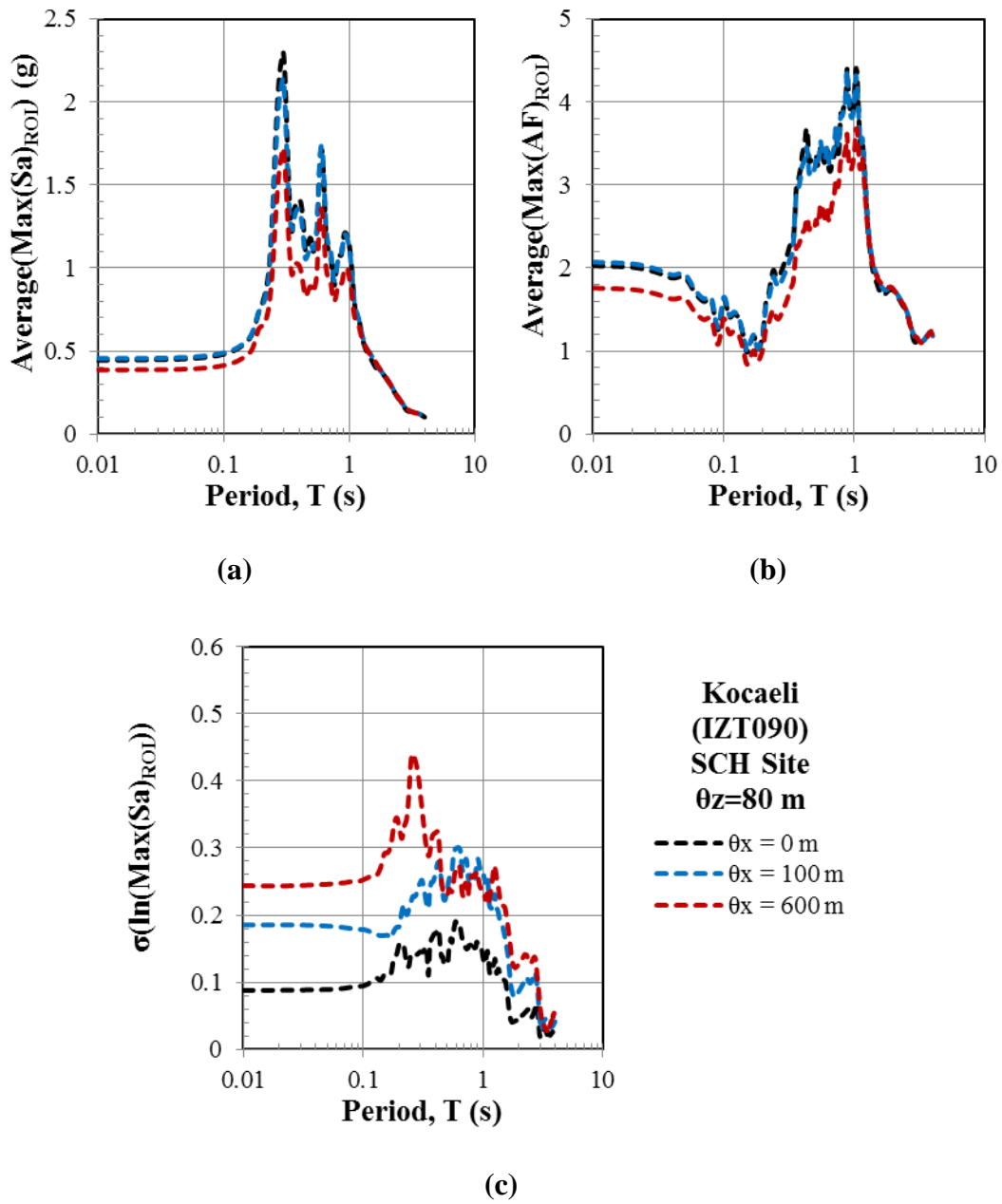


Figure 7.9 Influence of horizontal correlation distance on (a) Average($\text{Max}(S_a)_{\text{ROI}}$), (b) Average($\text{Max}(AF)_{\text{ROI}}$), and (c) $\sigma(\ln(\text{Max}(S_a)_{\text{ROI}}))$

7.4 Influence of Vertical Correlation on Two-Dimensional Site Response

The effect of vertical correlation distance on results from 2D site response analysis is investigated by propagating the Kocaeli motion through twenty 2D velocity fields generated with $\sigma_{\ln V_S}$ of 0.2, θ_x of 600 m, and θ_z of 0 m, 80 m, and 600 m. Because the influence of θ_z on the results is coupled with θ_x , a second set of analyses with variable θ_z are performed with θ_x equal to 0 m. Figure 7.10 plots the median response spectra across the ROI ($\text{Median}(Sa)_{\text{ROI}}$) for each of the twenty V_S realizations. The amplitude of the response spectra vary considerably for different vertical correlation distances. As the vertical correlation gets larger the median response across the ROI increases significantly, such that the peak spectral acceleration increases from 1.6 g for θ_z of 0 m, to 2.1 g for θ_z of 80 m, to 2.35 g for θ_z of 600 m.

Figure 7.11 illustrates the spatial variability in Sa across the ROI ($\sigma(\ln(Sa)_{\text{ROI}})$) for each velocity realization. The $\sigma(\ln(Sa)_{\text{ROI}})$ varies considerably from realization to realization but on average is larger for periods shorter than the period of peak response (i.e., periods shorter than 1.0 s). The largest $\sigma(\ln(Sa)_{\text{ROI}})$ is observed for $\theta_z = 0$ m due to the large velocity variability within each vertical profile of velocity with depth, which leads to more response variability at shorter periods.

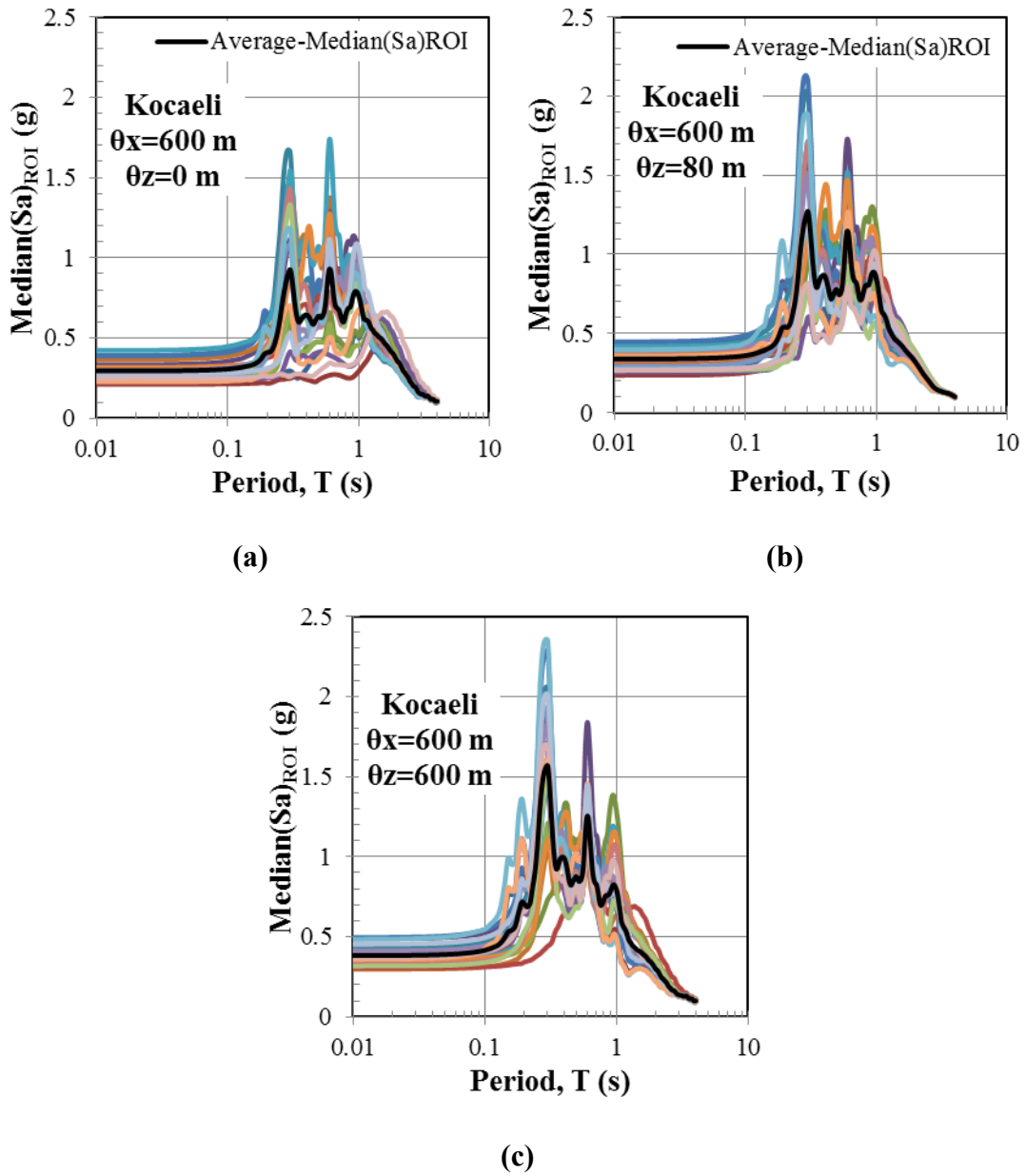


Figure 7.10 Median(Sa)_{ROI} obtained through 2D site response analyses of 20 of the 2D velocity fields generated with σ_{lnVs} of 0.2, θ_x of 600 m, and θ_z of (a) 0 m, (b) 80 m, and (c) 600 m.

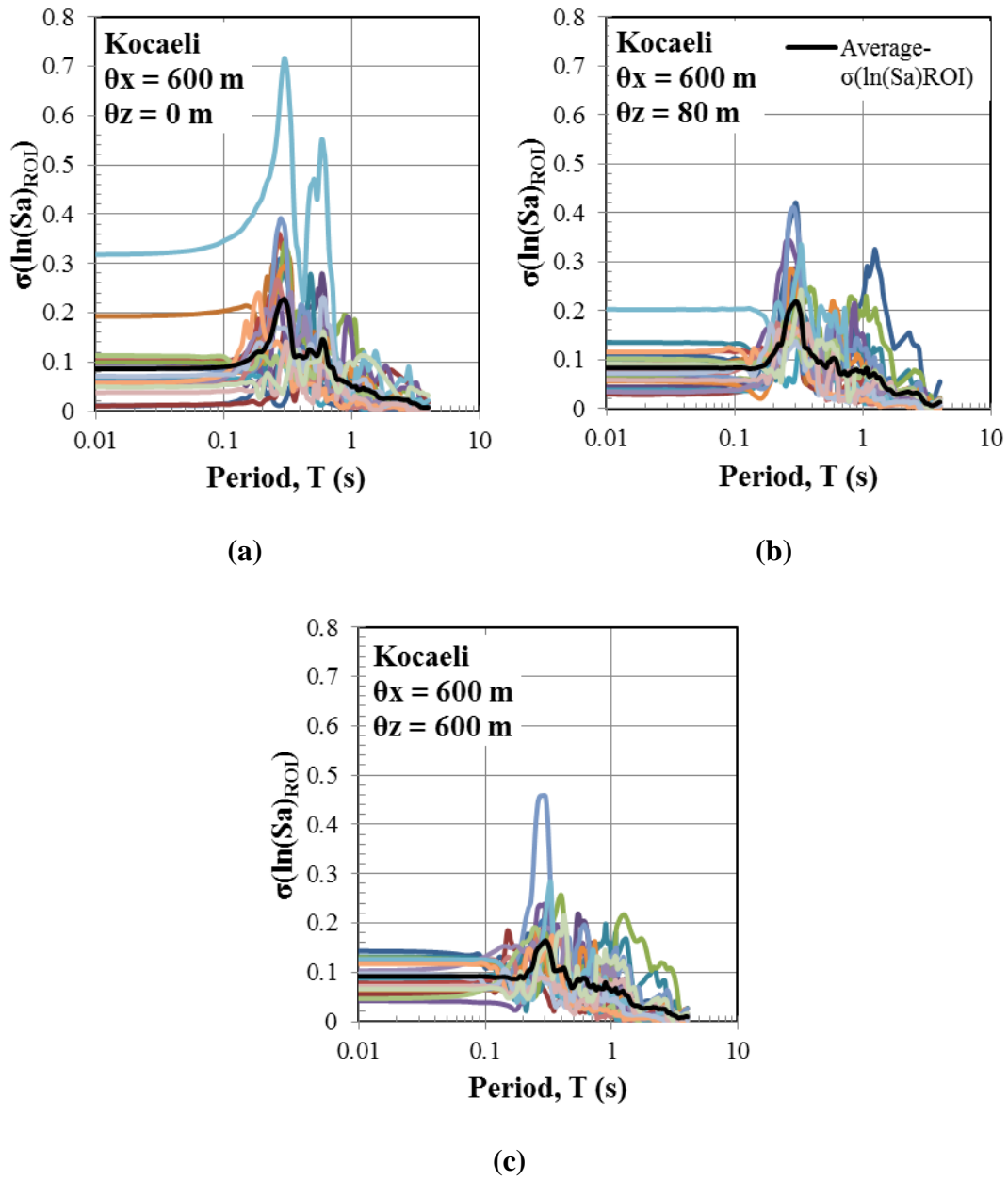
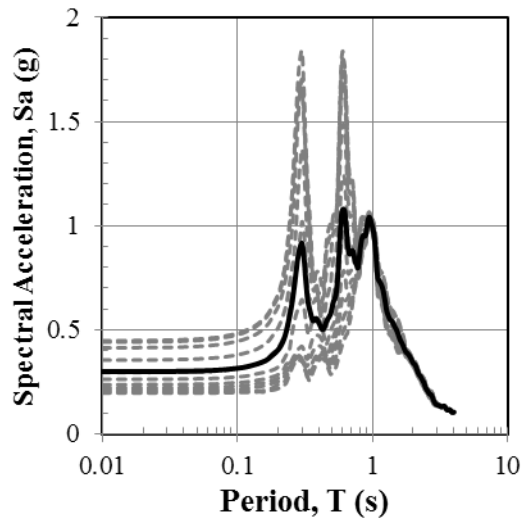


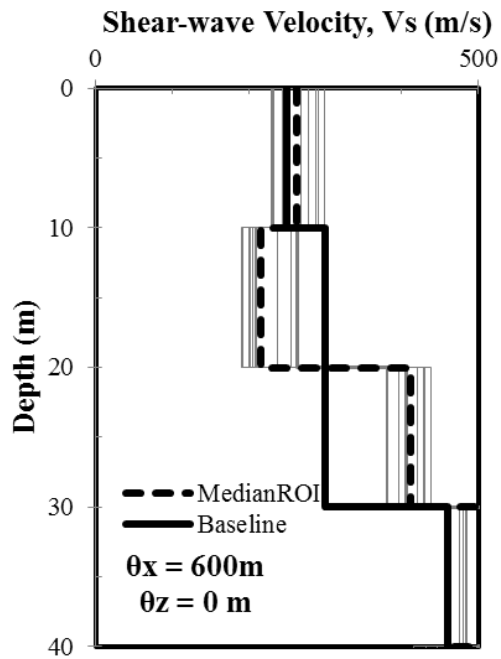
Figure 7.11 $\sigma(\ln(Sa)_{ROI})$ obtained through 2D site response analyses of twenty 2D velocity fields generated with σ_{lnVs} of 0.2, θ_x of 600 m, and θ_z of (a) 0 m, (b) 80 m, and (c) 600 m.

One velocity randomization in Figure 7.11a displays a significantly larger $\sigma(\ln(Sa)_{ROI})$ than the others. This ground motion variability is being driven by 5 very small responses and 4 very large responses across the ROI, as indicated by the surface response spectra in Figure 7.12a. These differences are being driven by differences in the velocity field across the ROI. The shear wave velocity profiles in the top 30 m across the ROI are shown in Figure 7.12b. The locations of the small responses are located adjacent to one another and are underlain by low velocities over depths of 10 to 20 m ($V_S \sim 190\text{-}200$ m/s), while the locations of the large responses are underlain by larger velocities over this depth range ($V_S \sim 250$ m/s). These differences lead to strains that are 5 to 10 times larger in the low velocity zone and thus the responses are smaller.

The influence of vertical correlation distance on the average response across twenty velocity realizations ($\text{Average}(\text{Median}(Sa)_{ROI})$, $\text{Average}(\text{Median}(AF)_{ROI})$), and the standard deviation of the median response across twenty velocity realizations ($\sigma(\ln(\text{Median}(Sa)_{ROI}))$) is presented in Figure 7.13. Figure 7.13a shows that $\text{Average}(\text{Median}(Sa)_{ROI})$ at periods less than 1.0 s decreases significantly (up to 40%) as the vertical correlation distance decreases. This result is related to the influence of θ_z on the velocity field when θ_x is large (i.e., 600 m in this case). Smaller values of vertical correlation distance result in larger fluctuations in velocity with depth, as shown in the median velocity profiles in Figure 7.14, and when



(a)



(b)

Figure 7.12 Surface response spectra and shear wave velocity profiles across ROI for a 2D velocity field realization with large $\sigma(\ln(Sa)_{ROI})$

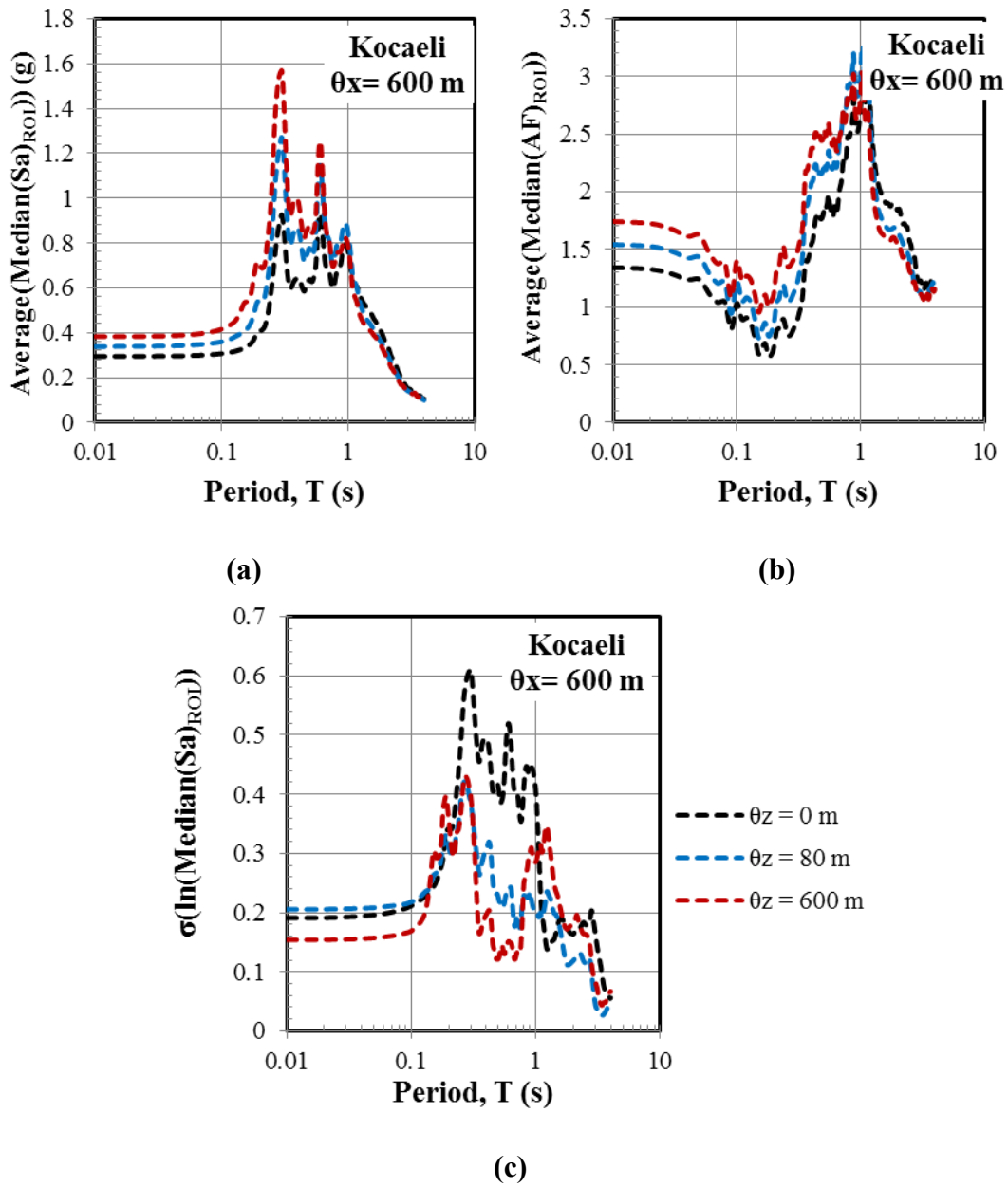


Figure 7.13 Influence of θ_z on 2D site response analysis with large θ_x (a) Average(Median(Sa)_{ROI}), (b) Average(Median(AF)_{ROI}), and (c) $\sigma(\ln(\text{Median}(Sa)_{ROI}))$

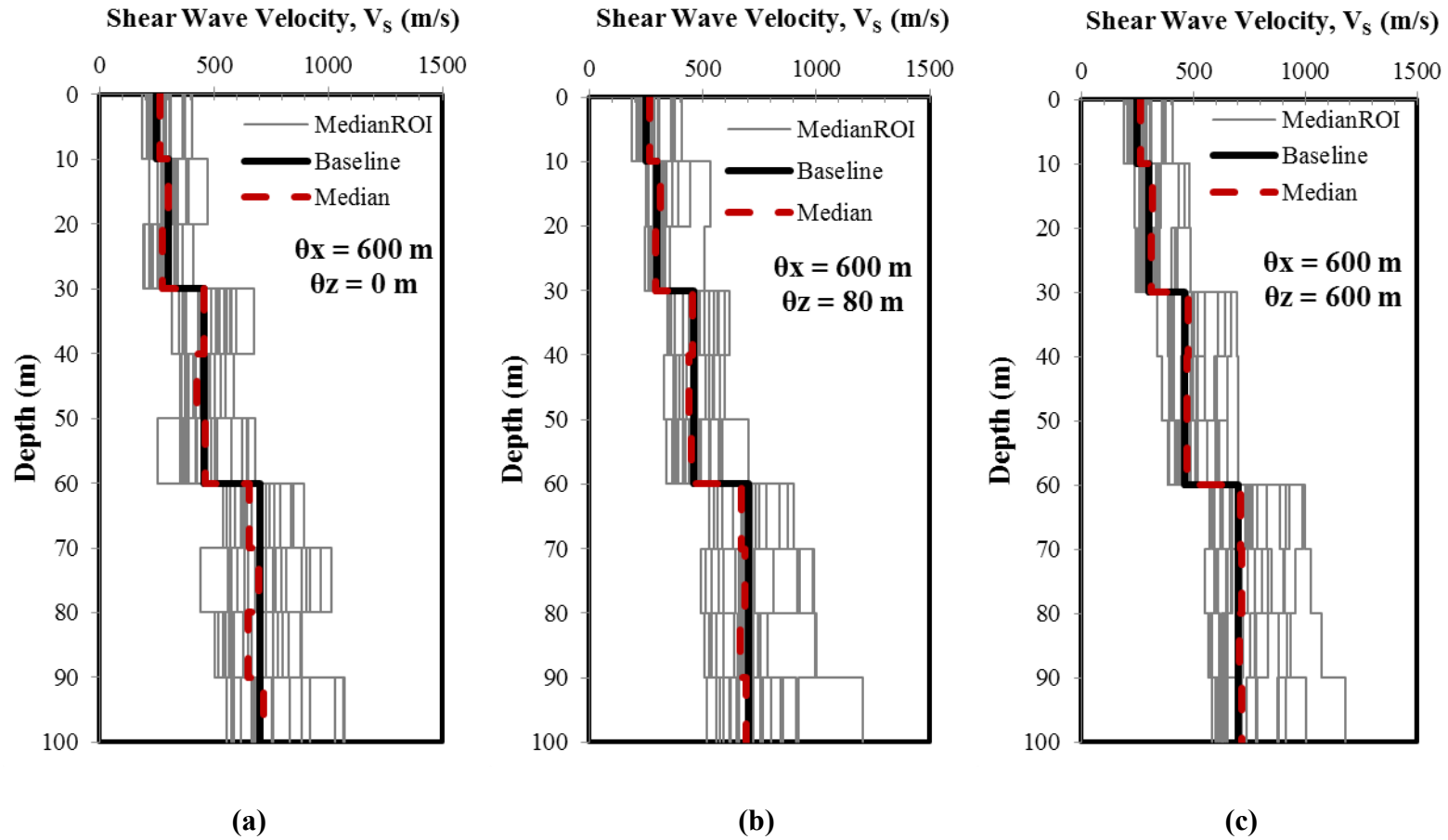


Figure 7.14 Median V_s profiles across the ROI of 20 2D V_s field realizations generated with σ_{lnV_s} of 0.2, θ_x of 600 m, and θ_z of (a) 0 m, (b) 80 m, and (c) 600 m, respectively

coupled with a large horizontal correlation distance, these variations in velocity extend significantly in the horizontal direction. These horizontally coherent vertical variations in velocity, in particular low velocity layers that strain more and lead to more damping, more strongly reduce the amplitude of the surface response. Similarly, the $\text{Average}(\text{Median}(AF)_{\text{ROI}})$ decreases with decreasing vertical correlation distance. The variability in the median surface response across the twenty realizations (i.e., $\sigma(\ln(\text{Median}(Sa)_{\text{ROI}}))$) is largest when the vertical correlation distance is 0 m, and becomes smaller with larger values of vertical correlation distance. Again, this result is caused by the horizontally coherent vertical variations in velocity, which cause significant differences in the computed responses from realization to realization.

The influence of the vertical correlation distance is further investigated through analyses with θ_x equal to 0 m (i.e. no horizontal correlation). Figure 7.15 presents the $\text{Average}(\text{Median}(Sa)_{\text{ROI}})$, $\text{Average}(\text{Median}(AF)_{\text{ROI}})$, and $\sigma(\ln(\text{Median}(Sa)_{\text{ROI}}))$ results obtained for these conditions. The median response spectra used to compute $\sigma(\ln(\text{Median}(Sa)_{\text{ROI}}))$ are shown in Figure 7.16. The results in Figure 7.15 show that the vertical correlation distance has little to no effect on the predicted average response (Figures 7.15a, 7.15b) when the horizontal correlation distance is zero. The variability in the median responses across the twenty realizations (Figure 7.15c) is similar for $\theta_z = 80$ and 600 m, but significantly

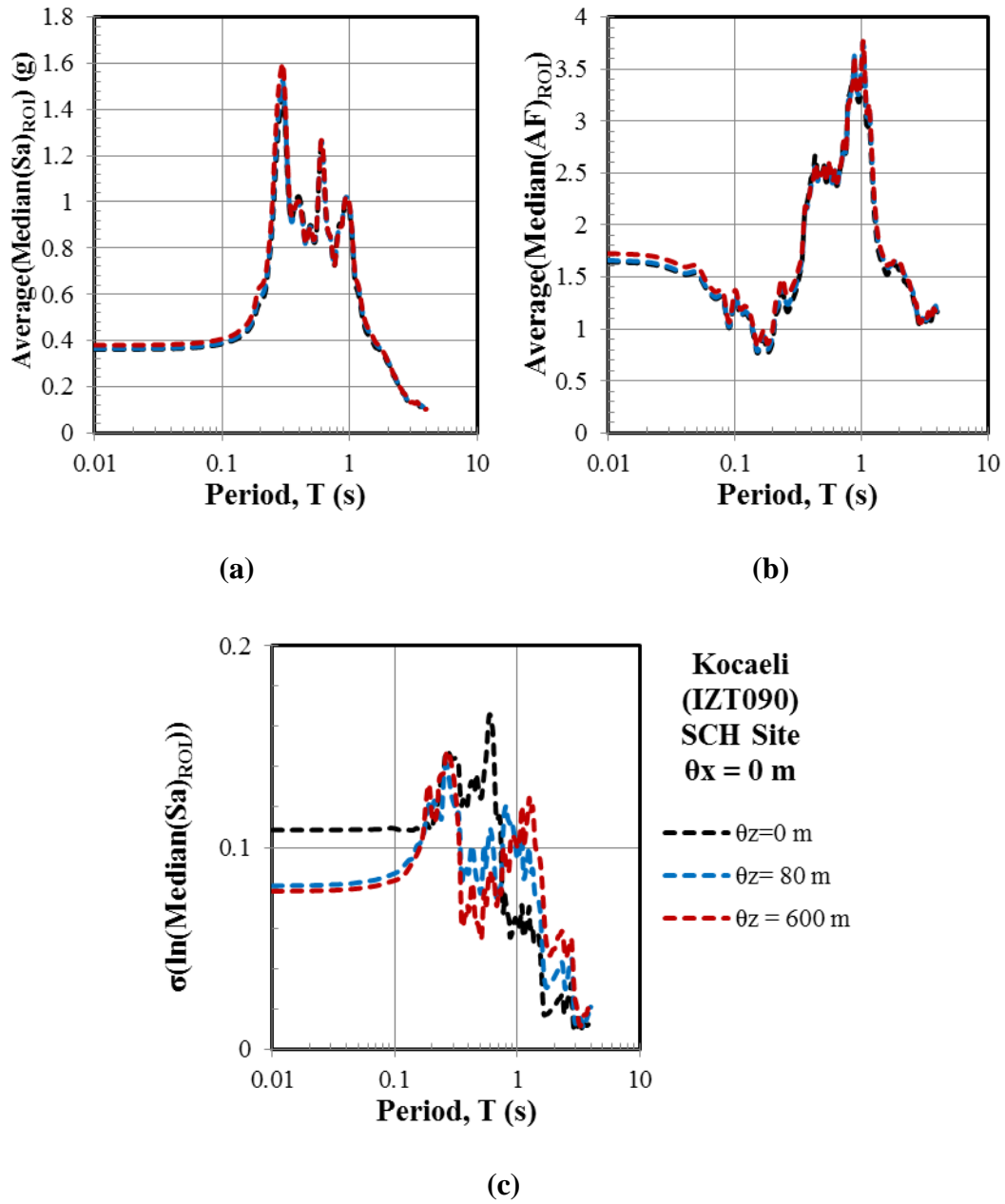


Figure 7.15 2D site response analysis results for 2D V_S field generated with θ_x of 0 m and θ_z of 0 m, 80 m, and 600 m (a) Average(Median(Sa)_{ROI}), (b) Average(Median(AF)_{ROI}), and (c) $\sigma(\ln(\text{Median}(Sa)_{ROI}))$

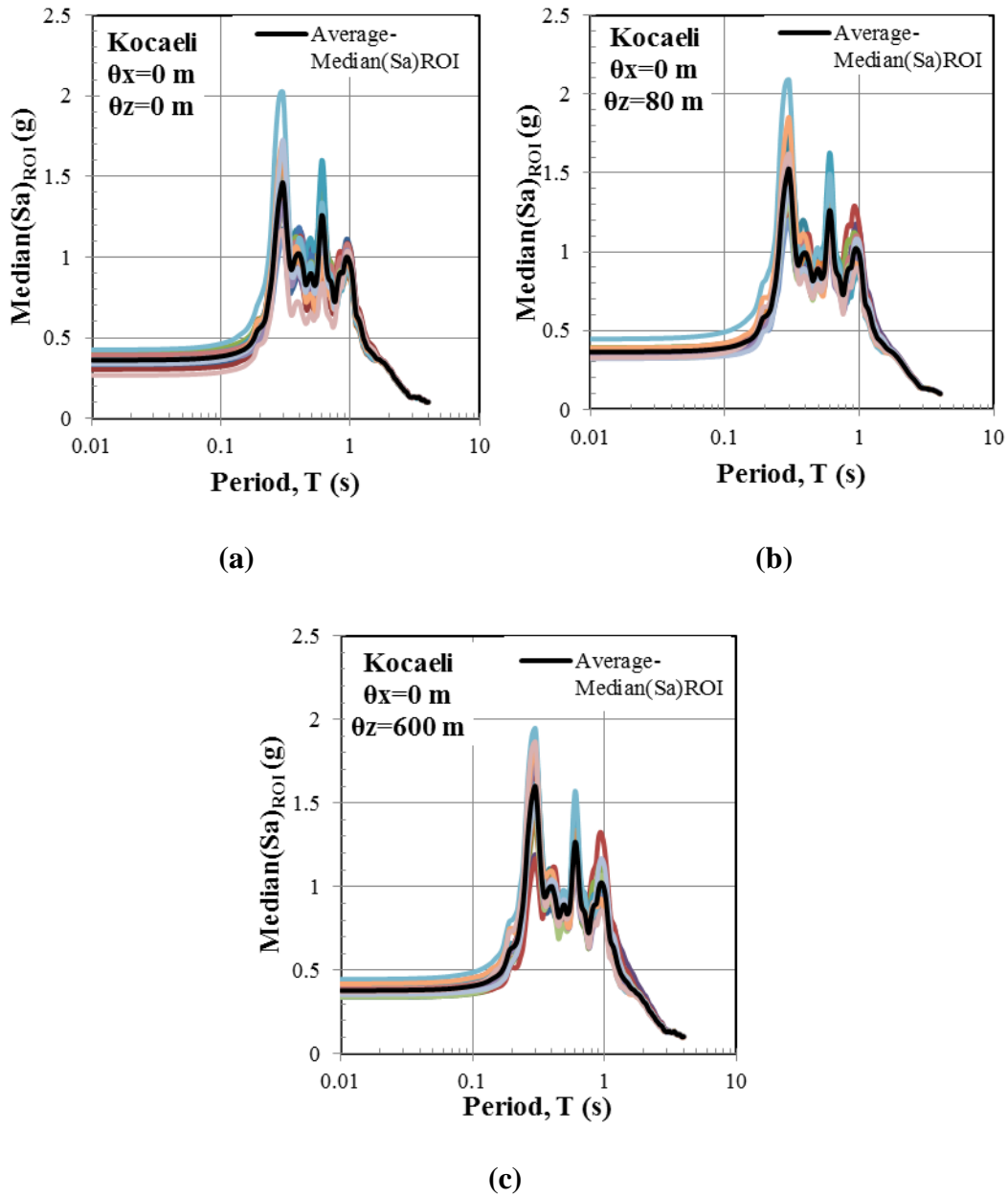


Figure 7.16 Median(Sa)_{ROI} spectra of 2D analysis performed on velocity fields generated for θ_x of 0 m and θ_z of: (a) 0 m. (b) 80 m, and (c) 600 m.

different for $\theta_z = 0$ m. At periods less than about 0.8 s $\theta_z = 0$ m displays the largest variability (Figure 7.15), while at longer periods $\theta_z = 80$ and 600 m display the largest variability. These results indicate that the vertical variations in velocity modeled by $\theta_z = 0$ m generate more variability at periods shorter than the site period, but they do not influence the variability significantly at longer periods. The values of $\sigma(\ln(\text{Median}(Sa)_{\text{ROI}}))$ in Figure 7.15c for $\theta_x = 0$ m are significantly smaller than the values in Figure 7.13c for θ_x equal to 600 m (0.05 to 0.15 vs. 0.2 to 0.6).

Figures 7.13 and 7.15 show that the effect of the vertical correlation on the computed response depends significantly on the horizontal correlation distance. The influence of the vertical correlation distance is very significant when the horizontal correlation distance is large and less significant when the horizontal correlation distance approaches 0 m. To further illustrate this effect, Figure 7.17 compares the responses obtained for the velocity fields generated for combinations of θ_x and θ_z equal to 0 m and 600 m. These correlation distances represent the “end members” in terms of no correlation and high correlation across an ROI of 100 m. The computed median responses across all realizations (Figure 7.17a, 7.17b) are similar at periods less than about 0.8 s except for the analyses performed with $\theta_x = 600$ m and $\theta_z = 0$ m, which predicts a smaller response by as much as 80%. At a period of around 1.0 s (i.e., \sim site period), the results from analyses with $\theta_x = 600$ m are about 20% smaller than the results from analyses with $\theta_x = 0$ m, no matter the value of θ_z . The variability in the median responses over the twenty realizations (Figure 7.17c)

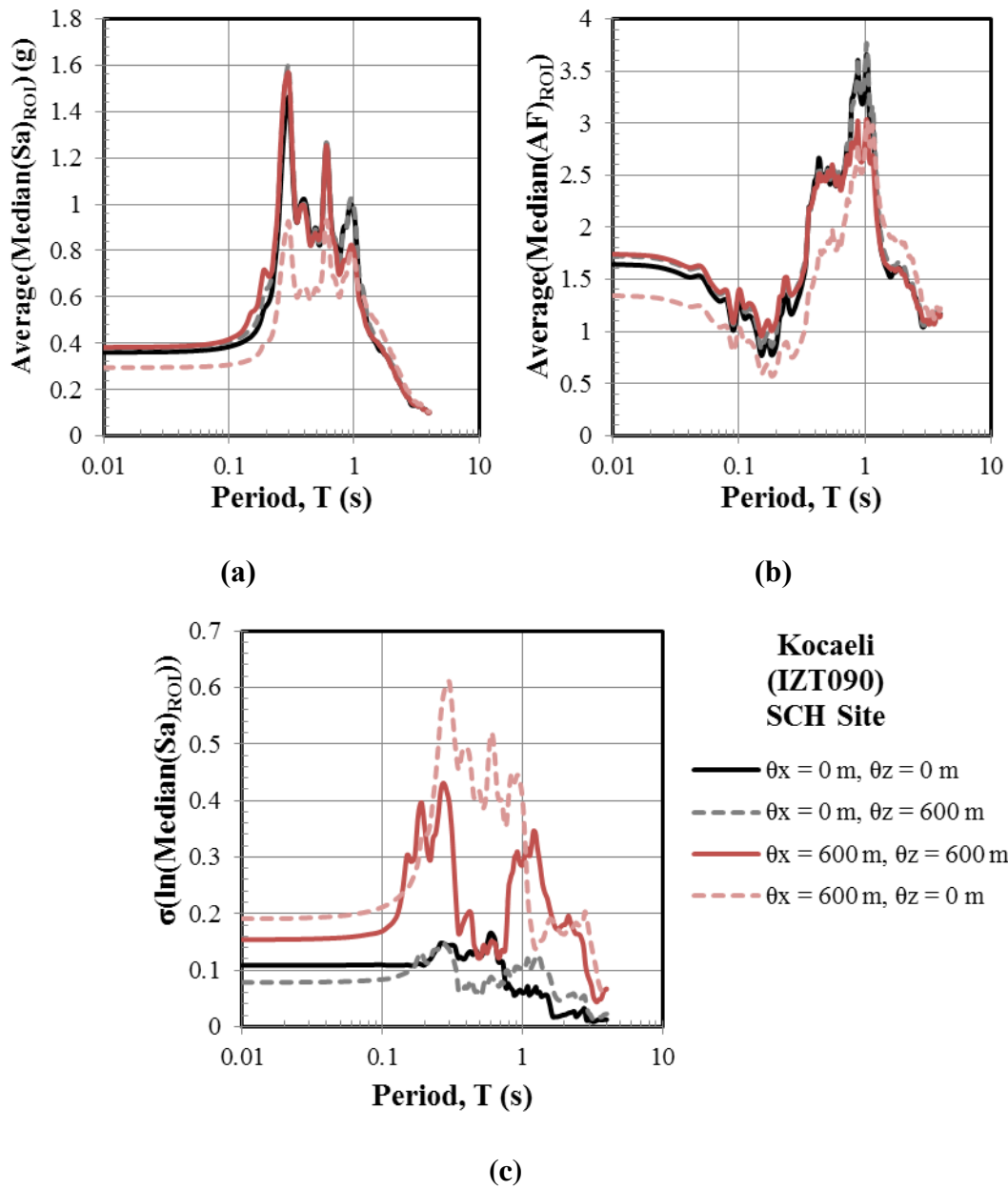


Figure 7.17 2D site response analysis results of 2D velocity fields generated with end-member correlation distances (a) Average(Median(Sa)_{ROI}), (b) Average(Median(AF)_{ROI}), and (c) $\sigma(\ln(\text{Median}(Sa)_{ROI}))$

changes significantly for the different correlation distances. The variability increases significantly with increasing horizontal correlation distance, and the largest values are observed for with $\theta_x = 600$ m and $\theta_z = 0$ m. Large horizontal correlation distances result in more variability between realizations because the median velocities across the ROI vary more significantly between realizations.

A final set of 2D site response analysis are performed with moderate level of horizontal correlation ($\theta_x = 100$ m) to investigate the effect of vertical correlation distance under a more realistic value of horizontal correlation. Figure 7.18 illustrates the results of twenty realizations with θ_x of 100 m and θ_z of 0 m and 80 m. The reduction in the average response (Figures 7.18a and 7.18b) with decreasing vertical correlation is still visible; however, it is not as significant as the reduction observed in Figure 7.13 for θ_x of 600 m.

The results presented previously focused on the median response across the ROI, the results in Figure 7.19 focus on the influence of the vertical correlation distance on the maximum response across the ROI for $\theta_x = 600$ m and θ_z of 0 m, 80 m, and 600 m. Similar to results for the average response, the maximum response averaged over the twenty realizations decreases with decreasing vertical correlation distance. However, the reduction is smaller (35% vs. 66%) than observed for the median responses (Figure 7.13). The variability of the maximum response across the twenty velocity realizations is largest for $\theta_z = 0$ m (Figure 7.19c), which again is similar to what was observed for the median response.

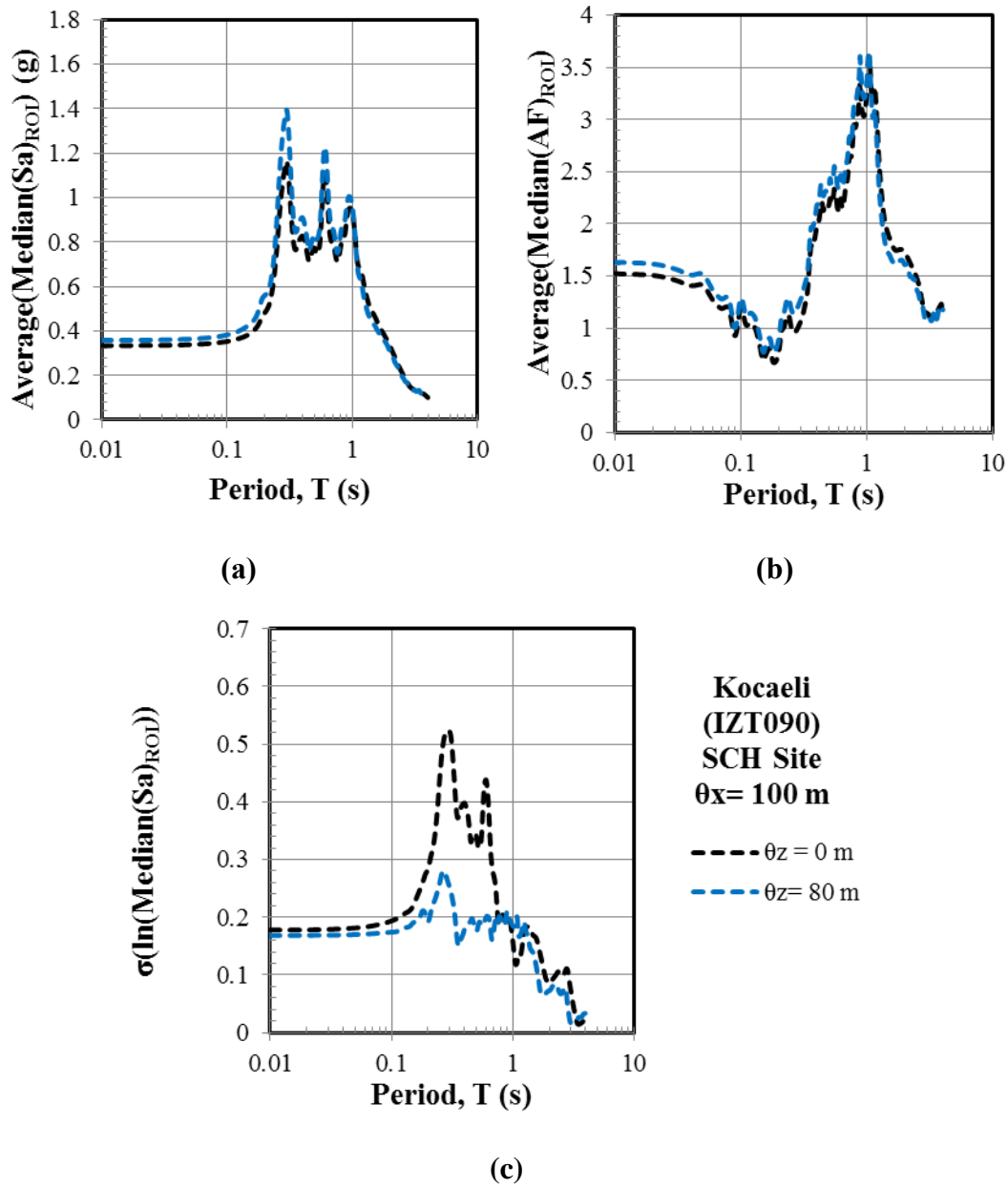


Figure 7.18 2D site response analysis results of 2D V_S field generated with θ_x of 100 m and θ_z of 0 m and 80 m (a) Average(Median(Sa)_{ROI}), (b) Average(Median(AF)_{ROI}), and (c) $\sigma(\ln(\text{Median}(Sa)_{ROI}))$)

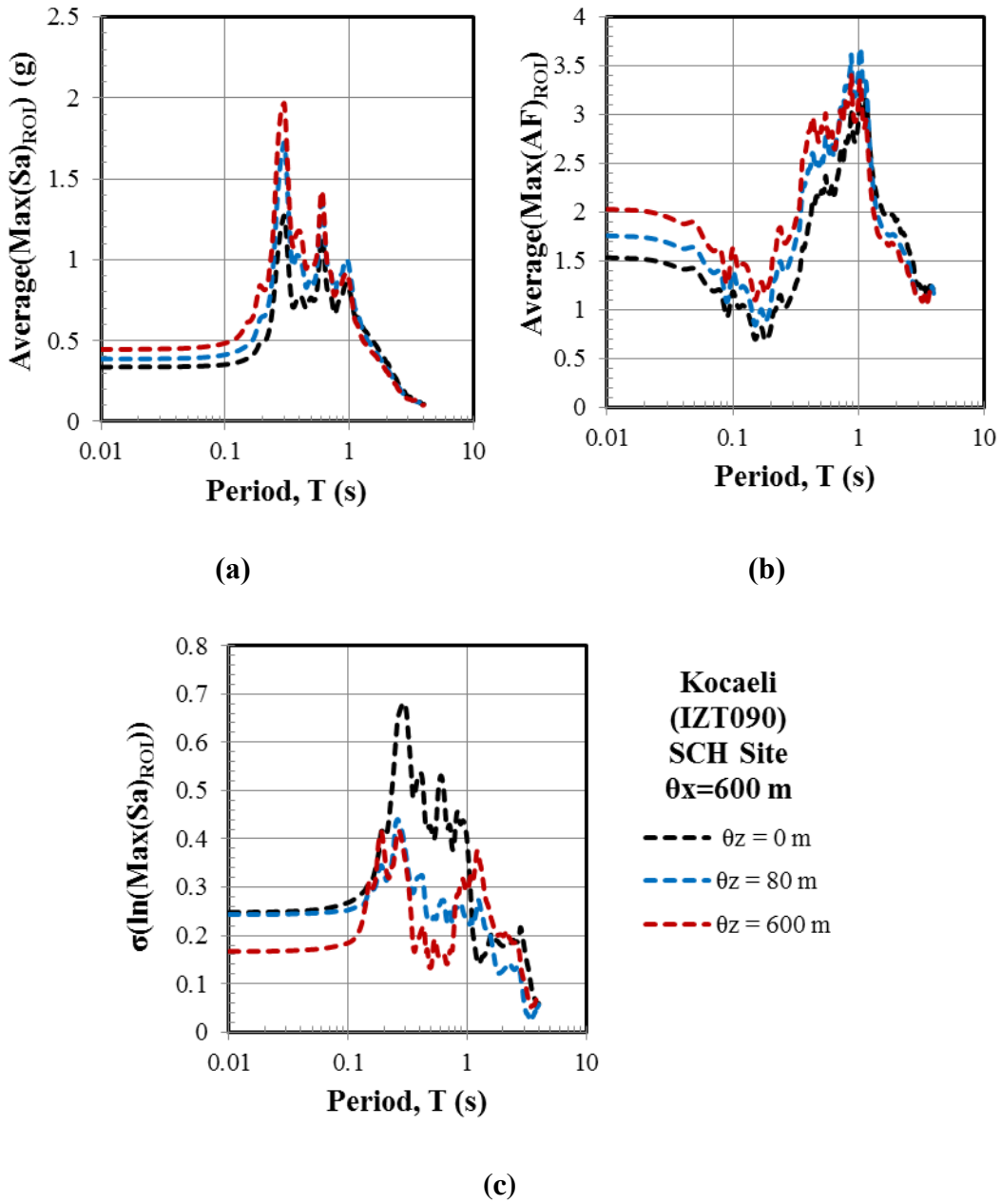


Figure 7.19 2D site response analysis results of 2D velocity fields generated with θ_x of 600 m and θ_z of 0 m, 80 m, and 600 m (a) Average($\text{Max}(S_a)_{\text{ROI}}$), (b) Average($\text{Max}(AF)_{\text{ROI}}$), and (c) $\sigma(\ln(\text{Max}(S_a)_{\text{ROI}}))$

7.5 Influence of Input Motion Characteristics on Two-Dimensional Site Response

Two dimensional site response analyses are further performed with four additional motions with different spectral shapes (Figure 7.2) to investigate the influence of the input motion characteristics on the surface response across ROI. Two-dimensional site response analyses are performed for the same 2D velocity fields discussed previously, but with the five selected input motions. Figure 7.20 presents the $\text{Average}(\text{Median}(Sa)_{\text{ROI}})$ obtained for the five inputs for the 2D velocity fields with varying horizontal correlation distance, while Figure 7.21 shows the results in terms of the amplification factor ($\text{Average}(\text{Median}(AF)_{\text{ROI}})$). These figures show that the influence of the horizontal correlation distance on the average response is similar for the five different input motions. The average response decreases with increasing horizontal correlation distance for every motion, and this effect is most clearly seen in the AF results. The amount of reduction in the average response slightly depends on the input motion characteristics; motions with larger Sa at periods around the site period, such as Kocaeli-IZT090, Northridge-0141-270, and Northridge-PAC265 (Figure 7.2), show the largest effect of correlation distance with reductions of 15 to 20 % in the response. These motions drive the site the hardest and induce the largest strains/damping which reduces the response when more variation,

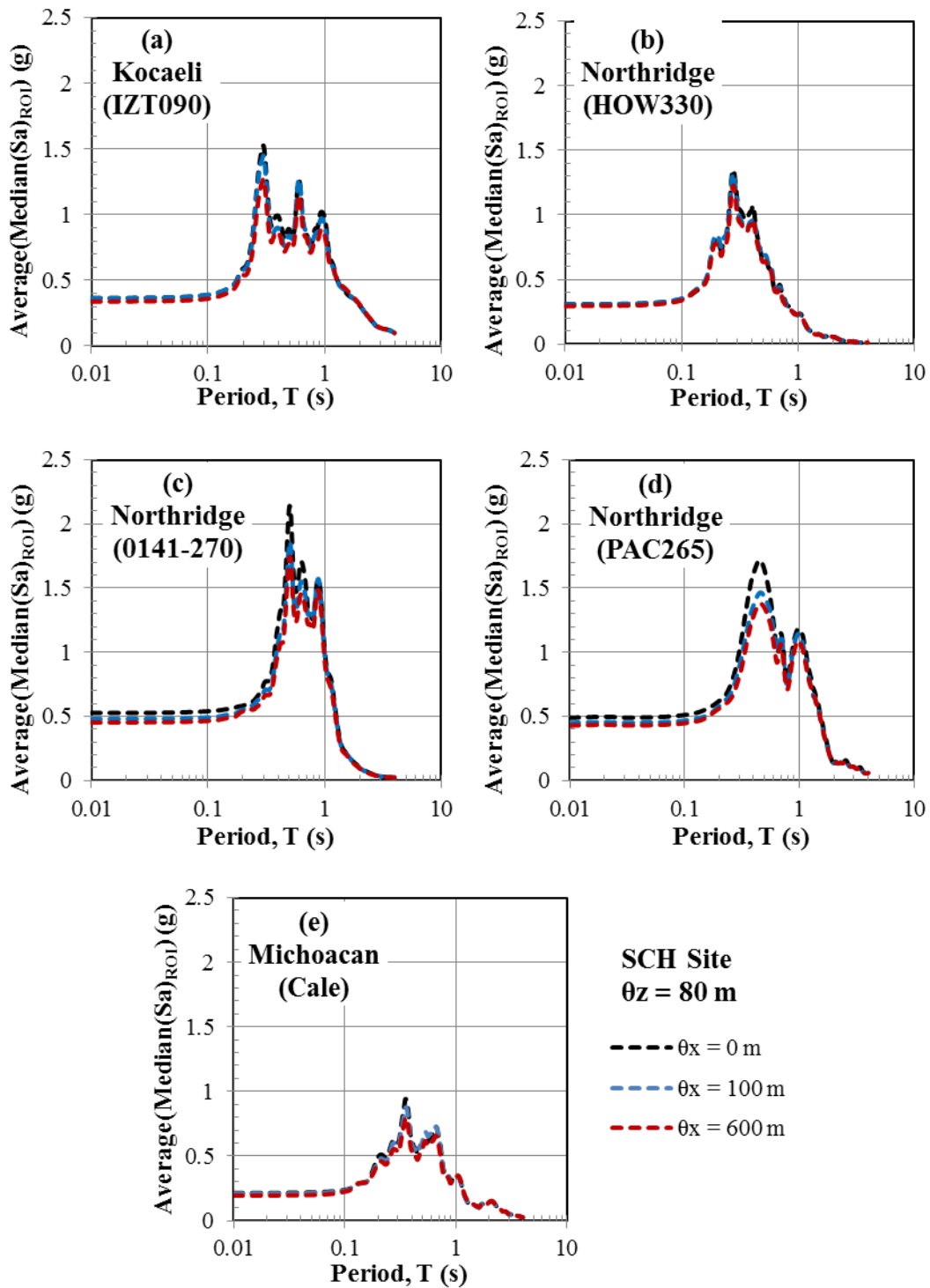


Figure 7.20 Influence of θ_x on the Average(Median(Sa)_{ROI}) of five input motions

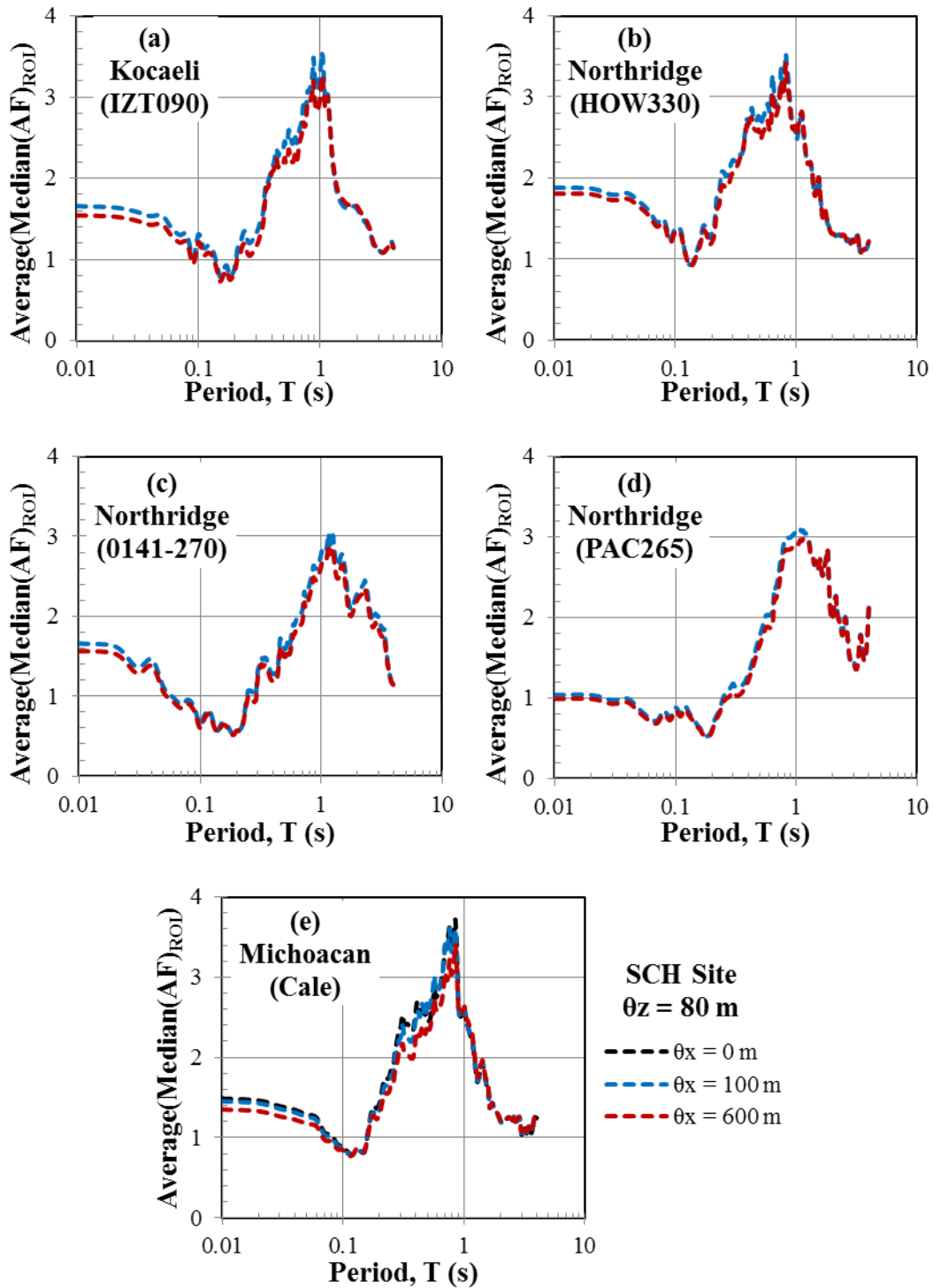


Figure 7.21 Influence of θ_x on the Average(Median(AF)_{ROI}) of five input motions

with more low velocity elements, is modeled in the site.

Figure 7.22 compares the variability in the median AF across velocity realizations (i.e., $\sigma(\ln(\text{Median}(AF)_{\text{ROI}}))$) for the different input motions and analyses performed with different horizontal correlation distances. For all analyses, the variability increases as the horizontal correlation distance increases. The variability is higher for the analyses performed with the ground motions with higher intensity at the site (i.e., Kocaeli-IZT090, Northridge-PAC265).

The influence of vertical correlation distance on the surface response for the different input motions is also investigated. Figure 7.23 presents the average response spectra for each motion across the twenty velocity realizations, while Figure 7.24 presented the average AF . Again, the average response decreases as the vertical correlation distance decreases. However, the reduction is smaller than observed for horizontal correlation distances, only between 10 and 15%.

The variability in the amplification factor across velocity realizations (i.e., $\sigma(\ln(\text{Median}(AF)_{\text{ROI}}))$) is shown in Figure 7.25 for each motion. The variability increases with decreasing vertical correlation distance for each motion. The influence of the vertical correlation distance on the $\sigma(\ln(\text{Median}(AF)_{\text{ROI}}))$ depends on the input motion, and it is more significant for motions with higher input intensities at the site period.

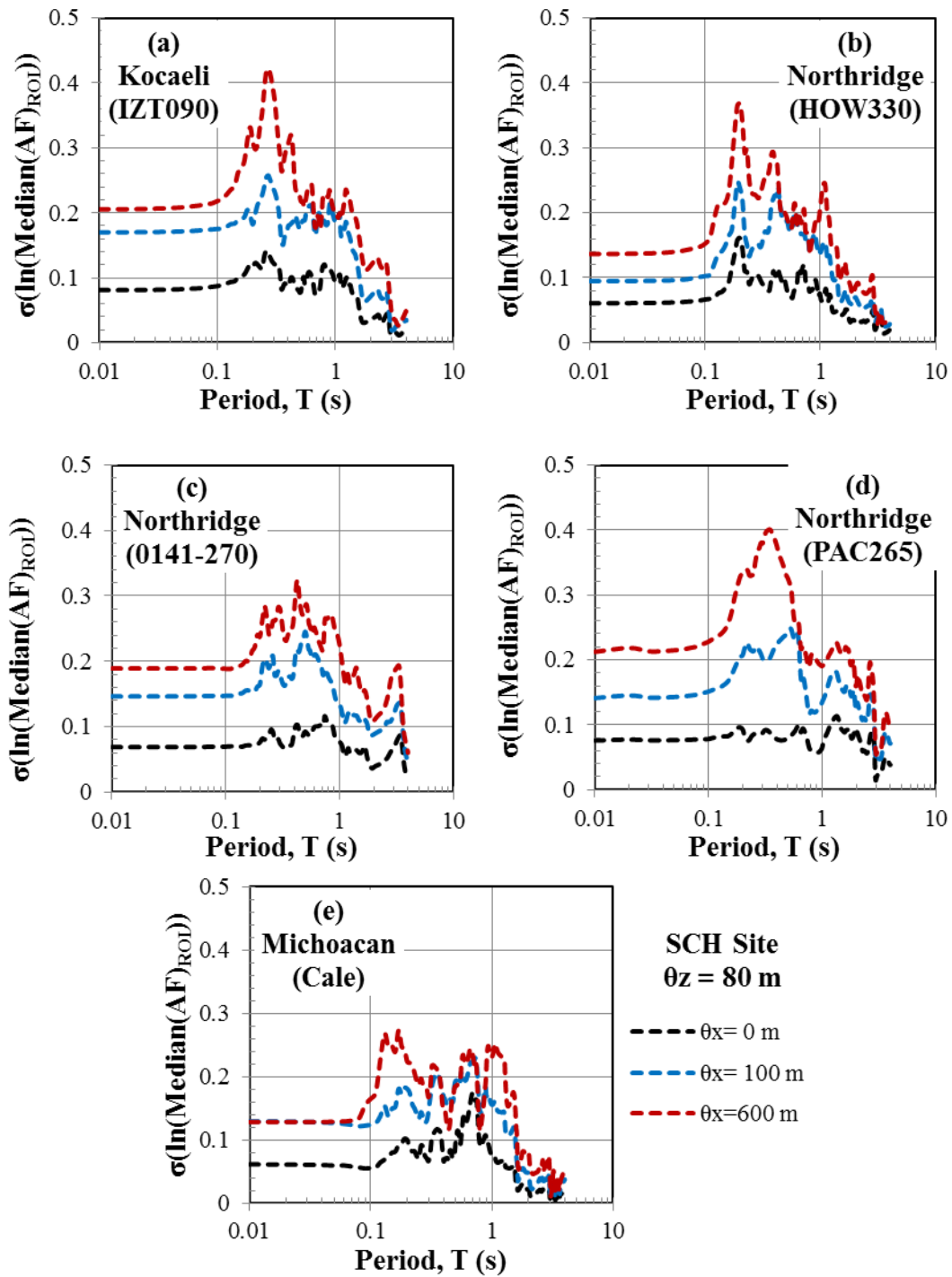


Figure 7.22 Influence of θ_x on the $\sigma(\ln(\text{Median}(AF)_{ROI}))$ of five input motions

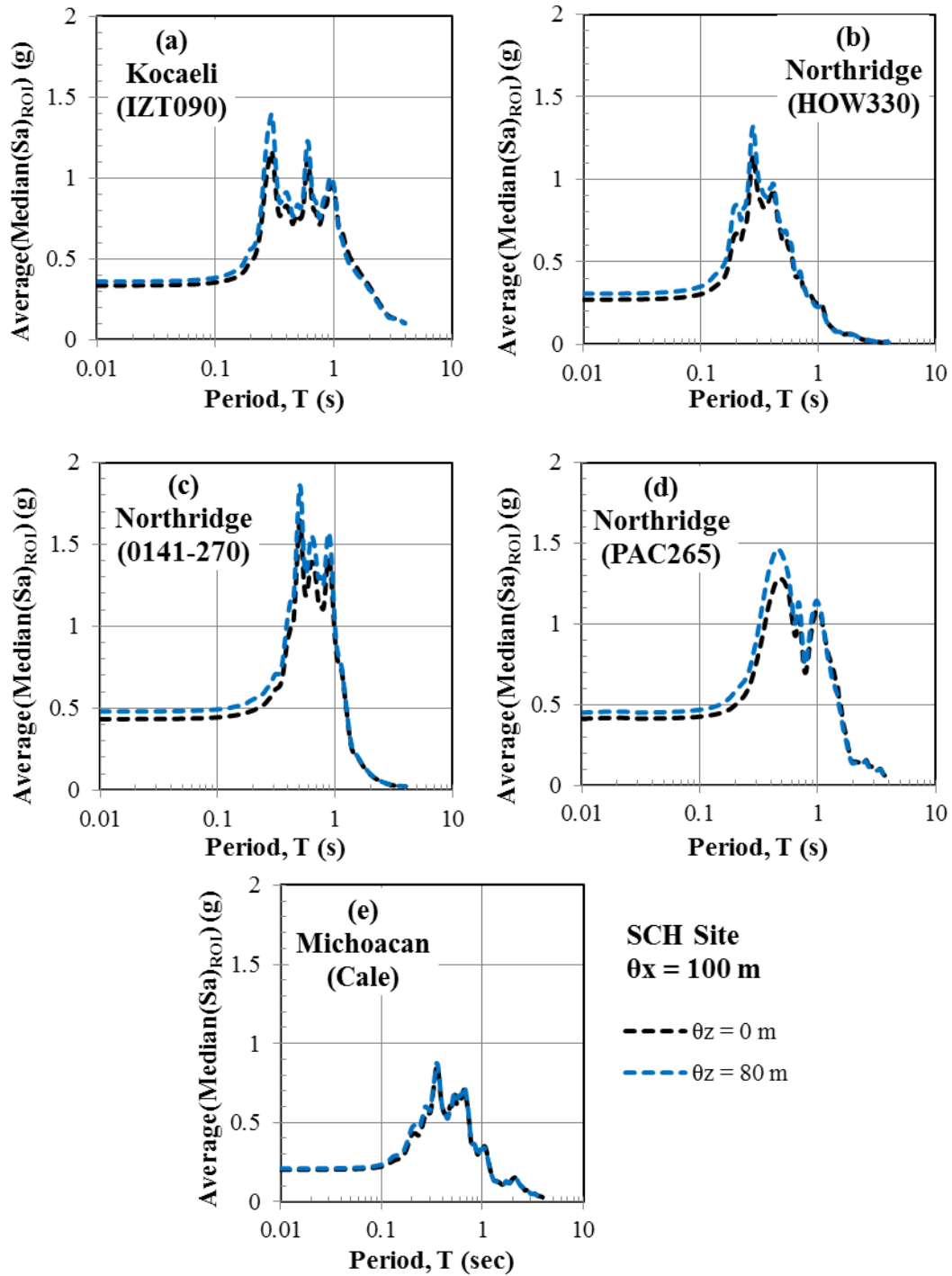


Figure 7.23 Influence of θ_z on the Average(Median(Sa)_{ROI}) of five input motions

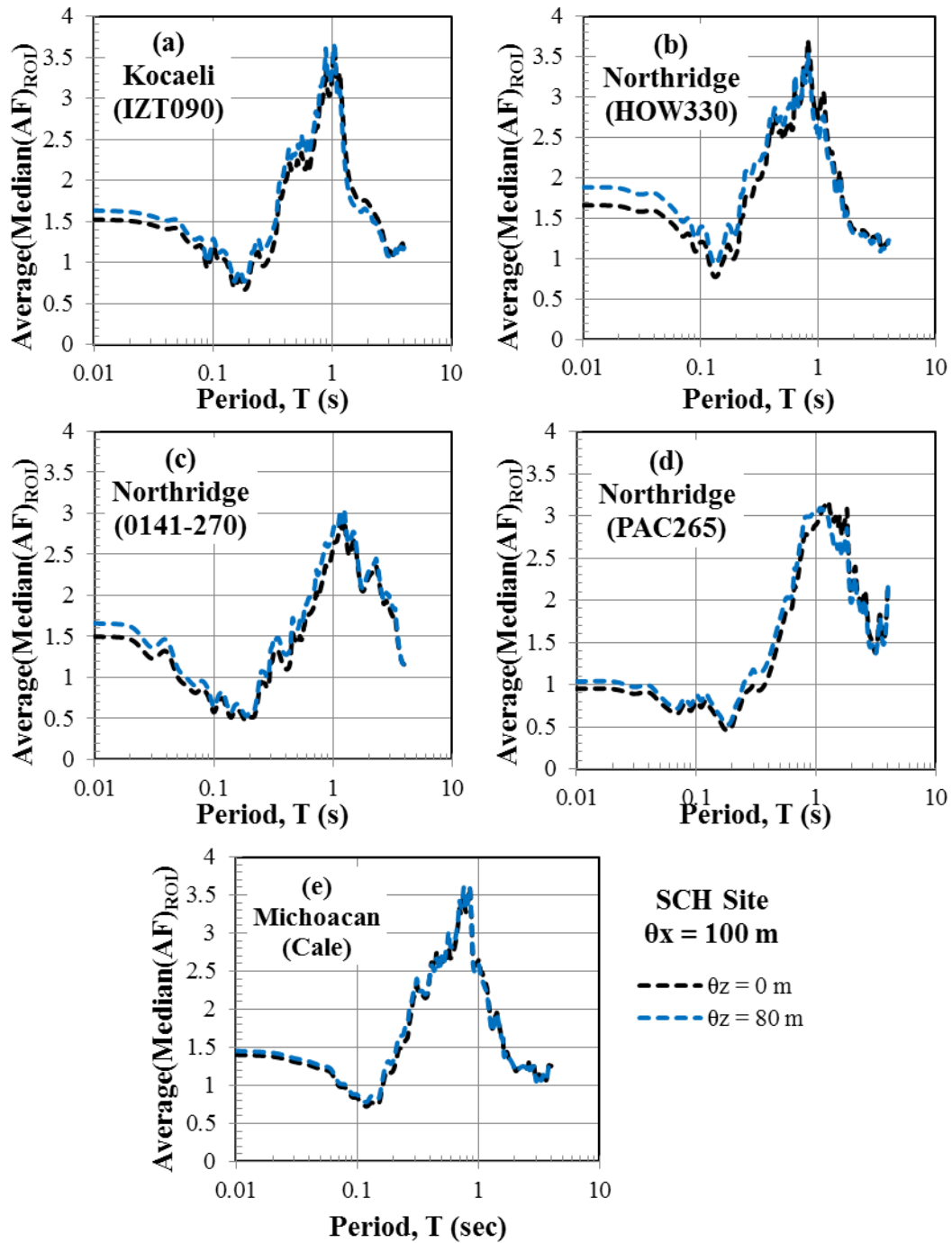


Figure 7.24 Influence of θ_z on the Average(Median(AF)_{ROI}) of five input motions

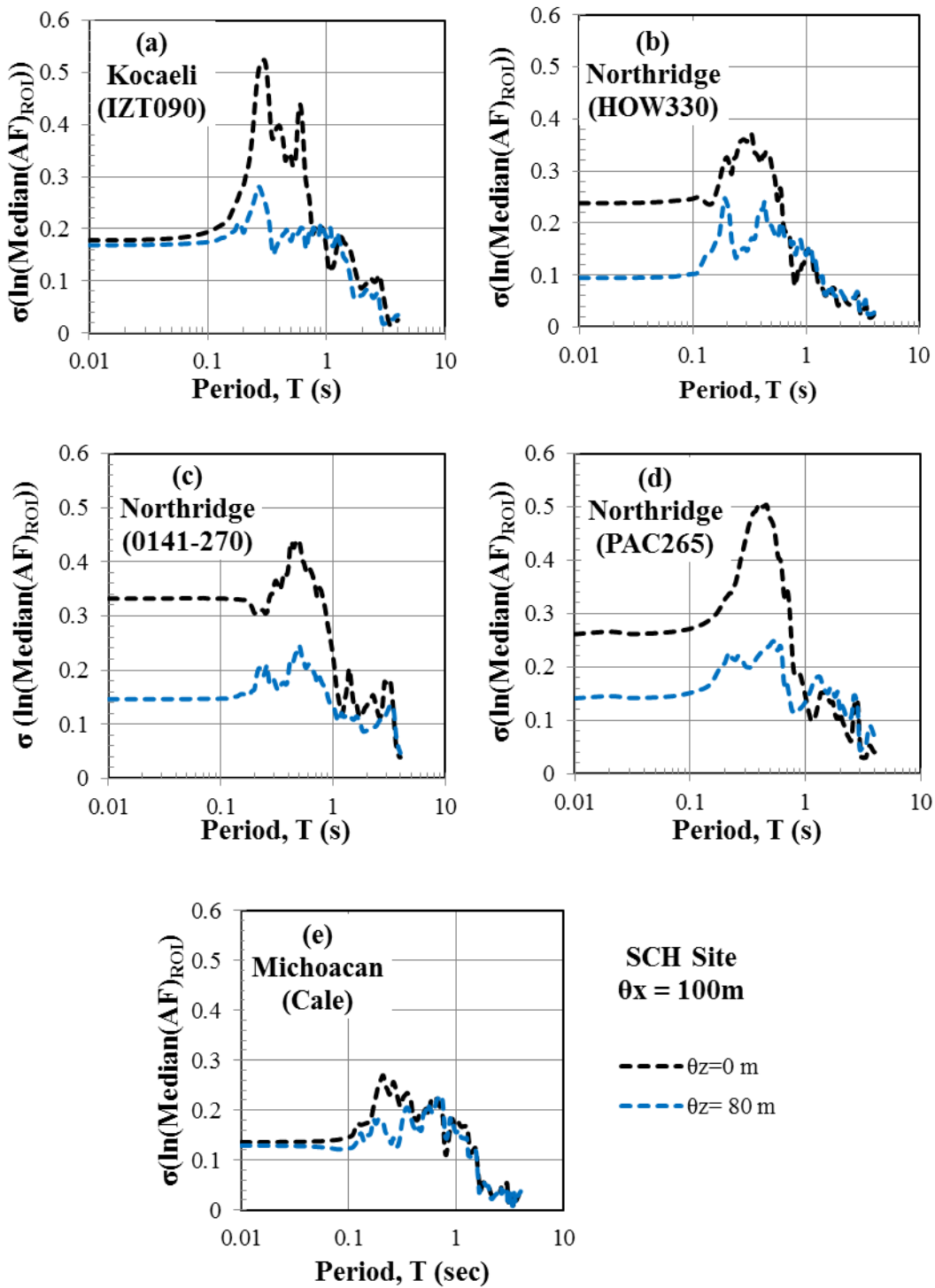
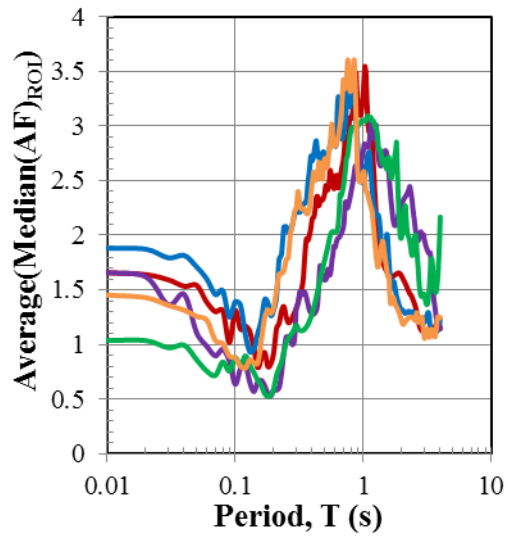
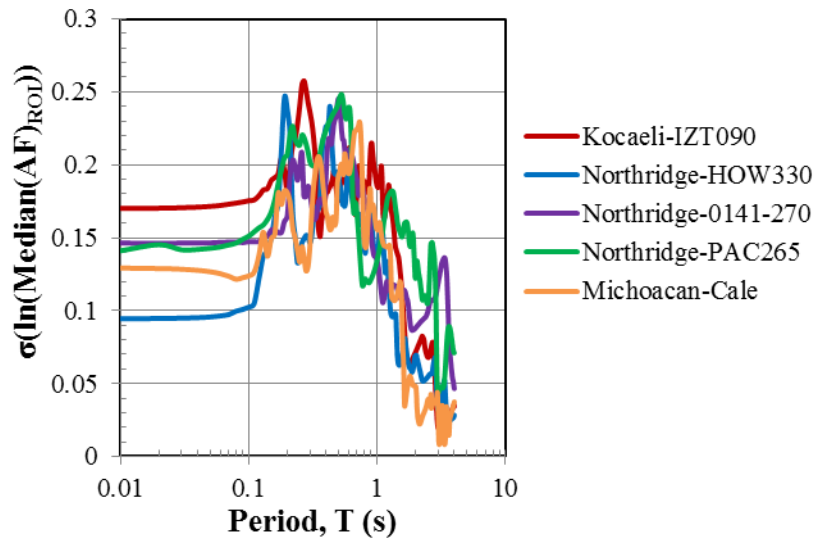


Figure 7.25 Influence of θ_z on the $\sigma(\ln(\text{Median}(AF)_{ROI}))$ of five input motions

Figure 7.26 summarizes the AF results from the 2D site response analyses for the five input motions. The results are shown for analyses performed with velocity fields generated with σ_{lnVs} of 0.2, θ_x of 100 m, and θ_z of 80 m. The peak in the Average(Median(AF)_{ROI}) ranges between 3.0 to 3.5 g at periods between 0.8 and 1.0 s. The smallest peaks are associated with the peaks at the longest period (i.e., ~ 1.0 s), indicating larger strains, more damping, and more period lengthening. These responses are induced by motions 0141-270 and PAC265, the motions with the largest intensity. Figure 7.27 plots the median strains induced across all realizations for the five input motions, and it is clear that 0141-270 and PAC265 induce the largest strains. The variability of Median(Peak Element Strain) across the velocity realizations ranges between 0.15 and 0.25 between periods of 0.1 and 1.0 s, where the largest variability is observed. The variability in median peak element strain is similar for each motion.



(a)



(b)

Figure 7.26 2D site response analysis results for 2D V_s field generated with $\sigma_{\ln V_s}$ of 0.2, θ_x of 100 m and θ_z of 80 m using five selected input motions

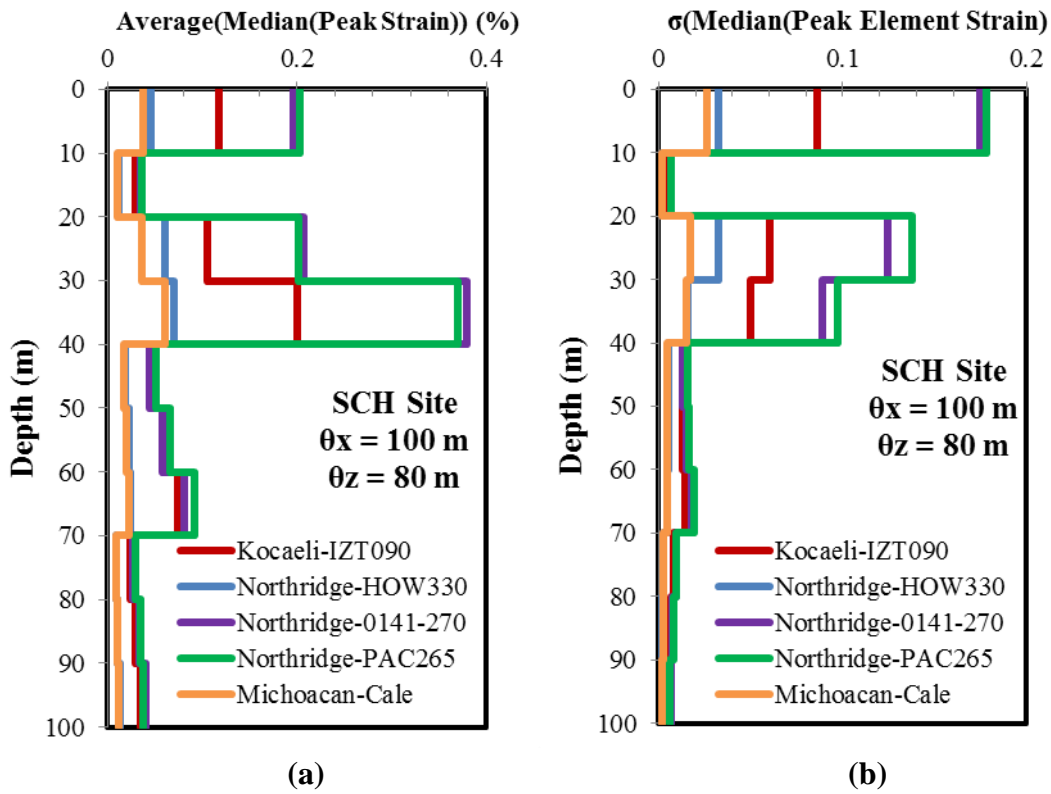


Figure 7.27 Comparison of (a) Average(Median(Peak Strain)) and (b) σ (Median(Peak Strain)) over twenty realizations for each input motion

7.6 Summary

This chapter describes 2D site response analyses performed on 2D velocity fields generated using the Monte Carlo simulation technique. The 2D velocity fields are generated using different levels of horizontal and vertical correlation, and the influence of the horizontal and vertical correlation distance on the surface response obtained across 100 m x 100 m region of interest (ROI) is investigated. The analysis result indicates that the median surface response decreases with increasing horizontal correlation distance and decreasing vertical correlation distance. The variability of the median surface response over twenty velocity realizations increases with increasing horizontal correlation distance and decreasing vertical correlation distance. The influence of vertical correlation distance on the surface response is more pronounced when the horizontal correlation distance is large. Similarly, the maximum response across the ROI decreases with increasing horizontal correlation distance and decreasing vertical correlation distance.

Two dimensional site response analyses are performed with five different input ground motions to investigate the effect of the input motion characteristics on the predicted response across the ROI. The influence of the horizontal and vertical correlation distances becomes more pronounced for input motions with larger intensity. These motions induce more nonlinearity (i.e., period lengthening and

increased damping) as the variability in the shear wave velocity field increases because the large variability realizations include more low velocity elements. As a result, the median response is reduced and some additional response variability is introduced.

8

COMPARISON OF ONE- AND TWO- DIMENSIONAL SITE RESPONSE ANALYSES WITH VARIABLE VELOCITY FIELDS

8.1 Introduction

Previous chapters have discussed the effects of shear wave velocity variability on site amplification. In one-dimensional (1D) site response analysis, the variability in the shear wave velocity is generally taken into account through multiple 1D site response analyses performed on statistically generated 1D velocity profiles. Each 1D analysis assumes that the given velocity profile extends infinitely in the horizontal direction. This approach does not reflect the condition in nature, where there exists variability in all three-dimensions. Two-dimensional (2D) site response analysis can account for the velocity variability in the horizontal direction

through the use of 2D velocity fields, although variability in the third dimension is not modeled. Similar to 1D analysis, multiple 2D analyses can be performed different realizations of statistically generated 2D velocity fields. As opposed to 1D analysis, each 2D analysis accounts for the variability in velocity in the horizontal direction.

This chapter compares the predictions of 1D and 2D site response analyses that model variability in the shear wave velocity. The SCH site is used for the analyses. The 2D site response analyses represent the results previously discussed in Chapter 7. The corresponding 1D site response analyses are performed on velocity profiles developed using two different approaches. First, 1D site response analyses are performed on one thousand realizations of 1D velocity profiles which are grouped into fifty sets of twenty realizations. The results of 1D site response analysis are similarly grouped into 50 sets of 20 realizations to estimate the confidence of in the predictions made with only twenty realizations performed for 2D analysis. Each of these 1D analyses models infinite horizontal correlation in velocity because of the 1D assumption. Results from these 1D analyses are compared with the results from 2D site response analyses performed on 2D velocity fields generated with different horizontal correlation distances. A second set of 1D site response analyses are performed that attempt to account for horizontal correlation in the velocity field. These 1D analyses are performed using sets of 1D velocity profiles that correspond to the ten columnar velocity profiles across the ROI of the 2D velocity fields. The

responses from the ten velocity profiles are averaged to represent one velocity realization with finite horizontal correlation. Each set of velocity profiles accounts somewhat for finite horizontal correlation, although the direct effect of variable adjacent velocities is not taken into account.

8.2 One-Dimensional Analysis with Infinite Horizontal Correlation

One dimensional analysis assumes infinite horizontal correlation; i.e. the same velocity extends infinitely in the horizontal direction at each depth. To statistically generate 1D velocity profiles, the Toro (1995) model is commonly used. This model assumes a log-normal distribution for shear wave velocity and assigns velocities to each layer based on a first-order, auto-regressive model and the interlayer correlation coefficient (Chapter 4). The velocity fields generated for 2D analyses in this study have used an approach that incorporates correlation distance, as discussed in Chapter 6. To equate these two approaches (i.e., correlation coefficient and correlation distance), 1D velocity fields for the SCH site were generated using vertical correlation distances between 0 and 600 m and used to

compute the equivalent interlayer correlation coefficient. For the developed velocity profiles for each vertical correlation distance, the interlayer correlation coefficient was computed based on the normalized residuals for adjacent layers. The computed interlayer correlation coefficients are plotted versus vertical correlation distance in Figure 8.1. As expected, the results clearly show an increase in the correlation coefficient with increasing correlation distance. Considering the vertical correlation distances of 0 m, 80 m, and 600 m used in the 2D analyses, the corresponding correlation coefficients are 0.0, 0.8, and 1.0. These correlation coefficients are used in the 1D analyses.

For each correlation coefficient considered, one thousand 1D velocity realizations are generated for the 1D analysis, and the results of the 1D analyses are grouped into 50 sets of 20 realizations. Sets of twenty 1D velocity realizations are used for consistency with the previous 2D Monte Carlo simulations and developing a large set of twenty realizations allows for the assessment of the uncertainty in the computed response (median and standard deviation) across a single set of twenty realizations. This assessment regarding the uncertainty in the computed response is performed using 1D analysis because 1D analysis can be performed very quickly as compared with 2D analysis but still captures the main components of uncertainty as 2D analysis. As a result, the uncertainty quantified via the 50 sets twenty 1D realizations is considered representative to the uncertainty in sets of twenty 2D realizations.

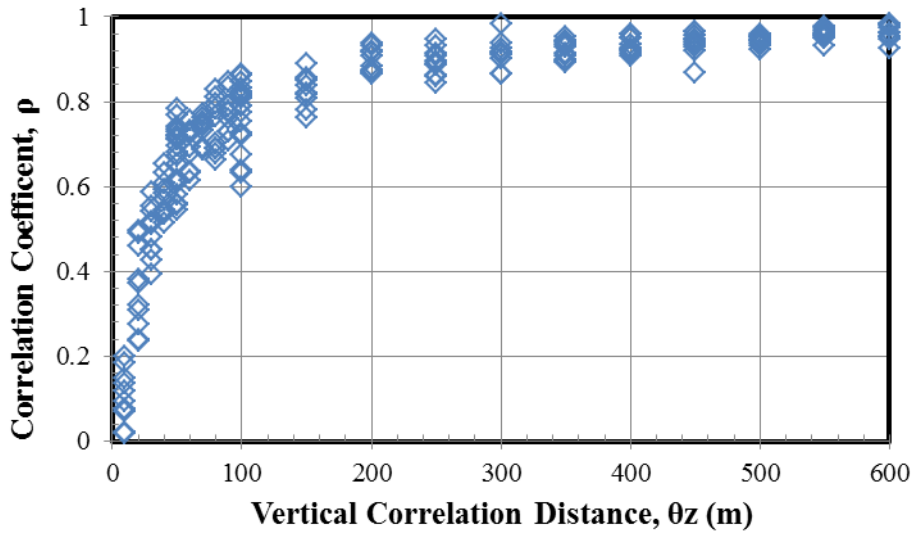


Figure 8.1 Correlation coefficients corresponding to the vertical correlation distances used to generate 2D velocity field.

The 1,000 1D velocity profiles are generated using the Toro (1995) velocity model integrated in Strata (Kottke and Rathje, 2008). Velocity profiles are generated for the SCH site with σ_{lnV_s} of 0.2 and vertical interlayer correlation coefficients (ρ) of 0.0, 0.8 and 1.0. Figure 8.2 presents twenty 1D velocity profiles from a single set of 20 velocity realizations out of 50 sets generated with the different correlation coefficients. The velocity profile for SCH includes 4 main velocity layers, and in each realization velocities are assigned to sub-layers in 10-m increments. As the vertical correlation coefficient increases, the shear wave velocity variability across adjacent sub-layers decreases. No vertical variability is observed between sub-layers

when the vertical correlation coefficient is 1.0 (Figure 8.2c) and significant variation is observed between adjacent sub-layers when the vertical correlation distance is 0.0 (Figure 8.2a). The median velocity profile predictions of each 50 set of 20 realizations are shown in Figure 8.3 for the velocity profiles generated with different correlation coefficients. The variability across the 50 median V_s profiles represents the uncertainty associated with a single set of 20 realizations and this uncertainty is similar for realizations generated with each correlation coefficient.

Each set of the twenty velocity realizations for each correlation coefficient is subjected to the Kocaeli input motion. The median Sa and AF for each set of 20 velocity realizations are averaged across the 50 sets of velocity realizations and shown together in Figure 8.4, along with the deterministic response obtained from the baseline velocity profile without any shear wave velocity variability. The median Sa and AF across the twenty realizations is largest for the deterministic analysis and decreases when the velocity variability is introduced in the analysis (Figure 8.4a and 8.4b). This effect is more clearly shown by normalizing the median AF for each p by the AF from the deterministic analysis with no variation (i.e., $\sigma_{lnV_s} = 0.0$, Figure 8.4c). The reduction due to velocity variability is the largest at the period of maximum Sa (~ 0.25 s) and a smaller reduction is observed at the site period (~ 1.0 s). These reductions are on the order of 10% to 30%. An increase in response of about 5% to 10% is observed at periods longer than the site period. The smallest

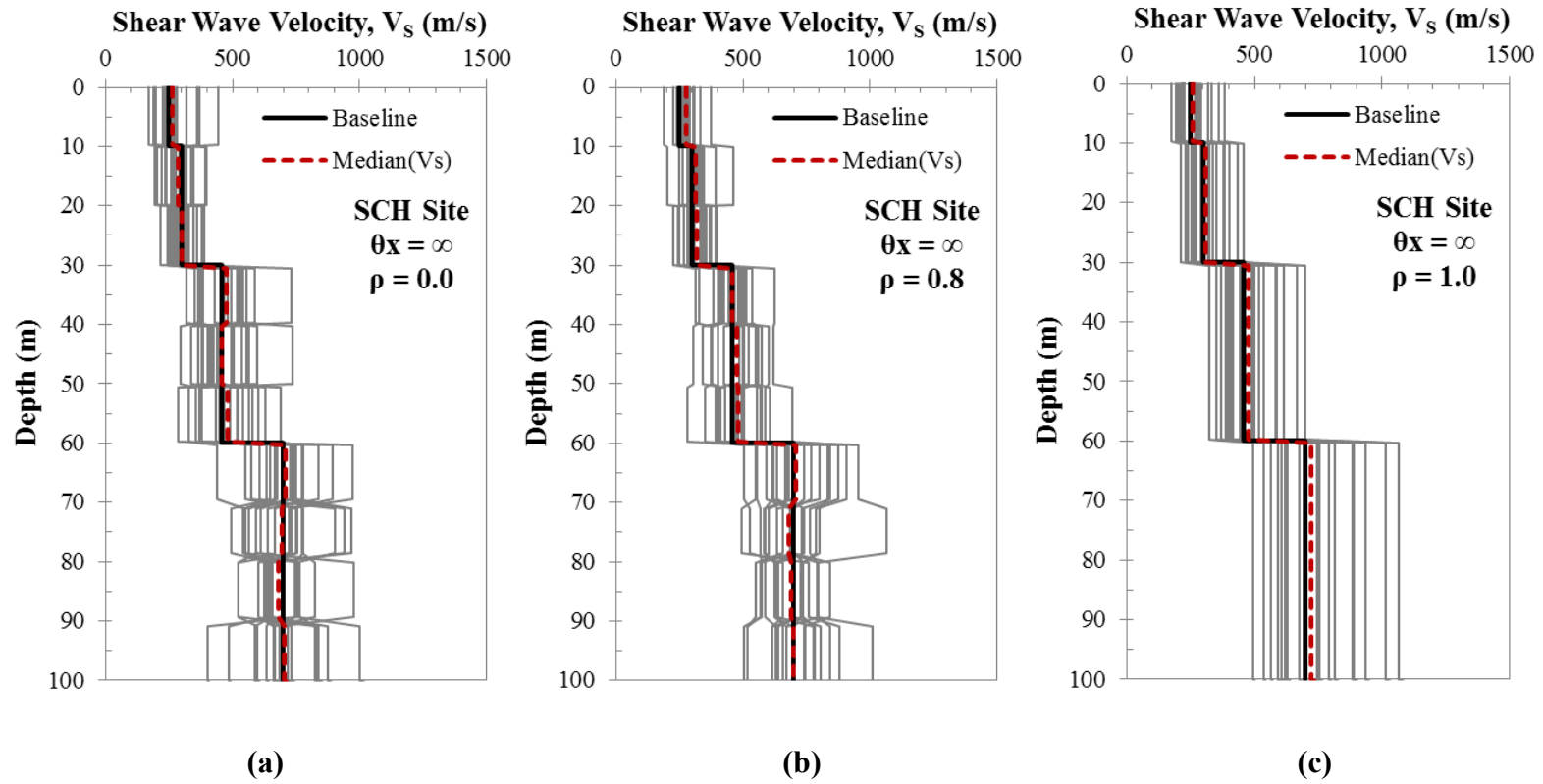


Figure 8.2 Shear wave velocity profiles in a generated set of 20 realizations for 1D analysis with ρ of: (a) 0.0, (b) 0.8 and (c) 1.0

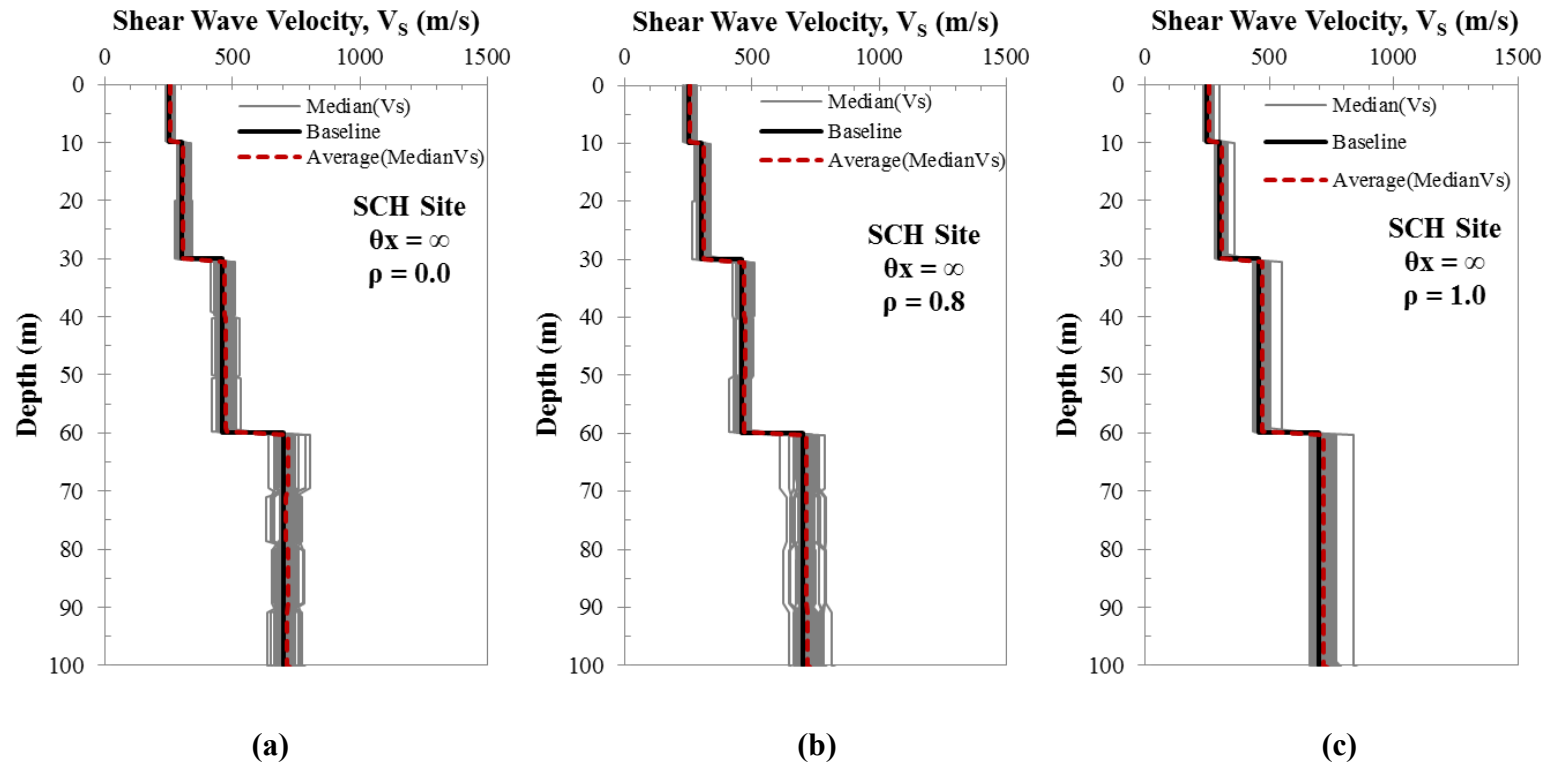


Figure 8.3 Median Shear wave velocity profiles from the 50 sets of 20 realizations generated for 1D analysis with ρ of: (a) 0.0, (b) 0.8 and (c) 1.0

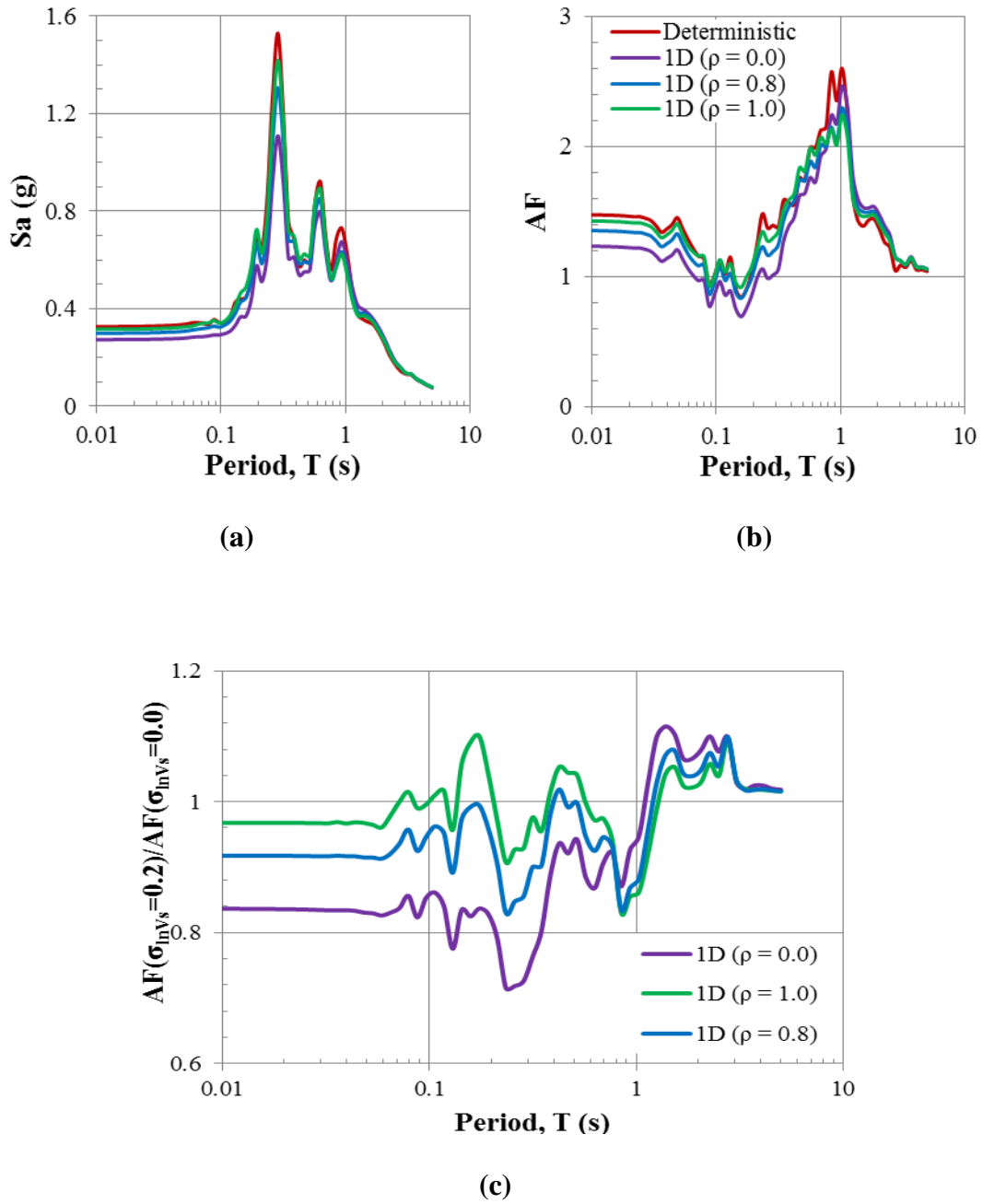


Figure 8.4 Median 1D responses from twenty shear wave velocity realizations generated with different ρ

response at short periods is obtained for the analysis performed with $\rho = 0.0$. The smaller response at shorter periods when the shear wave velocity is varied particularly for $\rho = 0.0$, is due to the fact that the different velocity profile realizations will have some softer layers, and these layers will strain more and induce more damping that lead less high frequency amplification. While realizations with stiffer layers also are present, these realizations do not lead to large enough responses to balance the smaller responses from the realizations with smaller velocities.

The standard deviation of $\ln(AF)$, $\sigma_{\ln AF}$, across twenty velocity realizations is plotted in Figure 8.5. Here, the average $\sigma_{\ln AF}$ across the 50 sets of twenty velocity realizations is shown for each value of ρ together with the 95th percentile confidence bounds. Over the period range of 0.3 s to 1.0 s $\sigma_{\ln AF}$ is largest for $\rho = 0.0$ and smallest for $\rho = 1.0$, while at periods between about 0.2 s and 0.3 s $\sigma_{\ln AF}$ is similar for $\rho = 0.0$ and $\rho = 1.0$ and at periods between about 0.1 s and 0.2 s $\sigma_{\ln AF}$ is largest for $\rho = 1.0$. To help explain the effect of ρ on the response variability, 1D site transfer functions are shown in Figure 8.6 for twenty velocity realizations for $\rho = 0.0$ and $\rho = 1.0$. Each velocity profile for $\rho = 0.0$ generates a transfer function of a different shape while each velocity profile for $\rho = 1.0$ generates basically the same transfer function but shifted to different periods. As a result of the groupings of peaks and valleys for $\rho = 1.0$, there are some periods that have less variability (i.e.,

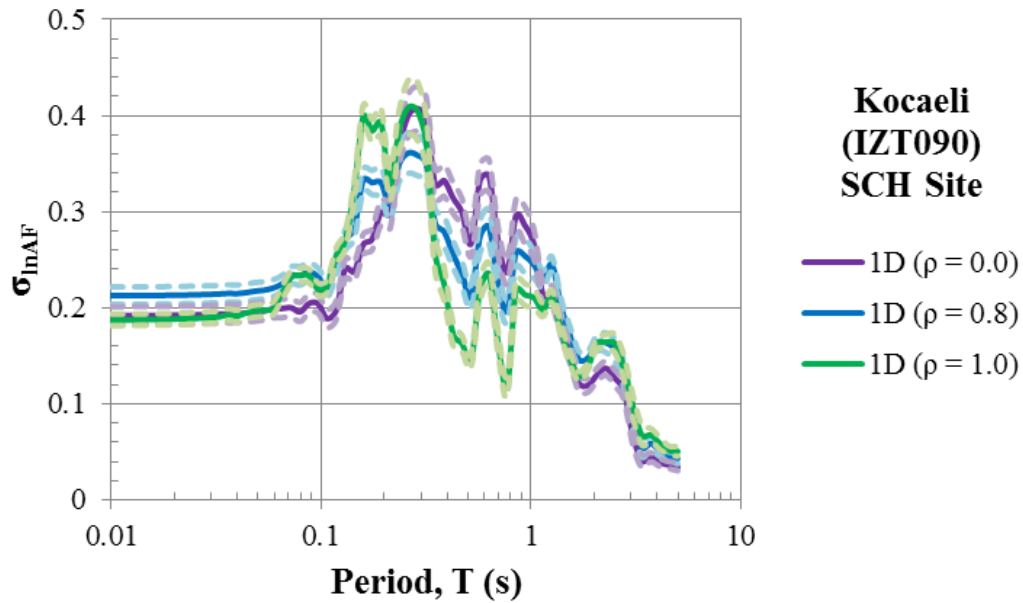
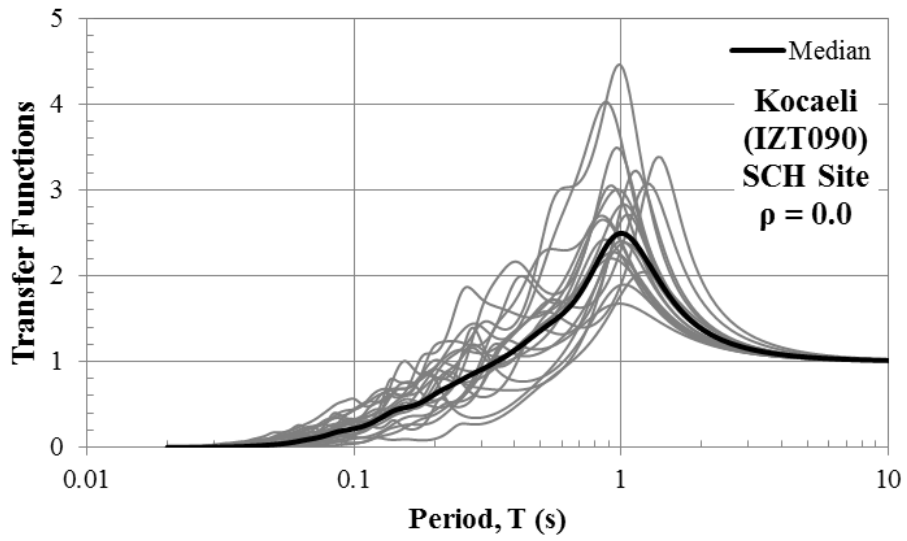


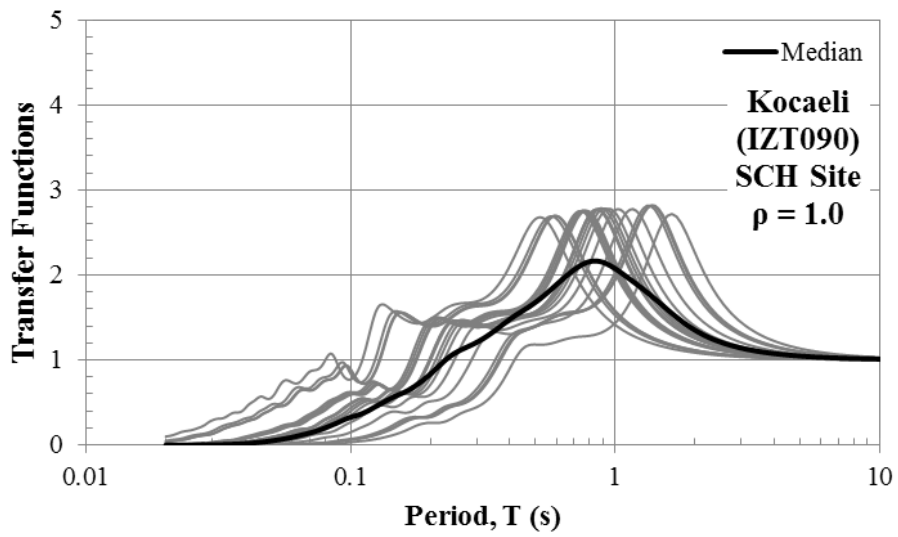
Figure 8.5 σ_{lnAF} from 1D analysis of twenty shear wave velocity realizations generated with different ρ

~ 0.4 s) and there are other periods that have more variability (i.e., ~ 0.2 s). These differences directly lead to the changes in σ_{lnAF} observed in Figure 8.5.

The confidence bounds for σ_{lnAF} in Figure 8.5 are very small except over the period range of 0.2 to 0.3 s which corresponds to the peak in the surface response spectrum. The larger confidence interval indicates that the response is most variable over this period range and thus the estimates of σ_{lnAF} most uncertain.



(a)



(b)

Figure 8.6 Comparison of the transfer functions of 20 velocity realizations generated with $\rho = 0.0$ and $\rho = 1.0$

The calculation of the responses of 50 sets of twenty velocity realizations allows for an evaluation of the variability in results between different sets of realizations. The standard deviation in the computed median AF ($s_{\hat{\mu}_{AF,50}}$) and the standard deviation in the computed σ_{lnAF} ($s_{\hat{\sigma}_{lnAF,50}}$) across the 50 sets of velocity realizations are shown in Figure 8.7 along with the coefficient of variation (COV, COV = standard deviation / mean). The $s_{\hat{\mu}_{AF,50}}$ (Figure 8.7a) range from about 0.04 to 0.12, which corresponds to COV of 0.04 to 0.09 (Figure 8.7b). These values indicate that the median AF predictions for a single set of 20 velocity realizations can show 5% to 10% variation. The $s_{\hat{\sigma}_{lnAF,50}}$ (Figure 8.7c) range from about 0.02 to 0.1, with the largest values occurring around a period of 0.3 s. These values of $s_{\hat{\sigma}_{lnAF,50}}$ correspond to COV of 0.1 to 0.2 (Figure 8.7d) except at periods greater than 2.0 s. The larger COV at longer periods is due to the smaller σ_{lnAF} values at these periods. The COV values for σ_{lnAF} are about twice as large as for the mean AF , indicating a single set of 20 velocity realizations has more uncertainty in the σ_{lnAF} prediction compared to median AF prediction. Based on the COV, 10% to 20% differences in the σ_{lnAF} predictions can be expected between different sets of 20 velocity realizations.

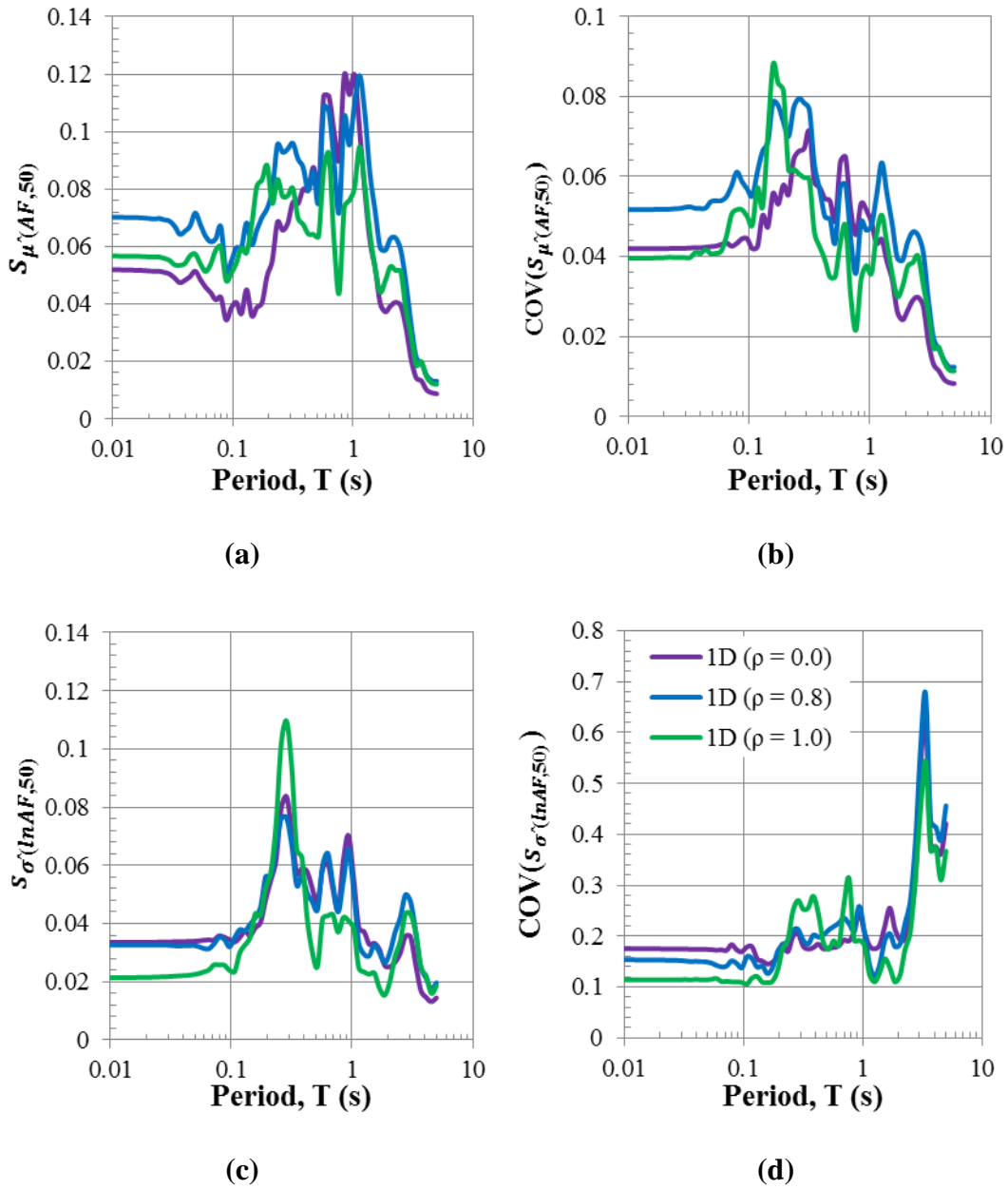


Figure 8.7 Standard deviation and COV of median AF and σ_{lnAF} predictions of 1D analyses across 50 sets of 20 realizations

Figure 8.8 compares the amplification factor results from 1D analysis with results from 2D analyses with different horizontal correlation distances. The 1D results represent the average of 50 sets of 20 velocity realizations, while the 2D results represent the response over a single set of 20 realizations. Because the 2D results are only based on a single set of velocity realizations, the computed responses are more uncertain. Based on the $s_{\hat{\mu}_{AF,50}}$ in Figure 8.7a, the 95% confidence bounds for the median AF from a single set of 20 velocity randomizations should be about 0.1 to 0.2. Based on the $s_{\hat{\sigma}_{\ln AF,50}}$ in Figure 8.7c, the 95% confidence bounds for the $\sigma_{\ln AF}$ from a single set of 20 velocity randomizations should be about 0.06 to 0.2. These confidence intervals should be taken into account when comparing the results from the 1D and 2D analyses.

Figure 8.8a compares the median AF results for velocity fields with no vertical correlation (i.e., $\rho = 0.0$, $\theta_z = 0$ m). For this case, 1D analysis predicts less amplification compared to the 2D analysis (i.e., about 30% less at the site period). The 2D amplification predictions decrease with increasing horizontal correlation distance, but the smallest 2D amplification is still larger than the 1D amplification (i.e., the 1D analysis is still about 15% smaller at the site period). One reason why 1D analysis predicts smaller amplification is that low velocity layers within a realization extend infinitely in the horizontal direction, which impedes vertical propagation of motion. For 2D analysis, a 2D velocity fields will have stiffer elements adjacent to softer elements even when using large horizontal correlation

distances. Therefore, low velocity elements within 2D analysis do not impede motion as much as low velocity layers in 1D analysis. Figure 8.8b compares σ_{lnAF} across twenty velocity realizations for the 1D and 2D analyses with no vertical correlation. These results show that the variability from 1D analysis is slightly lower than the variability from 2D analysis for horizontal correlation distances of 100 m and 600 m, although the differences are close to the confidence bounds for the 2D analysis. The variability from 2D analysis is significantly smaller for a horizontal correlation distance of 0 m.

Figure 8.8c compares the 1D and 2D amplification factors for $\rho = 0.8$ (1D) and $\theta_z=80$ m (2D). Again the 1D analyses fall below the 2D results, with the 1D analyses predicting about 30% to 50% smaller amplification at the site period. The σ_{lnAF} for this case (Figure 8.8d) is similar for the 1D and 2D analyses, except for the 2D analyses with $\theta_z=0$ m. The results for $\rho = 1.0$ (1D) and $\theta_z=600$ m (2D) are shown in Figure 8.8e. Again, 1D analysis predicts smaller amplification than 2D analysis. The σ_{lnAF} is shown in Figure 8.8f and the values from 1D analysis are similar to that from 2D analysis with a horizontal correlation distance 600 m. Again, the variability from 2D analysis with $\theta_x=0$ m is much smaller.

The results presented in Figure 8.8 are obtained for a single input ground motion. Different input motions with different intensities and spectral shapes may generate different results, and thus further analyses are performed with the additional four input motions described in Chapter 7. Additionally, the variability in the

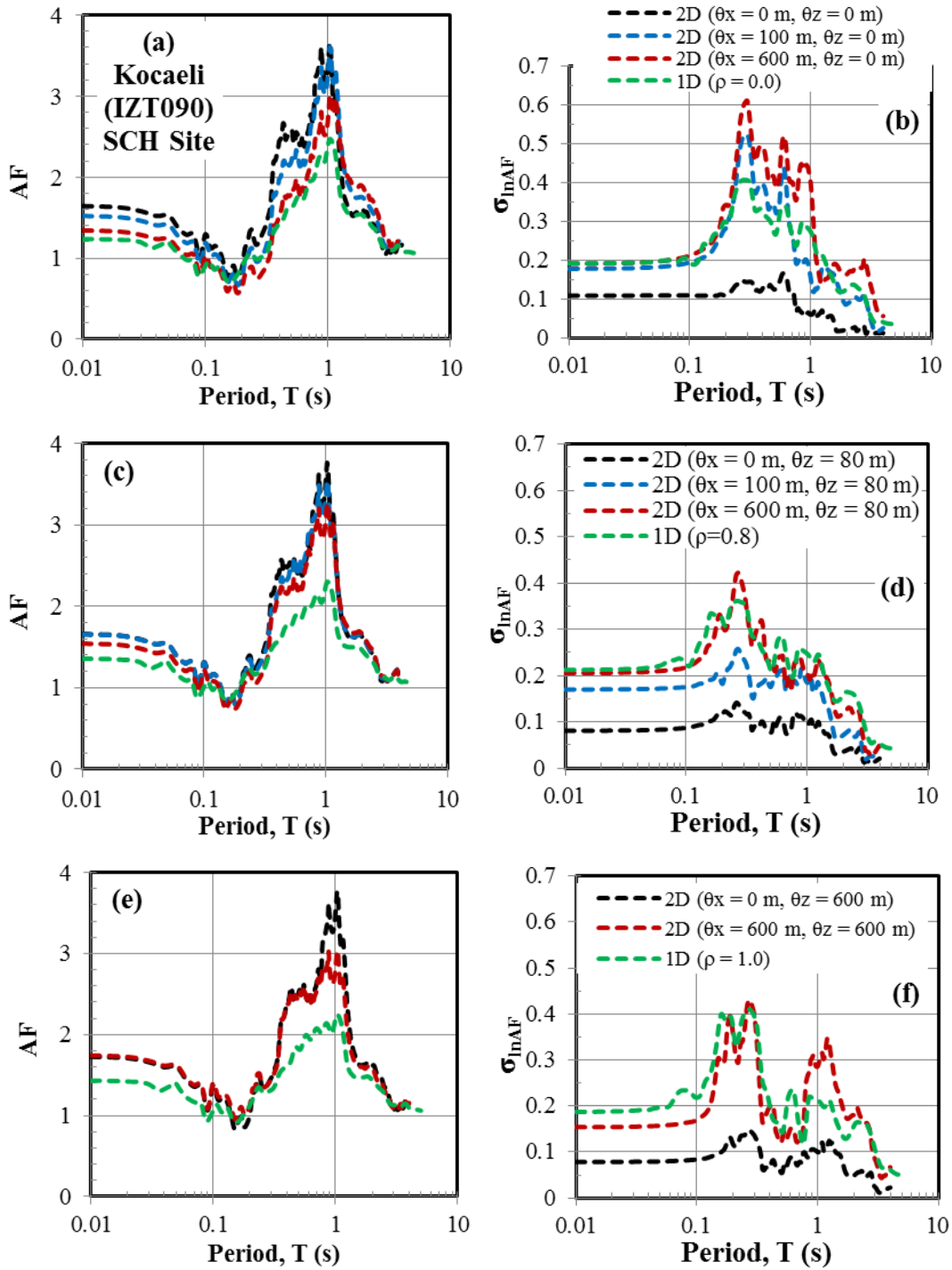
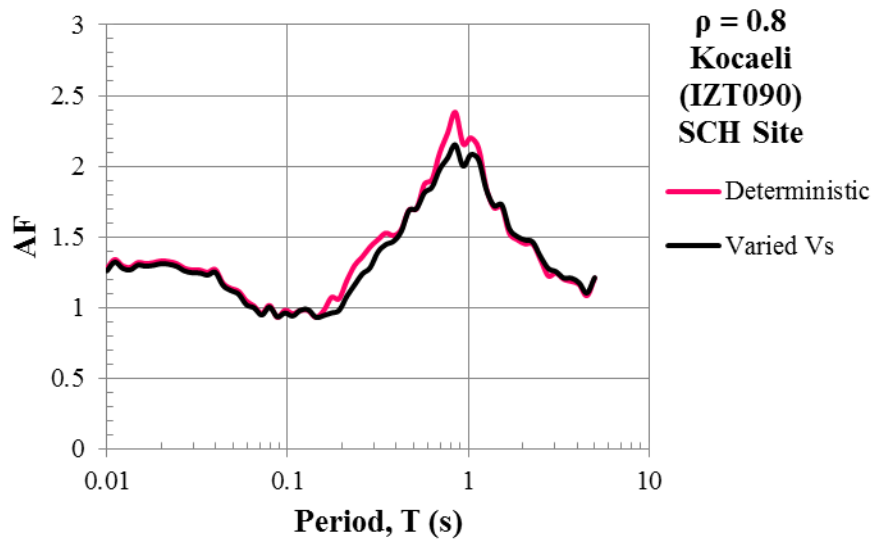


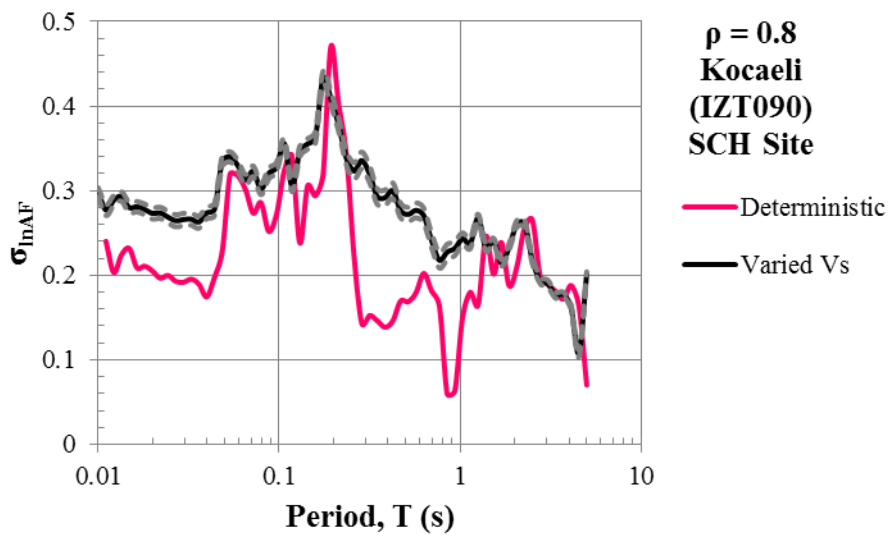
Figure 8.8 Comparison of 2D and 1D analysis results for different ρ

computed amplification factors will be influenced by both motion-to-motion variability as well as shear wave velocity variability. Performing Monte Carlo simulations with these additional input motions will allow these two sources of variability to be investigated together. Thus, 1D site response analyses are performed with the additional four input motions introduced in Chapter 7 and using 50 sets of twenty 1D velocity profiles generated with $\rho = 0.8$.

Figure 8.9 presents the median AF and σ_{lnAF} across 5 input motions and twenty velocity realizations from 1D analysis. The values shown are the average across the 50 sets of twenty velocity realizations. Also shown is the deterministic AF and σ_{lnAF} across 5 input motions computed for the baseline velocity profile. The median AF across the 5 input motions is very similar for the varied velocity profiles and the deterministic analyses, except at the site period. The σ_{lnAF} across the 5 motions is generally larger when shear wave velocity variability is included except at longer periods where the velocity variability does not influence the response.



(a)



(b)

Figure 8.9 Median AF and σ_{InAF} for five input motions for 1D analyses of velocity profiles generated with $\rho = 0.8$ and 1D deterministic analyses with no velocity variability.

The results of 1D analyses with motion-to motion variability and shear wave velocity variability (i.e., Figure 8.9) are compared to the corresponding results from 2D analysis with motion-to motion variability for 2D velocity fields generated with $\theta_x = 100$ m and $\theta_z = 80$ m. Figure 8.10 compares the median and σ_{lnAF} predictions obtained over the 5 input motions and 20 velocity realizations. The 95% confidence intervals are also shown in Figure 8.10 and note that the confidence intervals for the 2D analysis are larger than for the 1D analysis because the 2D analyses are based on only a single set of 20 velocity realizations.

The median AF from 2D analysis is generally larger than from 1D analysis, with the 2D analysis as much as 55% larger than the 1D analysis around the site period (Figure 8.10a). However, the level of σ_{lnAF} is similar for 1D and 2D analyses. Although there are some differences in the σ_{lnAF} from 1D and 2D analyses, the 1D results are generally within the confidence bounds for the 2D analysis.

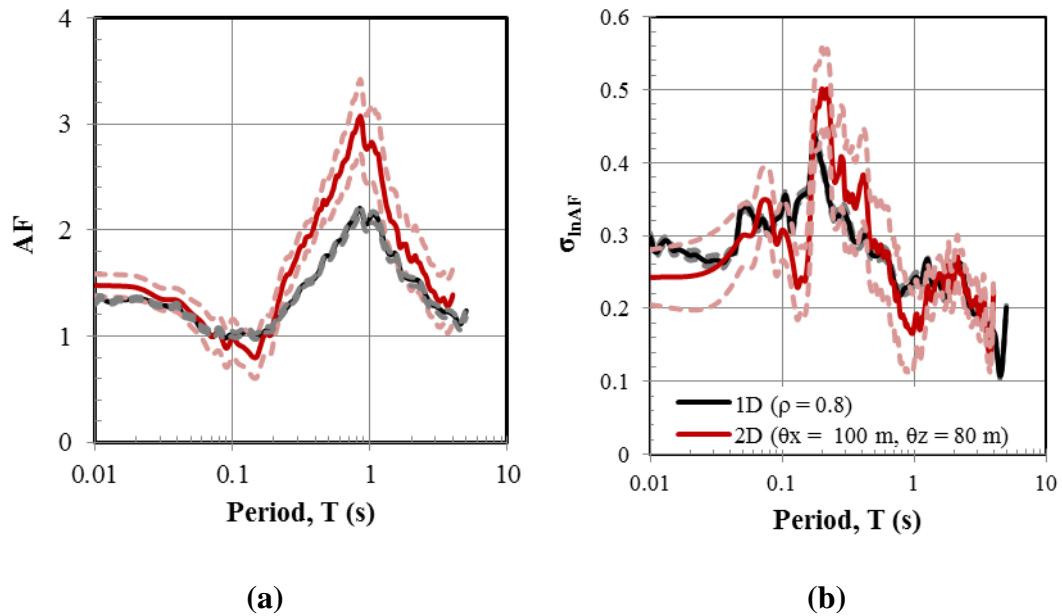


Figure 8.10 Comparison of *AF* predictions of 1D and 2D analysis results; reflecting both variability in shear wave velocity and the input motion.

8.3 One-Dimensional Analysis with Finite Horizontal Correlation

One reason that 1D analysis is predicting smaller amplification than 2D analysis is because 1D velocity realizations with low velocity layers impede the propagation of motion. A simple approach to account for 2D horizontal variations in velocity in 1D analysis is to perform multiple 1D analyses for horizontally correlated

velocity profiles and then average these responses across the ROI to represent the response to a single 2D velocity realization. To investigate this approach, 1D site response analyses are performed for the velocity fields generated for 2D site analysis with vertical and horizontal correlation distances of 80 m and 100 m, respectively. In this approach, a 2D velocity field is generated for the 2D finite element mesh shown in Figure 8.11a and the velocity profiles from the 10 one-dimensional soil columns across the ROI (Figure 8.11b) are used as input into 1D analysis (Figure 8.11c). One dimensional analysis performed on these 10 velocity profiles are averaged (in space) to represent the surface response across the ROI, similar to the approach used in 2D analysis where the surface response across the ROI is represented by the average response across 11 nodes across the ROI for each 2D velocity realization. While the velocity field modeled through the multiple 1D analyses will represent a horizontal correlation distance of 100 m, the 1D analysis results will not account for the 2D dynamic interaction between adjacent elements with different velocities.

The 1D site response analyses are performed with QUAD4M (Hudson et al., 1994) for each single column within each 2D velocity field realization, such that no difference in the solution procedure (i.e., time domain vs. frequency domain) is introduced. The 1D site response analyses are processed in a similar way to the 2D analyses; the median surface response across the ROI is computed as well as the average and standard deviation of these values across the twenty velocity realizations.

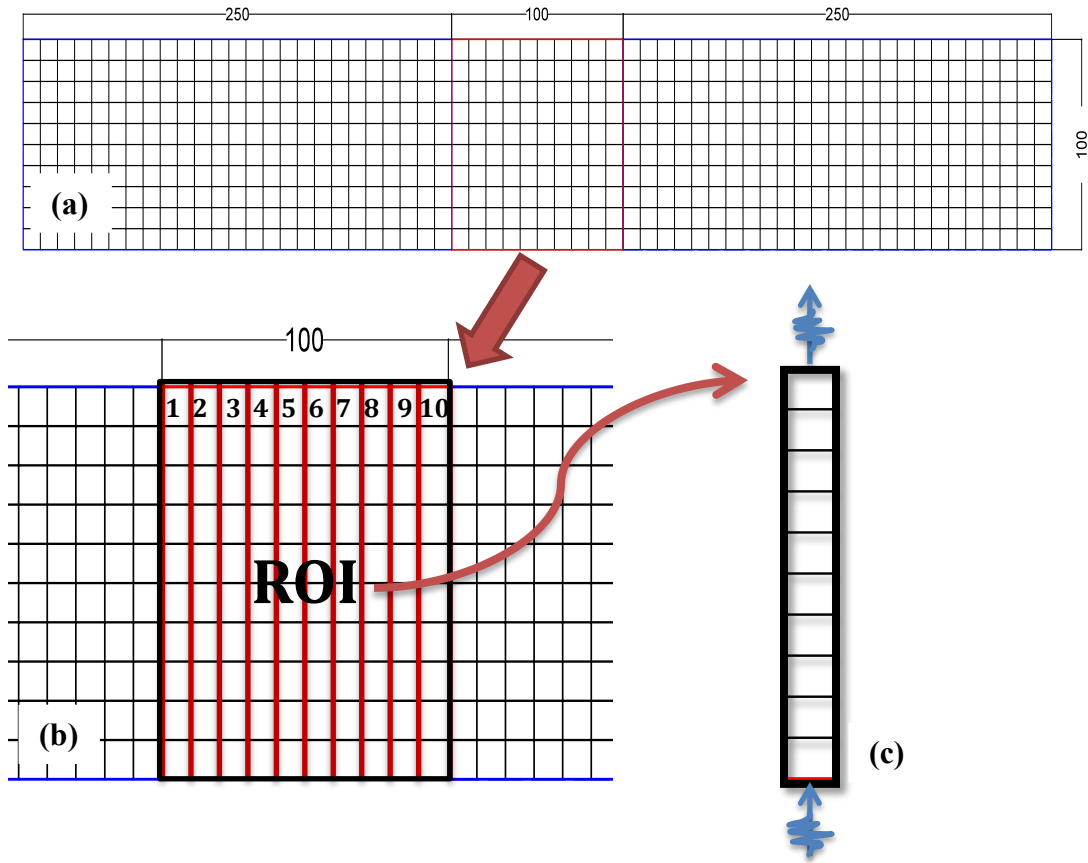


Figure 8.11 One-dimensional velocity profiles with finite horizontal correlation obtained from 2D velocity field realization

Figure 8.12 compares the 1D and 2D responses across the twenty 2D velocity realizations. The average response (i.e., Sa and AF) obtained from 1D analysis is somewhat smaller than from 2D analysis, with the largest discrepancy of 15% observed around the site period (Figure 8.12a). The σ_{lnAF} for the 1D analysis displays one major peak around a period of 0.3 s, which is about 23% larger than the

2D analyses prediction (Figure 8.12c). Two-dimensional analysis has a secondary peak in σ_{lnAF} around the site period of 1.0 s, which is not visible for 1D analysis. At this period the σ_{lnAF} from 2D analysis is about 40% larger than from 1D analysis.

Figure 8.13 compares the results from 1D analysis performed on 2D velocity fields with finite horizontal correlation (i.e., Figure 8.12), 1D analysis performed on 1D velocity profiles with infinite horizontal correlation (Figure 8.4), and 2D analysis performed on 2D velocity fields. These results show that 1D analysis of a 2D velocity field with finite horizontal correlation (i.e., $\theta_x = 100$ m) provides a larger response than 1D analysis of a 1D velocity field with infinite correlation (i.e., $\theta_x = \infty$ m), and this response is closer to the 2D response. The remaining discrepancy between the 1D and 2D analyses is most likely due to 1D analysis not capturing the 2D interactions between adjacent elements of different velocity. The σ_{lnAF} from 1D analysis changes substantially when the horizontal correlation is included. The σ_{lnAF} from 1D analysis decreases when modeling $\theta_x = 100$ m, and the σ_{lnAF} from 1D analysis with $\theta_x = 100$ m is more similar to that from 2D analysis.

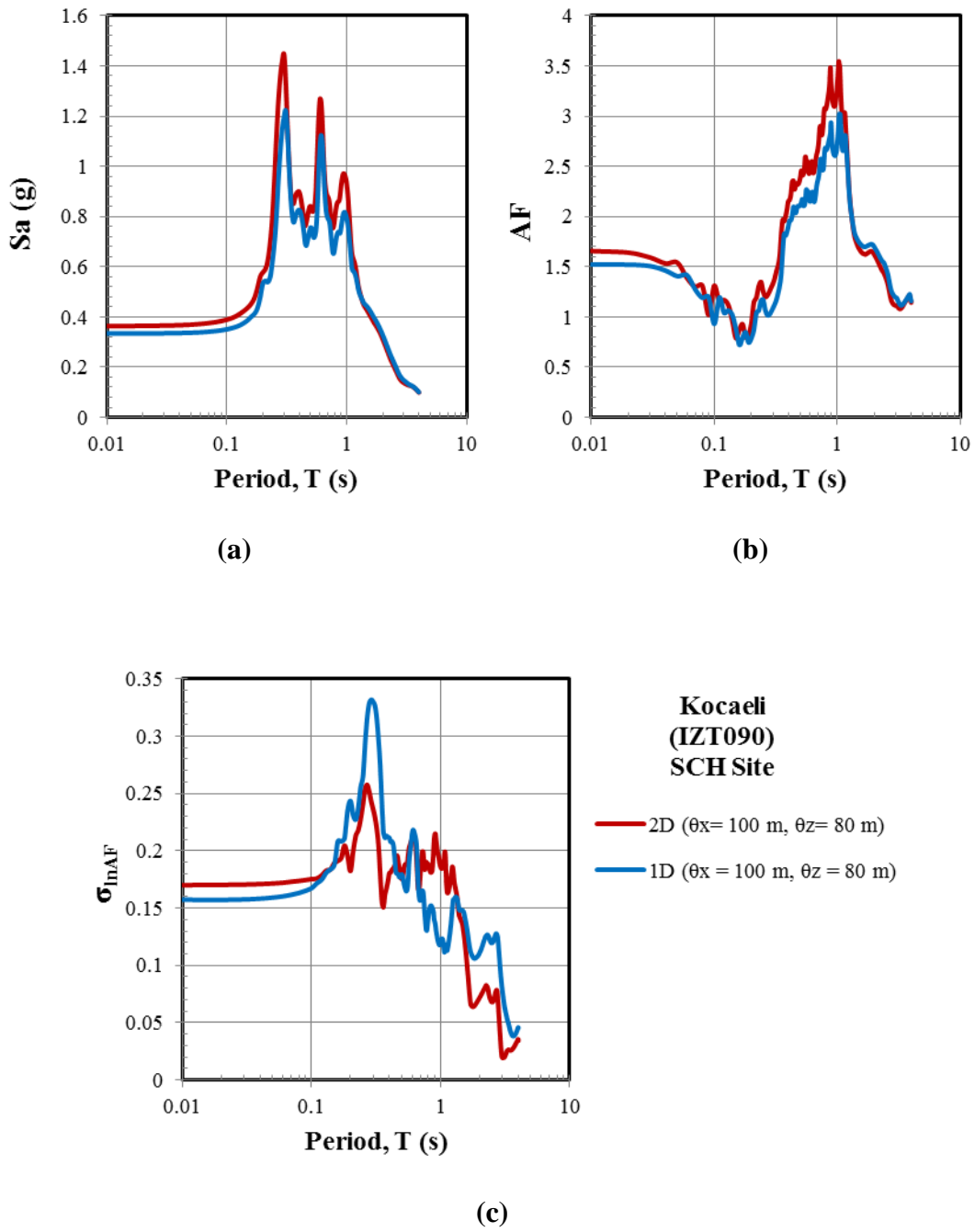


Figure 8.12 Comparison of 1D and 2D site response analyses performed on twenty velocity fields generated with horizontal correlation distance of 100 m

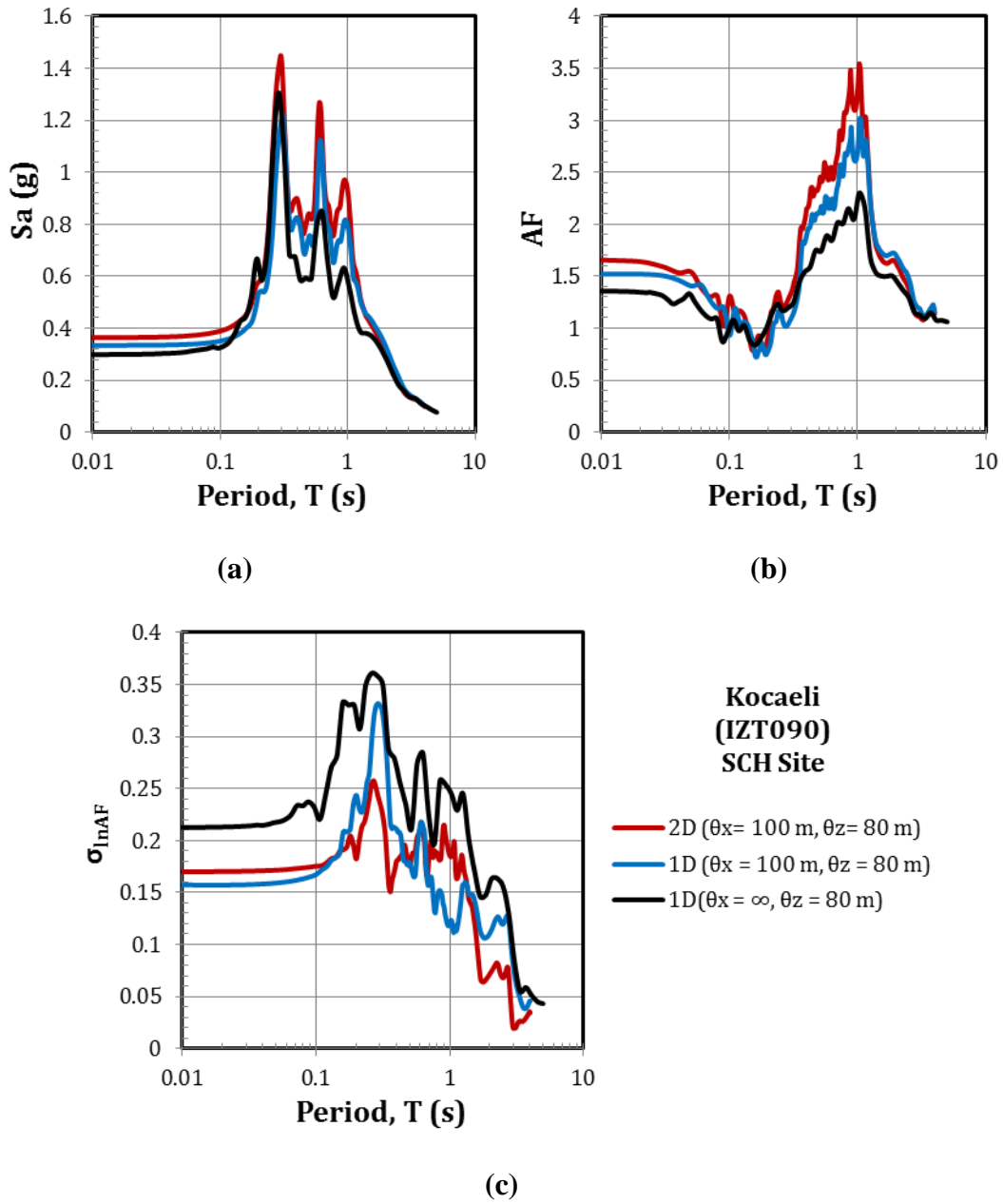


Figure 8.13 Comparison of results of 2D and 1D analysis performed on velocity fields with finite and infinite horizontal correlation distances

8.4 Summary

This chapter compares the results from 1D and 2D site response analyses that model the spatial variability in the shear wave velocity through Monte Carlo simulation. One-dimensional site response analyses are performed initially on 1D velocity fields with infinite horizontal correlation, which is the traditional approach to account for the shear wave velocity variability in a site. These results are compared with 2D analyses performed on 2D velocity fields for five different input motions. An additional set of 1D analyses are performed on velocity profiles generated with finite horizontal correlation. These analyses are also compared with 2D analyses.

9

SUMMARY, CONCLUSIONS, AND RECOMMENDATIONS FOR FUTURE WORK

9.1 Summary

Design of important structures such as nuclear facilities requires estimation of design ground motions corresponding to a specific hazard level at the ground surface based on probabilistic seismic hazard analysis. To assess ground shaking at the surface, the effects of the local soil conditions at the site must be taken into account. The common approach to account for these conditions is to perform site response analyses for the local soil conditions using as the input motion the uniform hazard spectrum for the rock level below the soil column. However, this approach does not account for the variability of site properties or the variability in the potential

site amplification. Bazzurro and Cornell (2004b) suggested integration of site response analysis into the probabilistic seismic hazard analysis through convolution of the rock hazard curve and a site amplification model. This site amplification model is derived from one-dimensional (1D) site response analyses performed on statistically varied shear wave velocity profiles for a site. The model includes a median prediction of amplification (AF) as a function of input motion intensity, as well as the variability in the amplification model represented by σ_{lnAF} . The main objectives of this study were: (1) to compare the different site amplification models and associated hazard curves developed from different site response methods and (2) to investigate the effects of one-dimensional and two-dimensional shear wave velocity variability on site amplification.

The comparisons of the site amplification models and hazard curves were performed for a shallow soil site (Sylmar County Hospital) and a deep soil site (Calvert Cliffs). Both time series (TS) and Random Vibration Theory (RVT) approaches were used in 1D equivalent linear site response analysis of the two sites. The variability in the shear wave velocity was introduced through Monte Carlo simulations in which multiple 1D shear wave velocity profiles were generated. Site response analyses were performed on the velocity profiles generated with different levels of variability. The median amplification models were developed for each analysis method (TS and RVT) performed with different levels of shear wave velocity variability.

The median amplification models together with the σ_{lnAF} were used in the convolution method to compute the site-specific soil hazard curves. The soil hazard curve developed from the different site response methods for the shallow and deep site were investigated. The influence of modeling the variation in σ_{lnAF} with input intensity was also explored.

As noted, the convolution approach models variability in the shear wave velocity through multiple 1D site response analyses performed on statistically generated 1D velocity profiles. Each 1D analysis assumes that the given velocity profile extends infinitely in the horizontal direction. This approach does not reflect the conditions in nature, where there exists variability in all three-dimensions. Two-dimensional (2D) site response analysis can account for the velocity variability in the horizontal direction through the use of 2D velocity fields. Similar to 1D analysis, multiple 2D analyses were performed for different realizations of statistically generated 2D velocity fields. In this study, twenty 2D velocity fields were generated using different vertical and horizontal correlation distances. The characteristics of the generated velocity fields were investigated

Two-dimensional site response analyses were performed on the 2D velocity fields generated using different statistical parameters and the influence of these parameters on the surface response across a 100 m x 100m ROI was investigated for a single input motion. Additionally, 2D analyses were performed with an additional

four different input ground motions to investigate the effect of the input motion characteristics on the predicted response across the ROI.

Finally the site amplification predictions from Monte Carlo simulations of 1D and 2D velocity fields were compared. The 1D site response analyses were performed on 1D velocity fields with infinite horizontal correlation, as well as on 2D velocity fields with finite horizontal correlation. These results were compared with 2D analyses performed on 2D velocity fields.

9.2 Conclusions

The major conclusions from this research study are listed below:

- In 1D site response analysis, the median amplification relationships from both TS and RVT analysis are similar except around the site period where RVT analysis can over-predict the site amplification by 20 to 30% as compared to TS analysis. The over-prediction was larger for the deep site than the shallow site. This study showed that introducing variability in the velocity profile via Monte Carlo simulation reduces the over prediction of RVT analysis at the site period to about 10% to 20%.

- RVT analysis does not include the effects of motion-to-motion variability; therefore the σ_{lnAF} from RVT analysis with no shear wave velocity variability is significantly smaller than the σ_{lnAF} from TS analysis. However, when the variability in shear wave velocity is introduced the σ_{lnAF} associated with RVT and TS analysis are at comparable levels even though RVT analysis only includes the effects of velocity variability (no motion-to-motion variability).
- RVT site response analyses were performed using a large set and a small set of input motions derived from different response spectra. The predicted amplification functions are very similar for both sets of analyses with a minor difference in the σ_{lnAF} predictions. Therefore, it is concluded that a smaller set of input motions can be used to predict the amplification model for RVT analyses.
- The soil hazard curves obtained from RVT analysis are very similar to the deterministic surface hazard curve because the σ_{lnAF} associated with the amplification function is close to zero. Both the median amplification model and the associated σ_{lnAF} influence the predicted hazard curves at low hazard levels. Generally, the amplification model with the largest σ_{lnAF} generates the largest ground motions at low hazard levels if the median amplification predictions are similar.
- Generally, σ_{lnAF} increases with input intensity and modeling this variation leads to larger design ground motions if the σ_{lnAF} associated with the large input intensities is larger than the constant σ_{lnAF} .

- For the generated 2D velocity fields, as the correlation distances increase the generated 2D velocity field becomes more uniform. For a single realization increasing the horizontal correlation distance reduces the variability in velocity across the ROI but the variability across twenty realizations increases because the velocity profiles for each realization assemble on one side of baseline profile. The influence of vertical correlation distance is more pronounced when the horizontal correlation distance is large, such that increase in vertical correlation reduces the variability across twenty velocity realizations. The variability across the ROI and across the realizations increases as the variability in the shear wave velocity (σ_{tnVs}) used to generate 2D velocity field increases.
- The statistical parameters used to generate 2D velocity fields have a major influence on the predicted median surface response. The median surface response across a 100 m wide ROI decreases with increasing horizontal correlation distance and decreasing vertical correlation. The influence of the vertical correlation distance on the surface response is more pronounced when the horizontal correlation distance is larger. The variability of the median surface response increases with increasing horizontal correlation distance and decreasing vertical correlation distance. Similarly, the maximum response across the ROI decreases with increasing horizontal correlation distance and decreasing vertical correlation distance.

- In the 2D site response analyses, the influence of the horizontal and vertical correlation distances becomes more pronounced for input motions with larger intensity. These motions induce more nonlinearity (i.e., period lengthening and increased damping) as the variability in the shear wave velocity field increases because the large variability realizations include more low velocity elements. As a result, the median response is reduced and some additional response variability is introduced.
- Comparison of 1D and 2D analyses in which the shear wave velocity was varied via Monte Carlo simulation showed that the median amplification from 1D analysis is 30 % to 40 % smaller than that from 2D analysis. In these analyses the 1D profiles had infinite horizontal correlation. To model the effects of horizontal correlation in the 1D analyses 2D velocity fields were generated and the ten 1D columns across the ROI were analyzed via 1D analysis. Thus, these analyses model some finite horizontal correlation. The amplification predictions from 1D site response analysis with finite horizontal correlation were still about 15% smaller than the results from 2D analysis. The difference between the predictions from 2D analysis and 1D analysis with finite horizontal correlation can be attributed to the influence of the adjacent velocity elements present in 2D analysis and not modeled in 1D analysis. The σ_{lnAF} associated with the 1D analysis (either with finite or infinite horizontal correlation) are generally similar

to the σ_{lnAF} associated with 2D analysis performed on velocity fields with larger horizontal correlation distances.

9.3 Recommendations for Future Work

The recommendations for future work are listed below:

- The amplification functions developed in this research were based on equivalent-linear site response analyses. The amplification functions predict amplification for a wide range of input intensities and at large input intensities the equivalent linear assumption may not be realistic due to the potentially large strain levels associated with high intensity motions. Nonlinear analysis is more appropriate at these large strain levels and should be performed to compute amplification at high input intensities.
- The 2D velocity fields developed in this study were based on assumed correlation distances. Research should be performed to investigate the horizontal and vertical correlation distances indicated by measured shear wave velocity profiles across sites. A correlation distance model could be developed similar to the Toro (1995) one-dimensional model.

- The site response analyses performed in this study only consider the variability in the shear wave velocity. The influence of the variability of other soil properties (e.g., nonlinear modulus reduction and damping curves) on the predicted surface response and the surface hazard curves should be investigated.
- Performing a large number of Monte Carlo simulations is very time consuming for 2D finite element analysis. Variance reduction methods can be examined to reduce the number of Monte Carlo simulations necessary to generate the required information regarding the uncertainty in amplification.

References

- Abrahamson, N. A., and Silva W. J. (1996). Empirical ground motion models. Report to Brookhaven National Laboratory.
- Abrahamson, N. and Silva, W. (2008). Summary of the Abrahamson & Silva NGA ground-motion relations. *Earthquake Spectra*, 24(1), 67-97.
- Bazzurro, P. and Cornell, C. A. (2004). Ground-motion amplification in nonlinear soil sites with uncertain properties. *Bulletin of the Seismological Society of America*, 94(6), 2090-2109.
- Bazzurro, P. and Cornell, C. A. (2004). Nonlinear soil-site effects in probabilistic seismic-hazard analysis. *Bulletin of the Seismological Society of America*, 94(6), 2110-2123.
- Boore, D. M. (2003). Simulation of ground motion using the stochastic method. *Pure and Applied Geophysics*, 160(3-4), 635-676.
- Boore, D. M. and Atkinson, G. M. (2008). Ground-motion prediction equations for the average horizontal component of PGA, PGV, and 5%-damped PSA at spectral periods between 0.01 s and 10.0 s. *Earthquake Spectra*, 24(1), 99-138.
- Campbell, K. W. and Bozorgnia, Y. (2008). NGA ground motion model for the geometric mean horizontal component of PGA, PGV, PGD and 5% damped linear elastic response spectra for periods ranging from 0.01 to 10 s. *Earthquake Spectra*, 24(1), 139-171.
- Cartwright, D. and Longuet-Higgins, M. (1956). The statistical distribution of the maxima of a random function. *Proceedings of the Royal Society of London. Series A, Mathematical and Physical Sciences*, 237(1209), 212-232.
- Chiou, B. J. and Youngs, R. R. (2008). An NGA model for the average horizontal component of peak ground motion and response spectra. *Earthquake Spectra*, 24(1), 173-215.
- Darendeli, M. B. (2001). Development of a new family of normalized modulus reduction and material damping curves. PhD thesis, The University of Texas, Austin.
- Gibbs, J., Tinsley, J., Boore, D., and Joyner, W. (1999). Seismic velocities and geologic conditions at twelve sites subjected to strong ground motion in the 1994 Northridge, California, earthquake: a revision of OFR 96-740. U.S.

- Geological Survey Open-File Report 99-446, U.S. Department of the Interior, U.S. Geological Survey.
- Hanks, T. C. and McGuire, R. K. (1981). The character of high-frequency strong ground motion. *Bulletin of the Seismological Society of America*, 71(6):2071–2095.
- Hudson, M., Idriss, I. M., and Beikae, M. (1994). QUAD4M — A computer program to evaluate the seismic response of soil structures using finite element procedures and incorporating a compliant base. Center for Geotechnical Modeling, Department of Civil and Environmental Engineering, University of California, Davis, CA.
- Kramer, S. L. (1996). *Geotechnical earthquake engineering*, Prentice–Hall, Upper Saddle River, N.J.
- Kottke, A., and Rathje, E. M. (2009). Technical Manual for Strata. Rep. No. 2008/10, Pacific Earthquake Engineering Research Center, Berkeley, Calif.
- Kottke, A., and Rathje, E. M. (2013). Comparison of Time Series and Random Vibration Theory Site Response Methods. *Bulletin of the Seismological Society of America*, 103(3)
- Petersen, M. D., Frankel, A. D., Harmsen, S. C., Mueller, C. S., Boyd, O. S., Luco, N., and Haller, K. M. (2013). The 2008 US Geological Survey national seismic hazard models and maps for the central and eastern United States. *Geological Society of America Special Papers*, 493, 243-257.
- Rathje, E. M., and Ozbey, M. C. (2006). Site specific validation of random vibration theory-based site response analysis. *J. Geotech. Geoenviron. Eng.*, 132(7), 911–922.
- Schnabel, P.B., Lysmer, J., Seed, H.B. (1972). SHAKE—A Computer Program for Earthquake Response Analysis of Horizontally Layered Sites. Report no. EERC 72-12. Earthquake Engineering Research Center, UCB, December.
- Schneider, J. F., Silva, W. J., Chiou, S. J., and Stepp, J. C. (1991). Estimation of ground motion at close distances using the band-limited-white-noise model. *Proc., 4th Int. Conf. on Seismic Zonation*, EERI, Stanford, Calif., Vol. 4, 187–194.
- Toro, G. R. (1995) Probabilistic models of site velocity profiles for generic and site-specific ground-motion amplification studies. Technical Rep. No.779574, Brookhaven National Laboratory, Upton, N.Y.
- UniStar Nuclear Services (2007). Calvert Cliffs nuclear power plant unit 3, combined license application, part 2: Final safety analysis report, rev. 6.

- US Nuclear Regulatory Commission. (2001). Technical basis for revision of regulatory guidance on design ground motions: hazard-and risk-consistent ground motion spectra guidelines. Report NUREG/CR-6728.
- US Nuclear Regulatory Commission. (2002). Technical basis for revision of regulatory guidance on design ground motions: Development of hazard- and risk-consistent seismic spectra for two sites, NUREG/CR-6769.
- Vanmarcke, E. (1983). Random Fields: Analysis and Synthesis. Cambridge MA. MIT Press.

Vita

Menzer Pehlivan was born in Ankara, Turkey on September 17th, 1986, to Ulku Gelisen and Osman Gelisen. She graduated from Middle East Technical University Foundation Private High School, Ankara, Turkey, in 2003. In June 2007, she graduated with a Bachelor of Science degree in Civil Engineering from Middle East Technical University, Ankara, Turkey. In September 2007, she entered the graduate program of the Civil Engineering Department at Middle East Technical University, Ankara, Turkey. She completed her Masters of Science in Civil Engineering in July 2009 with a thesis entitled “Assessment of Liquefaction Susceptibility of Fine Grained Soils”.

Permanent email: menzer.pehlivan@gmail.com

This dissertation was typed by Menzer Pehlivan.